ABSTRACT

Title of Dissertation: HIGH TEMPERATURE NANOMANUFACTURING FOR EMERGING TECHNOLOGIES

Yonggang Yao, Doctor of Philosophy, 2018

Dissertation directed by: Liangbing Hu,
Department of Materials Science and Engineering

High temperature processing can provide sufficient activation energy for materials' compositional, structural, and morphological evolutions, and is essential for various kinds of reactions, synthesis, and post-treatment. However, the current high temperature heating sources, mostly furnaces, are far from satisfying for nanomaterials processing owing to their bulky size and limited temperature and ramp range (~1300 K, ~10 K/min). In this thesis, we have focused on the study of electrical triggered Joule heating as a new route for high temperature engineering of nanomaterials toward nanomanufacturing. We developed facile, highly stable and controllable heating strategies for micro/nanoscale high temperature engineering.

Ultrahigh temperature annealing (>2500 K) is applied to carbon nanomaterials to address the defects and poor interfacial problems. In the carbon nanofibers (CNFs), the high temperature graphitizes the carbon nanomaterials with significantly improved crystallinity and less defects. Importantly, the rapid heating (~100 K/min) leads to

junction welding at fiber intersections. Similarly in carbon nanotubes (CNTs), welded CNTs is achieved by incorporating a thin polymer coating, followed by high temperature annealing to form 3D interconnected structures, defined as an "epitaxial welding" process.

Ultrafast thermal shock (~2000 K in 55 ms) is applied to metal salt loaded carbon substrates for *in-situ* synthesis of ultrasmall, well-dispersed nanoparticles. Metal salts decompose rapidly at high temperatures and nucleate into well-dispersed nanoparticles during the rapid cooling (rate of ~10^5 K/s). By varying the composition in salt mixtures, we synthesized bimetallic, multimetallic and high entropy alloy nanoparticles (HEA-NPs) containing up to 8 different and immiscible elements. The high temperature leads to atomic mixing in the liquid alloy state, while rapid quenching freezes the completely mixed state to form solid solution nanoparticles with a narrow size distribution. This is for the first time HEA-NPs were synthesized, enabled by the unique thermal shock method.

We also developed scalable approaches such as employing non-contact radiative heating for large scale substrates (either conductive or non-conductive) and continuous roll-to-roll production. The high temperature engineering on nanomaterials are highly facile, energy-efficient, and reliable toward scalable nanomanufacturing. More exciting results and products are expected for various nanomaterials during/after the unique high temperature engineering.

HIGH TEMPERATURE NANOMANUFACTURING FOR EMERGING TECHNOLOGIES

by

Yonggang Yao

Dissertation submitted to the Faculty of the Graduate School of the
University of Maryland, College Park, in partial fulfillment
of the requirements for the degree of
Doctor of Philosophy
2018

Advisory Committee:
- Associate Professor Liangbing Hu, Chair
- Professor Teng Li, Dean's Representative
- Professor Michael Zachariah
- Professor Lourdes Salamanca-Riba
- Assistant Professor Yifei Mo
- Associate Professor: Dongxia Liu

© Copyright by
Yonggang Yao
2018

Dedication

To my parents and all my family members, for their constant supply of love and support.

To my supervisor, colleagues, and all collaborators, who have helped me a lot through this journey.

Acknowledgements

I would like to thank all the people who helped me make this dissertation possible. Your invaluable input and support are critically important.

First of all, I want to thank my advisor Professor Liangbing Hu, for his continuous and supportive supervising. He has taught me how to be an outstanding scientist and also success in life. I am also grateful for all the opportunities he provided during and after my Ph.D. I would also like to thank my lab mates for their time and efforts. Together we built a strong and productive Hu group.

I wish to thank important collaborators: Dr. Reza Shahbazian-Yassar, Zhennan Huang, and Dr. Anmin Nie from University of Illinois Chicago; Dr. Chao Wang and Dr. Pengfei Li, and Tiancheng Pu from Johns Hopkins University; Dr. Michael Zachariah, and Dr. Rohit Jacob from University of Maryland; Dr. Ju Li and Dawei Yu from Massachusetts Institute of Technology. Also thanks to the advanced equipment from UMD NanoCenter and AIM lab.

Finally, I would like to thank the financial support from National Science Foundation.

Table of Contents

Chapter 1: Introduction

1.1 Nanomanufacturing

Nanomaterials are materials which have at least one dimension in 1-100 nm range, and often have unique optical, electronic, or mechanical properties due to size effect.[1] While there are lots of natural nanomaterials and nanostructures, most of the currently studied and applied nanomaterials are synthesized through various processing or engineering methods. Owing to the unique size-dependent effects (surface effect and quantum confinement),[2–5] nanomaterials shows drastically different structures and properties from their bulk counterpart, leading to the enormously increasing interests from both research and industry for the exploration of new materials/structures with superior properties that can be applied in various fields like energy storage, advanced electronics, biomedical engineering, medicine, environmental and life science, etc.

Although great breakthroughs in nanoscience have been made since past few years, successful transfer of these existing nanoscience to practically applicable devices and products is severely hindered due to the difficulty in precisely handling of nanomaterials at nanoscale and further scale up toward large-scale manufacturing.[6,7] Such a challenge has surged a new research area of “nanomanufacturing” - both the production of nanoscale materials and the manufacturing of parts “bottom up” from nanoscale materials or “top down” in smallest steps for high precision, according to the national nanotechnology initiative (NNI) of US.[7] The national nanotechnology initiative (NNI) has named nanomanufacturing as one in five of top priority areas and also one grand challenge, demonstrating the significance of developing nanomanufacturing techniques to turn the nanotechnology's potential into reality.

While the typical "top-down" nanofabrication have been developed for many years in the semiconductor industry and becomes more and more sophisticated and mature, the scalable "bottom-up" synthesis and fabrication remains largely unexplored. There is an urgent need to develop fast, high volume, high rate, cost-effective, reliable, scalable manufacturing techniques to fabricate parts through "bottom-up" technologies such as self-assembly, in-situ synthesis, etc. The current focus of nanomanufacturing is threefold (NNI): (1) effective and scalable nanoscale materials synthesis, (2) scale-up manufacturing for industrial mass production, and (3) system integration across various dimension scales. In this thesis, we aim at developing various high temperature processes as "bottom-up" nanomanufacturing through (1)-(3).

1.2 Nanomaterials and challenges

Currently, the most important nanomaterials are carbon-based nanomaterials, such as carbon nanotube and graphene, and nanoparticles including metallic nanoparticles and semiconductor quantum dots.[5,8] Carbon is called "The materials of the 21st century" because of its diversified allotropes and superior properties. Carbon nanomaterials have a lot of allotropes, from 0 dimension fullerenes, 1-dimensional carbon nanotube and carbon nanofibers, 2-dimensional graphene and reduced graphene oxide, to complex 3-dimensional carbon sphere, which all originated from the 2D graphene sheet structure (Figure 1.1a).[8] The strong sp2 hybridized (Figure 1.1b) carbon-carbon bond and perfect hexagonal structure in the 2D graphene sheet gives excellent mechanical properties while the one-dimensional confinement of electronic and phonon states lead to high in-plane electronic and thermal conductivity.[9] For example, single wall carbon nanotube (SWNT) has an exceptional in-plane Young's modulus of 1 TPa and tensile strength of 50-150 GPa, the high thermal conductivity of 3000-6000 W/m/K and electronic conductivity of 10E6-10E7 S/m. As a comparison, copper has a Young's modulus of 120 GPa, thermal conductivity of 400 W/m/K and electronic conductivity of 6*10E7 S/m, with a much higher density of 9 g/cm^3 (carbon-based < 2 g/cm^3).[9] With all these exceptional properties, carbon nanomaterials have been intensively studied for energy storage (Li-ion batteries, supercapacitors, fuel cells), advanced electronics to partially replace Si-based technologies, high performance lightweight composite materials with extraordinary mechanical properties, among other numerous applications.[8,9]

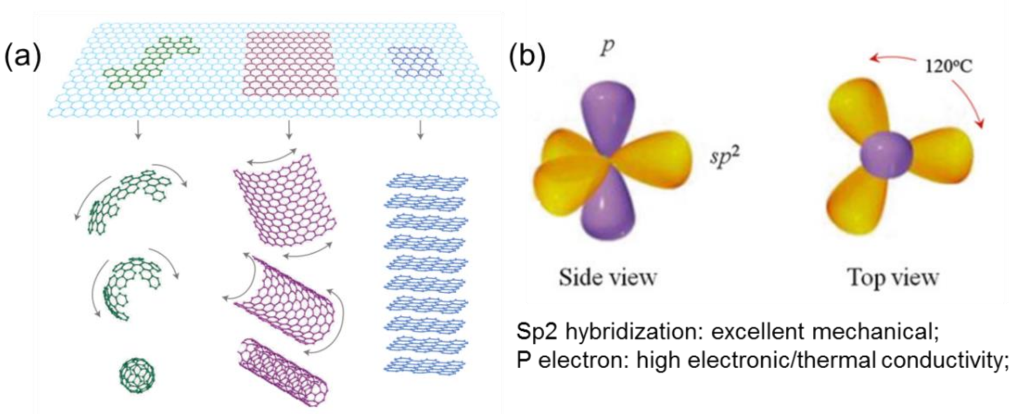

Figure 0.1. (a) Various allotropes originated from the 2D graphitic carbon sheet, in another word, graphene.[8] (b) The origin of superior properties in carbon-based nanomaterials: the sp2 hybridization and crystal structure gives excellent mechanical properties; the free p electron give high electronic and thermal conductivities.[9]

Unfortunately, these superior properties are often compromised as carbon nanomaterials are assembled into bulk structures on a macro scale, an issue of scaling (nanomanufacturing). For example, single-walled CNT are known to exhibit electrical conductivity above 10000 S/cm, but the reported conductivity of self-assembled CNT membranes is two orders of magnitude less, approximately 100 S/cm.[10–12] Such an issue of scaling limits the use of carbon nanostructures and is attributed to the poor physical contacts (van der Waals force) between these carbon nanostructures that give large contact resistance as well as easy sliding. It is reasonable to believe that by addressing the poor contacts between carbon nanomaterials, the bulk performance of interconnected carbon structures could be improved significantly.

On the other hand, nanoparticles are another important part of nanomaterials spanning from the metallic nanoparticle, semiconductor quantum dot, to ceramic nanoparticles and so on.[1,13] Due to its versatile variations in size, shape, structure, and compositions, they show various unique properties for application in energy storage, biomedical engineering, drug delivery, advanced imaging, and catalytic reactions. The essential feature of nanoparticles is that their physical and chemical properties are highly dependent on their size.[4,5,14] For example, Figure 1.2b shows the scaling of melting temperature of Au nanoparticle with decreasing in size as a surface scaling effect. Figure 1.2c shows the change of density of states as the spatial confinement increases as a quantum confinement effect in nanoparticles. Such a size effect originated from the increasing number of surface atoms which has very different electronic and bonding states compared with body atoms and therefore much higher reactivity. Since the properties and performances of nanoparticles are highly dependent on its size, the controllable synthesis of ultrafine nanoparticles with narrow size distribution is of very important and has been successfully realized by various wet chemistry methods[1,5,13,15–17] (Figure 1.2a).

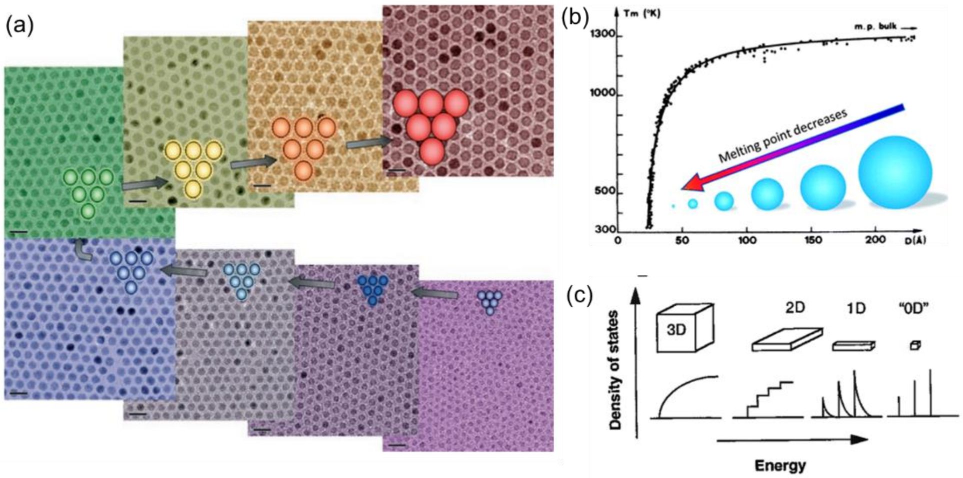

Figure 0.2. (a) TEM images of iron oxide nanoparticles with different diameters.[13] (b) Size-dependent of the melting temperature of Au nanoparticles due to surface effect.[14] (c) Change of density of states due to the spatial confinement.[5]

Similar to carbon nanomaterials, these synthesized nanoparticles also encountered serious obstacles in scaling up for mass production and device integration. For example, in many applications, the synthesized nanoparticles should be dispersed onto support for applications such as energy storage and electrochemical catalysis. While fine control over size distribution can be easily realized through wet chemistry methods, it is still very challenging to effectively disperse these nanoparticles onto support without losing their reactivity due to serious aggregation.[13,15] The highly reactive surface of nanoparticles are prone to aggregate during the redistribution process, rendering the loss of high performance of nanoparticles due to loss of reactive surfaces. Therefore, manufacturing of high-quality nanoparticles well dispersed onto the support in an efficient manner remains a challenge, especially due to agglomeration during assembly processes. In the meantime, due to the slow kinetics in wet chemistry, there is an increasing challenge in synthesizing multielements nanostructures as the number of elements increased, owing to the difficulties in the overall kinetic control of multiple elements with intrinsically different physical and chemical properties. Finally, since nanomaterials are in the scale way beyond our human handling capability, there is a fundamental challenge to develop effective and reliable methods for mass-production of their assembled structures without sacrificing their superior performances, namely protocols for “nanomanufacturing”.

1.3 High temperature nanomanufacturing

To effectively tackle the above-mentioned nanomanufacturing problems and challenges, fundamentally new processing and engineering methods are needed. In the manipulation of nanomaterials, the processing temperature is critically important. Specifically, high temperature processing provides sufficient activation energy which is critical to enable various kinds of reactions, synthesis, and treatments. In the bulk materials synthesis and processing, high temperature treatment is everywhere. For example, high temperature annealing of carbon-based materials is an effective way to increase the crystallinity and remove impurities/defects, leading to increased conductivity and mechanical properties. For nanoparticles, the high temperature is also essential for particle synthesis via thermal reduction or thermal decomposition.

However, currently, the high temperature heating source, namely furnaces, is far from satisfying to be applied as high temperature source for nanomaterials. First, furnaces are very bulky in size and are too large for precise temperature control and processing for nanomaterials (at the nanoscale). Second, due to the large chamber size and radiation heating strategy, the temperature and heating/cooling rate of furnaces are largely limited, typically with a temperature around 1300 K and heating/cooling rate of 10 K/min. Third, owing to the slow heating/cooling rate, the high temperature duration is often long and very often can cause severe aggregation of nanoparticles due to particle sintering/coarsen at high temperature. As a result, the current researches in nanoscience and technologies are mostly focused on the low-temperature behavior of nanomaterials with slow heating/cooling rate, leaving the study of extreme temperature treatment (high temperature, ultrafast heating/cooling rate) a virgin field to be explored.

In fact, high temperature can be well controlled via electrical triggered Joule heating where the electric power is converted into internal energy and revealed by increasing temperature. The temperature can be easily controlled by tuning the input electrical power. In history, carbonized bamboo fibers were the first commercial filaments used in Edison's light bulb for lighting, and have demonstrated excellent performances as high temperature lighting/heating source. Previously, Joule heating was also applied to study the high temperature lighting behavior of various carbon materials.[18–22] Unfortunately, these works all focus on the lighting and high temperature phenomena, while leaving these materials after high temperature treatment not well characterized and studied, and therefore, excluding the possibility of utilizing Joule heating induced high temperature as a synthesis or manufacturing methods for nanomaterials.

We have found that there are several merits of using Joule heating as a new route for high temperature treatment of nanomaterials. (1) The temperature can be easily and precisely controlled by input electrical field. (2) The maximum temperature can reach up to 3000 K, which is far beyond most furnace temperatures and provides a great opportunity for ultrahigh temperature treatment of nanomaterials which is rarely studied. (3) The ramping rate can reach up to unparalleled $10E^5$ K/s, a record high heating/cooling rate that can enable non-equilibrium treatment of nanomaterials that is again rarely studied before. (4) Joule heating is directly applied to the object itself and nearly 90% of electrical energy is effectively converted into Joule heat, making the process highly effective and economic for scalable nanomanufacturing.

Importantly, the structures and properties of nanomaterials changed significantly after high temperature treatment, especially under extreme conditions such as ultrahigh temperature or ultrafast heating/cooling, which are seldom studied before. Such a highly controllable heating strategy can act as a new protocol for nanomaterials processing and manufacturing and provides the possibility for the high temperature engineering and manufacturing of various nanomaterials for the development of new structures and improved properties for advanced applications.

1.4 Summary and motivation

Since most studies and researches on nanomaterials are at low temperature with slow heating/cooling rate, it is of great interest for us to employ high temperature engineering methods to study those nanomaterials, especially under/after extreme high temperature treatments (ultrahigh temperature, ultrafast heating/cooling), in order to develop new materials and structures with drastically improved properties, and potentially a new way for scalable nanomanufacturing.

Based on the high temperature experiments we developed recently, in this thesis, I will present and discuss in mainly three parts. (1) Develop of highly stable and controllable high temperature heating source for microscale/nanoscale heating, and study of related high T phenomena. (2) Study the behaviors of various nanomaterials under/after the extremely high temperature conditions: (i) high temperature annealing of carbon-based nanomaterials; and (ii) Rapid thermal shock synthesis of various nanoparticles. (3) Develop of rapid and efficient high temperature processing methods toward scalable manufacturing.

(Part I) Develop a highly stable high temperature source capable for microscale and nanoscale heating with well-controlled temperature, heating/cooling rate. Besides the 2D flexible carbon film for high temperature lighting, we developed a three-dimensional (3D) printed reduced graphene oxide (RGO)-based heaters to function as high-performance thermal supply with high temperature (3000 K) and ultrafast heating rate (10^5 K/s). Compared with other heating sources, such as furnace, laser, and infrared radiation, the 3D printed heaters have the following distinct advantages: (1) the RGO based heater can operate at high temperature up to 3000 K because of using the high temperature-sustainable carbon material; (2) the heater temperature can be ramped up and down with extremely fast rates ~20,000 K/second; (3) heaters with different shapes can be directly printed with small sizes and onto different substrates to enable heating anywhere. The 3D printable RGO heaters can be applied to a wide range of nanomanufacturing when precise temperature control in time, placement, and the ramping rate is important.

(Part II) The structure and properties change of nanomaterials under/after extreme high temperature treatment can be very interesting and it is expected new structures with excellent performances can be achieved via extreme high temperature engineering. We mainly focused on two aspects: (1) high temperature annealing of carbon-based nanomaterials and (2) ultrafast thermal shock for the synthesis of well-dispersed nanoparticles.

High temperature annealing was applied to carbon nanofibers (CNFs) to temperatures greater than 2500 K at a heating rate of 200 K/minute. After the high temperature treatment, not only the CNFs become highly crystalline with improved conductivity and purity, but also the individually intertwined CNFs were welded at junctions, namely, these CNFs are fused together for adjacent CNFs. The welded-CNFs shows greatly improved conductivity and mechanical properties as a result of forming 3D interconnected CNFs structure, addressing the poor interface problems in many carbon-based nanomaterials. Based on this finding, we continue to weld crystalline CNTs together by incorporating a thin layer of the polymer as the welder to link the crystalline CNTs to form 3D interconnected structures, defined as an "epitaxial welding" process. The pristine individual CNTs were connected by the thin polymer shell on CNTs; after high temperature annealing, these polymer shells were in situ converted into the graphitic shell using the embedded CNTs as growth templates. The final 3D CNTs shows enhanced conductivity and mechanical properties by addressing the poor interface problems. The high temperature annealing not only help remove the defects in carbon-based nanomaterials, but also bring these nanomaterials together into an interconnected structure, which is critical to transfer their excellent properties at nanoscale to macroscale.

We also successfully realized a rapid thermal shock method (RTS) to *in-situ* synthesize well-dispersed nanoparticles on a conductive fiber matrix from metal precursor salts. The carbon nanofibers coated with metal salts was ramped from room temperature to ~2000 K in 5 milliseconds, which corresponds to a rate of 400,000 K/s. Metal salts decompose rapidly at such high temperatures and nucleate into well-dispersed metallic nanoparticles during the rapid cooling step (cooling rate of ~100,000 K/s). These ultrafine, well-dispersed nanoparticles on conductive substrates can be utilized directly for catalytic reactions. Based on this finding, we synthesized bimetallic nanoparticles by tuning the initial precursor into salt mixture. The high temperature is well above the decomposition temperature of both salts and even above their melting point, therefore, leading to atomically mixed nanoparticles owing to the atomic mixing at high temperature (liquid alloy state). The homogeneous alloy structure shows high catalytic properties.

Further exploration of these extreme high temperature engineering was applied to the synthesis of multimetallic nanoparticles. In our method, the high temperature (~2000 K, 55 ms) enables complete mixing of up to 8 immiscible elements (e.g. PtPdNiFeCoAuCuSn) in the liquid metal state; rapid quenching (rate of ~105 K/s) freezes the completely mixed state to form solid solution nanoparticles with a narrow size distribution. The thermal shock method leads to homogeneous solid solution nanoparticles (i.e. high entropy alloy nanoparticles, HEA-NPs), where each element is uniformly distributed (no phase separation) to maximize the mixing entropy. This is for the first time we synthesized HEA-NPs through the unique high temperature shock method which combines high temperature and rapid quenching to enable unique HEA structure and nanoparticle formation. The HEA-NPs exhibit highly improved catalytic performances for ammonia oxidation.

(Part III) It is obvious that novel nanomaterials and nanostructures are enabled by high temperature engineering, especially those with extreme conditions (ultrahigh temperature, ultrahigh heating/cooling rate). It is found these high temperature engineering methods are also highly facile, efficient, and reliable towards scalable nanomanufacturing. We also developed methods to even further speed up the process. For example, thermal shock of 3D carbonized wood structure enables synthesis of nanoparticles in a 3D bulk structure with 100x increase in particle production efficiency. Also, by employing non-contact radiative heating, large-scale substrate can be easily incorporated and a continuous roll-to-roll production process is possible for the rapid synthesis of nanoparticles on either conductive or non-conductive substrate, pushing the synthesis capability even further.

Chapter 2: Literature Review

The literature review consists of basic properties and challenges in materials selected (carbon nanomaterials and nanoparticles), and existing high temperature processing methods. Other background information for specific problems will be reviewed separately in the introduction part of each chapter.

2.1 Carbon-based nanomaterials

In my research, carbon nanomaterials are subjected to high temperature annealing for the new structure and improved properties. Previously there a lot of studies focused on the structures and properties of carbon nanomaterials, which can be a good reference data for our experiments. Below, we will briefly review the structure and properties of carbon nanomaterials from literature.

Raman is a very powerful and versatile tool to characterize the vibration modes and phonons in nanomaterials and particularly useful for the investigation of carbon materials due to the resonance effects. Four characteristic Raman bands, namely the radial breathing modes (RBMs), G-band, D-band, and 2D-band are distinct in Raman spectra of carbon materials with RBMs only appears in nanotubes[9,23] For example, in Figure 2.1a, the Raman spectrum of SWNT is presented with all feature peaks. The RBM is the vibration modes in which all the carbon atoms are moved perpendicularly to the nanotube axis and can be used to determine the nanotube chirality. The G band originates from the vibration of nearby carbon atoms in reverse directions along the nanotube axis. This peak is the most important information about the crystallinity of carbon materials in terms of its graphitic degree. On contrary, the D band involves phonon scattering in the process and is related to the defect or sp3 hybridized carbon bond in the sample materials. Similarly, the structure and bond of carbon-based materials can be revealed by X-ray diffraction (XRD) and x-ray photoelectron spectroscopy (XPS) with different information. XRD give the crystallinity of carbon materials and also the featured interlayer distance, while the XPS shows clearly the bonding information and content/purity of carbon nanomaterials (Figure 2.1b and c).

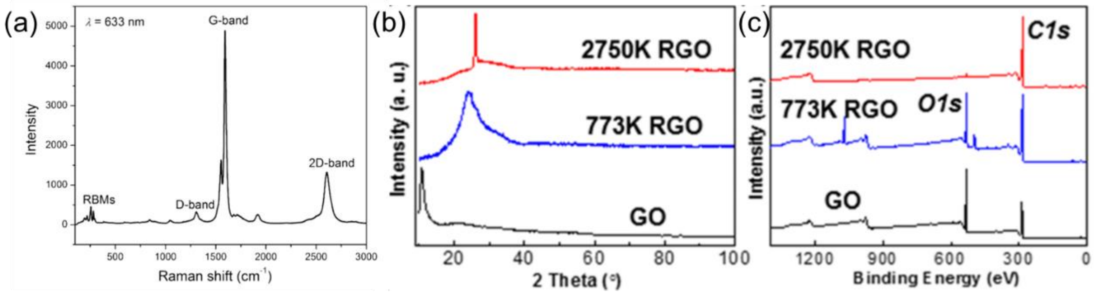

Figure 2.1. Typical structure characterization of carbon-based nanomaterials. (a) Raman spectrum of SWNT.[9] (b) XRD and (c) XPS characterization of GO and RGO at different treatment temperature.[24]

As stated before, carbon-based nanomaterials have excellent mechanical properties and high electronic and thermal conductivity originated from its increased graphitic sp2 layer. These properties have been well studied before. As an example, we compared those mechanical properties of carbon nanotube with carbon fiber and copper (Table 2.1),[9] and carbon nanomaterials still show superior properties. Unfortunately, these excellent properties are not inherited into the assembled form of these nanomaterials due to the poor interface between carbon nanomaterials: only weak van der Waals force between neighborhood nanomaterials. We will show how high temperature annealing can help improve the performances of assembled nanomaterials by several orders, especially in conductivity.

Table 2.1: Physical properties of CNTs compared with other engineered materials [9]

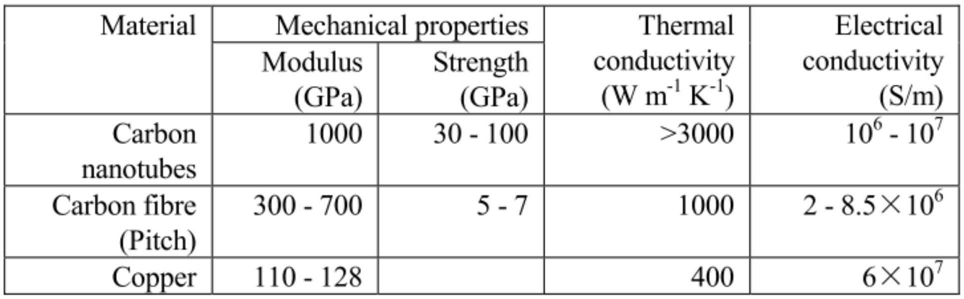

Material	Mechanical properties		Thermal conductivity ($W m^{-1} K^{-1}$)	Electrical conductivity (S/m)
	Modulus (GPa)	Strength (GPa)		
Carbon nanotubes	1000	30 - 100	>3000	10^6 - 10^7
Carbon fibre (Pitch)	300 - 700	5 - 7	1000	$2 - 8.5\times10^6$
Copper	110 - 128		400	6×10^7

2.2 Nanoparticles

In my research, I tried to use high temperature thermal shock for the in situ, ultrafast synthesis of nanoparticles well dispersed on carbon support for advanced applications. Previously literature also cover a lot of synthesis methods for nanoparticles and their applications, which can be good reference/comparison for our experiments. Below, we will briefly review the synthesis methods for nanoparticles and the applications we are interested.

Nanoparticles can be made using a variety of synthesis methods and can be classified into two categories as physical top-down process and chemical bottom-up assembly. Physical top-down methods include ion beam lithography, X-ray lithography, and high energy ball milling and laser ablation. Although physical methods are usually simple, they are highly energy sensitive and it is very difficult to control the size and shape of final nanoparticles by these top-down process. In contrast, the chemical bottom-up process uses atoms as building blocks to self-assemble into large cluster and nanoparticles. Chemical bottom-up synthesis can be realized by numerous ways with precise control ability on the final particle size, shape, crystal facets, and composition, and therefore are widely applied for the synthesis of nanoparticles.[1,13,15–17]

In wet chemistry synthesis, the nanoparticles are dispersed in solution, which is difficult to handle, prone to aggregates, and not suitable for many application which requires dispersed nanoparticles on conductive matrix. The support not only provides mechanical strength but also chemical and sinter resistance. In the meantime, the support can interact with nanoparticles as heterogeneous catalysts for improved performances. There are typically three ways to prepare nanoparticles dispersed onto a support (Figure 2.2a). A widely used approach is to impregnate the porous support into precursor solution for in situ thermal/chemical reduction/decomposition after drying. Another one is to fill the porous support with a melt of phase by a molten precursor and then in situ formation of nanoparticles. However, if one want precise control of nanoparticles formed without the influence of support, the NPs can be synthesized by conventional colloidal methods and then impregnated into the porous support. Although it is possible to incorporate pre-synthesized nanoparticles into the support, more often the nanoparticles are prepared in situ onto and with the help of support to avoid serious aggregation as well as poor dispersion of nanoparticles inside the porous support.

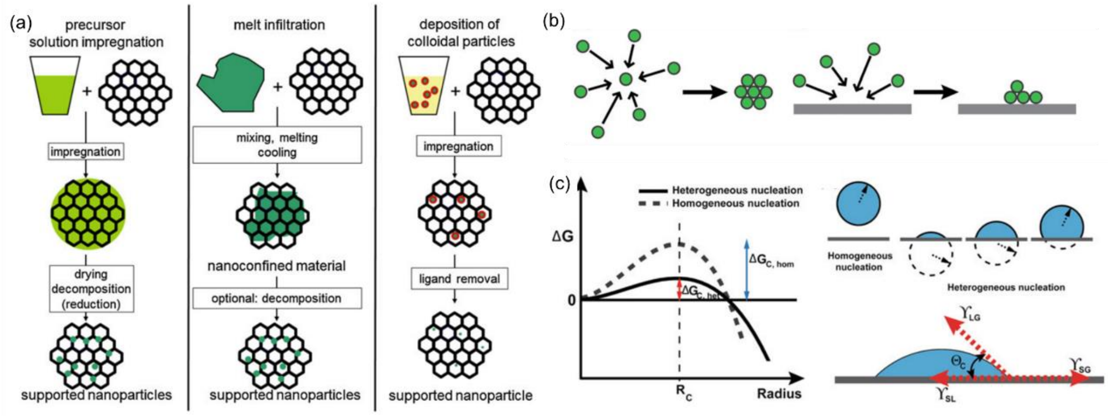

Figure 2.2. (a) General methods for preparation of nanoparticles onto the mechanical support.[1] (b) The difference in the nucleation and growth of nanoparticle in the homogeneous and heterogeneous environment. (c) The free energy and particle formation schematic to show the difference.[1,16,17]

It should be noted that with the present of support, the nucleation of nanoparticles becomes very different from those in homogeneous solution. The difference is schematically shown in Figure 2.2b and c.[16,17] For nucleation process, homogeneous nucleation goes through a large nucleation energy barrier and only when the size of nuclei reaches large enough (> critical size), the nanoparticles can be thermodynamically favored and stabilized. In contrast, the heterogeneous nucleation on the surface of the support is easier with lower activation energy. The stable interface between nuclei, support and solution form a non-spherical shape which has much large diameter curvature and helps to minimize the activation energy required for the further stabilization and growth. This is clearly demonstrated in Figure 3-4c with Gibbs free energy comparison of two cases and the comparison of diameters. Therefore, with the presence of support, the nucleation is much easier for the nanoparticles to in situ grow onto a porous support.

2.3 Existing high temperature methods

In my research, high temperature annealing and high temperature thermal shock were applied to the processing of carbon nanomaterials and synthesis of nanoparticles, respectively. Previous literature also reported high temperature methods for the similar purpose, which can be a good reference and compared with our data. Below, we will briefly review the existing high temperature methods for annealing and synthesis of nanoparticles.

For high temperature annealing, the most used methods are furnaces because they are the only way available for the constant supply of high temperature. However, the furnace and hotplate are bulky in large size and the heating strategy used is thermal radiation heating, leading to a very energy intensive and consuming of using these for high temperature annealing. Most important, the nanomaterials are often very tiny and small, such a bulky design is definitely not suitable for nanoscale material processing. In the meantime, due to the large size and radiation heating method, the furnace and hotplate has very limited temperature control ability: the typical heating rate is around 10 K/min and the maximum temperature is 1300 K. Such a limited capacity is definitely not enough to explore the temperature, especially the high temperature, annealing effect on nanomaterials.[25] Therefore, the extremely high temperature is hard to obtain and the rate control is very limited to be used for high temperature annealing.

On the other hand, high temperature is also applied for the nanoparticle synthesis by mainly combustion synthesis and aerosol spray pyrolysis (Figure 2.3).[26–34] Since nanoparticles are prone to aggregate to minimize its surface energy, high temperature can be detrimental to the uniform size distributions. Therefore, precisely short time control at high temperature is critical for synthesizing ultrafine nanoparticles. Combustion synthesis is an effective method to synthesize ceramics, refractory materials, intermetallic, and even thermoelectric, by using the exothermic reaction heat generated by the reactive precursors after ignition. According to the initial reaction phase, combustion synthesis can be classified as conventional solid-state self-propagating high temperature synthesis (SHS), solution combustion synthesis (SCS), and gas-phase combustion. As a high temperature synthesis method, SHS can achieve temperature as high as 4000 K with a heating rate around 10E3 K/s in a relatively short time (0.05-5 s), demonstrating the capability for fast high temperature reaction.[30,31]

For preparation of nanoparticles, the most used method are solution based combustion owing to the uniformity of size distribution of resultant nanoparticles.[26] The typical SCS heating curve is shown in Figure 3-3b, with maximum temperature around 1200 K and a maximum rate around 120 K/s due to the loss of thermal energy through water medium.[35] Aerosol spray pyrolysis involves the process of making aerosol particles and fast synthesis of nanoparticles on the gas flame (Figure 2.3c). The initial precursor droplets are heated above 1200 K in seconds and cooling down subsequently. The key to such method is rapid heating of precursor allows the quick formation of nanoparticles. The short duration time and fast subsequent cooling can freeze the nanoparticles in the matrix.[28] However, since the synthesis is carried out in the gas phase, this method can only be used for materials that can be atomized. It is hard to synthesise nanoparticles in situ inside of integrated substrate or substrate that are sensitive or cannot sustain high temperature by aerosol spray pyrolysis.

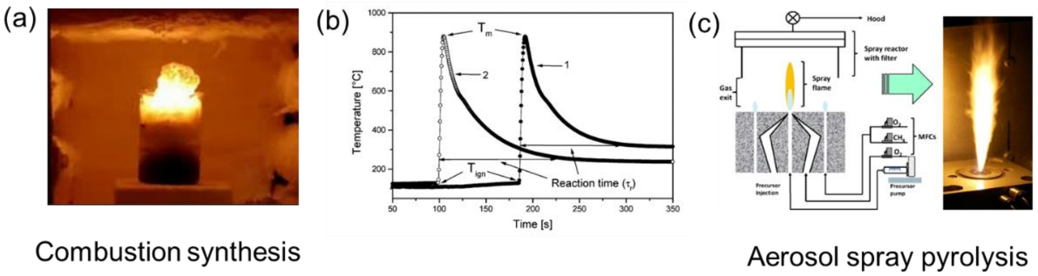

Figure 2.3. (a) High temperature synthesis of nanoparticles by combustion. (b) Typical temporal temperature profile during a solution combustion synthesis.[35] (c) High temperature aerosol spray pyrolysis.[28,29]

For above mentioned two kinds of high temperature methods, although they have demonstrated high temperature with fast heating and cooling rate, there are still remain challenges and disadvantages of using these methods for nanoparticles synthesis: (1) in both cases, the substrate is not preserved and it is extremely hard to incorporate these synthesized nanoparticles into support by post-treatment; (2) the product are limited to reactive products which are mainly oxides, carbides, intermetallic etc. (3) they usually result in coarse particles and need follow-up treatment such as ball milling or chemical treatment; (4) although the high temperature duration for both cases is short (several seconds), the high temperature duration is still too long for nanoparticles and importantly they are hard to control in both cases. For Joule heating used in our experiments, the temperature, heating/cooling rate, and high temperature duration time can be precisely controlled for the formation of nanoparticles on integrated support with controlled size distribution.

Chapter 3: Experimental setup and characterizations

3.1 Materials preparation

Preparation of graphene oxide (GO) ink: GO was prepared from graphite according to the modified Hummer's method.[15] Briefly, 1.5 g graphite was added to 200 mL H_2SO_4/H_3PO_4 (volume ratio 9:1) solution. 9 g $KMnO_4$ was gradually added to above solution and stirred for 12 h at 250 rpm at 50 °C. The solution was then cooled to room temperature and poured onto 400 mL ice and 3 mL H_2O_2 was added to the solution while stirring. The solution was washed with 30 mL 37% HCl and followed by washing with distilled water by centrifuging at 8000 rpm. The upper clear solution was dumped and refilled with distilled water for centrifugation until there is no visible AgCl precipitation in a test solution by adding $AgNO_3$. The resulted GO solution was freeze-dried (- 50 °C, 0.6 Pa) to remove the solvent and then distilled water was controllably added to form highly concentrated GO inks. For 3D printing purpose, the printable GO ink had a concentration of 80 mg/ml in water. The highly concentrated GO can be stored in a refrigerator at 7 °C.

Carbon nanofibers (CNF) preparation: Polyacrylonitrile (PAN) was purchased from Sigma-Aldrich and dissolved in dimethylformamide (DMF) to form an 8%wt solution and stirred at 60 °C for 12 hours. The resulting transparent solution was electrospun at a voltage of 10 kV, a spinning distance of 15 cm and a feeding rate of 1 ml/hour. The electrospun nanofibers were collected by a rotation drum at a speed of 80 rpm. The PAN nanofibers were then stabilized at 260 °C for 2 hours in the air and carbonized at 600 °C in an argon protected atmosphere.

Preparation of CNF with metal salts: The PAN nanofibers were first stabilized at 533K for 5 hours in the air and then carbonized at various temperatures (873 K, 1073 K, 1273 K) for 2 hours in argon. Although the CNF-873K has a higher defect concentration to disperse nanoparticles, the sample requires a higher voltage and power to induce CTS (sometimes beyond the external power source's voltage/power limit depending on the sample's size). CNF-1273K is highly crystalline (fewer defects) and demonstrates poor nanoparticle dispersion capabilities. CNF-1073K acted as the ideal carbon support due to its defect density for nanoparticle dispersion and ease of applying an electrical pulse within the limits of the external power source. In this work, CNF-1073K is the carbon support used unless stated otherwise.

For aqueous precursor solutions, the CNF films were dipped into the mixed metal salt solutions (0.01 mol/L for each element), placed under vacuum for 30 minutes, and then suspended in a 60°C oven to dry. For ethanol-based precursor solutions, the mixed solutions (0.05/n mol/L for each element, where n is the total number of elements) were directly dropped onto the suspended CNF film with a loading of ~120 $\mu L/cm^2$ and left to dry at room temperature. In general, the ethanol-based solutions result in more uniform loading (and particle dispersion) owing to improved wettability to carbon.

3D printing process: 3D printing was performed by a 3D printer (Fisnar F4200n) with capability for programmable patterning in three dimensions built layer-by-layer. In our experiments, a 3D printing nozzle (diameter 300 µm) was used with pressure controlled at 60 psi and the nozzle's moving speed was 1-5 mm/s. The dimension of 3D printing was input into the system as design. The whole printing process took less than 10 minutes for a 3D heater with 12 layers. After printing, the printed structures were freeze-dried at – 50 °C with a vacuum pressure of 0.6 Pa to remove the water solvent and maintain the 3D structures.

3.2 High temperature setup and process

The Joule heating process was controlled by an electric field to the set temperatures with at a controllable rate. The Joule heating setup is displayed in Figure 3.1a. The CNF samples were connected to copper electrodes by silver paste and suspended on a glass substrate to avoid the thermal damage during the Joule heating process. The CNF films were heated to a high temperature in an argon protected atmosphere or vacuum.

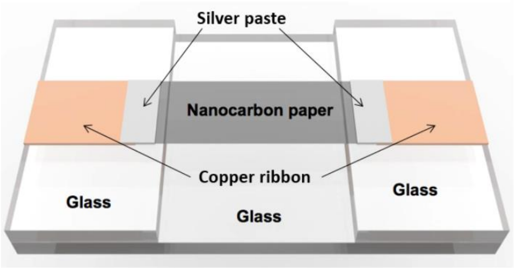

Figure 3.1. Schematic of sample setup for high temperature treatment.

Joule heating for RGO heater: Joule heating was performed in either glove box with argon protection atmosphere or under vacuum to protect RGO heater from burning in air at high temperatures. The as-printed GO heater was first reduced at 600 °C for 1 hour under Argon flow (100 ml/minute) in a tube furnace with a ramping rate of 10 °C/min to obtain suitable conductivity for Joule heating (~ kΩ). The thermally reduced RGO nanostructures were connected with copper electrodes by silver paste (SPI Supplies) to improve the electrical contact between RGO heater and the copper electrodes. The RGO heater was suspended on a ceramic substrate to avoid the high temperature damage to the substrate. Keithley 2400 source meter was used as electrical input power source for current below 1 A or power below 20 W. A higher power transformer (Volteq HY6020EX) was used for higher current (up to 10 A) or higher power (to 60 W) input.

Joule heating for CNF film: Joule heating was performed in an argon-filled glove box. The CNF film was connected to copper tape electrodes by silver paste. A Keithley 2400 source meter was used as an input power source for current below 1 A or power below 20 W. A higher power transformer (Volteq HY6020EX) was used for current up to 20 A. The current was controlled by LabVIEW program for targeted temperature and heating/cooling rates.

Rapid thermal shock for CNF-metal salts: Rapid thermal shock was realized by electrical Joule heating in an argon-filled glovebox. The metal precursor loaded CNF film was connected to copper electrodes and the interfaces were glued together with silver paste. The external current source was supplied by a Keithley 2400 SourceMeter by programming “sweep function” with the amplitude and duration adjustable. Typically, thermal shock duration of 5 ms, 55 ms, and 505 ms are used for particle synthesis.

3.3 Temperature measurement

Figure 3.2a schematic shows a clear and simple image to illustrate the high temperature setup. The emitting light spectra at high temperature was collected by optical fiber with a diameter of 400 μm for extracting of temperature by fitting the emitted spectra to gray body radiation equation. The optical fiber was connected to a spectrometer (Ocean Optics) for wavelength splitting and calibrated by a National

Institute of Standards and Technology (NIST) traceable light source to quantify the measured intensity. We fitted the spectra profiles of the gray body radiation equation (Eq. 3.1), obtaining the temperature as a fitting parameter.[24,25,36]

$$B_\lambda(\lambda,T) = \gamma\varepsilon\frac{2hc^2}{\lambda^5}\frac{1}{e^{hc/\lambda k_B T}-1} \quad \text{(Equation 3.1)}$$

where ε is the gray emissivity (~0.8 for carbon materials),[37] k_B is the Boltzmann constant, h is the Planck constant, c is the speed of light, λ is the wavelength, and the constant γ is introduced for fitting.

As an example, Figure 3.2b shows the collected spectra from the lighted sample at high temperature, and the corresponding fitted temperatures are plotted in Figure 3.2c.

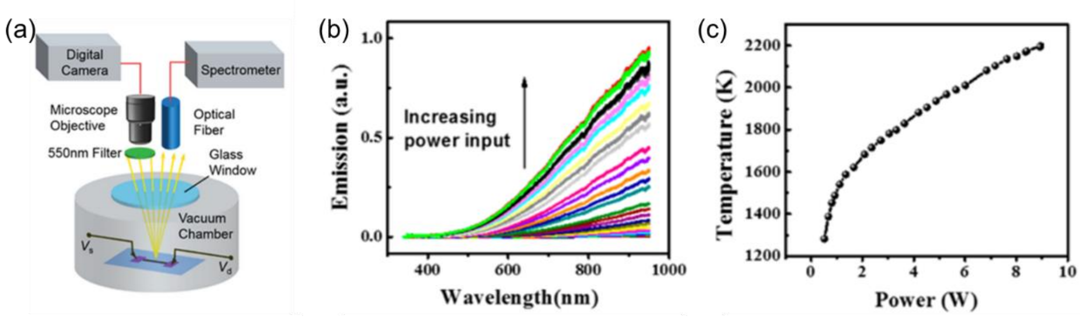

Figure 3.2. (a) Schematic diagram for electrical Joule heating and spectrum collection. (b) Collected spectra from 350-900 nm. (c) Fitted temperature according to the light spectra.

3.4 T-t measurement

For the ultrafast thermal shock, owing to milliseconds time scale which excluded the use of photo-diodes or charge-coupled device (CCD) for the spectrum capture, the emitted light at high temperature was collected by a specifically designed, on-line, time-resolved pyrometer that can disperse light at a spatial resolution of 0.8 nm/mm and a temporal resolution as low as 2.5 μs, enabling us to capture the fast switching process by electrical pulse (Figure 3.3). Briefly, the system employed a 0.5

m spectrometer (Sp-500i) with a dynamic choice of 150, 600 and 1200 grooves/mm gratings that can disperse light at a resolution of 6.5, 3.2, and 0.8 nm/mm. The dispersed light was collected by a 32-channel PMT array (H-7260), where the temporal spectra can be integrated and plotted as a function of time. By fitting the full spectrum collected at a specific time to the blackbody radiation equation (Eq. 3.1.), the fitted parameter T (i.e. approximate sample temperature) can be approximated. Note that the system offers a temporal resolution as low as 2.5 μs, which enables us to capture the fast switching process from the electrical pulse. By using a high-speed video camera, we were able to capture the spatial temperature evolution in the CNF-based sample during a 55 ms shock process (Figure 3.3b). The sample showed relatively uniform lighting in the chamber reaching a temperature of ~2000 K.

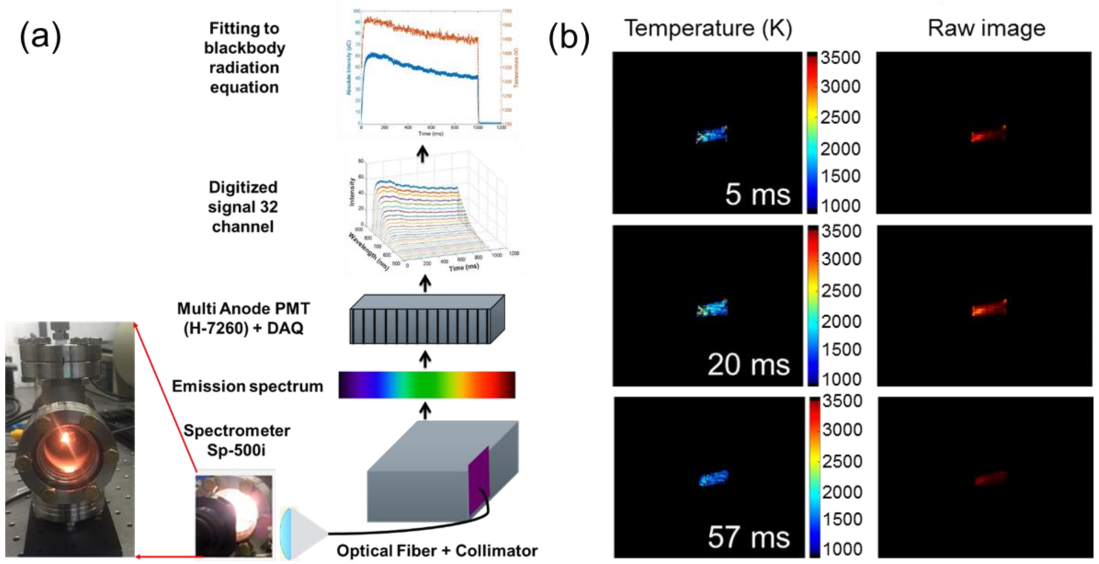

Figure 3.3. (a) Schematic configuration of a time-resolved pyrometer for spectrum collection during the rapid, high temperature process. (b) Spatial temperature evolution captured by a high-speed camera during a 55 ms thermal shock. Temperature distribution in the CNF-based sample as well as the raw lighting images captured by the high-speed video camera at 5 ms, 20 ms, and 57 ms, respectively.

3.5 Characterization and measurements

Characterization: The rheological study of GO ink was conducted on a stress-controlled AR 2000 rheometer (TA Instruments). The temperature was maintained at 25 °C throughout the entire rheology experiment. A shear rate sweep was performed for viscosity as a function of shear rate from 0.01 to 100 s^{-1}, and an oscillatory stress sweep at a frequency of 1 Hz was performed to obtain storage (G') and loss modulus (G") as a function of shear stress (0.1-1000 Pa). The microstructure and morphology were characterized by Hitachi SU-70 FEG-SEM at 10 kV and JEOL 2100 LaB6 TEM at 200 kV. Raman spectra were characterized by Horiba Jobin-Yvon with laser wavelength 532 nm and the integration time 4 seconds repeated for 4 times. XPS analysis was performed on a Kratos Axis 165 X-ray photoelectron spectrometer. XRD data were collected by a D8 Advanced (Bruker AXS, WI, USA). The mechanical strain-stress curves were measured by dynamic mechanical analysis (DMA Q800) with TA Instruments.

High-resolution TEM: The microstructure and morphology of the prepared samples was observed by a scanning electron microscope (SEM) (Hitachi SU-70 FEG-SEM at 10 kV) and transmission electron microscopes (TEM) (JEOL 2100F FEG TEM/STEM operated at 200 kV, and JEOL TEM/STEM ARM 200CF equipped with high angle annular dark field (HAADF) and annular bright field (ABF) detectors). A 22 mrad probe convergence angle was used to perform STEM imaging. HAADF detector in t the JEOL 2100 FEG TEM with 90 mrad inner-detector angle was utilized to obtain the Z-contrast atomic-resolution images. For EDS data collection, an Oxford X-max 100TLE windowless X-ray detector was utilized. The average particle size and distribution were determined by ImageJ software using at least three microscopy images per sample

Conductivity measurement: The conductivity of the CNF films and single fibers were measured by a four-point probe. For the single fiber conductivity, a single carbon nanofiber was sonicated from the CNF film and transferred to a silicon wafer. A shadow mask was used to deposit Au electrodes and then the single fiber was prepared by electrical Joule heating and the conductivity was measured by the two electrodes method with a bias voltage of 10 mV.

Chapter 4: 3D printable high temperature heaters[*]

Abstract

High temperature heaters are ubiquitously used in materials synthesis and device processing. In this work, we developed three-dimensional (3D) printed reduced graphene oxide (RGO)-based heaters to function as high-performance thermal supply with high temperature and ultrafast heating rate. Compared with other heating sources, such as furnace, laser, and infrared radiation, the 3D printed heaters demonstrated in this work have the following distinct advantages: (1) the RGO based heater can operate at high temperature up to 3000 K because of using the high temperature-sustainable carbon material; (2) the heater temperature can be ramped up and down with extremely fast rates, up to ~20,000 K/second; (3) heaters with different shapes can be directly printed with small sizes and onto different substrates to enable heating anywhere. The 3D printable RGO heaters can be applied to a wide range of nanomanufacturing when precise temperature control in time, placement, and the ramping rate is important.

4.1 Introduction

Heaters are widely used in materials synthesis and processing such as high-temperature chemical reactions and localized high temperature processing.[38–42] Conventional heating solutions are limited by factors such as low maximum heating temperatures and slow ramp rates. These limitations will hinder many processes that

---

[*] The results in this chapter have been published: Yao, Y.; Fu, K. K.; Yan, C.; Dai, J.; Chen, Y.; Wang, Y.; Zhang, B.; Hitz, E.; Hu, L. Three-Dimensional Printable High-Temperature and High-Rate Heaters. *ACS Nano* **2016**, 10, 5272–5279.

are desirable for materials synthesis and processing. Furnaces are the most widely used heating devices but they are often bulky in size and weight. In addition, the temperature ramp rate is also slow for furnaces, which is normally less than 100 K per minute.[43] Different from furnace heating, laser heating features high temperature capabilities and precise location control.[44–47] However, laser heating is expensive, has poor temperature distribution throughout the sample (*i.e.* temperature is higher on the surface), and is highly dependent on the absorption of the target material.

Meanwhile, with the advancement of micro/nanoscience and engineering, materials, structures, and devices have been designed and developed into micro-/nanoscale. To study physical and chemical properties, especially thermal-related behaviors, it is important to provide a heating element with a high temperature range to the target object in a small dimensional environment. The shape and size of heaters can be also fully dependent on the heating requirement of materials synthesis and processing to maximize the thermal efficiency and at the same time to avoid the damage of surrounding parts of the system. Therefore, it is desirable to design a minimized three-dimensional (3D) heating element, which would lead to a locally more uniform temperature distribution with precise temperature control. Heating elements in microscale have been extensively studied and demonstrated by using micro-hotplate as heating source.[48–51] A minimized heating element in the form of micro-sized hotplate down to 100 μm was developed with photolithography.[50,51] However, the minimized heater is limited to a 1000 K maximum temperature due to the poor high temperature stability of the materials in their micro-heaters.[48–51] In addition, these planar microhotplates are two-dimensional (2D) in shape and provide a 2D heating that can cause a temperature gradient in the target objects along the heating directions.

We report a printable heater by using 3D printing of viscous GO aqueous solution to form a series of complex GO architectures, followed by Joule heating *via* electrical current to generate high temperature up to 3000 K in a controlled manner. The temperature ramping response is fast and the heating rate can be up to ~20,000 K/s. The high viscosity of concentrated GO ink and the high resolution of direct 3D printing together lead to control over both size and shape. The heater can be printed into arbitrary shapes and dimensions. The 3D heater also demonstrated excellent stability at high temperature and stable temperature switching between room temperature and 2000 K for more than 2000 cycles. The excellent performance and potentially lower cost of the 3D heater fabricated by scalable 3D printing provide a promising heating solution for a range of applications, especially when high temperatures and 3D shapes are preferred.

4.2 Result and discussion

Highly viscous graphene oxide (GO) dispersion in water was prepared by following the modified Hummer's methods.[52] The GO aqueous dispersion with suitable viscosity can be directly 3D printed into different shapes *via* a layer-by-layer fashion controlled by a computer program. We have printed microsized heaters with feature size down to 200 μm by our 3D printer setup. As shown in schematic Figure 4.1a, a horse-shoe 3D structure was printed for this study. Figure 1a inset shows microsized heaters with a chamber diameter of 1.5 mm, much smaller than a quarter coin. A photo image of the horseshoe-shaped 3D heater is shown in Figure 4.1b. The as-printed, horseshoe-like 3D heater was thermally reduced at 873 K (600 ^{o}C), leading to a suitable conductivity of 3 S/cm. We then employed a simple and effective Joule heating process to further reduce the RGO structures at high temperature, up to 3000 K. The unique high-temperature reduction of the 3D heater containing RGO flakes effectively increases the conductivity, as described later. The resultant 3D RGO nanostructures function excellently as a heater at high temperature, up to 3000 K (Figure 4.1c). The temperature of the 3D RGO heater can be readily controlled by the applied current and can be inferred based on blackbody radiation (Figure 4.1d).[53]

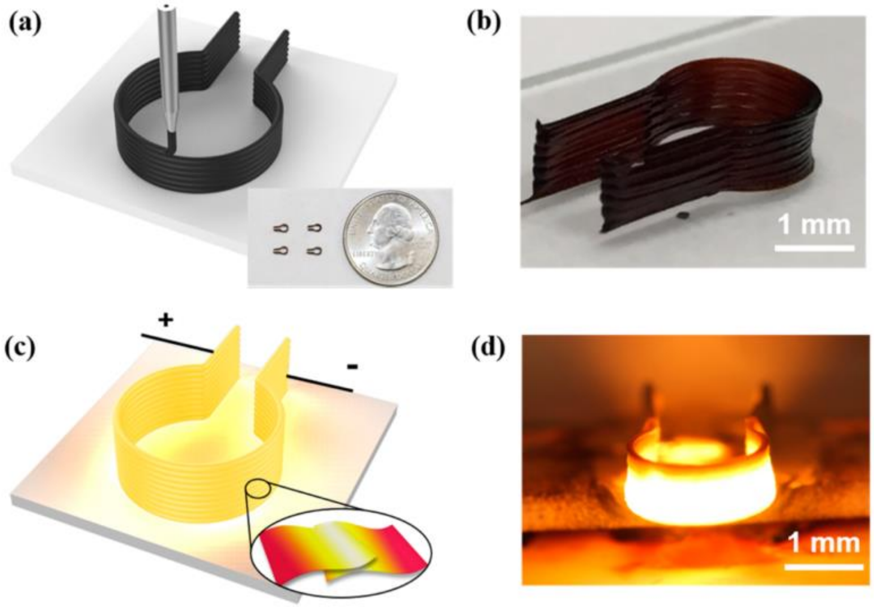

Figure 4.1. Schematic demonstration of 3D printable heater. (a) High concentration GO ink was used for 3D printing of RGO heater. Arrays of 3D printed heaters with chamber size 1.5 mm are also shown in the inset. (b) Image of as-printed horseshoe-like 3D heater. (c) The operation of RGO heater at high temperatures is achieved by applying a driving current. The contact area between two RGO flakes is expected to experience a higher temperature due to larger contact resistance. (d) Image of 3D printed RGO heater under high temperature operation.

The properties of the GO ink, especially its rheological behaviors, significantly affect the 3D printing process and the stability of printed architecture.[54–61] The aqueous

GO solution was freeze-dried into powders, followed by concentrating GO with water into 80 mg/ml for a proper viscosity. The rheological properties of the printing GO inks are shown in Figure 4.2a-c. The apparent viscosity of the GO ink in Figure 4.2a shows a linear decrease in shear stress on a logarithmic scale, indicating a non-Newtonian fluid property of the concentrated GO solution that exhibits a shear-thinning behavior. Figure 4.2b displays the modulus as a function of shear stress for the aqueous GO inks. These high yield stress and plateau moduli values are essential for the layer-by-layer stacked architectures to have good shape retention. An oscillatory time sweep for both moduli was also applied with a shear stress of 6 Pa at a frequency of 1Hz for three hours. The storage and loss moduli as a function of time were plotted in Figure 4.2c. No apparent change in G’ or G’’ was observed for continuous 2-hour testing, indicating an excellent rheological stability of GO inks for long-term printing.

Figure 4.2d shows a photo image of the printing process. A multilayered 3D RGO heater was printed by using a 3D printer with a pre-programmed printing path. The excellent rheological properties of GO inks enable the continuous layer-by-layer printing with a uniform printing diameter. After printing, the as-printed architecture can maintain the shape and its dimension for a few hours under ambient environment. The printed sample was then freeze-dried to remove the solvent to further stabilize the 3D structure. The scanning electron microscopy (SEM) images of the printed architecture are shown in Figure 4.2e. The layer structure consists of stacked filaments with a size of ~ 200 μm in diameter. The magnified SEM image of the printed heater surface (Figure 4.2f) shows rough large GO flakes as the building blocks.

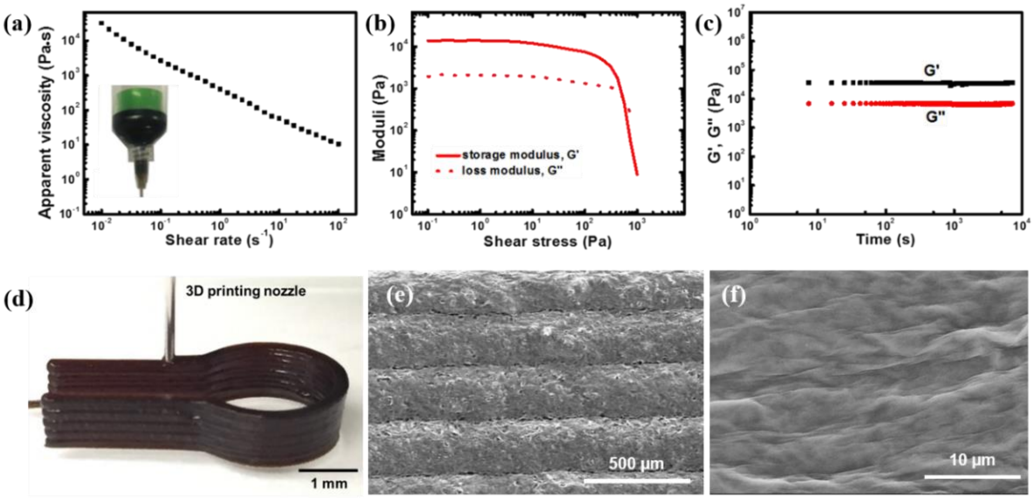

Figure 4.2. The rheological properties of GO inks and morphological characterizations of 3D printed heaters. (a) Apparent viscosity as a function of shear rate. The inset shows a picture of GO ink used for printing. (b) Storage and loss moduli as a function of shear stress. (c) Stability of GO ink is shown by storage and loss modulus evolving with time at a shear stress of 6 Pa. (d) Picture of the layer-by-layer 3D printing process. (e) SEM image of the printed heater after removal of solvent and (f) magnified surface morphology.

The 3D printed heater was freeze-dried to remove the water solvent and then thermally pre-annealed at 600 ^{o}C in an argon environment. The thermally reduced 3D RGO heater was attached to copper electrodes for high temperature reduction by Joule heating (Figure 4.3a). Figure 4.3b shows the 3D RGO heater operated at different input power levels (0.5 W, 3 W, 6 W) corresponding to different temperatures (1300 K, 1800 K, 2000 K). Figure 4.3c shows the resistance (R) and voltage (V) of RGO heater as a function of driving current (I) during the Joule heating process. The resistance of RGO heater decreased by a factor of 56, revealed by a change in the conductivity from 3 S/cm to 144 S/cm before and after the high-temperature reduction, respectively. The RGO heater after annealing through Joule heating exhibits a stable resistance and a linear I-V curve up to 8V, which corresponds to a wide temperature range (Figure 4.3d).

The stable I-V curves for 1st and 50th scans also indicate the excellent stability of 3D RGO heaters after thermal annealing by Joule heating.

Raman spectra were measured to investigate the structural changes induced by the high temperature Joule heating (Figure 4.3e). The RGO heater after Joule heating at high power shows a higher degree of graphitic structure characterized by the sharp graphitic (G) peak and the ultralow intensity disordered (D) peak, in contrast to the pre-annealed RGO heater (at 873 K) which showed broad G and D peaks.[62,63] The low $I_{D/}I_G$ peak ratio (~0.1) achieved in our RGO nanostructure after Joule heating is lower than the typical values reported by others. Figure 4.3f shows the X-ray diffraction (XRD) profile of as-printed 3D heater and compared with thermally annealed RGO heater by Joule heating. After high temperature reduction by Joule heating, the (002) XRD peak became much sharper, indicating a higher crystalline structure due to the removal of defect atoms and reconfiguration of carbon during high temperature reduction.

Figure 4.3g-h show the SEM images of 3D RGO heater after Joule heating annealing. The surface morphology is very different from as-printed graphene oxide heater as shown in Figure 4.2f. After annealing, the flakes became rugged due to deformation caused by high temperature reduction. The cross-section SEM image (Figure 4.3h) also showed the porous structure of RGO heater with RGO flakes interconnected (inset). The porosity comes from 3D printing process as well as the reduction of graphene oxide. GO ink for 3D printing contained water solvent and was not densely packed. After removal of water by freeze-drying, the 3D structure was porous already. The thermal reduction of GO further increased the porosity of RGO heater because gasses were released during the thermal reduction process. The porous structure, as well as the poor contact between RGO flakes, decreased the conductivity of RGO heater. However, as stated before, these increased resistances were critical for cultivating Joule heating energy for effective heating.

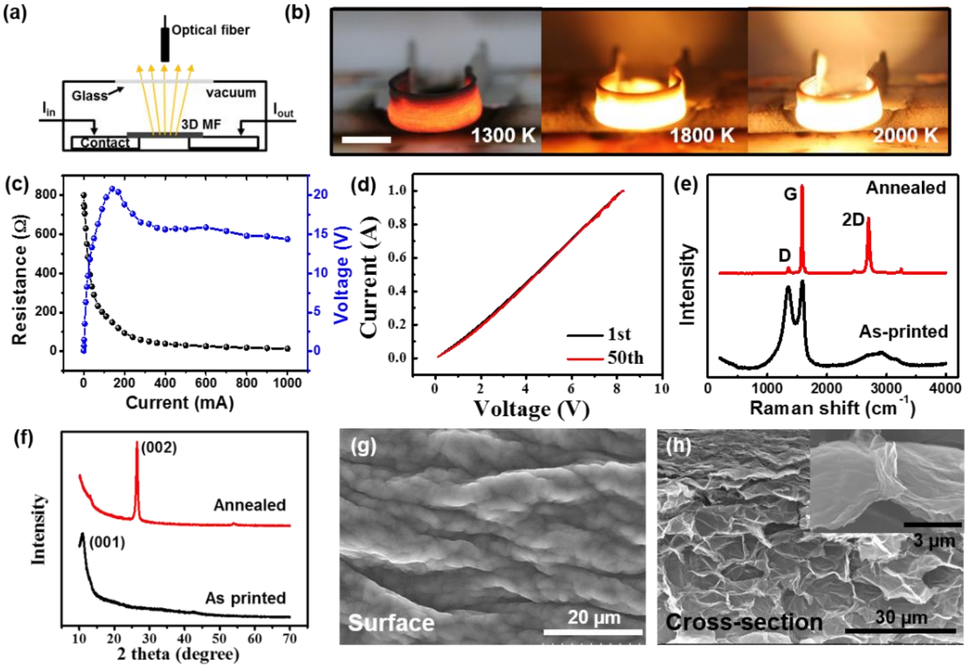

Figure 4.3. High temperatures annealing of printed RGO heaters. (a) Schematic for Joule heating setup. (b) Photographs of a 3D printed RGO heater under Joule heating with different powers. Scale bar is 1 mm. (c) Resistance and measured voltage vs. annealing current for the RGO heater. (d) Current-voltage profiles for the RGO heater after high temperature annealing. Only the 1st and 50th curves were shown in the figure. (e) Raman spectra of RGO before and after high-temperature annealing by Joule heating. (f) XRD profiles of as-printed and thermally annealed 3D heater. SEM images of RGO heater after annealing for (g) surface and (h) cross-section. The inset shows the contact between RGO flakes.

The temperature of the 3D RGO heater was obtained through measurement of light emission using an optical fiber (experimental section). Figure 4.4a shows the radiation spectra of the 3D RGO heater under different input powers, as collected by the optical fiber (400 μm diameter, Ocean Optics software) in the range from 360 nm to 950 nm. The relationship of temperature vs. input power of the specific 3D RGO heater was established (Figure 4.4b). A heating temperature of 3016 K was achieved (Figure 4.4c).

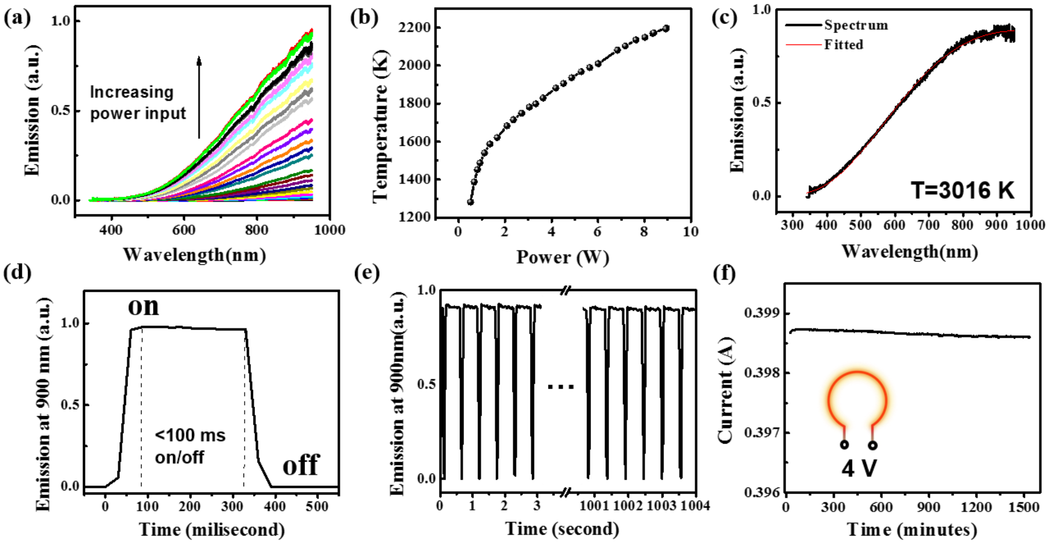

Figure 0.4. The performance of printed 3D RGO heater at high temperature. (a) The emission spectrum of an RGO heater under different input powers. (b) The temperature of RGO heaters under different input powers fitted with a blackbody radiation model. (c) The emission spectrum and fitted high temperature of 3016 K in RGO nanostructures. (d) The emission of RGO heater was turned on and off in less than 100 milliseconds. The temperature for the "on" state is 2000 K. (e) The RGO heater can be turned on and off repeatedly for 2000 cycles without degradation. (f) Current stability of 3D RGO heater under a 4V bias voltage was demonstrated (temperature of 1500K) over a 24-hour period.

Besides the high temperature capability, the 3D RGO heater can be turned on and off with a high ramping rate (Figure 4.4d). The 3D RGO heater can reach 2000 K from room temperature in less than 100 milliseconds (ms). The turn-off time from 2000 K to no-emission (less than 1000 K) is also less than 100 ms. As a conservative estimation, we can achieve ~20,000 K/s heating rate in the device easily, which is several orders of magnitude higher than that of current furnaces. Figure 4.4e shows the repeated cycling performance of the 3D RGO heater for more than 2000 cycles, where RGO heater shows no observable change. These results indicate that after Joule heating reduction, the RGO heater has excellent pulse thermal heating capability. By holding the driving voltage at 4V (~1500 K) for 24 hours, the measured current showed a negligible change (from 0.3987A to 0.3986A), which indicates excellent thermal stability for long-term operation.

The printed 3D RGO heaters can be used for a range of materials synthesis and processing techniques. We 3D printed and then freeze-dried the GO nanostructure. The 3D printed GO was reduced at 600 °C followed by a unique high-temperature reduction through Joule heating. The RGO heater on ceramic substrates can operate effectively as a 3D high temperature heater (Figure 5.5a). Local temperatures at different locations of the 3D heater under different input power levels were measured by a K-type thermocouple with a detection range from room temperature to 1500 K (Figure 5.5b). The temperature distribution profile shows that center of the horseshoe heater exhibits the highest temperature, much higher than the surrounding areas, indicating that the designed RGO heater can generate and accumulate Joule heating locally.

Three metals with different melting temperatures and shapes were placed in the RGO heater to observe their morphology change under heating (Figure 5.5c). Effective melting was achieved for Sn ball (T_m 505 K), Al block (T_m 933 K), and Cu block (T_m 1357 K), all of which became more spherical as shown in the inset photo images compared the morphology change before and after heating. Since our RGO heater has a 3D shape, this benefits those metal pillars and balls with more uniform temperature field, in contrast to the planar heating source which has a large thermal gradient along the heating directions. Because of the flexible design of the 3D printing technology, we can integrate the printed RGO heaters into the circuit as a controllable heating element, as shown in Figure 5d. The heating elements were triggered passively by the applied voltage. Such passive-matrix heating arrays with high temperature capabilities and fast on-off switching can enable a range of materials synthesis and processing techniques.

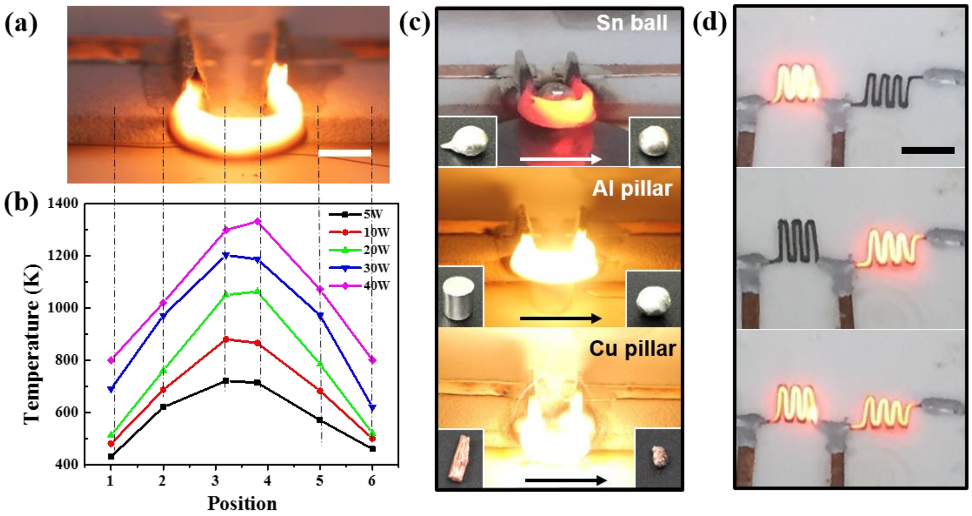

Figure 5. Demonstrations of 3D printed RGO heating elements. (a) 3D RGO heater with a chamber diameter of 4 mm and (b) its local temperature profiles at different power levels. (c) Metal melting experiments for Sn, Al, and Cu at different power levels. Insets are the morphology changes before and after high T. (d) Selective and controllable heating demonstration with printed RGO heaters. Scale bar: 2 mm.

4.3 Conclusion

The 3D printable RGO heater fabricated by a 3D printing technique followed by Joule heating can function as an effective heating source with arbitrary shapes. Joule heating was used to effectively reduce RGO at high temperature. The resulting 3D heater with RGO flakes can reach a high heating temperature, up to 3000 K, and can be turned on and off with high switching rates, up to ~20,000 K/s for 2000 cycles without performance decay. We demonstrated that the 3D RGO heater can be used to melt metal particles effectively. The printable RGO heater, therefore, offers a thermal strategy for micro-/nanoscale materials and devices with designed 3D heating patterns, outstanding temperatures, and heating rates that can enable a range of processing and high temperature synthesis.

4.4 Experimental

Preparation of graphene oxide (GO) ink, Temperature measurement, and Characterizations: see Chapter 3 Experimental section.

3D printing process: 3D printing was performed by a 3D printer (Fisnar F4200n) with capability for programmable patterning in three dimensions built layer-by-layer. In our experiments, a 3D printing nozzle (diameter 300 µm) was used with pressure controlled at 60 psi and the nozzle's moving speed was 1-5 mm/s. The dimension of 3D printing was input into the system as design. The whole printing process took less than 10 minutes for a 3D heater with 12 layers. After printing, the printed structures were freeze-dried at – 50 °C with a vacuum pressure of 0.6 Pa to remove the water solvent and maintain the 3D structures.

Joule heating process: Joule heating was performed in either glove box with argon protection atmosphere or under vacuum to protect RGO heater from burning in air at high temperatures. The as-printed GO heater was first reduced at 600 °C for 1 hour under Argon flow (100 ml/minute) in a tube furnace with a ramping rate of 10 °C/min to obtain suitable conductivity for Joule heating (~ kΩ). The thermally reduced RGO nanostructures were connected with copper electrodes by silver paste (SPI Supplies) to improve the electrical contact between RGO heater and the copper electrodes. The RGO heater was suspended on a ceramic substrate to avoid the high temperature damage to the substrate. Keithley 2400 source meter was used as electrical input power source for current below 1 A or power below 20 W. A higher power transformer (Volteq HY6020EX) was used for higher current (up to 10 A) or higher power (to 60 W) input.

4.4 Supporting Materials

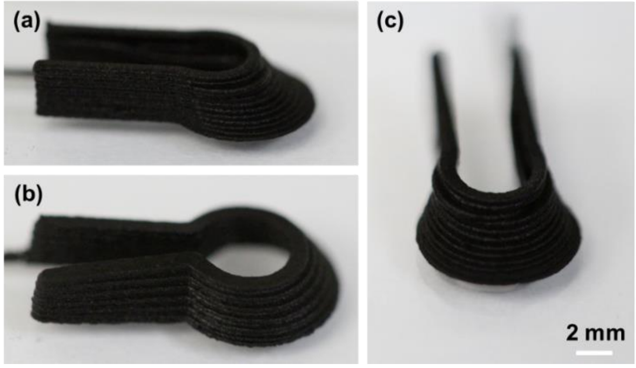

Figure 4.6. Dome-like suspended structure with printable graphene oxide.

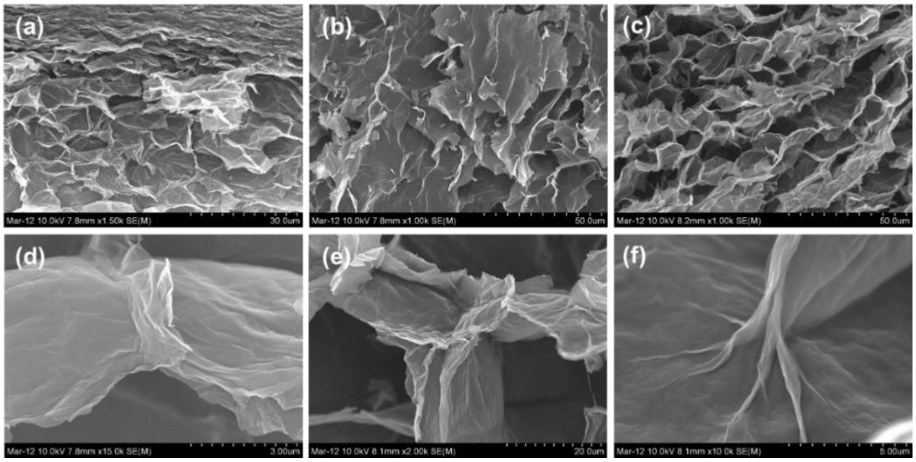

Figure 4.9. (a)-(c) Cross-section SEM images of 3D heaters and (d)-(f) magnified SEM images to show the contact between RGO flakes.

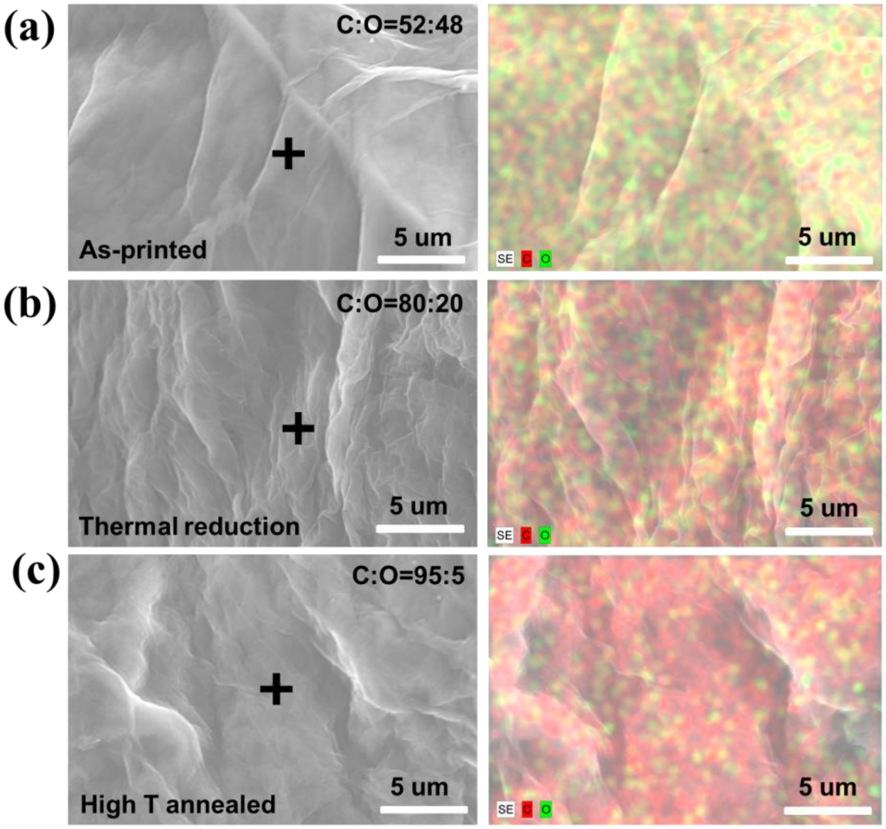

Figure 4.10. EDX point and mapping analysis of (a) As-printed GO. (b) Thermal reduction at 600°C and (c) high temperature reduction by the Joule heating at 2500 K. The cross point shows the EDX sample point.

Chapter 5: Carbon welding by ultrafast annealing[*]

Abstract

Carbon nanomaterials exhibit outstanding electrical and mechanical properties but these superior properties are often compromised as nanomaterials are assembled into bulk structures. This issue of scaling limits the use of carbon nanostructures and can be attributed to poor physical contacts between nanostructures. To address this challenge, we propose a novel technique to build a 3D carbon matrix by forming covalent bonds between carbon nanostructures. A Joule heating method was developed to bring the carbon nanofiber (CNF) film to temperatures greater than 2500 K at a heating rate of 200 K/minute to fuse together adjacent CNFs, forming a 3D interconnected carbon network. The bulk electrical conductivity of the carbon matrix increased four orders of magnitude to 380 S/cm with a sheet resistance of 1.75 Ω/sq. The Joule heating method enables graphitization of carbon materials at high temperature and provides a new strategy to build covalently bonded, interconnected carbon networks by welding adjacent carbon fibers. We anticipate that this method can be extended to other carbon nanomaterials such as graphene and carbon nanotubes using proper surface modifications to build advanced structures.

5.1 Introduction

Carbon-based nanomaterials such as carbon nanofiber (CNF), carbon nanotube (CNT), graphene are featured with lightweight, flexible, anti-corrosion, highly

---

[*] The results in this chapter have been published: Yao, Y.; Fu, K. K.; Zhu, S.; Dai, J.; Wang, Y.; Pastel, G.; Chen, Y.; Li, T.; Wang, C.; Li, T.; Hu, L. Carbon Welding by Ultrafast Joule Heating. *Nano Lett.* **2016**, *16*, 7282–7289.

conductive and high surface area, which are important materials as conductive host for electrocatalysis and electrochemical energy storage applications.[24,64–68] However, attempts to mechanically join and create bulk structures from individual carbon nanomaterials often results in the loss of key performance metrics.[65,69–77] For example, single-walled CNT are known to exhibit electrical conductivity above 10000 S/cm, but the reported conductivity of assembled CNT membranes is two orders of magnitude less, approximately 100 S/cm.[10–12] This decrease can be attributed to the poor physical contacts between nanotubes that lack effective bonding to maintain the intrinsic, nanoscale properties. It is reasonable to believe that by addressing the poor contacts between carbon nanomaterials, the bulk performance of 3D carbon structures could be improved significantly and could open up new areas of large-scale development of high performing, bulk carbon-based materials from nanostructures.

In the literature, there are many techniques reported to mechanically or chemically fuse carbon nanomaterials.[71,73–75,78–82] Materials can be uniformly deposited along junctions to form a continuously interconnected structure using chemical vapor deposition (CVD) of amorphous carbon,[83] SiC,[79] or atomic layer deposition (ALD) of Al_2O_3.[84] For example, Z. Lin, *et al*. report an increase in the compressive strength of CNT sponges with an amorphous carbon coating by three orders to 72 MPa.[71] To form a covalent chemical bond at junctions between carbon nanostructures, boron doping has been reported to form elbow junctions with B-C bonds.[75] Although extensive studies have been conducted, none of the reported methods offer a cost-effective and scalable approach to fundamentally improve the contacts between carbon nanostructures for macroscale designs.

To address this challenge, we propose a simple, repeatable method to build a 3D interconnected network by forming covalent bonds between carbon nanostructures to achieve high conductivity and good mechanical performance. Although 3D covalently bonded carbon structures have been predicted by theoretical simulations,[85] as far as we know, no experimental work has been achieved. In this communication, we for the first time report a 3D covalently interconnected carbon network by applying a Joule heating method to polyacrylonitrile (PAN) based carbon nanofibers at a high temperature (> 2500 K) and an ultra-fast rate (~200 K/minute). The heat generated by applying an electrical current to carbon nanofibers can produce a high temperature environment that enables further carbonization of the nanofibers and induces welding between adjacent nanofibers. After welding, the bulk electrical conductivity of the CNF network exhibited four orders of magnitude improvement to ~380 S/cm and a sheet resistance of 1.75 Ω/sq, compared to the pristine CNF membrane with 0.0133 S/cm bulk conductivity and 18400 Ω/sq sheet resistance. The Joule heating method not only enables graphitization of carbon materials at a high temperature but more importantly, it provides a new strategy to build a covalently interconnected carbon network by welding adjacent carbon fibers together. We envision that this method can be extended to other carbon materials such as graphene and CNTs with certain surface chemical modifications to build advanced high-performance structures.

5.2 Results and discussion

Figure 5.1a shows an electric current is applied to the pristine intertwined CNFs to induce an ultrafast heating rate and result in (1) highly crystallized CNFs, as well as, (2) covalently welded CNFs at their junctions. The high crystallinity of CNFs after high-temperature Joule heating was revealed in the Raman spectra as shown in Figure 5.1b. After Joule heating to 2800 K in 10 minutes, the D band peak was almost completely suppressed for the welded CNFs and the intensity of all other peaks in the Raman spectra became much sharper in comparison to for the spectra of CNFs pre-carbonized at 873 K. The intensity ratio between D peak and G peak (I_D/I_G) decreases from 1.14 for pristine CNFs to 0.035 for welded CNFs. This is the lowest value reported in the literature for carbonized CNFs characterized by Raman spectroscopy.[86,87] The graphitization process takes ~10 minutes by Joule heating but would take days by furnace heating, further illustrating the high efficiency and practicality of the Joule heating method.[88]

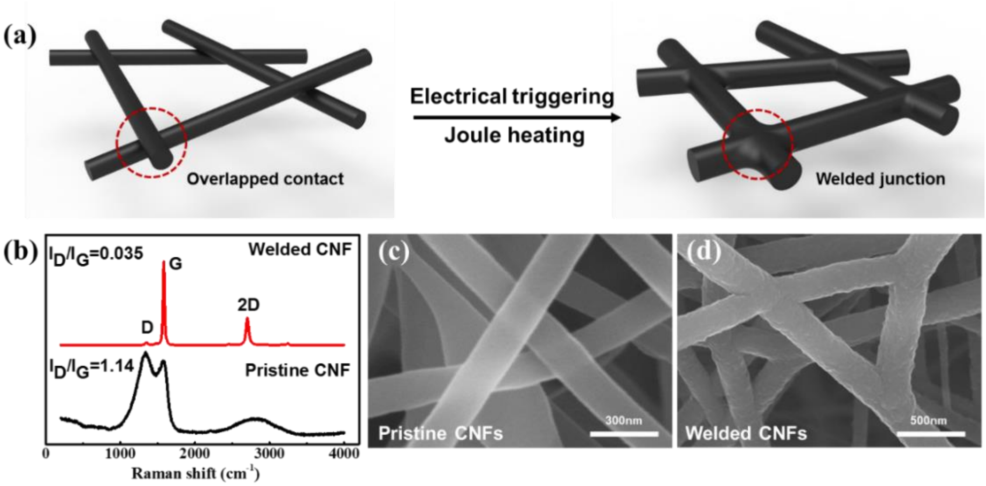

Figure 0.1. Schematic of the welding process of CNFs and selected characterization results. (a) Schematic of the carbon welding process of CNFs triggered by Joule heating. (b) Raman spectra of pristine CNF and Joule heated CNF. The change in the ratio between I_D/I_G and an increase in peak sharpness is indicative of the high crystallinity and graphitization of welded CNFs. (c) and (d) SEM images of the pristine CNF and welded CNF.

The welding of CNFs at junctions was shown by SEM images in Figures 5.1c-d. For pristine CNFs, the individual fiber has a smooth surface and is semi-transparent due to its amorphous structure. Overlapping nanofibers in the pristine CNF matrix are in physical contact with their neighbors but Van der Waals interactions are weak. After Joule heating, the smooth fibers become rough and the physical contacts were welded at junction points, forming an integral fiber network (Figure 5.1d).

CNF films were obtained by the electrical spinning of PAN in dimethylformamide (8 wt. %) followed by thermal stabilization at 260 °C and carbonization at 600 °C. The Joule heating process was controlled by an electric field to the set temperatures with at a controllable rate. The Joule heating setup is displayed in Figure 5.2a. The CNF samples were connected to copper electrodes by silver paste and suspended on a glass substrate to avoid the thermal damage during the Joule heating process. The CNF films were heated to a high temperature in an argon protected atmosphere. Figure 5.2b demonstrates a large CNF film (20 mm*3 mm*30 μm in length, width, and thickness) loaded at 15 W, with a temperature of around 2000 K. The optically emissive behavior indicates that high temperature is reached by the CNF films. The Joule heating process was also carried out on CNF film (4 mm*2 mm*30 μm in length, width, and thickness) with the driving current increasing from 0.1 mA to 1 A (Figure 5.2c). In comparison to the linear current-voltage (I-V) profile of a pure resistor, the measured resistivity of the CNF film shows a continuously decreasing profile for 4 orders of magnitude during the Joule heating process. The temperature of lighted CNF can be calculated by fitting the emitted light spectra to the gray body radiation equation as shown in Figure 5.2d. With an increase in input power, the intensity of emitted light gets higher and brighter in emission. The temperature versus power relation in Figure 5.2e illustrates a sublinear relation due to the decrease of heating efficiency at high temperatures. This repeatable temperature-power relation can be used to precisely control the temperature of the Joule heating technique for future CNF experiments. The whole heating process takes about 10 minutes, with an average heating ramp rate of 200 K/minute.

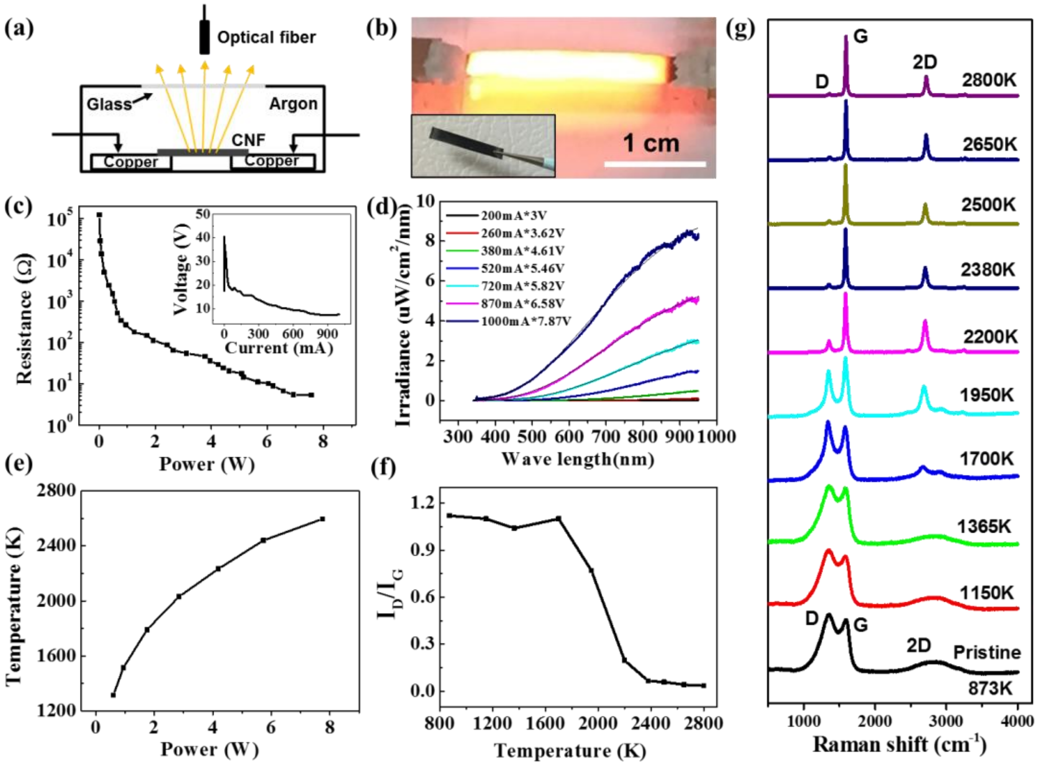

Figure 5.2. Joule heating process of CNF. (a) Schematic to show the Joule heating experiment and setup of the temperature measurements. (b) The real image of the Joule heated CNF at high power and inset is the film after Joule heating. (c) The calculated resistance (R=V/A) vs. power plot during the Joule heating process with the measured voltage as a function of input current, inset. (d) The emitted spectra at high temperatures fitted to gray body radiation for temperature measurements at different powers. (e) Temperature vs. power curve for a typical CNF sample. (f) and (g) Plots of the I_D/I_G ratio and Raman profiles during the graphitization process for CNF.

Figures 5.2f-g demonstrate the evolution of Raman spectra at different temperatures to reveal the bonding structure evolution during the Joule heating process. With increasing input power, there is a clear tendency for the D band peak to become suppressed while the G band and 2D peaks become sharper. Figure 2f summarizes the I_D/I_G relation at different temperatures, showing a drastic decrease from 1600 K to 2400 K, which corresponds to the carbonization and graphitization of CNFs that occurs above 1600 K. After Joule heating to 2800 K, the lowest I_D/I_G ratio of 0.035 was obtained, which indicates that the majority of carbon bonds in CNFs are sp^2 bonds graphitic carbon (graphene structure) after Joule heating.

The highly graphitic structure of the CNF network after Joule heating was confirmed by high-resolution transmission electron microscopy (HR-TEM) in Figure 5.3a. Before Joule heating, the main structure of the CNF is dominated by amorphous carbon and few graphitic carbon layers can be observed by TEM. By applying the Joule heating treatment, the CNF film formed a highly crystallized carbon structure with graphitic carbon layers in the longitudinal direction as indicated by the arrow in Figure 5.3a. During the high temperature Joule heating process, hydrogen and nitrogen are removed from the PAN-derived carbon structure, facilitating the cross-linking into a crystallized carbon structure. Figure 5.3b shows TEM images of the junctions between welded carbon nanofibers after the Joule heating process. Highly crystallized carbon layers are clearly observed at the junction point that bridges the neighboring CNFs. As far as we know, this is the first report of welding behavior for PAN-derived carbon materials.[87,88]

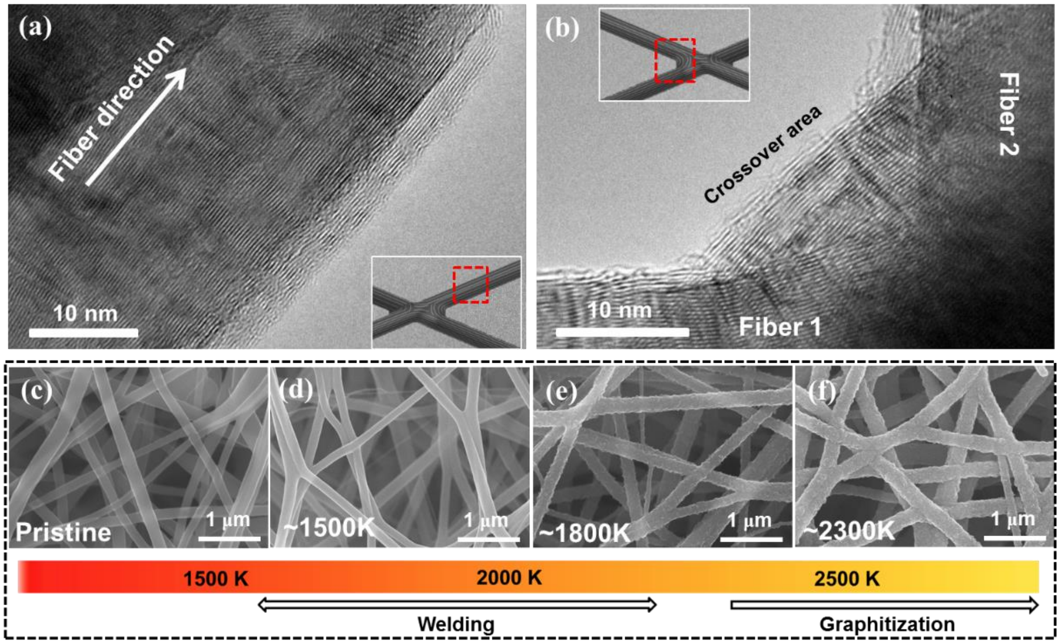

Figure 0.3. Morphological characterization of the welded CNF structure. High-resolution TEM images of (a) Joule heated CNF and (b) the junction between Joule heated CNFs. (c)-(f) SEM images showing the morphological evolution of CNFs by Joule heating at (d) 1500 K, (e) 1800 K, and (f) 2300 K.

To understand the welding behavior in the context of the Joule heating treatment, we controlled the temperature induced by Joule heating to observe the morphological evolution of CNFs as shown in Figures 5.3c-f. The pristine CNF film displays smooth, intertwined fibers with a diameter around 200 nm and semi-transparent optical properties due to their amorphous structures. After Joule heating to 1500 K, fibers start to stick together both in parallel, therefore forming a “Y” shape, as well as in crossover, forming a “+” shape. Clear boundaries between these fibers were still present at 1500 K which indicates incomplete welding between the carbon nanofibers. At 1800 K, the fiber surface becomes rough and the nanofibers start to merge and weld together, resulting in ambiguous boundaries between fibers. At 2300 K, the fiber junctions are completely welded together without distinct boundaries can be seen. The micro-morphology of CNFs at different temperatures during the Joule heating process confirms the fusion of CNFs between 1500 and 2300 K.

From above experiments, it can be concluded that fast heating to high temperature played a key role in the formation of welded graphitic carbon structures. Another important condition for the welding of fiber junctions lies in the starting materials of amorphous CNFs whose structure can be tuned at high temperatures. To study the Joule heating effect on different carbon structures, CNT was selected due to its highly crystallized carbon structure, which is used to compare with the amorphous carbon of CNF. A thin CNT film was prepared and tested under similar conditions as the amorphous CNF samples. The lack of fusion between CNT fibers is due to the high crystallinity of the as-prepared carbon nanotube structures (supporting materials). As schematically shown in Figure 5.4a, even though high temperatures can be generated at the junction between carbon nanotubes (c-Carbon), the highly crystalline carbon structure cannot weld together without first deforming the stable C-C bonds and CNT structure that are already present.[20] For amorphous carbon fibers (a-Carbon), Joule heating enables the defects of nitrogen and hydrogen in the amorphous structure to activate at a high temperature. With the removal of H and N, Bergman cyclization between adjacent CNFs takes place and new bonds are formed to weld the amorphous nanofibers together. Nitrogen elemental mapping of the CNF films before and after Joule heating is given in Figures 5.4b-c. A large amount of nitrogen can be detected on the pristine CNF surface, and only a small amount of nitrogen can be observed on the welded CNF films, especially at the junctions between nanofibers. The elimination of nitrogen is an indication of the improved graphitization of carbon at high temperatures during the Joule heating method.

To study the welding behavior of PAN-derived carbon on an atomic scale, molecular dynamic (MD) simulations were performed using a large-scale atomic/molecular massively parallel simulator (LAMMPS)[89] and REAXFF potential[90,91] (Figure 5.4d). Due to the higher resistance at the contact point between CNFs, a higher temperature environment at the junction is expected and helps initiate the welding and ordering of the amorphous carbon matrix. On the atomic level, we envision that Joule heating could greatly accelerate the purification and ordering of CNFs, particularly at the high temperature junctions between nanofibers. During Joule heating, the collisions between electrons that produce a current and the atoms in the nanofibers cause excessive vibrations of the amorphous carbon layers. The equilibrium structure at 300 K was heated to 3000 K and a certain degree of nucleation of carbon chains is observed. After cyclically removing the nitrogen molecules from the system and keeps running the simulation, carbon atoms begin to nucleate. After continuing to remove hydrogen molecules from the system, eventually, carbon atoms nucleates into the graphitic structure. Detailed simulation can be found in supporting information. Since the temperature of the Joule heating technique is highly dependent on the resistance of the CNF matrix, the welding of amorphous nanofibers benefits from the larger contact resistance at junction points, and graphitic structure can be expected after defects removal at high temperature.

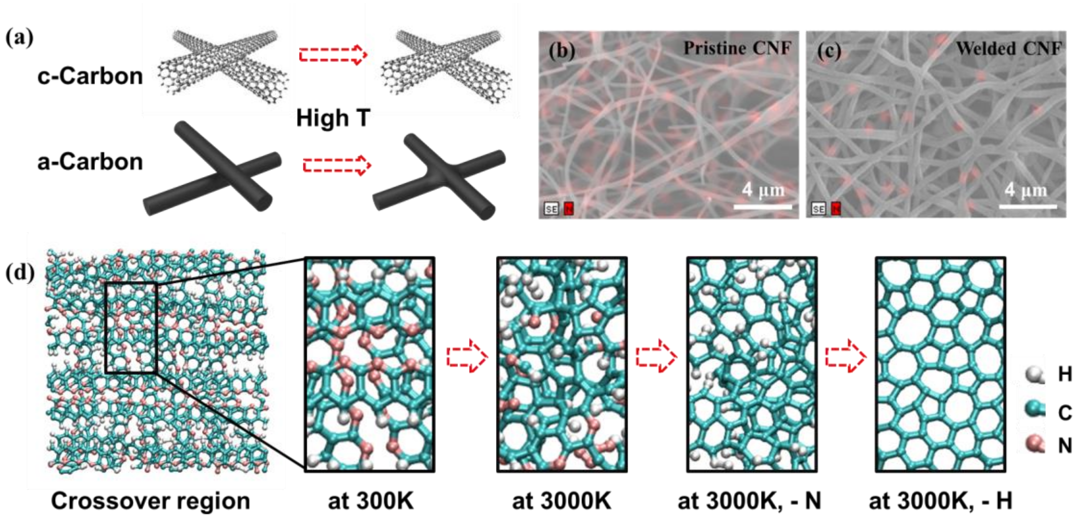

Figure 5.4. Molecular dynamic simulation of carbon welding at fiber junction. (a) Schematic of the crystalline (c-Carbon) and amorphous (a-Carbon) carbon fibers before and after the high temperature Joule heating technique. (b-c) SEM elemental mapping of nitrogen for pristine CNF and welded CNF. (d) Evolution of the amorphous carbon structure at fiber crossover region in LAMMPS. The equilibrium structure started at room temperature (300 K) and was heated to 3000 K. After the removal of nitrogen and hydrogen atoms, highly crystalline and graphitic structure was formed. Cyan: carbon. Pink: Nitrogen. White: Hydrogen.

Both the high graphitization and junction welding of welded CNF film can benefit the electron transport in bulk scale CNF structures and result in significantly improved conductivities. The electrical conductivity of the CNF film increased by a factor of 30,000 from 13.3 mS/cm to 381 S/cm, and a sheet resistance of 1.75 Ω/sq (Figure 5.4a). This calculation is determined without subtracting the porosity of the CNF film with a density of around 0.1 g/cm^3. To understand the role of junction welding in the enhancement of electrical properties, we measured the conductivity of a single fiber by a shadow-mask technique (Figure 5.4b). A single fiber was sonicated from CNF film and transferred to a silicon wafer. 100 nm Au electrodes were deposited through a shadow mask to either end of the fiber (Figure 5.4b inset). The low temperature carbonized CNF shows a conductivity of 4.67 S/cm, which is in accordance with literature studies.[92] After high temperature Joule heating, the conductivity of the single fiber increases ~180 times to 822 S/cm by two-probe measurement. The electrical conductivity of a pristine CNF film, a welded CNF film, a single CNF fiber and a single CNF fiber after Joule heating are presented in Figure 5.4c. After Joule heating, both the film as well as single fiber conductivity increased substantially but by different magnitudes. The change in conductivity of the CNF film is a factor of 30000 times while the single nanofiber only increased by a factor of 180. We speculate that the welding of nanofiber junctions in CNF film is also critically important to the enhancement and purification of the carbon matrix.

Besides the tremendous enhancement in conductivity, the unique 3D interconnected carbon structure of the welded CNF film can also be used for other bulk structures and composites.[70,77] For instance, after polymer infiltration the conductivity of the CNF film is maintained and therefore provides a conductive matrix for other designs and applications. The 3D interconnected CNFs with fused junctions form a continuous electrically conductive backbone, while the external coating from polymer infiltration has no effect on the electron transport inside the CNF matrix. As shown in schematic Figure 5.5d, the nanofibers of a pristine CNF film will experience a large contact resistance when infiltrated by polymer layers.[70,77] In comparison, the welded CNF film forms an interconnected structure with well-bonded junctions, and the outer polymer coating will not affect the electron transport inside the interconnected matrix.

We infiltrated epoxy resin into the open structure of a welded CNF matrix to create a composite material with improved mechanical properties as well as excellent bulk electrical conductivity (supporting materials). The poor physical contacts in the pristine CNF film leads to poor mechanical strength and toughness as amorphous nanofibers slide over one another in response to a load. After high temperature Joule heating, nanofibers in the welded CNF films become highly crystalline and fuse together to form stiffer interlocked structures. The fused junctions in the post-process CNF matrix can prevent cross-slip between fibers and result in approximately10 times higher tensile strength and toughness from 0.31 MPa to 3.86 MPa and from 1.265 kJ/m^3 to 20.65 kJ/m^3. After polymer resin infiltration, the tensile strength and toughness were further enhanced to 10.6 MPa and 501.1 kJ/m^3. As shown in Figure 5.5e, the conductivity after epoxy resin infiltration remained relatively constant, due to the 3D interconnected porous structure.

We summarized the electrical conductivity of CNF films and compared with typical fiber networks and fiber-polymer composites in Figure 5.5f.[12,69,70,93–98] The conductivity of the CNF film increases with an increase in the graphitization temperature. It is expected that a higher conductivity can be obtained if the CNF film is more densely packed before it is Joule heated. In the meantime, our CNF-polymer composite exhibits a higher conductivity (340 S/cm) over most of the CNT-enhanced polymer composites reported in the literature, which proves that this material and the Joule heating technique could lead to further promising developments in the field of highly conductive polymer composite design.

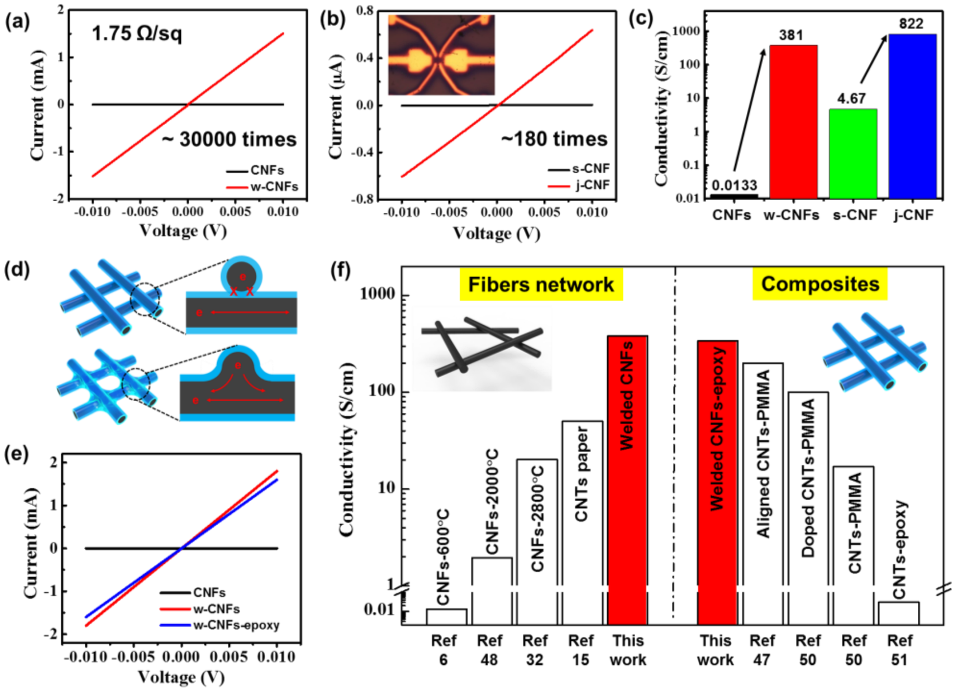

Figure 0.5. The electrical conductivity of the welded CNF (w-CNFs). (a) Conductivity results for the CNF film before and after the high T Joule heating process. (b) Conductivity measurement results for a single fiber before and after Joule heating. (c) The conductivity of a pristine CNF film, a welded CNF film (w-CNF), a single fiber CNF (s-CNF) and a Joule heated single fiber CNF (j-CNF). (d) Schematic diagram to show the change in the structure of separate and welded fibers after polymer resin infiltration. (e) Conductivity measurement results of pristine CNFs, welded CNFs, and welded CNFs after polymer infiltration (w-CNFs-epoxy). (f) Chart comparing the conductivity of CNF films, CNT films, and their composites.

5.3 Conclusion

A Joule heating method was developed to bring the CNF film to high temperatures (> 2500 K) at an ultrafast rate (~200 K/minute), thereby significantly improving the bulk electrical and mechanical properties. The bulk electrical conductivity of the carbon structure increased four orders of magnitude to ~ 380 S/cm and a sheet resistance of 1.75 Ω/sq. This work demonstrates a high temperature Joule heating method that can enable graphitization of carbon materials at a high temperature, and also provide a new strategy to build a covalently interconnected carbon network by welding adjacent carbon fibers together.

5.4 Experimental

CNF preparation, Joule heating process, Temperature and Conductivity measurement, and Characterizations: see Chapter 3 Experimental sections.

5.5 Supporting materials

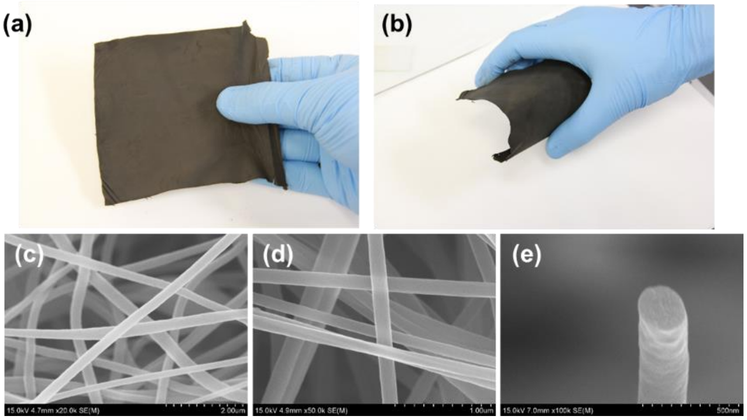

Figure 5.6. (a)-(b) Images of pristine CNF in a flat and bent state. (c)-(e) SEM images of the pristine CNF at different magnifications.

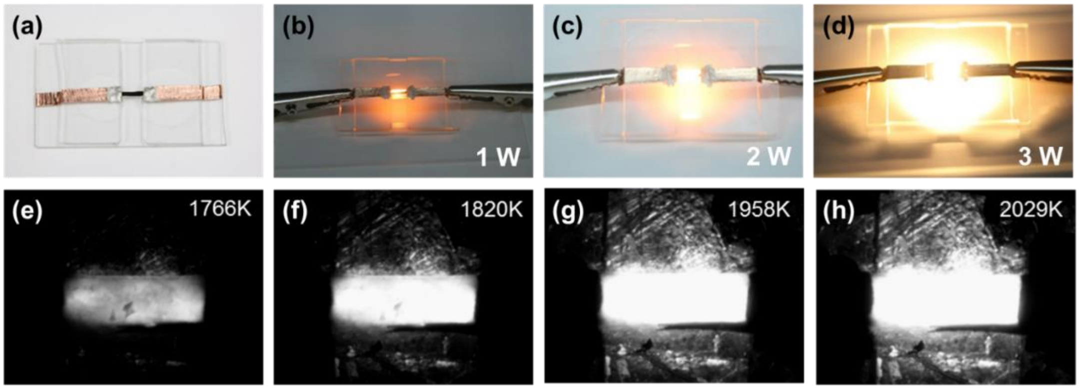

Figure 5.7. (a)-(d) *In-situ* images and (e)-(f) thermal microscope images for the lighting process induced by Joule heating at different powers and temperatures.

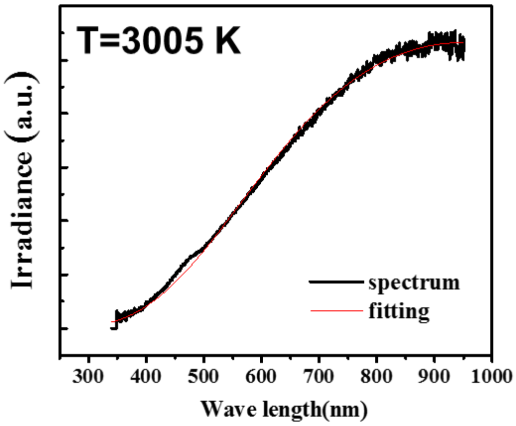

Figure 5.8. Temperature fitting from the device emission spectra at close to 3000 K.

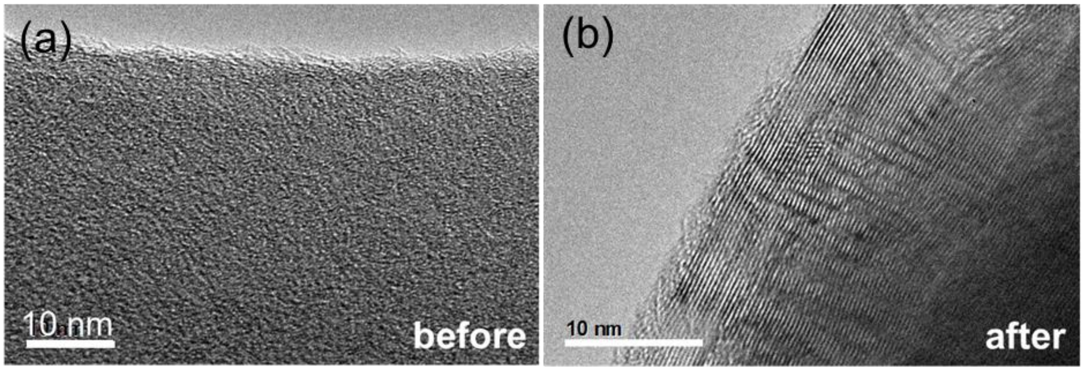

Figure 5.9. (a) HRTEM image of the pristine CNF film and (b) the CNF after Joule heating.

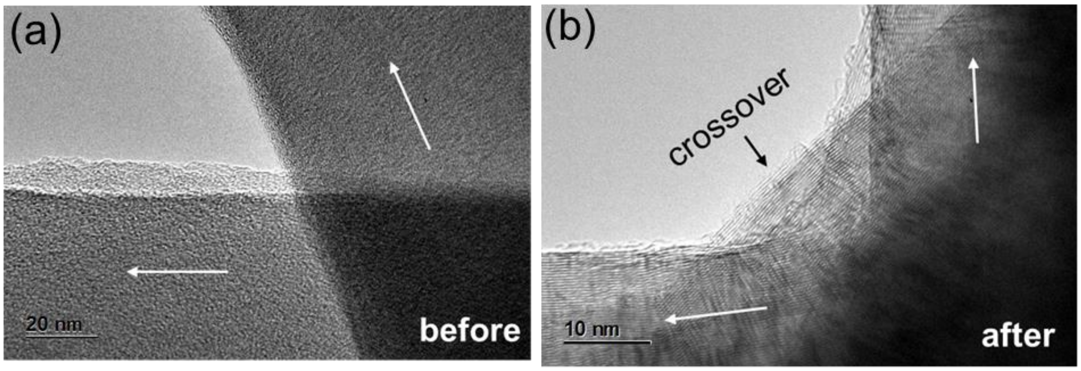

Figure 5.10. (a) HRTEM observation of a pristine CNF at a fiber junction. The white arrows indicate the fiber directions. (b) HRTEM observation of a Joule heated CNF at a fused fiber junction. The white arrows indicate the previous fiber directions. A continuous weld or fusion between two fibers is observed.

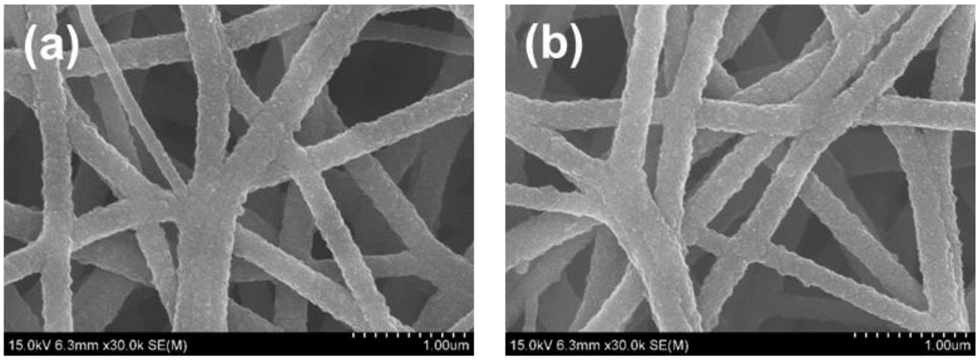

Figure 5.11. (a)-(d) SEM images of the welded CNF.

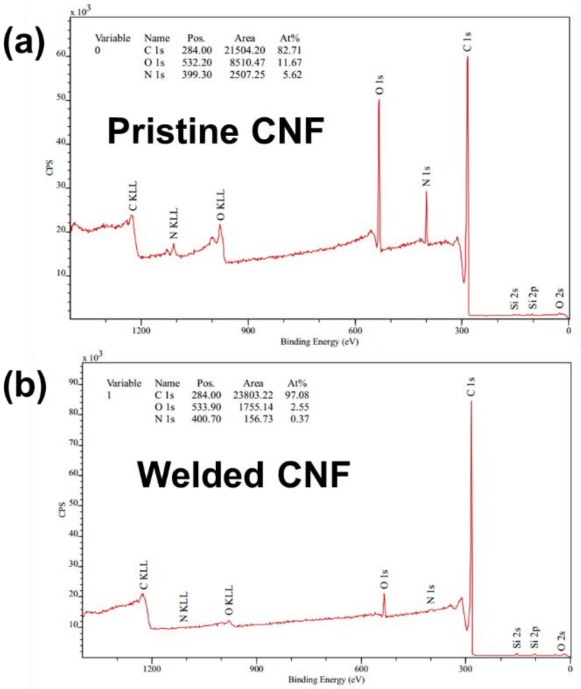

Variable	Name	Pos.	Area	At%
0	C 1s	284.00	21504.20	82.71
	O 1s	532.20	8510.47	11.67
	N 1s	399.30	2507.25	5.62

Variable	Name	Pos.	Area	At%
1	C 1s	284.00	23803.22	97.08
	O 1s	533.90	1755.14	2.55
	N 1s	400.70	156.73	0.37

Figure 5.12. XPS elemental analysis of the CNF film before and after the high temperature Joule heating technique.

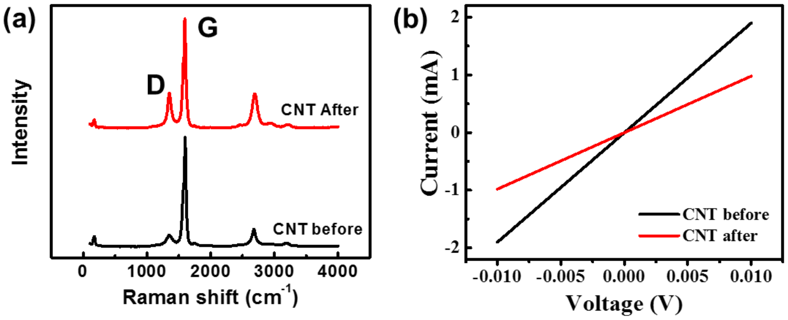

Figure 5.13. Raman spectra and conductivity measurements of the CNT film before and after Joule heating process.

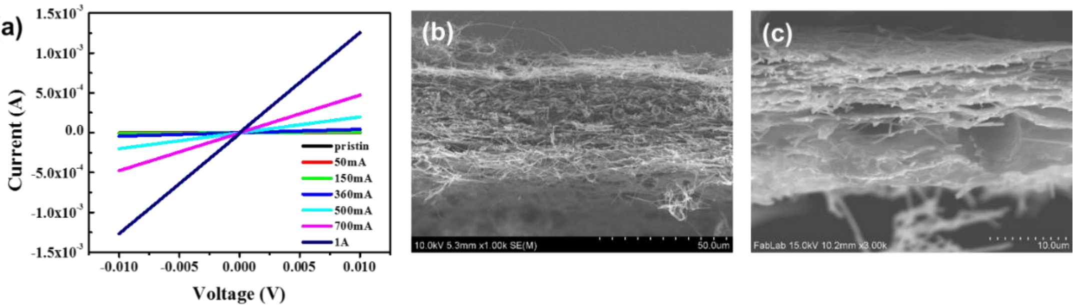

Figure 5.14. CNF film conductivity measurement results. (a) Voltage-current profiles of the CNF film after different Joule heating conditions (driving currents). (b) and (c) Cross-section SEM images of pristine and welded CNF films.

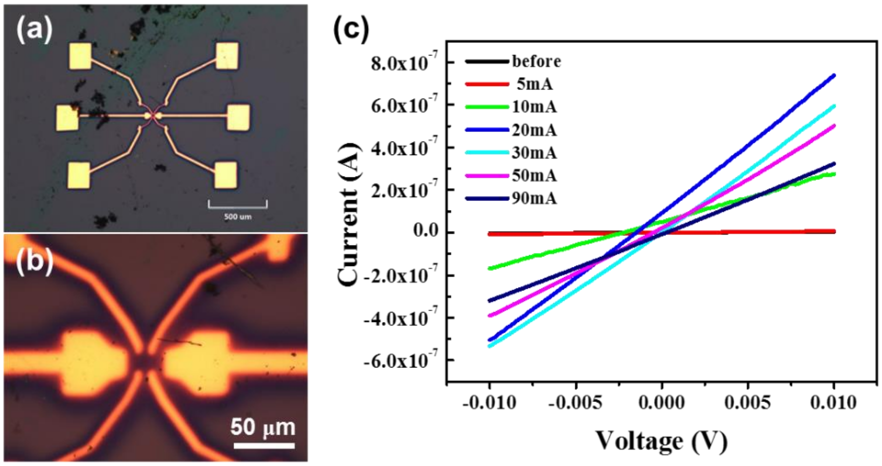

Figure 5.15. Single fiber conductivity measurement. (a) and (b) Au electrodes on a single carbon nanofiber made by a micrometer sized shadow mask. (c) Single fiber voltage-current profiles under a bias field of 10 mV.

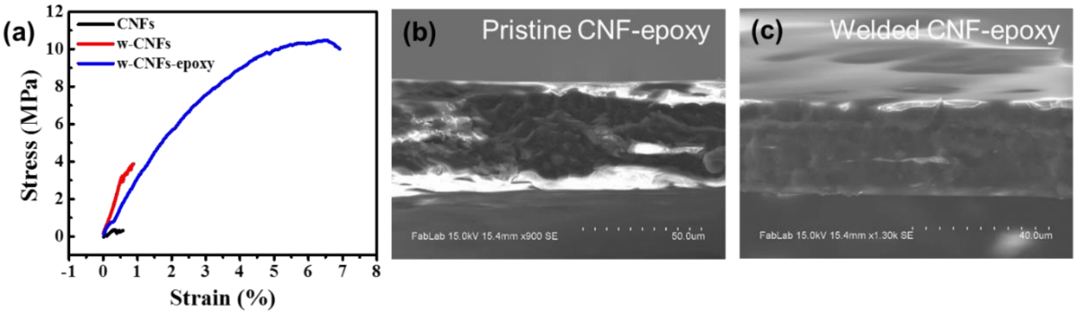

Figure 5.16. (a) The strain-stress curves for pristine CNFs, welded CNFs (w-CNFs), and welded CNFs after polymer infiltration (w-CNFs-epoxy). (b) and (c) Cross-sectional SEM images of the pristine and welded CNF after polymer infiltration.

Chapter 6: Epitaxial welding of carbon nanotubes[*]

Abstract

Carbon nanomaterials are desirable candidates for lightweight, highly conductive, and corrosion-resistant current collectors. However, a key obstacle of utilizing carbon nanomaterials is the weak interconnection between adjacent nanostructures, which renders orders of magnitude lower electrical conductivity and mechanical strength in the bulk assemblies. Here we report an "epitaxial welding" strategy to engineer carbon nanotubes (CNTs) into highly crystalline and interconnected structures. Solution-based polyacrylonitrile was conformally coated on CNTs as "nano-glue" to physically join CNTs into a network, followed by the rapid high temperature annealing (>2800 K, in ~30 mins) *via* electrical Joule heating to graphitize the polymer coating into epitaxial layers using the embedded CNTs as growth templates. The newly formed graphitic layers effectively bridge the adjacent CNTs and contribute to both a high conductivity (~1500 S/cm) and a high tensile strength (~120 MPa) for the contact-welded CNTs (W-CNTs). In addition, the W-CNTs display chemical and electrochemical stabilities in strong acidic/alkaline electrolytes (>6 mol/L) when potentiostatically stressing at both cathodic and anodic potentials. With these exceptional properties, the W-CNT films are optimal as high-performance current collectors and were demonstrated in the state-of-the-art aqueous battery using a "water-in-salt" electrolyte.

---

[*] The results in this chapter have been submitted: Yao, Y.; et al; Hu, L. Epitaxial Welding of Carbon Nanotube Networks for Aqueous Battery Current Collectors. *ACS Nano*, submitted, 2018.

6.1 Introduction

The crystalline allotropes of carbon nanomaterials such as carbon nanotubes (CNT) and graphene are widely studied due to their high surface areas, superb electrical and thermal conductivities, and excellent mechanical properties.[8,99–105] Importantly, unlike metals, highly graphitic carbon shows considerable stability in harsh chemical environments like highly concentrated acidic/alkaline solutions, owing to the chemically inert carbon bonds that do not react with the active H^+ or OH^- in these solutions.[20,21,106] Therefore, highly crystalline carbon nanomaterials are intensively investigated as flexible, lightweight, highly conductive, and corrosion-resistant current collectors for batteries and catalysts, to replace traditional metallic current collectors that are bulky, heavy, and liable to erode in the corrosive environments.[24,102,107–111] Recently, the increasing market demands in high-performance and intrinsically safe aqueous batteries[110,112,113] boosted the research of carbon-based current collectors that are stable in the strong acidic or alkaline aqueous electrolytes, which rule out metallic current collectors that are subject to severe corrosion.[114,115]

The key obstacle of using carbon-based current collectors lies in the orders of magnitude performance degradation in bulk assemblies of carbon nanomaterials as compared to their nanoscale building blocks,[71,79,116,117] which can be ascribed to the weak or even lack of effective interconnections between individual nanostructures.[71,117] Previously, heteroatoms or amorphous carbon are often employed to bridge adjacent CNTs by two major approaches: (1) non-covalent physical bonding, where a continuous layer of material is deposited to connect the adjacent CNTs by physical means, such as atomic layer deposition (ALD) of Al_2O_3 or chemical vapor deposition

(CVD) of amorphous carbon and SiC,[71,79,83,84] and (2) covalent chemical bonding, where divalent bonding elements such as B or S are intentionally introduced to covalently join adjacent CNTs into elbow structures during CNT synthesis.[68,75,118] However, the introduced foreign elements, impurities, and amorphous coating layers in these approaches can be a huge problem in the corrosive chemical and electrochemical environments which requires highly graphitic carbon to achieve stabilities. Ideally, building intrinsic covalent carbon bonds among CNTs is strongly preferred;[119,120] yet considering the high stability and high C-C bond energy (ΔH=85 kcal/mol), opening and reforming covalent carbon bonds between CNTs presents a great challenge. Successful demonstration has only been achieved through high energy radiation (by electron, ion beam, or plasma),[121–126] or by high pressure (up to 55 GPa) combined with shear deformation.[126–128] These approaches not only have limited scalability owing to special equipment needed, but also can easily cause physical/radiative damages to the original CNTs and introduce a lot of undesired defects into the system. Therefore, a more constructive and scalable method is needed for the formation of bulk interconnected CNT assemblies.

Here we report an “epitaxial welding” method as a scalable and cost-effective approach for the formation of highly crystalline and interconnected CNT assemblies bearing the merits required as high-performance current collectors. Solution-based polyacrylonitrile (PAN) was dip-coated onto CNTs as “nano-glue” to physically connect CNTs together and the PAN coated CNT film was rapidly annealed at a high temperature (>2800 K, in ~30 mins) *via* electrical Joule heating, which *in situ* graphitize the polymer coating on CNTs into continuous graphitic layers through epitaxial growth. The newly formed graphitic layers effectively eliminate the poor contacts in CNT assemblies by bridging adjacent CNTs together and contribute to both high electrical conductivity (~1500 S/cm) and mechanical strength (~120 MPa), which are 5 and 20 times higher than the un-welded CNT assemblies, respectively. Moreover, the high-temperature graphitization also effectively removes the defects and helps the formation of highly crystalline carbon showing chemical and electrochemical stabilities in the corrosive environments. The proposed "epitaxial welding" method can be generally applied to other graphitic carbon nanomaterials as an effective strategy to form highly crystalline and interconnected carbon nanostructures.

6.2 Result and discussion

A dry-processed CNT film drawn from vertically aligned CNT forest was selected as a model system owing to its simple and ordered structure.[99,108,129–132] The as-grown CNTs are continuous and parallel with each other in the length direction and have an average diameter of 43±7.5 nm. Due to the weak van der Waals interaction among individual CNTs, the CNT film presents a porous and loosely packed structure that could be easily pulled apart when handling. By applying polymer coating through immersion into 2% PAN/dimethylformamide (DMF) solution and subsequent drying, PAN chains can assemble on the surface of CNTs to form a conformal coating (Fig. 6.1a). Also, the structure becomes dense and compact as indicated by the reduced thickness from 20-30 μm for pristine CNT to ~10 μm for CNT-PAN. The epitaxial growth of the coated PAN layer into highly crystalline graphitic carbon was initiated by high temperature annealing using embedded CNTs as the template, which is achieved by electrically triggered Joule heating to over 2800 K in ~26 minutes and holding for 5 minutes (Fig. 6.1a inset).[133,134] As PAN conformally coats along the outer surface of CNTs and binds adjacent CNTs together at the intersections, the derived graphitic layer can also simultaneously weld CNTs together as a graphitic welder, to obtain a welded CNT film (W-CNT). This process is denoted as “epitaxial welding”.

In the “epitaxial welding” process, the polymer coating provides the carbon source for graphitic welding between adjacent CNTs at high temperature, and PAN was chosen owing to its simple structure and high yield in graphitic carbon production.[135] Meanwhile, the Joule heating process is especially effective as it directly heats the samples other than the bulky chamber/furnace and therefore is both fast and energy efficient: a typical heating process to >2800 K takes less than 30 minutes (heating rate ~ 100 K/min) with a consuming power less than 20 W. Additionally, as the temperature in the Joule heating process is directly related to the resistance ($P=I^2R$), the junctions or contact points between CNTs having higher resistance than the crystalline CNTs will be selectively heated to higher temperature, demonstrating an effective/targeting graphitization at the junctions.

The microstructure evolution from pristine CNT to CNT-PAN and W-CNT during the “epitaxial welding” process is examined by scanning electron microscope (SEM) images (Fig. 6.1b-d). It is clear that pristine CNT film shows a porous and loosely packed structure due to poor physical contact; after PAN coating, CNTs are densely packed together through polymer binding, showing significantly reduced gaps among the CNT bundles. After Joule heating at above 2800 K, the W-CNT film remains compact and forms interconnected networks of CNTs (Fig. 6.1d).

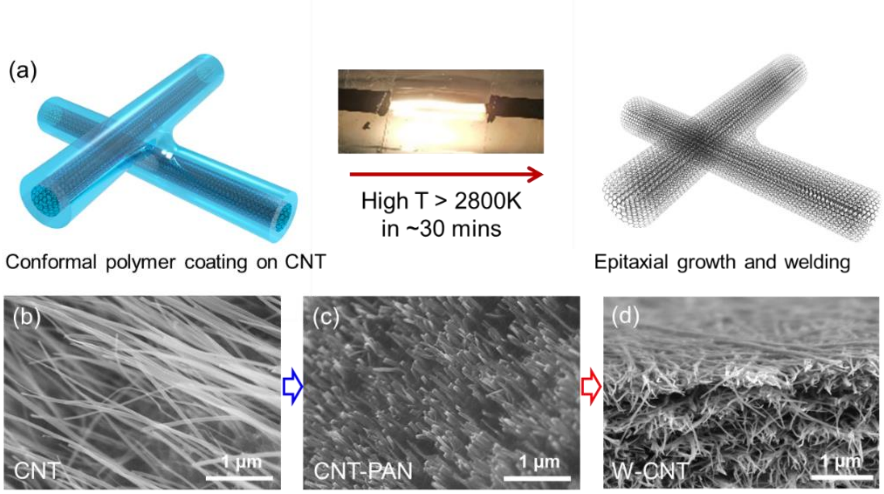

Figure 6.1. “Epitaxial welding” for the formation of interconnected W-CNTs. (a) Schematic of CNTs with a conformal polymer coating and after high temperature heating. The inset shows the picture of CNT-PAN film under high temperature (2800 K) Joule heating. SEM images of (b) CNT, (c) CNT-PAN, and (d) W-CNT, showing the microstructure evolution at each step.

The structural evolution over the entire “epitaxial welding” process was examined in further detail in Fig. 6.2. The pristine CNT film is porous and loosely packed (Fig. 6.2a), which is difficult to handle and lacks the performance required for practical implementation. After coating with PAN solution, pressing, and drying, the individual CNTs were effectively glued with a much denser packing structure, showing at least 2-4 times thinner thicknesses in CNT-PAN (from 20-30 μm to 5-10 μm) (Fig. 6.2b). The densely packed structure facilitates the intimate contact and subsequent welding of adjacent CNTs. This densely packed structure can be well maintained after high temperature annealing, indicating that all CNTs remain binding with each other without losing the structure integrity (Fig. 6.2c).

Electrically triggered Joule heating is adopted as a facile means for high temperature annealing of carbon materials, demonstrating several advantages as compared with conventional furnace heating: (1) ultrahigh temperatures up to 3000 K inside the sample (most annealing furnaces have maximum temperature of 1500 K or lower), which is critical to achieve highly graphitized carbon structure; (2) unprecedented heating and cooling rates up to 10^4-10^5 K/s (the rate for furnace heating is roughly ~ 10 K/min), enabling fast ramp to high temperature for efficient heating; (3) easily controllable temperature, duration, and heating ramp rate that can be programmed in the electrical power source; and (4) highly energy efficient as mentioned before.

The CNT-PAN film was connected to an electrical power source through conductive silver paste and copper tape, spanning across a trench between two separated glass slides to prevent contamination and damage at high temperature (Fig. 6.2d). High temperature annealing can be easily achieved by slowly increasing the current from 0 to 3.15 A at 0.002 A/s in a gradual annealing process performed in an argon-filled glovebox. During the annealing, the film lit up as a high temperature blackbody radiation source at above 1000 K (Fig. 6.2d).[21,25,106,117] The emitted spectrum was collected by an optical fiber from 350 nm to 950 nm (Fig. 6.2e) and then fitted to the blackbody radiation equation to obtain T as a close approximation of temperature reached in the sample (Fig. 6.2f). By using the direct Joule heating developed in our lab,[36] the CNT samples can be heated above 2800 K by simply increasing the input power with a heating rate of 100 K/s. All these temperature controls can be performed by a programmable electrical power source, making the high temperature annealing process more controllable.

Fig. 6.2g-i show the compositional and structural evolutions from CNT, CNT-PAN to W-CNT revealed by Raman and X-ray photoelectron spectroscopy (XPS) spectra. Overall, these characterizations show that PAN coating initially introduces impurities (N, O) and amorphous structures into CNT film, while after high temperature annealing, the W-CNT shows similar or even better purity and crystallinity than pristine CNT film. In the Raman spectra, typical D-mode (D) and G-mode (G) peaks can be seen for all samples, where the D peak represents the disordered or defective carbon bonds and G peak indicates the graphitic sp^2 carbon bonds.[62,117] CNT-PAN film has a large background that obscures the peaks due to the addition of polymer coating. The W-CNT film shows a lower D peak and correspondingly reduced D/G ratio of $I_D/I_G=0.1$ compared with the $I_D/I_G=0.3$ for the pristine CNT film, which is a strong indication of increased graphitic structures in W-CNT after high temperature annealing, even compared with the pristine CNT. Note the decrease in 2D peak intensity comes from the increased diameter of W-CNTs.[62] Additionally, in the XPS spectra, the typical C, N, and O peaks were detected and the C:N:O ratio evolved from (98.8:0:1.2) for CNT, to (79.8:8.9:11.3) for CNT-PAN, and to (98.9:0:1.1) for W-CNT, confirming slightly improved purity (reduced O content) in W-CNT after high-temperature annealing. It should be noted that N is introduced from the air stabilized PAN and is only observed in the CNT-PAN sample, suggesting that all polymer coating has been converted into carbon materials in W-CNT. The above characterizations prove the effectiveness of high-temperature annealing by Joule heating for fast graphitization and confirm the highly crystalline and graphitic carbon achieved in the W-CNT film.

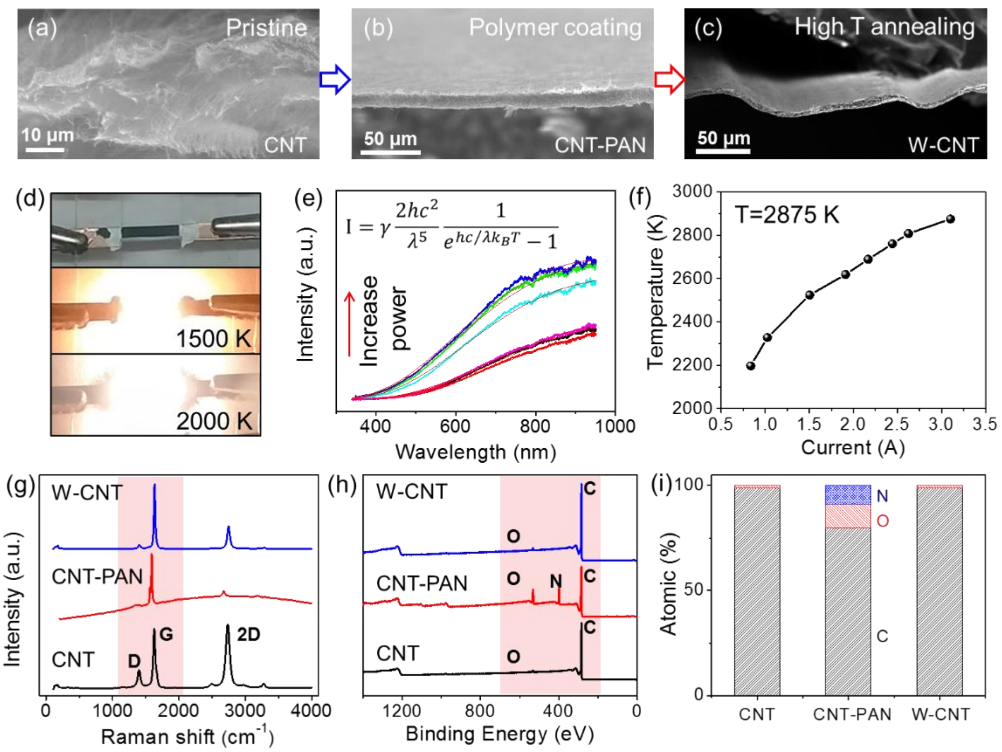

Figure 6.2. The “Epitaxial welding” process and associated structural evolution. (a)-(c) SEM cross-section images of CNT, CNT-PAN, and W-CNT. (d) Picture for Joule heating set-up, and the lighting pictures during Joule heating at 1500 K and 2000 K. (e)-(f) The emitted light spectra at increased power input and corresponding fitted temperatures according to the blackbody radiation equation. Structural evolutions observed in (g) Raman and (h)-(i) XPS for CNT, CNT-PAN, and W-CNT.

The aforementioned structural evolution was further corroborated by the high-resolution TEM images. The pristine CNT shows a highly crystalline structure with fiber diameter averaging around 40 nm (Fig. 6.3a). After polymer coating and high-temperature annealing, a radial growth of CNT was found to be around 10-20 nm in thickness (Fig. 6.3b). Most significantly, these additional graphitic layers have the same atomic stacking and alignment as the initial CNTs, showing the growth of epitaxial layers (EL) *via* high temperature annealing. Here, the embedded CNTs act as templates for the epitaxial growth of PAN layers along the CNT direction during the high temperature graphitization. The epitaxial growth of graphitic layer can also be observed at the junction point, showing that the newly formed graphitic layers can successfully bridge CNTs together (Fig. 6.3c for pristine CNTs and 3d for W-CNTs). The epitaxial graphitic layers continue to grow from one CNT to the other, behaving as a bridge to connect adjacent CNTs for forming a continuous pathway for electron conduction and mechanical force transfer, leading to increased electronic conductivity and mechanical strength that will be discussed in the following section.

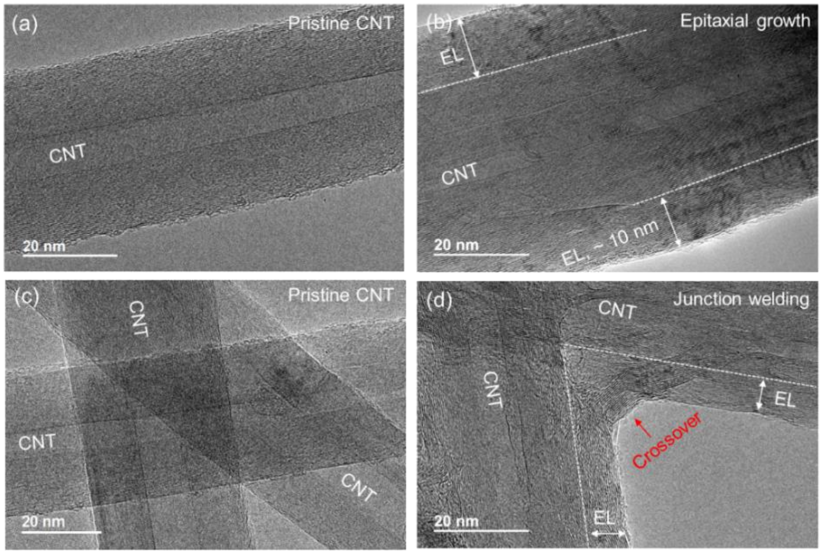

Figure 6.3. Microstructures of pristine CNTs and W-CNTs. (a) TEM image of pristine CNT with a diameter around ~ 35 nm. (b) TEM image of W-CNT to show the epitaxial growth of graphitic layers from PAN using CNT as a template. EL stands for epitaxial layer. The new layer is clear and has the same atomic packing as the embedded CNT. (c)-(d) TEM images of pristine CNTs and W-CNTs at junctions to show the junction welding and formation of crossover layers between CNTs after “epitaxial welding”.

To further prove the effectiveness of epitaxial growth of graphitic layer by high temperature Joule heating, the electrical conductivity and mechanical properties of W-

CNT films were measured and compared with those of pristine CNT films. Fig. 6.4a-c show the electrical conductivity and mechanical stress-strain curves for CNT, W-CNT-0.5 (using 0.5%PAN solution), and W-CNT-2 (using 2%PAN solution). The conductivity of CNT film increased from 314 S/cm to 900 S/cm for W-CNT-0.5, and up to 2000 S/cm for W-CNT-2 (averaged around 1500 S/cm). Similarly, the mechanical yield strength also increased from 5.6 MPa (CNT), to 22.5 MPa (W-CNT-0.5), and to 126 MPa (W-CNT-2) (Fig. 6.4b), with the maximum Young's modulus reaching to ~30 GPa for W-CNT-2, which is approximately 5000 times greater than the 63 MPa Young's modulus for the pristine CNT film. Thus, after epitaxial welding, the W-CNT film forms compact and interconnected structures that simultaneously boost the electrical conductivity and mechanical performance. It is worth noting that both the conductivity and mechanical properties of W-CNT-2 are higher than those of W-CNT-0.5, which can be explained by the limited available welding agent and graphitic coatings for using dilute 0.5% PAN. Decreasing the polymer concentration (0.5% PAN) resulted in only non-continuous, partially graphitic layers formed on CNT.

Besides the improved conductivity and mechanical strength, the highly graphitic carbon in W-CNT film also ensures excellent chemical and electrochemical stabilities in acidic and alkaline solutions. Fig. 6.4d shows the schematic of T-cell setup for corrosion evolution to mimic the actual aqueous battery cells. The fixed electrodes geometry in T-cell setup also guarantees the accuracy of repeated measurements. The electrochemical corrosion was evaluated by measuring the cyclic voltammograms (CVs) of W-CNT film before and after potentiostatically stressing (Fig. 4e). The chemical and electrochemical stabilities of W-CNT were investigated in highly concentrated acidic (5 mol/L H_2SO_4) and alkaline (5 mol/L KOH + 1 mol/L LiOH) electrolytes at both cathodic and anodic potentials (1.7 V and -0.5 V vs Ag/AgCl for acid; 0.65 V and -0.9 V vs Hg/HgO for alkaline). These potentials were chosen to mimic the voltage limits in typical acidic and alkaline batteries. The highly concentrated electrolytes and aggressive holding potentials were chosen to accelerate the corrosion of those electrodes.

Fig. 6.4f shows cyclic voltammograms (CVs) before and after holding the W-CNT film at fixed cathodic and anodic potentials in both acidic and alkaline electrolyte solutions. In the alkaline electrolytes, W-CNT shows excellent stability with minor changes in CV area and peak height after potentiostatically holding. The minute differences between the 0 h and 48 h curves are due to an initial wetting process of the electrodes. Under acidic conditions, there are redox peaks at ~ 0.5V, which is characteristic of a quinone-hydroquinone (Q-HQ) redox reaction and can be used for measuring carbon corrosion along with an overall increase in voltammetric current. At the anodic potential, CVs of W-CNT show no increase in Q-HQ peak height or CV area after stressing, indicating that W-CNT is very stable under the anodic holding in acidic conditions under these reduction potentials. For the cathodic potential hold of 1.7 V in acid, the current associated with the Q-HQ region as well as the area under the CV curves increased slightly after stressing, indicating minute unstable corrosion in W-CNT film under cathodic potential in acidic electrolytes.

As a comparison, a commercially available carbon-based current collector, activated carbon cloth (ACC), was used for the corrosion test under the same condition. The ACC carbon is not as stable as W-CNT films in either acid or alkaline aqueous solutions, as indicated by the large value of current in CVs as well as the increase of areas inside the C-V curves after longtime holding. During the 48 h potential hold in acidic electrolyte at cathodic potential, the total peak height of Q-HQ redox reaction increased by a factor of 4.8 times for commercial ACC current collectors, as compared to an increase of 1.5 times for W-CNT films, demonstrating higher stability of W-CNT compared to ACC when used in harsh aqueous conditions.

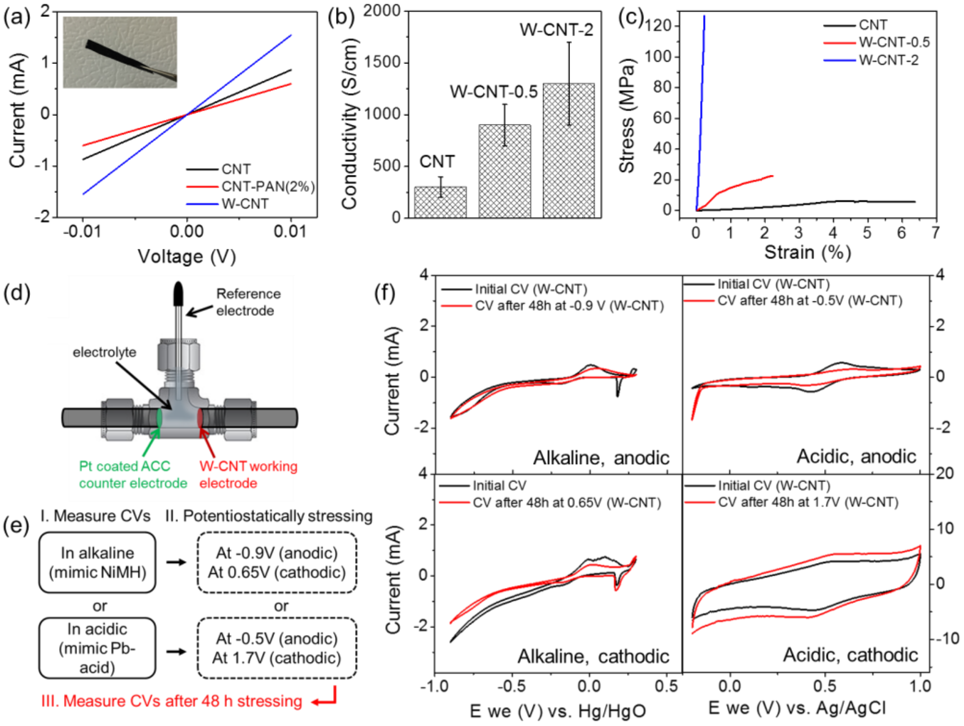

Figure 6.4. Properties of W-CNT films. (a)-(b) Electrical conductivities of CNT and W-CNT films (using 0.5% PAN and 2% PAN, respectively). The inset is the film used in four-point conductivity measurement. (c) Mechanical stress-strain properties of CNT and W-CNT films. (d) Schematic of three electrodes T-cell setup for corrosion evaluation. (e) Evaluation process: I. CVs measured at the beginning; II. Potentiostatically stressing at various conditions for 48 hours; III. CVs measured after 48 hours stressing. (f) CVs before and after holding the W-CNT film and commercial ACC carbon at cathodic and anodic potentials in the acidic or alkaline electrolyte, as indications for the degree of surface corrosion after potentiostatically stressing.

The above performance data clearly show the effectiveness of the epitaxial welding process and also the potential of W-CNT films to be used as lightweight, highly conductive, mechanically strong, and corrosion resistant current collectors. Here we demonstrate using W-CNT films as a superb current collector for the state-of-the-art "water-in-salt" aqueous battery with high performance and electrochemical stability. Fig. 6.5a shows the cycle voltammetry (CV) of W-CNT films in highly concentrated "water-in-salt" electrolyte: 21 mol/kg lithium bis(trifluoromethane sulfonyl)imide (LiTFSI) in water.[113,137] The LiTFSI possesses high solubility in up to 21 mol/kg high concentration aqueous solution, which shows high stability against hydrolysis. This, therefore, enables a larger electrochemical stability window, ranging from ~ 2 to 4.5 V (vs. Li^+/Li), corresponding well with a measured window of stable performance shown by the W-CNT film in Fig. 6.5a.

A full cell of lithium-ion battery was evaluated using $LiMn_2O_4$ as a cathode, Mo_6S_8 as the anode material (denoted as LMO/MS) and W-CNT films as current collectors for both electrodes. Fig. 6.5b shows a typical charge-discharge curve for the full battery cell in conventional coin cell configuration. The battery shows great stability in this highly concentrated "water-in-salt" aqueous electrolyte with a high capacity of 120 mAh/g (based on the mass of the anode) at 2 C rate (1 C = 125 mA/g) and a Coulombic efficiency >99.5% after the first few cycles (Fig. 6.5c). The exceptional electrochemical performance should be attributed to the stability of "water-in-salt" electrolyte as well as the W-CNT current collector, which is stable even in the extremely concentrated electrolyte solution and wide electrochemical window.

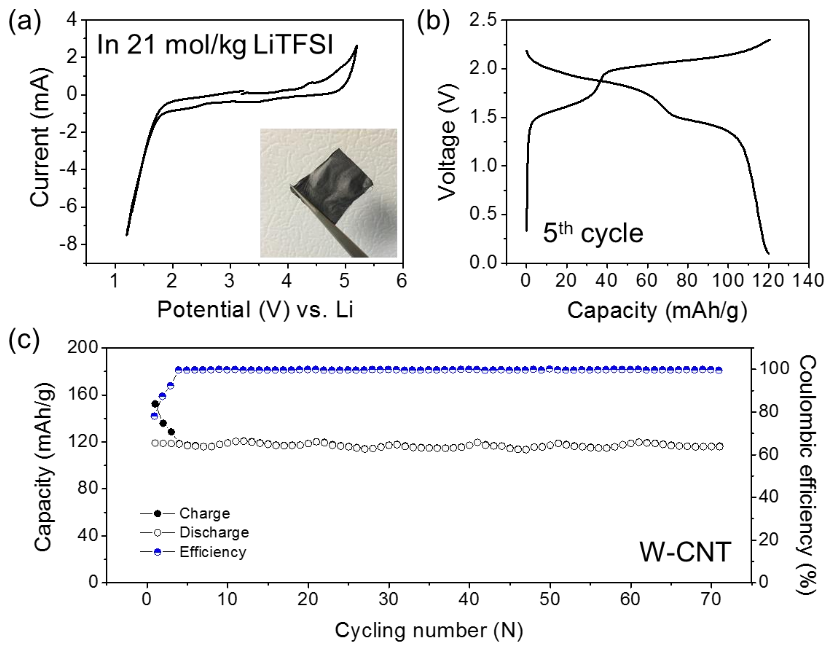

Figure 6.5. W-CNT films as current collectors for “water-in-salt” aqueous battery. (a) CV curve showing the electrochemical stability window of the W-CNT film in the “water-in-salt” electrolyte. (b) Stable (5th) charge-discharge curve and (c) cycling performance of full battery cell (LMO/MS) using W-CNT films as current collectors.

6.3 Conclusion

In this work, we demonstrate an “epitaxial welding” process as an effective method to form highly crystalline and interconnected CNTs by utilizing thin and epitaxial graphitic layers to bridge adjacent CNTs together into a 3D covalent CNTs networks, which can subsequently lead to improvement of both electrical conductivity and mechanical properties in the bulk CNT assemblies without sacrificing the structural and compositional purity. The resultant W-CNT film is highly conductive (~1500 S/cm), mechanically strong (~120 MPa), and chemically and electrochemically stable in acidic/alkaline solutions, showing great promises as high-performance current collectors for various applications (*e.g.* aqueous battery). Both the solution-based polymer coating and high-temperature annealing in the “epitaxial welding” process are considerably simple and scalable for industrial scale production, and can also be generally applied to various carbon materials where the interconnection between carbon nanostructures is a problem.

6.4 Experimental

CNT synthesis: Firstly, vertically aligned CNTs (CNT forest) were grown on a quartz through chemical vapor deposition from acetylene (600 sccm), argon (395 sccm), and Cl_2 (5 sccm), using $FeCl_2$ as the catalyst at 760 °C, 3 Torr for 15 minutes.[131] Dry-processed CNT film (20-30 μm thick) was directly drawn from the as-grow CNTs forest through a tail-to-head manner.[131]

PAN coating and Joule heating: A piece of CNT film (typical geometry 2 cm*0.5 cm, for battery current collectors geometry 2 cm*2 cm) was immersed into a 2% PAN/DMF solution for 1 min, and then the fully saturated film was pressed between glass slides to remove the excess polymer and solvent, resulting in a compact CNT-PAN film. The film was then heated to 60 °C on a hot plate in a fume hood to evaporate absorbed solvent, leaving a PAN coated CNT film for Joule heating experiment. For Joule heating, the CNT-PAN film was bridged between two laterally separated glass slides, and both ends of the film were connected to copper electrodes using conductive silver paste. The film was heated in an argon-filled glove box by introducing increasing electrical current from 0 to 3.15 A (0.002 A/s) and kept at 3.15 A for 5 minutes and then cooled down to room temperature slowly at a rate of 0.01A/s.

Corrosion test: Electrochemical measurements were conducted using a perfluoroalkoxy alkane (PFA) T-cell in a three-electrode configuration. Graphite rods were used to hold the CNT-PAN film as a working electrode and Pt-coated activated carbon cloth (ACC) counter electrode (0.5 in diameter) in place, sealing the T-cell and acting as a current collector. The T-cells were filled with 5 mL of 5.0 mol/L H_2SO_4 for testing in acidic conditions or 5mL of 5.0 mol/L KOH + 1.0 mol/L LiOH for testing in basic conditions.silver/silver chloride (Ag/AgCl) and mercury/mercury oxide (Hg/HgO) reference electrodes were used for testing in acidic and basic electrolytes, respectively. A BioLogic EC-Lab VSP modular potentiostat was used to hold the CNT-PAN at fixed cathodic and anodic potentials of 1.7 V and -0.5 V *vs.* Ag/AgCl, respectively, for tests with acid electrolyte. In basic electrolyte, CNT-PAN was held at cathodic and anodic potentials of 0.65 V and -0.9 V *vs.* Hg/HgO, respectively. The CV scan rate is 0.5 mV/s. Due to oxygen and hydrogen evolution during electrochemical tests, the electrolyte solution was periodically refilled with water.

Battery test: The high-concentration aqueous electrolyte was prepared by dissolving LiTFSI (Tokyo Chemical) in purified water to its solvation limit of about 21 mol/kg. The anode material Mo6S8 was prepared according to the previously reported leaching method from Cu2Mo6S8.[113] The cathode material LiMn2O4 was purchased from MTI. Electrodes materials were directly coated onto the surface of the W-CNT film and showed good wetting and attachment. Cyclic voltammetry measurement was performed on the CHI 600E electrochemical workstation at a scanning rate of 10 mV/s to determine the electrochemical stability window. The full battery cell was assembled in CR2032-type coin cell and evaluated on a Land BT2000 battery test system (Wuhan, China) at room temperature.

6.5 Supporting materials

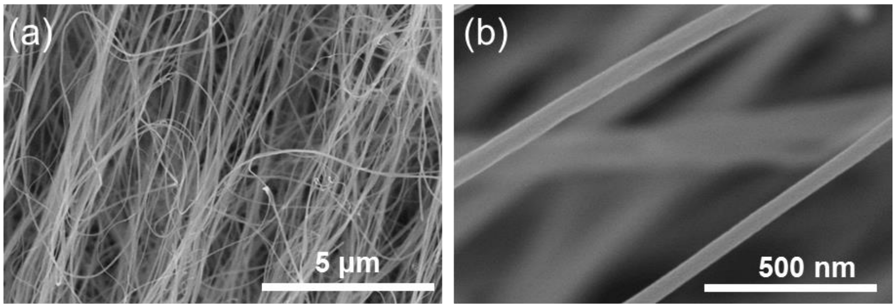

Figure 6.6. (a)-(b) SEM of pristine dry-processed CNT film.

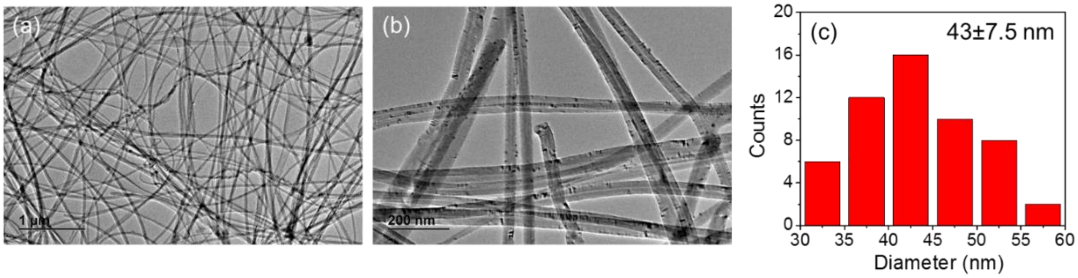

Figure 6.7. (a)-(b) TEM images of pristine CNT, and (c) statistical analysis of CNT diameter distribution in pristine CNT.

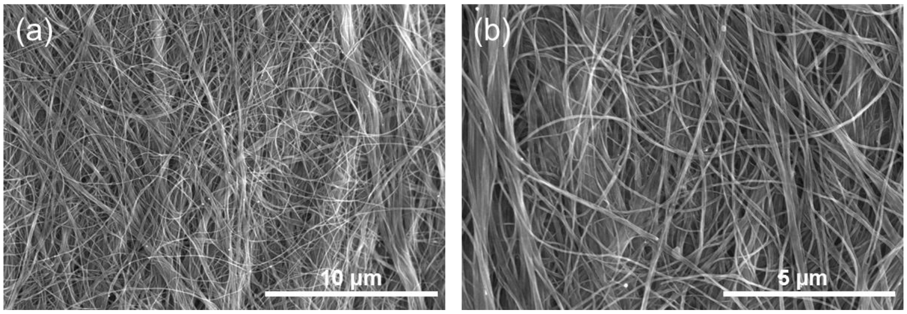

Figure 6.8. (a)-(b) SEM images of PAN coated CNT (CNT-PAN).

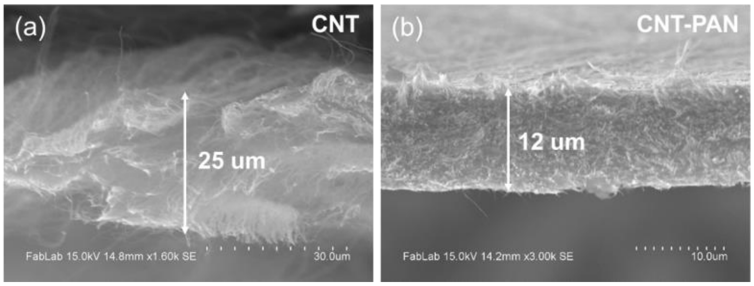

Figure 6.9. (a)-(b) SEM images of pristine CNT and CNT-PAN film (cross-section).

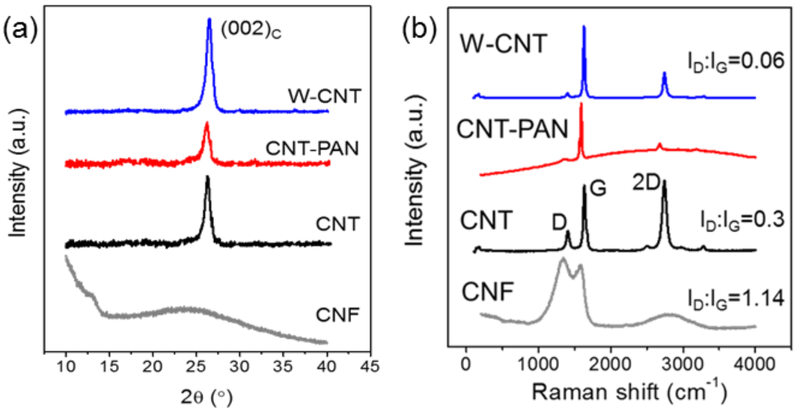

Figure 6.10. (a) XRD profiles and (b) Raman for pristine CNT, CNT-PAN, W-CNT, and a control sample: low temperature (873K) carbonized CNF. The high crystallinity of W-CNT can be indicated by the sharp crystalline (002) peak in the XRD profile, and by the low intensity of D peak as well as the low D:G ratio.

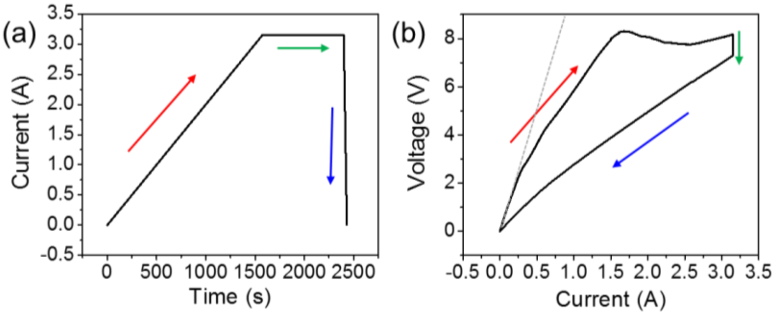

Figure 6.11. The high temperature annealing process. (a) Current as a function of time and (b) Measured voltage as a function of driven current.

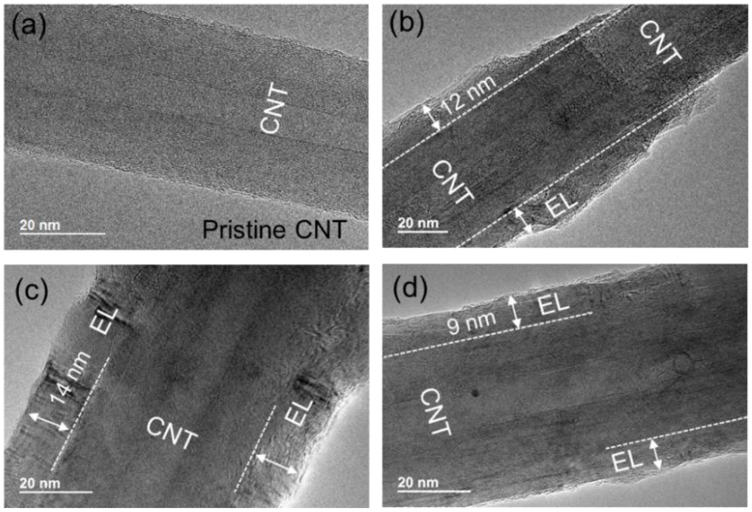

Figure 6.12. TEM images of (a) pristine CNT and (b) CNT with a broken coating which clearly shows the coating thickness around 10 nm. (c)-(d) Epitaxial growth of CNTs after polymer coating and high temperature annealing. EL stands for epitaxial layers.

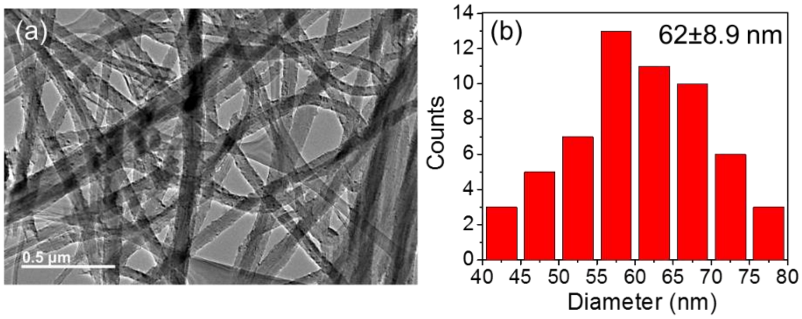

Figure 6.13. (a) TEM images of W-CNT and (b) statistical analysis of diameter distribution in W-CNT.

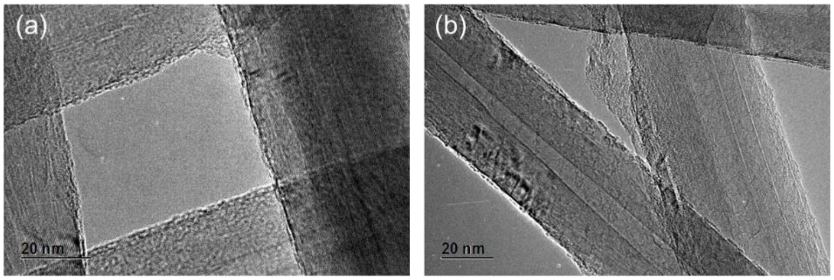

Figure 6.14. (a) and (b) TEM images of W-CNT welded using a 0.5% PAN solution.

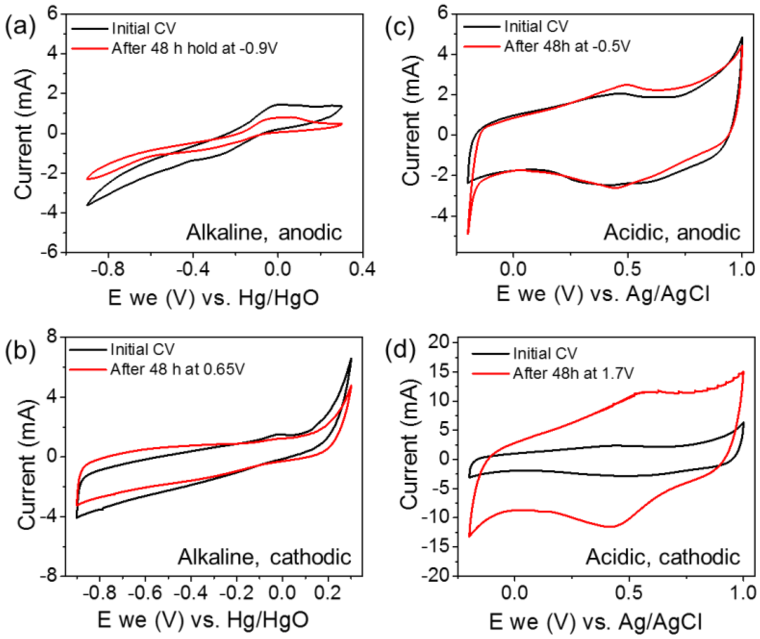

Figure 6.15. Corrosion evaluation of commercially available ACC carbon. CV before and after holding the W-CNT film in alkaline electrolyte at (a) -0.9 V (anodic potential) and (b) 0.65 V (cathodic potential) (vs. Hg/HgO); and in acidic electrolyte at (c) -0.5 V (anodic potential) and (d) 1.7 V (cathodic potential).

Chapter 7: High-Temperature annealing for other applications

7.1 High temperature lighting[*]

Besides the high temperature heating aspect, the electrical triggered Joule heating also leads to bright light emission which can act a high-performance light source. We also report highly efficient broadband thermal radiation from reduced-graphene-oxide (RGO) paper mixed with single-walled carbon nanotubes (CNTs). The RGO-CNT paper can be fabricated by scalable spray coating or 3D printing from ink, and processed into different shapes and formats. High-temperature pre-annealing self-stabilizes the RGO-CNT paper, leading to unprecedented crystallinity and a record-high DC electrical conductivity. Flexible, even foldable paper-thin lighting with different shapes is demonstrated, including long (> 3 mm) and thin (< 1 μm) suspended ribbons acting as incandescent light sources. The high efficiency of incandescent emission is due to the relatively low thermal conductivity, high emissivity, long, thin, planar structure, high operating temperature, and ability to operate in vacuum. These RGO-CNT paper ribbons routinely reach 3,000 K before failure, with some samples exceeding 3,300 K, higher than any other carbon nanomaterial. Excellent performance was achieved, with ~90% radiation efficiency, 200,000 on/off cycles, fast (~13 ms) on/off response time, and stable operation for more than 50 hours. The visible lighting efficiency is comparable to and potentially higher than standard tungsten filament bulbs in Ar. This study demonstrates that RGO-CNT paper can enable emerging lighting

---

[*] The results have been published: Bao, W.; Pickel, A. D.; Zhang, Q.; Chen, Y.; Yao, Y.; Wan, J.; Fu, K.; Wang, Y.; Dai, J.; Zhu, H.; *et al.* Flexible, High Temperature, Planar Lighting with Large Scale Printable Nanocarbon Paper. *Adv. Mater.* **2016**, *28*, 4684–4691. (Yao. Y is the co-first author.)

solutions where arbitrary shapes, manufacturability, cost, and response time are important.

7.2 High temperature annealing of carbonized grass for sodium ion batteries[*]

Through electrical Joule heating, we can obtain high-quality carbon in a rapid and efficient manner. The graphitic carbon (i.e. hard carbon) can be applied for many applications such as high performance, corrosion resistant current collectors, promising anode candidate for room temperature sodium ion batteries etc. We employed switchgrass as a biomass example to be carbonized at an ultra-high temperature, 2050 °C, induced by Joule heating to create hard carbon anodes for sodium ion batteries. Switchgrass derived carbon materials intrinsically inherit its three-dimensional porous hierarchical architecture, with an average interlayer spacing of 0.376 nm. The larger interlayer spacing than that of graphite allows for the significant Na ion storage performance. Compared to the sample carbonized under 1000 °C, switchgrass-derived carbon at 2050 °C induced an improved initial Coulombic efficiency. Additionally, excellent rate capability and superior cycling performance are demonstrated for the switchgrass-derived carbon due to the unique high temperature treatment.

---

[*] The results have been published: Zhang, F.; Yao, Y.; Wan, J.; Henderson, D.; Zhang, X.; Hu, L. High Temperature Carbonized Grass as a High Performance Sodium Ion Battery Anode. *ACS Appl. Mater. Interfaces* **2017**, 9, 391–397.

7.3 High temperature thermal electrics[*]

The development of ultrahigh-temperature thermoelectric materials could enable thermoelectric topping of combustion power cycles as well as extending the range of direct thermoelectric power generation in concentrated solar power. However, thermoelectric operation temperatures have been restricted to under 1,500 K due to the lack of suitable materials. Here, we demonstrate a thermoelectric conversion material based on high-temperature reduced graphene oxide nanosheets that can perform reliably up to 3,000 K. After a reduction treatment at 3,300 K, the nanosheet film exhibits an increased conductivity to ~4,000 S cm^{-1} at 3,000 K and a high power factor $S^2\sigma = 54.5\ \mu\mathrm{W\ cm^{-1}\ K^{-2}}$. We report measurements characterizing the film's thermoelectric properties up to 3,000 K. The reduced graphene oxide film also exhibits a high broadband radiation absorbance and can act as both a radiative receiver and a thermoelectric generator. The printable, lightweight and flexible film is attractive for system integration and scalable manufacturing.

---

[*] The results have been published: Li, T.; Pickel, A. D.; Yao, Y.; Chen, Y.; Zeng, Y.; Lacey, S. D.; Li, Y.; Wang, Y.; Dai, J.; Wang, Y.; *et al.* Thermoelectric Properties and Performance of Flexible Reduced Graphene Oxide Films up to 3,000 K. *Nat. Energy* **2018**, *3*, 148–156.

7.4 Ultrafast annealing toward carbon booming

Carbon-based nanomaterials are featured with lightweight, flexible, anti-corrosion, highly conductive and high surface area, which are important materials as conductive host for electrocatalysis and electrochemical energy storage applications. However, attempts to create high surface area carbon materials with enhanced mechanical properties often result in the loss of key performance metrics. Here we report an interconnected carbon network with increased carbon surfaces by applying Joule heating to polyacrylonitrile (PAN) based carbon nanofibers at a high temperature (> 2500 K) and an ultra-fast heating rate (10^4-10^5 K/min). The ultrafast heating produces a high temperature environment that enables further carbonization of the nanofibers and induces bombing of CNF in diameters, forming a 3D hollow carbon network. Since the carbonization occurs in several seconds or minutes, the drastic releasing of defective C, H, O (most in gaseous forms) cause the expansion of carbon fibers layer by layer and creates concentric circles like morphology owing to the rapid heating is from shell to inner core. In contrast, prolonged slow heating (10 K/min) results in the shrinkage of carbon fiber as the result of slow graphitization. The high temperature Joule heating not only enables fast graphitization of carbon materials at high temperature but also provides a new strategy to build high surface area of graphitic carbon networks from an amorphous carbon source. Because of the high electrical conductivity, good mechanical structures as well as anti-corrosion properties, this 3D interconnected carbon membrane can be potentially used in energy storage applications.

Chapter 8: Thermal shock synthesis of uniformly distributed nanoparticles*

Abstract

Nanoparticles (NPs) dispersed within a conductive host are essential for a range of applications including electrochemical energy storage, catalysis as well as energetic devices. However, manufacturing high-quality NPs in an efficient manner remains a challenge, especially due to agglomeration during assembly processes. Here we report a rapid thermal shock method to *in-situ* synthesize well-dispersed NPs on a conductive fiber matrix using metal precursor salts. The temperature of the carbon nanofibers (CNFs) coated with metal salts was ramped from room temperature to ~2000 K in 5 milliseconds, which corresponds to a rate of 400,000 K/s. Metal salts decompose rapidly at such high temperatures and nucleate into metallic nanoparticles during the rapid cooling step (cooling rate of ~100,000 K/s). The high temperature duration plays a critical role in the size and distribution of the nanoparticles: the faster the process is, the smaller the nanoparticles are, and the narrower the size distribution is. We also demonstrated that the peak temperature of thermal shock can reach ~3000 K, much higher than the decomposition temperature of many salts, which ensures the possibility of synthesizing various types of nanoparticles. This universal, *in-situ,* high-temperature thermal shock method offers considerable potential for the bulk-synthesis of unagglomerated nanoparticles stabilized within a matrix.

---

* The results in this chapter have been published: Yao, Y.; Chen, F.; Nie, A.; Lacey, S. D.; Jacob, R. J.; Xu, S.; Huang, Z.; Fu, K.; Dai, J.; Salamanca-Riba, L.; et al. In Situ High Temperature Synthesis of Single-Component Metallic Nanoparticles. *ACS Cent. Sci.* 2017, 3, 294–301.

8.1 Introduction

Well-dispersed functional nanoparticles (NPs) in a conductive carbon host are particularly important for electrochemical energy storage, electrochemical catalysis, and photocatalysis, among other applications.[138–143] The conductive support cannot only effectively transport electrons and heat generated during electrochemical reactions, but also disperse the nanoparticles from severe aggregation.[144] To date, two main strategies have been developed for the synthesis of NPs decorated on carbon-based materials: (1) synthesis-then-assembly[142,145–147] and (2) *in-situ* growth[148–153]. For synthesis-then-assembly methods, suspension of synthesized nanoparticles is introduced to the porous carbon matrix by impregnation and then drying. Such approaches allow for precise control of the NPs' size, phases, and structures by wet chemistry synthesis and then the synthesized NPs are re-dispersed onto support.[154–157] Dispersion agents are usually required to stabilize the nanoparticle solutions, which can leave a residue on the nanoparticle surface and may deteriorate performance.[151,158–161] More often the NPs are prepared *in-situ* onto a carbon support *via* chemical reduction or hydrothermal reaction as a simple and low-cost method,[148–153] and sometimes physical methods, such as electron beam radiation[162–164] and selectively surface functionalization[165]. Since carbon is non-wetting with most metals and the interaction between metal NPs and carbon surface is weak,[166] the as-formed nanoparticles are prone to agglomerate and redistribute during the synthesis and post heat treatments.[153,161,167–170]

As the growth and aggregation of nanoparticles are time-dependent diffusion and migration processes, it is critical to synthesize ultrafine NPs over a short time and quench the process to prevent, or at least, minimize agglomeration. While conventional high temperature syntheses methods, such as spray pyrolysis and combustion, are fast (several seconds to minutes), a well controllable heating method is desirable for the control of both the high temperature heating process and also the resultant particle size and distribution.[171–173]

Here we report a one-step thermal shock method for rapid, *in-situ* and surfactant-free synthesis of well-dispersed nanoparticles on a carbon matrix. Ultrafast thermal decomposition (400,000 K/s ramp rate) of metal salts on a carbon support was achieved by electrical Joule heating for 5 milliseconds at high temperature (~2000 K). Palladium (Pd) nanoparticles acted as the model system, however, gold (Au), iron (Fe), and tin (Sn) were also demonstrated using the proposed universal synthesis method. Due to a short thermal shock duration followed by ultrafast cooling, the metal atoms have limited time for migration, resulting in uniformly distributed NPs on the carbon support. In addition, the size distribution of the NPs strongly depends on the thermal shock duration; namely, a faster thermal shock process yields smaller nanoparticles with a more uniform size distribution. Compared to other synthesis methods for assembling nanoparticles on a carbon matrix, the proposed thermal shock process is facile, ultrafast and yields high purity and evenly distributed nanoparticles. By Joule heating, the temperature can reach ~3000 K, which enables the decomposition of most metal salts. Thus, a range of nanoparticles can be readily fabricated on carbon-based materials using this universal and ultrafast thermal shock method.

8.2Results and Discussion

Fig. 8.1a is a schematic representation of the proposed high temperature thermal shock method where NPs are rapidly assembled onto carbon nanofibers (CNFs). Pd nanoparticles were chosen as the model system to investigate the process-structure relationship in the proposed synthesis method. The pristine CNFs were dipped in an aqueous solution of $PdCl_2$ (1 mg/ml) and dried in an oven to prepare $PdCl_2$-coated CNFs for the rapid thermal shock process. The rapid thermal shock was triggered by Joule heating, where the thermal energy can be easily controlled by the applied current. In a typical process, CNF-$PdCl_2$ was heated to ~2000 K for 5 milliseconds and cooled down immediately. The high temperature in the thermal shock process leads to the *in-situ* thermal decomposition of $PdCl_2$ at 590-740 ºC and the formation of Pd nanoparticles on the CNFs; the short shock time limits the diffusion and migration of the as-formed Pd nanoparticles and enables a uniform NP distribution across the CNFs. Note that CNFs were chosen as a suitable carbon matrix due to its open network structure for gas releasing and also can be used for filtration purposes such as air or water purification.

Fig. 8.1b-c depicts the scanning electron microscopy (SEM) and transmission electron microscopy (TEM) images of Pd-decorated CNFs after a one-second and 5-millisecond thermal shock at ~2000 K. Large number of Pd nanoparticles were formed and uniformly distributed along the CNFs. The average size of Pd nanoparticles formed by the 5-millisecond shock (~ 4 nm) is much smaller compared to the one-second shock (~ 27 nm), demonstrating the temporal confinement of shock time on the synthesis of ultrafine NPs. The corresponding SEM images of CNF, CNF-$PdCl_2$ can be found in supporting materials.

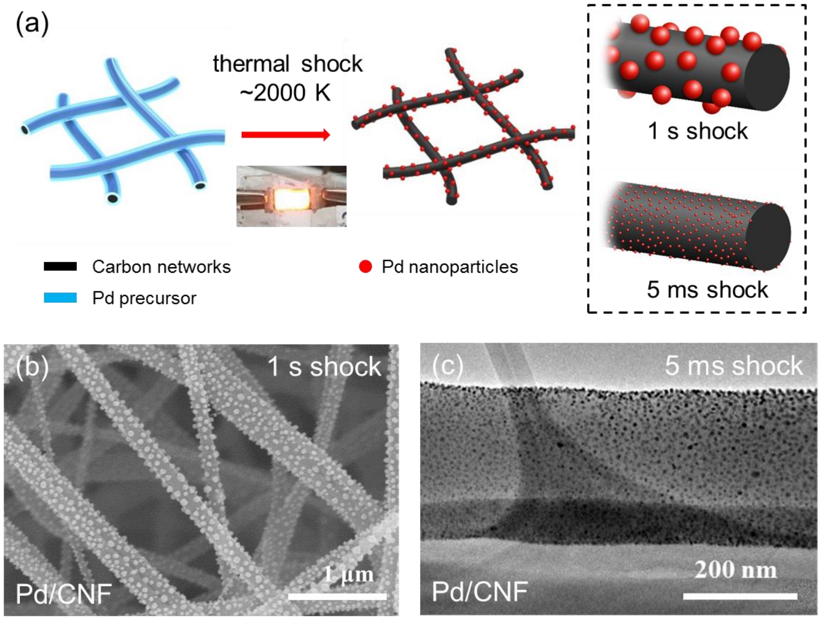

Figure 8.1. Synthesis of Pd NPs on CNFs via a rapid, high temperature thermal shock method. (a) Schematic to show the Pd NP formation process. Metal salt precursor $PdCl_2$ is formed on the pristine CNF surface by a dip-coating method and then treated with a rapid thermal shock by Joule heating, which results in Pd NPs loading the carbon matrix. By utilizing different shock times, the NP size can be tuned: a faster shock creates smaller particle sizes. (b) SEM image of Pd/CNF formed by a one-second thermal shock. (c) TEM image of Pd/CNF formed by a 5-millisecond thermal shock.

The rapid thermal shock process was triggered by electrical Joule heating and its temperature was controlled by the input electrical power.[22,25,36,106,117,174,175] The carbon-based samples were attached to copper electrodes and placed in an argon environment and connected to an external current source (Keithley 2400). Fig. 8.2a shows images of the CNF-$PdCl_2$ (3 mm x 1 mm x 30 um) before and during the thermal shock process. In this example, a one second 100 mA current (or 1.54 W) pulse was applied to the sample whose temperature was raised up quickly due to direct Joule heating. Carbon materials at high temperatures will emit bright light as a radiation source due to gray-body radiation, and the spectrum can be used for temperature evaluation according to blackbody theory. The emission spectrum was collected by an optical fiber (400 μm, ocean optics) and dispersed using a spectrometer (Ocean Optics USB 2000+).

Fig. 8.2b depicts the temporal evolution of emitted light intensity during the rapid high temperature process at 800 nm, and overlaid with the 100 mA pulse. The emission intensity induced by the 100 mA pulse saturated within 0.1 seconds, equilibrated, and subsequently dropped after the pulse ended. Both an ultrafast heating and cooling rate were achieved during the thermal shock process, owing to the direct Joule heating, the good thermal conductivity of carbon materials, and also small sample size. The full spectrum from 350 nm to 950 nm was collected and fitted to the gray-body radiation equation to determine the sample temperature during thermal shock (Fig. 2c).[25,37,117] Although carbon materials are not exactly a blackbody source, they have a stable emissivity around 0.8 for the measured wavelength range to ensure the fitting accuracy.[36] In this one-second shock process, the estimated temperature was approximately 1950 K, which confirms that the temperature induced by the thermal shock method was more than enough for $PdCl_2$ decomposition.

The exceptional temperature control via Joule heating can be further illustrated by an ultrafast 5-millisecond thermal shock duration (Fig. 8.2d-e). The rapid thermal shock held for 5 milliseconds is beyond the temporal resolution of commercial spectrometers. Thus, a specially designed spectrometer, capable of sub-millisecond diagnostics with a temporal resolution down to 2.5 μs, was used to monitor the thermal shock pulse as shown in Fig. 8.2d. Both the electrical pulse and above spectrometer were triggered at the same time for the measurement. Despite the thermal shock duration is 5 milliseconds, the emitted light was monitored from 0 ms to 20 ms to cover both the heating and subsequent cooling period. These spectra at different times during the shock were fitted to the gray body radiation equation to extract the temperature vs. time profiles (Fig. 8.2e). As the spectrometer cannot properly detect below 1000 K, the temporal light emission at 800 nm was overlapped with the temperature evolution curve to illustrate the heating and cooling process. To heat from room temperature to the peak temperature of 2100 K takes a mere 5 milliseconds, which roughly translates to a ramp rate of 400,000 K/s.

Fig. 8.2f summarizes and compares the ramp rates of the proposed thermal shock method to conventional heating in a furnace. For furnace-based heating, the heating/cooling ramp rate is limited to 10 K/min (< 1 K/s) due to slow radiation heating and an expansive heating volume. For electrically triggered Joule heating via thermal shock, the temperature increases by direct Joule heating effects and the size of the sample is orders of magnitude smaller than a conventional furnace chamber size. This enables the ramp rate for the proposed thermal shock method to be exceptionally large. For a one-second thermal shock, the heating and cooling processes occurred within 100-130 ms (Fig. 8.2b), which corresponds to a heating/cooling rate of ~15,000 K/s. For the 5-millisecond thermal shock, a 400,000 K/s heating rate was demonstrated (Fig. 8.2e). Since initial cooling from 2100 K to 1200 K takes only 5 milliseconds (180,000 K/s), the cooling rate was roughly estimated to be ~100,000 K/s for a total cooling time of 20 milliseconds. Thus, the exceptional ramp rates of the Joule heating process and the ability to tune the thermal pulse time provides extreme kinetic control for the synthesis of nanoparticles.

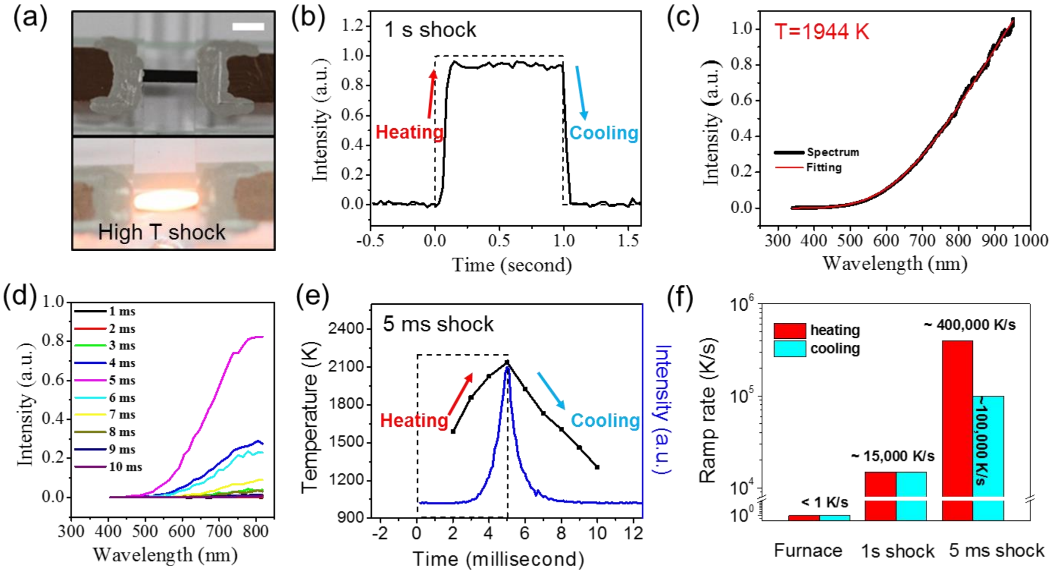

Figure 8.2. Characterization of the rapid high temperature thermal shock method. (a) Digital images of the CNF-$PdCl_2$ sample before and during thermal shock. Scale bar: 2 mm. (b) Evolution of light emission intensity during the one-second thermal shock treatment with a 100 mA current pulse. (c) Emitted light spectrum for the one-second shock at 100 mA. The spectra are fitted to the gray body radiation model using a temperature of 1944 K. (d) Light emission spectra at different times from 0 ms to 10ms, covering both the heating and cooling of 5-millisecond thermal shock at 100 mA. (e) The temporal evolution of temperature and light intensity at 800 nm for the 5-millisecond thermal shock. (f) Temperature ramp rate for conventional furnace heating, one-second thermal shock, and 5-millisecond thermal shock.

Besides the formation of NPs on the CNFs, we also investigated the impact of the thermal shock method on the CNF substrate and data is included in supporting materials. Although the high temperature achieved by the thermal shock process is much higher than the CNF carbonization temperature (600°C), the thermal shock pulse is not detrimental to the substrate due to its short duration and the inert atmosphere during the application of the shock pulse. This is confirmed by Raman and XRD analysis that shows no change before and after the thermal shock method. In contrast, our CNFs under extended pulse time (100 s) at high temperature carbonizes the fibers further and results in substantial changes in both the Raman and XRD spectra. Therefore, a short thermal shock duration causes the sample to reach high enough temperatures to induce thermal decomposition with minimal impact to the substrate (i.e. CNFs).

The microstructure of the *in-situ* synthesized Pd nanoparticles on the CNF matrix was examined by SEM and TEM. Based on the thermal pulse duration, the proposed rapid thermal shock method creates nanoparticles with specific sizes and distributions. After a one-second thermal shock at 100 mA, Pd nanoparticles are uniformly distributed across the entire CNF sample (Fig. 8.3a). The formation of metallic Pd nanoparticles from $PdCl_2$ by thermal decomposition was confirmed by X-ray photoelectron spectroscopy (XPS) (supporting materials), showing the metallic Pd 3d peak. Fig. 8.3b-c are TEM images of the aforementioned Pd nanoparticles with an average size of approximately 27 nm. The as-formed Pd nanoparticles are anchored to the CNF surface, ensuring the maximum exposure of NPs as a contrast with NPs buried inside the carbon matrix.[142,146,147,161,176] The attached Pd nanoparticles were firmly anchored onto the CNF surface which was verified by sonicating the TEM samples for several hours in ethanol before imaging the well-preserved NPs. Fig. 8.3d-e exhibits Pd nanoparticles on CNF using a 100 mA pulse for 5 milliseconds. Using a short thermal shock duration, the average Pd NP size is approximately 4 nm. This verifies the proposed mechanism where an extremely short shock duration enables the synthesis of smaller nanoparticles due to temporal limitations on mass diffusion and migration.

The synthesized Pd NPs possess a highly crystalline structure as shown in the high-resolution TEM image (Fig. 8.3e). Thus, the rapid thermal shock method can fabricate high purity nanoparticles on carbon-based materials in a facile manner.

Fig. 8.3f shows a typical low magnification high angle annular dark field scanning TEM (HAADF-STEM) image of the synthesized Pd nanoparticles on CNFs using a one-second thermal shock. Since the intensity of the HAADF-STEM image is proportional to the atomic number $Z^{1.7}$ of the sample,[177] the CNF matrix appears dark, however, the Pd nanoparticles can be easily identified. The energy dispersive X-ray mapping (EDX) illustrates the elemental distribution of Pd on the sample. The Pd mapping coincides with the nanoparticles on the CNF surface which confirms the chemical composition of the synthesized nanoparticles. In order to obtain more detailed structural information of the synthesized Pd nanoparticles, atomic-scale HAADF-STEM was employed (Fig. 8.3g-h). The atomic-scale HAADF-STEM image coincided with the $[1\bar{1}0]$ zone axis of the Pd nanoparticle since the d-spacing of the main lattice planes matches well with the (111) and $(11\bar{1})$ planes of the fcc Pd metal (Fm-3m, a = b = c = 3.867, JPCDF 87-0645). Notably, this Pd nanoparticle contains several twin boundaries (TBs) and stacking faults (SFs) along the {111} planes, which are marked by red arrows in Fig. 8.3h. The existence of TBs and SFs in the Pd nanoparticles may have an effect on the electrocatalytic activity of the Pd/CNFs. More specifically, these planar defects are favorable in chemical reactions[178] and ionic diffusion[179] due to their high lattice energy.

The catalytic properties of the synthesized Pd/CNFs were also evaluated (supporting materials). A CNF matrix uniformly loaded with Pd nanoparticles is an ideal structure for electrical catalysis, specifically fuel cells, lithium-oxygen batteries, and flow catalysis, among others.[28,150,180,181] The porous CNF matrix provides a conductive support structure for Pd nanoparticles while facilitating gases/solutions to flow throughout the structure for catalysis. In this work, we demonstrate the aforementioned Pd/CNFs for the favorable catalytic decomposition of methylene blue.

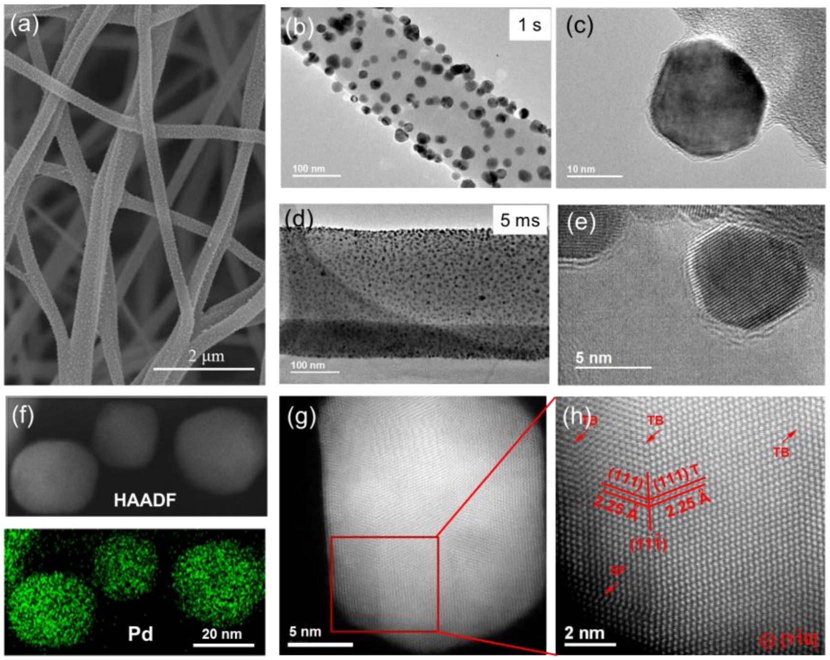

Figure 8.3. The microstructure of Pd/CNFs using the rapid thermal shock method. (a) SEM image and (b)-(c) TEM images of Pd nanoparticles formed on CNFs by a one-second thermal shock treatment. (d)-(e) TEM images of Pd nanoparticles formed on CNF by a 5-millisecond thermal shock treatment. (f) HAADF-STEM image and EDX elemental map of the Pd/CNF sample fabricated with a one-second thermal shock. (g-h) Atomic-scale HAADF-STEM image of a Pd nanoparticle formed on CNF surface along the $[1\bar{1}0]$ zone axis. Twin boundaries (TBs) and stacking faults (SFs) are present due to the non-equilibrium rapid thermal shock.

To evaluate the dependence of nanoparticle size and distribution on the high temperature thermal shock conditions, the Joule heating time and temperature were varied. Fig. 8.4a-c exhibits SEM images of the Pd/CNFs formed with a 100 mA Joule heating over various shock durations (5 ms, 1 s, and 100 s). By altering the duration time of the high temperature synthesis, the average nanoparticle size and distribution change dramatically, where shorter thermal shock times lead to smaller nanoparticle sizes with narrower size distributions. More specifically, for the one-second and 5-millisecond shock, the average nanoparticle size changed from 27.7 nm to 4.2 nm with a size distribution ranging between 4.5 nm and 0.5 nm, respectively. In contrast to the rapid thermal shock method, Fig. 8.4c shows the SEM image of Pd/CNF subjected to 100 s of high-temperature heating. The resultant Pd nanoparticles have a broad size distribution with a much larger particle size (~ 140 nm) than the rapid thermal shock durations (5 ms and 1 s). Additionally, by 100 s of high-temperature heating, some CNF areas were not loaded with Pd particles while others suffered from aggregation. This indicates that severe nanoparticle migration occurs with prolonged high temperature heating.

Fig. 8.4d summarizes the average size of the Pd nanoparticles as a function of thermal shock time. It is clear that the size distribution is dominantly affected by thermal shock time as a temporal constraint in the NPs synthesis: the faster thermal shock can lead to smaller size nanoparticles with narrower size distribution. The rapid thermal shock temperatures were also varied by tuning the applied current pulse (100 mA, 50 mA, and 20 mA) (supporting materials). Based on the temperature vs. applied current plot, the thermal shock conditions for 100 mA, 50 mA and 20mA correspond to temperatures of 2000 K, 1700 K, and 1300 K, respectively. As the thermal shock changed from 100 mA to 50 mA, and to 20 mA, the average size changes subtlely from 27 nm to 21 nm, and to 19.7 nm. Therefore, compared to the size dependence on shock time, the dependence of nanoparticle size on shock temperature is much weaker.

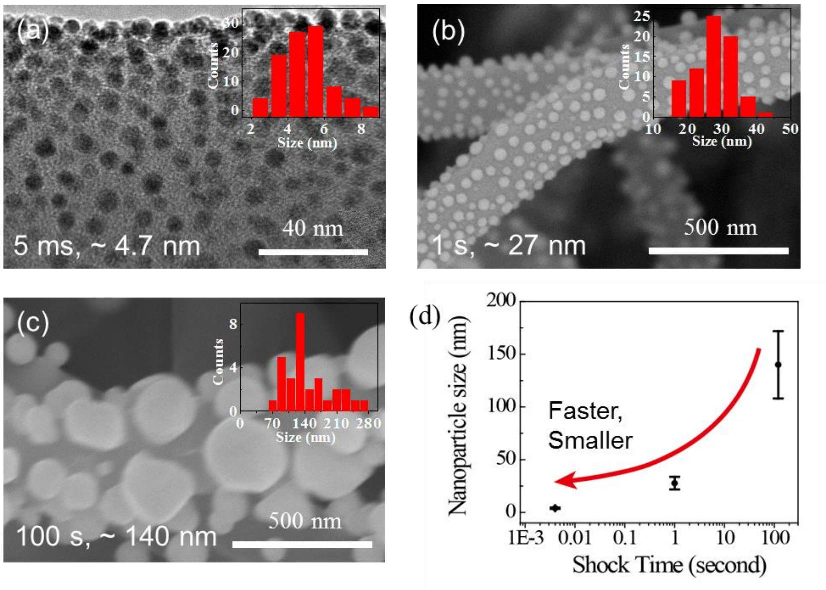

Figure 8.4. Kinetic variations in the formation of Pd/CNFs. (a) TEM and (b)-(c) SEM images of the Pd/CNFs formed with a 100 mA thermal shock for 5 milliseconds, one second, and 100 seconds, respectively. Insets are histograms of the particle size distribution for each thermal shock condition. (d) Average nanoparticle size as a function of shock duration time. As the thermal shock time decreases, the nanoparticles size become smaller with a more uniform distribution. Scale bar: standard deviation.

Since the thermal decomposition of metal salts is a universal reaction mechanism, the synthesis of NPs with the proposed rapid thermal shock method can be easily extended to numerous other metals. By electrical Joule heating, the temperature of the thermal shock can reach ~3000 K (Fig. 8.5a). The high temperature achieved by the thermal shock method is high enough to decompose most metal salts, such as platinum (Pt), gold (Au), iron (Fe), tin (Sn), and nickel (Ni), among others.[182] Fig. 8.5b exhibits a selected number of metal salt decomposition temperatures compared to the peak thermal shock temperature of the proposed high temperature synthesis method. Similar to the synthesis of Pd nanoparticles, when the metal salts are exposed to the sufficiently high thermal shock temperature for a short duration of time, metal nanoparticles can readily form. Au-, Fe- and Sn-based CNF samples were Joule heated to ~2000 K for one second to enable the *in-situ* synthesis of uniformly distributed nanoparticles on the CNF surface. Fig. 8.5c exhibits the synthesized NP/CNF (Au, Fe, Sn) samples to demonstrate the universality of the proposed thermal shock method.

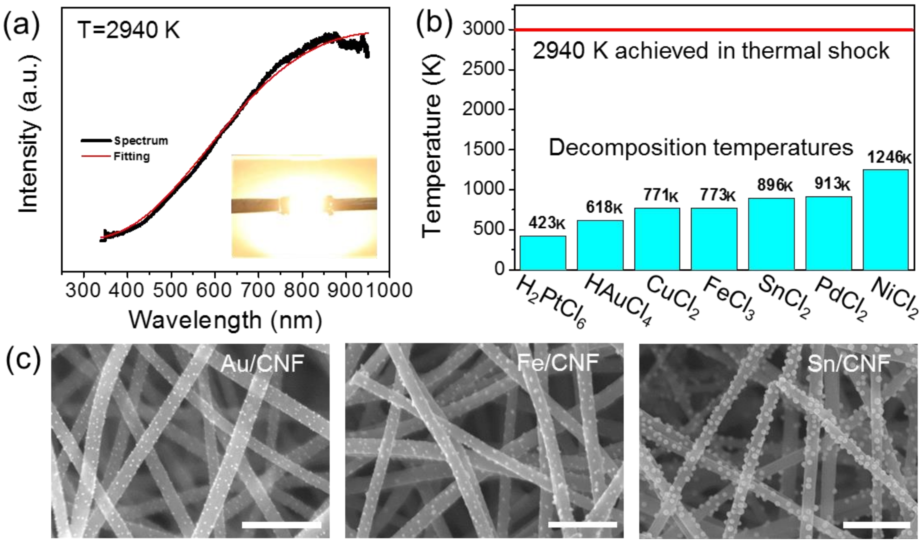

Figure 8.5. Rapid thermal shock as a universal NP synthesis method. (a) A plot demonstrating the high temperature (~3000 K) achieved by Joule heating. The inset is a digital image of the sample during the high temperature process. (b) Thermal decomposition temperatures of metal (chloride-based) precursor salts. (c) Synthesis of NP/CNFs (Au, Fe, Sn) by thermal shock at 2000 K. Scale bar: 1 μm.

8.3 Conclusion

In summary, we reported a universal high temperature method for *in-situ* synthesis of nanoparticles on a carbon fiber matrix using metal precursor salts. This high temperature thermal shock method can be used for a range of applications such as water treatment, energy storage, and electrochemical water splitting. With Pd nanoparticle as the model system in the study, we thoroughly investigated the temporal distribution of temperatures with high-resolution spectrometer down to milliseconds. The typical ramp rates are ~ 400,000 K/s for heating and ~ 100,000 K/s for cooling, which are orders of magnitudes higher than values reported in the literature for other NP synthesis, and are crucial for achieving smaller nanoparticles with a more uniform size distribution. We extended the high temperature thermal shock method to the synthesis of other nanoparticles including Au, Fe, and Sn, suggesting that the method can be applied for the synthesis of a wide range of other nanoparticles with salt decomposition temperatures less than ~ 3000 K.

8.4 Experimental

Preparation of CNF with metal salts: The CNFs mat was then stabilized at 260°C for 5 hours in the air and carbonized at 600°C in an argon atmosphere for 2 hours to obtain the CNFs. The CNF film was then dipped in a 1 mg/mL $PdCl_2$ solution (with vacuum assistance) and dried in an oven. The as-prepared CNF-$PdCl_2$ film was used directly for high temperature thermal shock experiments.

Rapid thermal shock synthesis: Rapid thermal shock was realized by electrical Joule heating in an argon-filled glovebox. The CNF-$PdCl_2$ film was connected to copper electrodes and the interfaces were glued together with silver paste. For the ultrafast thermal shock of 5 ms, which is beyond the resolution capability of the optical fiber, and we used a specifically designed on-line pyrometer with a 1200 grooves/mm gratings that can disperse the light at a spatial resolution down to 0.8 nm/mm. The dispersed light was then collected by a 32-channel PMT array to form the full spectrum, with a temporal resolution down to 2.5 μs.

Characterization and temperature measurement: See Chapter 3 Experimental section.

8.5 Supporting materials

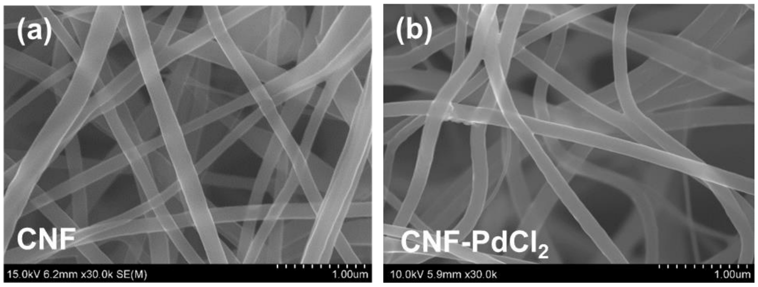

Figure 8.6. (a) SEM image of pristine carbon nanofibers (CNF) fabricated by electrospinning. (b) SEM image of CNF after dipping into $PdCl_2$ and dried. The CNFs are uniformly coated with $PdCl_2$.

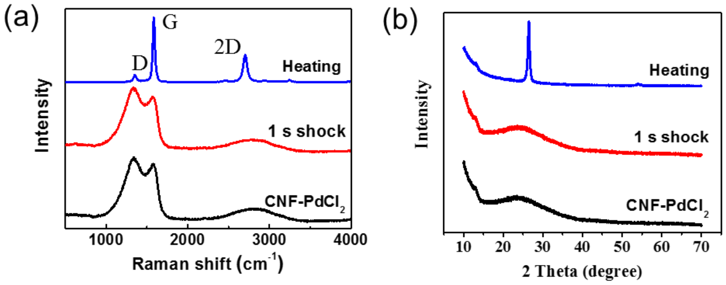

Figure 8.7. (a)-(b) Raman spectra and XRD structure changes of Pd/CNF by one-second thermal shock and longtime heating.

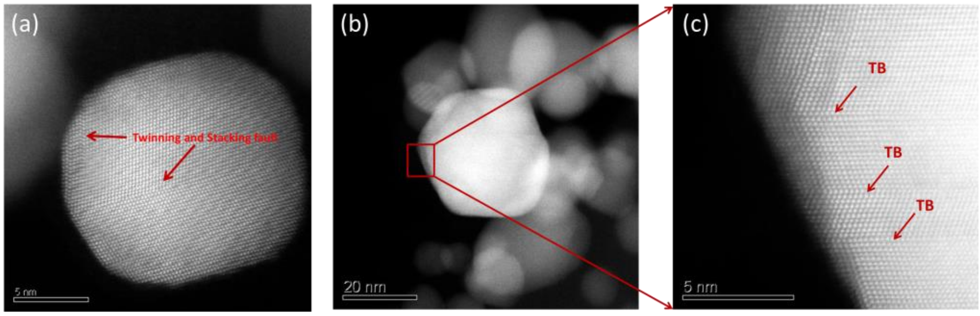

Figure 8.8. (a-c) High-resolution high angle annular dark field scanning TEM (HAADF-STEM) images of to show the twin boundaries and stacking faults in different size Pd nanoparticles formed by rapid thermal shock.

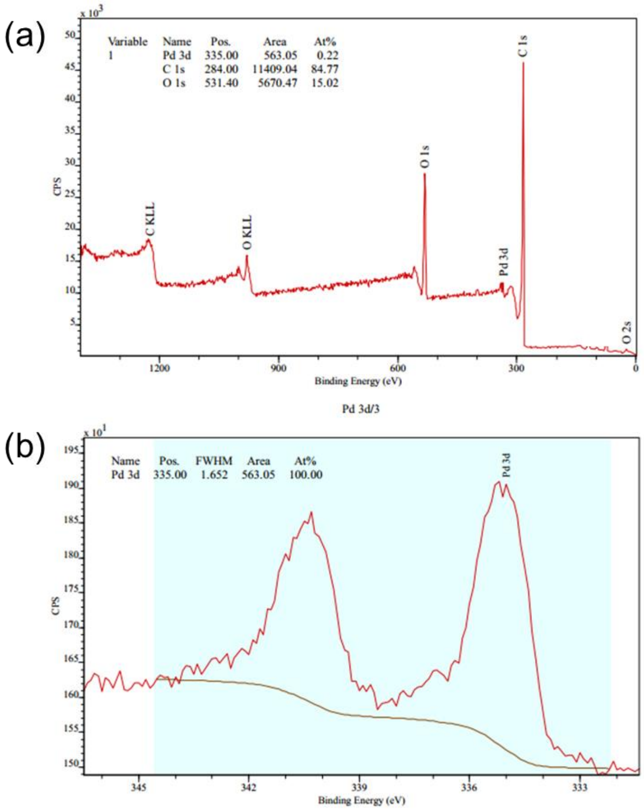

Figure 8.9. XPS analysis of (a) Pd/CNF composite and (b) the metallic Pd 3d state.

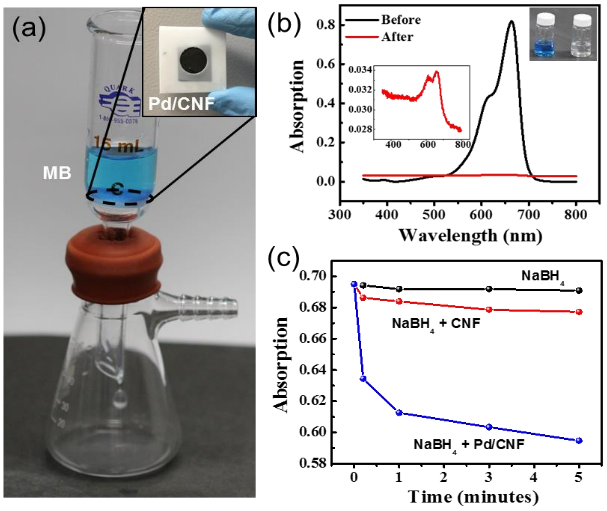

Figure 8.10. Catalytic properties of Pd/CNF synthesized by RTS. (a) The catalysis effect of Pd/CNFs on the degradation of methylene blue (MB) in a flow stream. (b) UV-Vis absorption spectra of MB solution before and after going through Pd/CNF film. The inset shows the magnified curve. (c) Static reduction and catalysis effect of $NaBH_4$, $NaBH_4$ + CNF and $NaBH_4$ + Pd/CNF on the MB degradation over time.

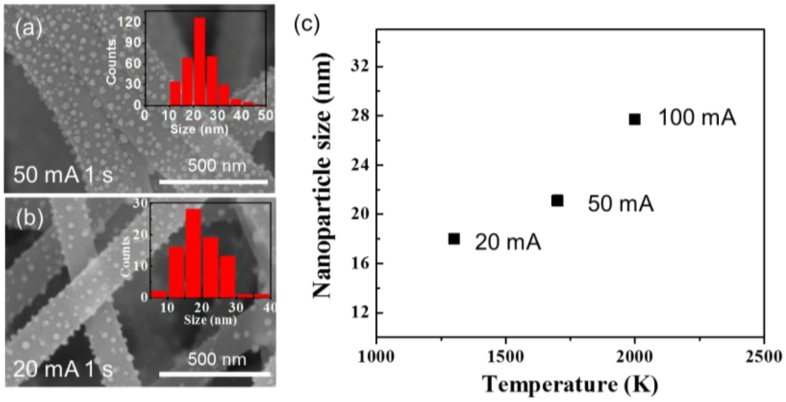

Figure 8.11. The size distribution of NPs synthesized with different temperatures for one second. (a)-(b) SEM images of Pb/CNF synthesized at different driving currents of 50 mA and 20 mA, respectively. (c) The average size of Pb NPs on CNF vs. shock temperature. When compared with Figure 8.4, the *in-situ* synthesized nanoparticle by the high temperate pulse method is much more sensitive to ramping speed than the pulse temperature.

Chapter 9: Thermal shock synthesis of atomically mixing bimetallic nanoparticles[*]

Abstract

Supported bimetallic alloy nanoparticles are of great interest in various catalytic applications due to the synergistic effects of different metals for improved catalytic performance. However, it still remains a challenge to efficiently synthesize atomically mixed alloy nanoparticles with uniform dispersion onto a desired substrate. Here we report *in situ*, rapid synthesis of atomically mixed bimetallic nanoparticles well-dispersed on a conductive carbon network *via* a one-second high temperature pulse (RTS, ~1550 K, duration 1 s, the rate of 10^4 K/s). The high temperature facilitates the total (atomic) mixing of different metals, while the rapid quenching ensures the uniform dispersion of nanoparticles with fine features such as twin boundaries and stacking faults, which are potentially beneficial to their catalytic performances. By varying the ratio of the precursor salts and parameters in the RTS process, we can easily tune the composition, size, and morphology of the resultant nanoparticles. Moreover, the synthesized bimetallic (PdNi) nanoparticles present excellent electrocatalytic performances for hydrogen evolution reaction and hydrogen peroxide electrooxidation. This work provides a general strategy for a facile and rapid synthesis of bimetallic nanoparticles directly from their salts for a range of emerging applications.

---

[*] The results in this chapter have been submitted: Chen, F.; Yao, Y.; et al; Hu, L. High Temperature Atomic Mixing Toward Well-Dispersed Bimetallic Electrocatalysts. *Advanced Energy Materials*. Submitted, 2018. (Chen, F and Yao, Y. contributed equally)

9.1 Introduction

Recently, much attention has been focused on bimetallic nanostructures, such as heterogeneous core-shell structures, homogeneous alloy nanoparticles, and ordered intermixed nanoparticles, due to their diversified applications in electronics, biology, and catalysis.[183–185] By tailoring the compositions, atomic orderings, and nanoparticle sizes, the chemical and physical properties of bimetallic nanostructures can be designed and improved accordingly.[154,183,184,186,187] In particular, bimetallic nanoparticles with atomically mixing can be very effective at both separating the active surface sites and adjusting the surface electronic properties. Various bimetallic nanostructures have been synthesized by multi-process or co-reduction methods, among others.[155,188–190] However, due to the different reduction potentials of each component in the multicomponent system, inhomogeneity often occurs where as-formed alloy nanoparticles usually contain heterogeneous clusters with phase separation or elemental segregation.[155,191]

Meanwhile, in order to effectively disperse the nanoparticles and improve their suitability for emerging applications, the nanoparticles are often supported by conductive matrices such as graphene, carbon nanotubes, and conductive polymers to accommodate the electrical currents used in electrochemical energy storage and electrocatalysis. Typically, nanoparticles are first synthesized and subsequently deposited on a conductive network (i.e. *ex-situ* synthesis).[155,191,192] The deposition process often involves surface functionalization of the conductive network as well as the dispersion of the nanoparticles in a solvent, which can damage the carbon structure and particle surfaces and adversely affect their catalytic performances. Also, inevitable agglomeration occurs when these ultrafine nanoparticles are re-dispersed on to carbon substrate. Therefore, developing a facile and fast strategy for the *in-situ* synthesis of atomically mixed bimetallic nanoparticles uniformly distributed onto a carbon support remains a great challenge.

Here, we report rapid thermal shock (RTS) synthesis of bimetallic nanoparticles with the atomic-scale mixing of two elements from their precursors directly. The nanoparticles are *in-situ* formed and well dispersed on a conductive network in an extremely simple and fast manner: (i) loading of a precursor mixture onto the carbon matrix; and (ii) treating the precursor-loaded carbon with a one-second RTS (~ 1550 K for 1 s). The high temperature facilitates the total (atomic) mixing of different metals while the rapid quenching ensures the small size and uniform dispersion of nanoparticles. The atomic-scale mixing of the resultant PdNi nanoparticles was confirmed by a high angle annular dark field aberration-corrected scanning transmission electron microscopy (HAADF-STEM) and atomic resolution energy-dispersive X-ray (EDX) elemental mapping. Electrochemical study of the synthesized nanoparticles on the CNF network shows excellent electrocatalytic performance for both hydrogen evolution reaction (HER) and hydrogen peroxide electrooxidation. We chose PdNi as the model material, but this approach can be extended to other bimetallic compositions by simply varying the precursors and their molar ratios.

9.2 Result and discussion

Figure 9.1a illustrates the schematic process for the proposed RTS synthesis. Typically, the carbon nanofiber (CNF) network was soaked in the $PdCl_2$-$NiCl_2$ aqueous solution and left for dry in the oven at 60 °C. After the solvent evaporation, a thin, homogeneous layer of the salt mixture was left on the CNF surface. The CNF network was then heated to a high temperature (1550 K or higher) for one-second by electrically triggered Joule heating and subsequently quenched down by shutting off the current. The RTS synthesis involves the following steps: (1) fast thermal decomposition of $PdCl_2$ and $NiCl_2$ precursors to Pd and Ni clusters upon heating; (2) rapid diffusion and mixing of Pd and Ni clusters at a high temperature (formation of solid solution PdNi); and (3) self-assembly of PdNi alloy nanoparticles with atomic scale mixing upon the quenching process. A high density, uniform distribution of PdNi bimetallic nanoparticles on the CNFs was observed after the RTS synthesis.

A typical scanning electron microscope (SEM) image of CNFs coated with $PdCl_2$ and $NiCl_2$ (with a molar ratio of 1:1) shows a homogeneous coating of the salt mixture without aggregation (Figure 9.1b). The salt-loaded CNF network was subjected to a one-second RTS as shown in Figure 9.1c. The bright light emitted from the sample indicates the sample's high temperature through Joule heating, as a blackbody radiation source. After the one-second RTS, numerous PdNi alloy nanoparticles were uniformly dispersed on the CNF surface, with an average diameter of 10 ± 1.5 nm (Figure 9.1d). Additional TEM images and corresponding particle size distributions can be found in Figure S2. Note that the $PdCl_2$ and $NiCl_2$ salts decomposed at 948K and 1300 K, respectively. Because the temperature of Joule heating can reach ~ 3000 K,[24,193,194] which is higher than the decomposition temperature of most metallic salts, the RTS method can be extended to the synthesis of other bimetallic alloy nanoparticles from their precursors.

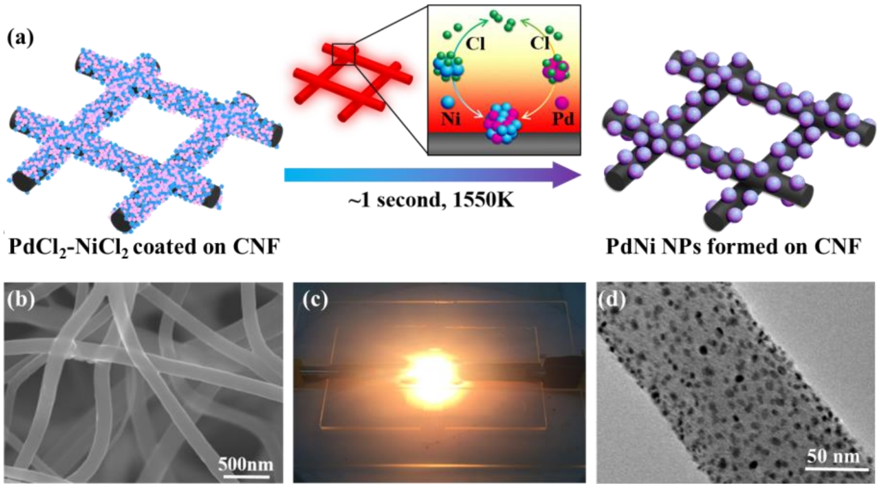

$PdCl_2$-$NiCl_2$/CNF High Temperature Pulse PdNi NPs/CNF

Figure 9.1. (a) Schematic of RTS synthesis of atomically mixed bimetallic nanoparticles on a conductive network. PdNi nanoparticle on a CNF network is used as the model system in this study. (b) SEM image of a CNF network conformably coated with a thin layer of $PdCl_2$ and $NiCl_2$ salt mixture with the molar ratio of 1:1. (c) The photo image of a $PdCl_2$-$NiCl_2$/CNF film under Joule heating at 1550 K. (d) The TEM image of PdNi alloy nanoparticles formed on the surface of CNF.

We investigated the structure of the bimetallic PdNi nanoparticles by aberration-corrected scanning transmission electron microscopy (STEM) using the high angle annular dark field (HAADF) and corresponding energy-dispersive X-ray (EDX) maps. The HAADF-STEM imaging (also known as a Z-contrast image) can provide intuitive structural and compositional information of materials whose contrast is dependent on the atomic number Z of the atomic column. The observably uniform intensity of the HAADF-STEM image in Figure 9.2a indicates a uniform composition of the PdNi alloy nanoparticles, which is also confirmed by the uniform distribution of PtNi by the EDX maps. In addition, the overlap of Pt and Ni maps shows homogeneous pattern without noticeable elemental segregation. Further atomic-scale HAADF-STEM images acquired along the [1-10] zone axis with EDX elemental mapping are shown in Figure 9.2b, confirming the uniform distribution of Pd and Ni in each atom column. With the atomic-scale evidence of uniform mixing, we, therefore, name the PdNi alloy as atomically mixed bimetallic nanoparticles.

The detailed crystal structure, composition, and bonding of the PdNi nanoparticles were analyzed. The *d*-spacing of the planes was measured to be 2.25 Å (Figure 9.2b), which is highly close to that of the *fcc* Pd metal structure (Fm-3m, $a=b=c=$ 2.23 Å, JPCDF 87-0645). Quantitative analysis of the PdNi alloy nanoparticles using EDX spectroscopy resolved a composition with a molar ratio of 1.11, which is close to the initial ratio of salt precursors. Moreover, macroscopic X-ray photoelectron spectra (XPS) were also collected for PdNi/CNF. The major peaks of Pd($3d_{5/2}$) and Ni($2p_{3/2}$) were detected at 335.5 eV and 855.6eV, respectively, which yielded an increase of 0.5 eV and 0.4 eV compared to the standard peaks of Pd and Ni.[28] Such a binding energy shift can be ascribed to the changes in crystal field potential and formation of PdNi alloys.[29]

The fast quenching (non-equilibrium process) in RTS also leads to some unique fine structures in the bimetallic nanoparticles, such as high-density twin boundaries (TBs) and stacking faults (SFs), which can be potentially beneficial for many applications as reported before.193 Figure 9.2c is a typical HAADF-STEM image of individual PdNi alloy nanoparticles along the [1-10] zone axis, showing several TBs and SFs (indicated by red arrows). The enlarged HAADF-STEM image and corresponding model (Figure 9.2d) clearly depict the atomic configurations of the TBs and SFs in the PdNi alloy with the (111) plane orientation. Generally, the (111) atomic planes of the perfect *fcc* PdNi structure have an ABCABCABC stacking sequence. With a 1/6<112> slipping, the stacking sequence of the (111) planes will change, leading to the formation of TBs and SFs. The grain boundaries, TBs, and SFs can play very important roles in determining the material properties, especially when they occur in the nanometer range.[179] Correspondingly, the TB and SF defects in the synthesized PdNi alloy nanoparticles may be favorable in chemical reactions and ionic diffusion due to their higher lattice energy.

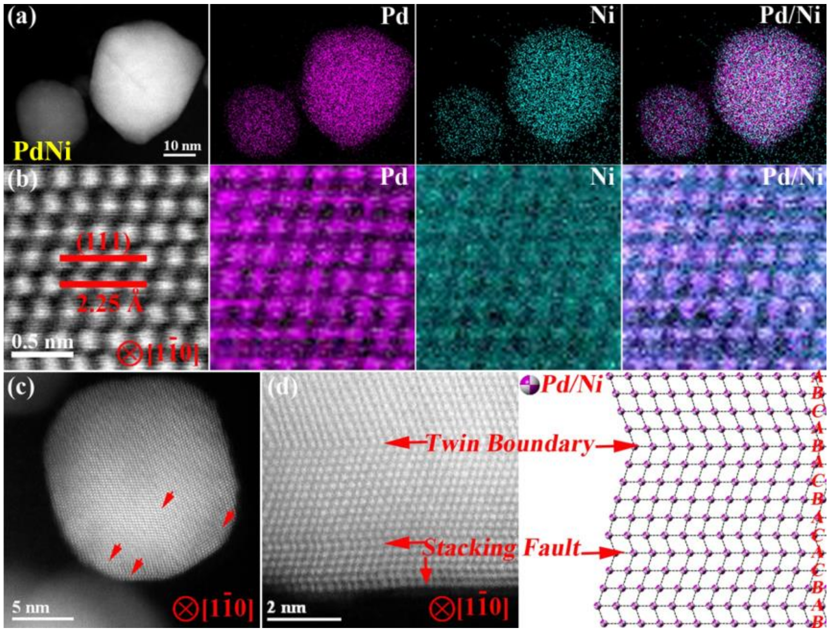

Figure 9.2. (a) HAADF-STEM images and corresponding EDX elemental maps of PdNi nanoparticles on CNF (after one-second RTS). The Pd and Ni elements are distributed uniformly at the nanoscale. (b) Atomic-scale HAADF-STEM images taken along the [1-10] zone axis and corresponding EDX elemental maps of the PdNi alloy nanoparticles on CNF, showing uniformity at the atomic scale. (c) Low magnification HAADF-STEM image of a single PdNi alloy nanoparticle on CNF took along the [1-10] zone axis. TBs and SFs are indicated by red arrows. (d) Atomic-scale HAADF-STEM image and atomic model showing the structure of TBs and SFs in the PdNi nanoparticles on the CNFs.

The RTS synthesis based on high temperature decomposition and nucleation also allows us to control the atomic composition by simply tuning the precursor ratios in the salt mixture. In addition to the 1:1 ratio demonstrated above, we synthesized PdNi nanoparticles with a Pd and Ni molar ratio of 1:2 and 2:1 in the precursor solution, using the same synthesis procedure. The morphologies and compositions of $PdNi_2$ and Pd_2Ni alloy nanoparticles were characterized by TEM, HAADF-STEM, EDX elemental mapping, XPS, and inductively coupled plasma mass spectrometry (ICP-MS) (Figure 9.3). Similar to the 1:1 PdNi experiments, $PdNi_2$ and Pd_2Ni bimetallic nanoparticles are formed and uniformly dispersed on CNFs (Figure 9.3a-b). Both the $PdNi_2$ and Pd_2Ni alloy nanoparticles exhibit good crystallinity and well-defined lattice fringes with a lattice spacing of 0.223 nm for $PdNi_2$ and 0.226 nm for Pd_2Ni, which can be indexed to the (111) plane of the PdNi alloy (Figure 9.3b and 9.3e). In addition, the HAADF-STEM images and corresponding EDX elemental mapping confirm the uniform distribution of Pd and Ni in the $PdNi_2$ and Pd_2Ni alloy nanoparticles (Figure 9.3c and 9.3f), displaying atomically mixed Pd and Ni in both alloy nanoparticles.

Besides the structure, the compositions of $PdNi_2$ and Pd_2Ni alloy nanoparticles were determined by EDX, ICP-MS, and XPS (Table 9.1). The EDX provides the microscopic composition ratio in several individual nanoparticles, which is similar to that measured by macroscopic XPS and ICP-MS. Importantly, the composition ratios measured resemble the initial composition design in the salt mixture, demonstrating the effectiveness of RTS synthesis in composition control. Note that the XPS results also indicate that the binding energies of Pd(3d) and Ni(2p) in $PdNi_2$ and Pd_2Ni shifted to higher values, which could be ascribed to the formation of an alloy structure.

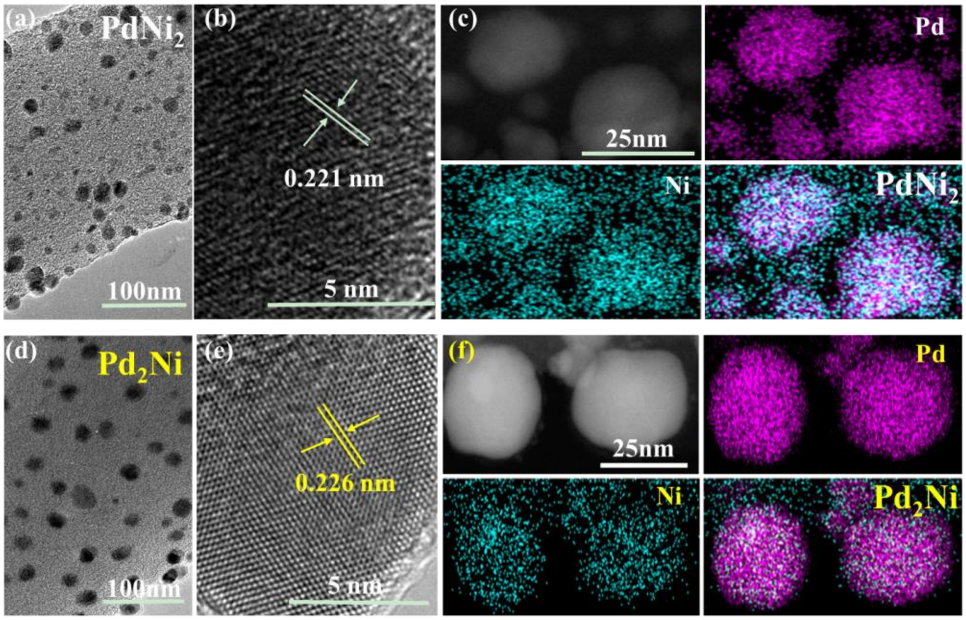

Figure 9.3. (a) TEM image of $PdNi_2$ nanoparticles on CNF. (b) HRTEM image of a $PdNi_2$ nanoparticle. (c) HAADF-STEM image and corresponding EDX elemental mapping of $PdNi_2$ alloy nanoparticles on CNF. (d) TEM image of the Pd_2Ni nanoparticle. (e) HRTEM image of a Pd_2Ni nanoparticle. (f) HAADF-STEM image and corresponding EDX elemental mapping of Pd_2Ni alloy nanoparticles.

Table 9.1. Summary of EDX, XPS, and ICP analysis results for compositions of PdNi alloy nanoparticles formed on CNF after one-second RTS.

Precursor (PdNi) molar ratio	**EDX analysis At%**	**XPS analysis At%**	**ICP analysis At%**
$PdNi_2$	$PdNi_{1.89}$	$PdNi_2$	$PdNi_{1.93}$
PdNi	$Pd_{1.11}Ni$	$Pd_{1.04}Ni$	$Pd_{1.07}Ni$
Pd_2Ni	$Pd_{2.13}Ni$	$Pd_{2.17}Ni$	$Pd_{2.24}Ni$

To understand the underpinning mechanism for the bimetallic nanoparticle synthesis, we investigated in detail the time-temperature profile of the RTS. Figure 9.4a shows our homemade setup for the fast Joule heating synthesis. The CNF network was attached to two electrodes for Joule heating and suspended on a glass substrate to avoid thermal leakage. At high temperature, the CNF network will emit visible light owing to the blackbody radiation. The light spectra were collected by an optical fiber capable of detecting light within a wavelength range of 380 nm to 950 nm.[194,195] The collected light spectra at different powers (triggered by different electrical pulses) and the corresponding temperature profiles are shown in Figure 9.4b-c, respectively. The Joule heating temperature increases with the increase of the input electrical power/current, making the RTS process finely controllable.

For the one-second Joule heating process, the whole process can be divided into three steps (Figure 9.4d). Firstly, upon driving constant current (50 mA) through the CNF sample, the temperature increased sharply from room temperature to 1550 K in about 0.3 seconds (an estimated heating rate of ~1.2×10^4 K/s). Secondly, the temperature was saturated at 1550 K for the duration of slightly less than 1 second. Lastly, the sample rapidly cooled when the current was turned off to 0 mA. The Joule heating temperature is 1550 K in this study, which can be up to 3000 K—high enough to decompose many types of metal salts. In the RTS process, the high temperature is essential for the salt decomposition and alloy mixing, while the rapid quenching process ensures particle formation as opposed to particle coarsening.

To understand the particle formation during RTS synthesis, we also carried out a Monte Carlo simulation to calculate the adsorption energy of Pd or Ni atoms on CNF during Joule heating (Figure 9.4e). In the RTS heating process (Figure 4e, stage I), the Pd precursor begins to decompose first and begins to adsorb on the CNF and form clusters of Pd. When the temperature increases to 1300 K, $NiCl_2$ starts to decompose and Ni atoms are adsorbed on the Pd clusters to form a core-shell structure. When the temperature is higher than 1450 K (Figure 9.4e, stage II), the Ni atoms in the shell diffuse dramatically, as high temperature provides sufficient dynamic energy; some of the Ni atoms move in and exchange positions with Pd atoms. After 400 ps, a well-mixed PdNi nanoparticle is obtained. Finally, during the cooling process (Figure 9.4e, stage III), atomically mixed PdNi alloy nanoparticles are formed and absorb on the CNFs. We conclude that high temperature provides the activation energy for the thermal decomposition of salt precursors and the atomic mixing of Pd and Ni atoms toward the *in-situ* formation of PdNi nanoparticles.

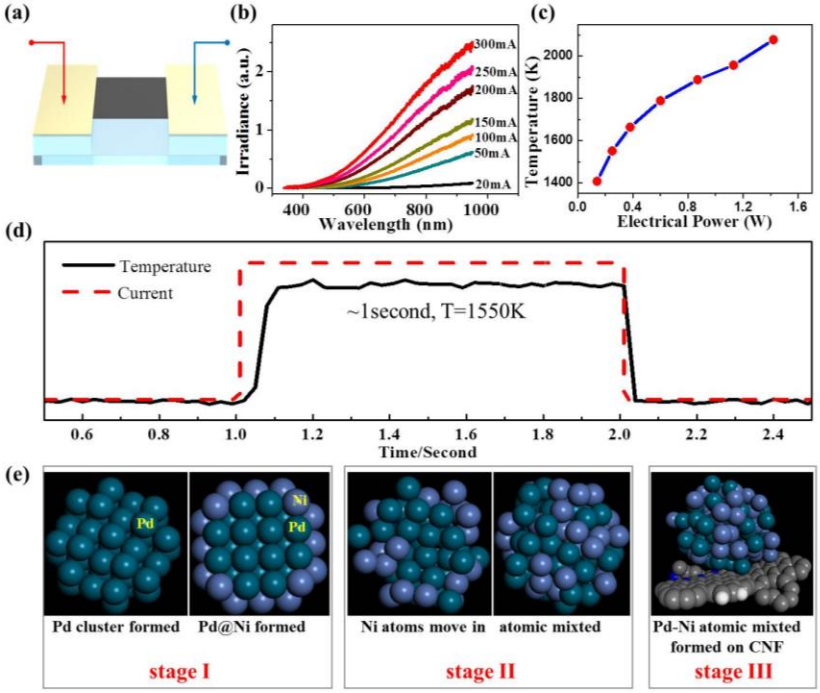

Figure 9.4. (a) Experimental setup for carrying out RTS synthesis. (b) Light emission spectra of CNF at different current levels. (c) The temperature of CNF at different power levels. (d) Temporal evolution of triggering current and corresponding temperature in the one-second Joule heating to 1550 K (50 mA). (e) Simulation reveals that Pd@Ni core-shell nanoparticles form on the CNF first (stage I); then high temperature diffusion leads to intermixing of Pd and Ni atoms (stage II); and finally, PdNi alloy nanoparticles are formed on CNF during cooling (stage III).

These *in-situ* formed bimetallic nanoparticles can find important use in a broad range of emerging applications. Specifically, bimetallic nanoparticles anchored on the conductive carbon surface are ideal for the direct application of electrocatalytic reactions. In this study, the electrocatalytic activity of PdNi/CNF was evaluated by electrocatalytic hydrogen evolution reaction (HER) and hydrogen peroxide oxidation. The HER was performed in a 0.5 M H_2SO_4 solution using a typical three-electrode cell set-up. Figure 9.5a shows the linear-sweep voltammogram (LSV) at a scan rate of 2 $mV\cdot s^{-1}$, which clearly reveals the catalytic reactivity of PdNi/CNF on HER reaction through the following parameters: onset potential, overpotential, and the derived Tafel slope. The PdNi/CNF shows impressive HER activity with a small onset potential (beyond which the cathodic current increases rapidly) of 30mV and the overpotential of -0.2 V at a current density of 100 mA cm^{-2}. Additionally, the Tafel slope value is as low as 60 $mV\cdot dec^{-1}$, which is desirable to drive a large catalytic current density at low overpotential (Figure 9.5b).[196]

The hydrogen peroxide oxidation was performed in a 4 $mol\cdot L^{-1}$ KOH and a 0.9 $mol\cdot L^{-1}$ H_2O_2. We then compared the LSVs of the CNF and PdNi/CNF electrodes (Figure 9.5c), where the oxidation current density of the PdNi/CNF electrode is tremendously increased compared to CNF electrode at the same scan rate (10 $mV\cdot s^{-1}$). The oxidation current density of the PdNi/CNF electrode (281 $mA\cdot cm^{-2}$ at 0.2 V) was 25 times higher than that of the CNF electrode (11 $mA\cdot cm^{-2}$ at 0.2 V). The onset oxidation potential for H_2O_2 electro-oxidation using PdNi/CNF electrode was about -0.22 V (*vs*. saturated Ag/AgCl electrode), which is ~42 mV less than that of the CNF electrode. The catalytic stability of the PdNi/CNF electrode for H_2O_2 electrooxidation at different applied potentials was further studied by chronoamperometric measurement. Figure 9.5d shows that after initial decay, the oxidation current densities remain nearly stable under different control potentials (−0.10, 0.10 and 0.30 V) and exhibit scarcely any reduction within a 1000 s test period, indicating excellent catalytic stability. The superior electrocatalytic performance of PdNi bimetallic nanoparticles can be attributed to the ultrafine size and uniform dispersion of the nanoparticles on 3D interconnected CNFs, which can expose more active catalytic sites and consequently enable the high utilization of PdNi surfaces.

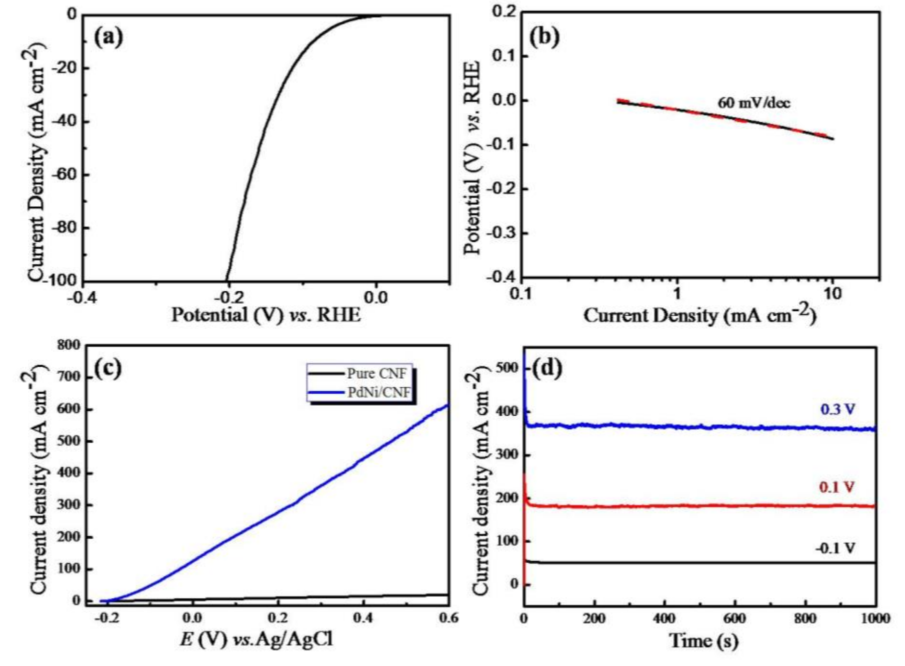

Figure 9.5. The electrocatalytic performance of PdNi bimetallic nanoparticles hosted on a 3D interconnected CNFs. (a) The linear sweep voltammetry in 0.5 M H_2SO_4 with a scan rate of 2 mV·s^{-1}. (b) Fitted (red dash) and observed (black) Tafel plots under the same conditions. (c) Comparative linear-sweep voltammetry of the CNF and PdNi/CNF electrode in 4 mol·L^{-1} KOH and 0.9 mol·L^{-1} H_2O_2 at a scan rate of 10 mV·s^{-1}. (d) Chronoamperometric curves for H_2O_2 electro-oxidation on the PdNi/CNF electrode at different applied potentials in 4 mol·L^{-1} KOH and 0.9 mol·L^{-1} H_2O_2.

9.3 Conclusion

In summary, we report an *in-situ*, rapid synthesis of atomically mixed bimetallic alloy nanoparticles from their salt precursors *via* a one-second high temperature pulse. The bimetallic nanoparticles were uniformly dispersed on the surface of the CNF, which can be readily used for a wide range of emerging applications. The high temperature (up to 3000 K) facilitates the total (atomic) mixing of different metals and also expands the generality of RTS method to other metals as well. The rapid quenching (~10^4 K/s) ensures the ultrafine nanoparticle formation and leads to fine features such as twin boundaries and stacking faults in the resultant nanoparticles, which are potentially beneficial to their catalytic performances. By tuning the precursor salt mixture and parameters in the RTS process, the composition, size, and morphology of the resultant nanoparticles can be readily adjusted. Since carbon has excellent heat absorption capability, the RTS triggered by Joule heating could also be replaced by a rapid radiation heating toward scalable nanomanufacturing.

9.4 Experimental

The material, Joule heating process and Characterization. Similar as Chapter 8.

Electrochemistry. For HER testing, a freestanding network with a size of 3mm×3mm was directly used as the working electrode in a standard three-electrode apparatus. A platinum foil and a standard Ag/AgCl electrode were used as the counter electrode and reference electrode, respectively. The electrolyte was 0.5M H_2SO_4 aqueous solution. The activity of the catalyst was evaluated by linear sweep voltammetry from 0V to -0.6V (vs. RHE) with a scan rate of 2mV/s. For H_2O_2 electro-oxidation testing, the electrocatalytic performance of the as-prepared electrodes was studied in a mixture of

KOH and H_2O_2 solution using a typical three-electrode set-up with a Pt wire as the counter electrode, saturated Ag/AgCl electrode as the reference electrode and the as-obtained specimen as the working electrode. The electrochemical performance of electrodes for H_2O_2 electro-oxidation was investigated by chronoamperometry (CA) and linear sweep voltammetry (LSV). All of the electrochemical measurements were conducted using a Bio-Logic potentiostat (VMP3/Z).

9.5 Supporting materials

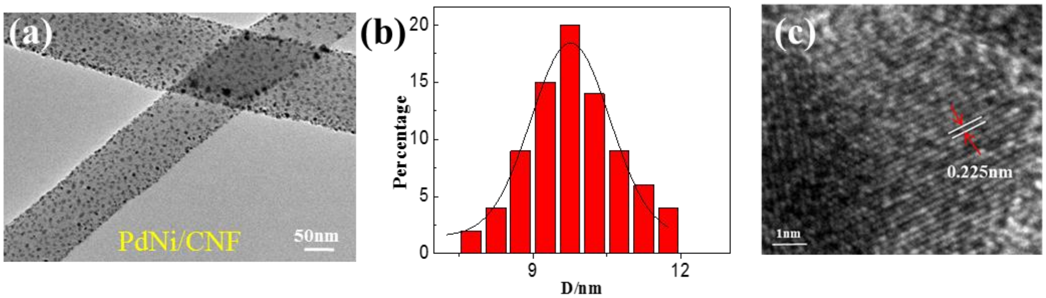

Figure 9.6. (a) Typical TEM characterization of PdNi bimetallic nanoparticles formed on CNF by one-second RTS at 1550K. (b) The histogram of the size distribution of PdNi nanoparticles showing an average diameter of around 10 nm. (c) HRTEM images of PdNi alloy nanoparticles with a lattice spacing of 0.225 nm, corresponding to the (111) plane family.

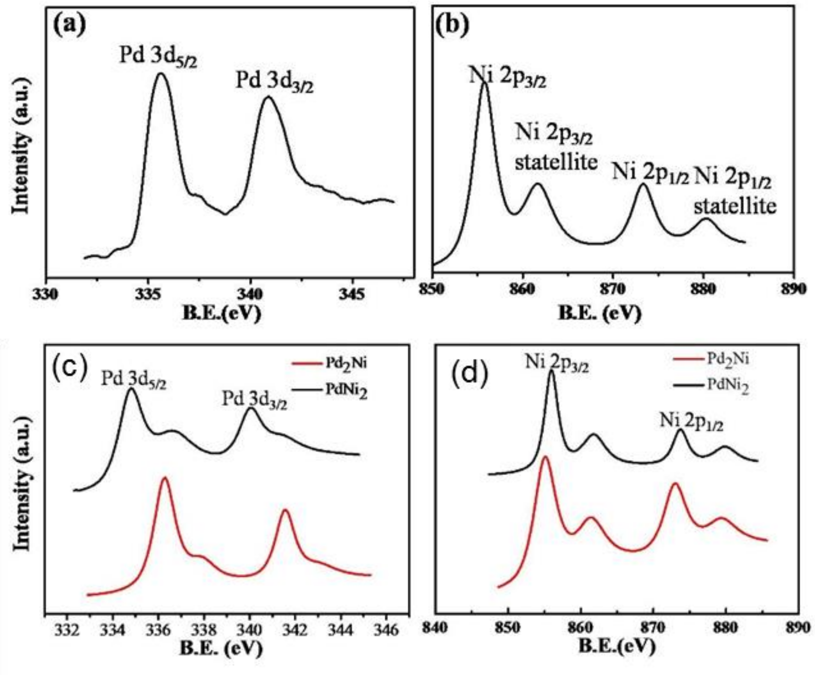

Figure 9.7. XPS spectra of PdNix nanoparticles on CNF after RTS synthesis. (a)-(b) The binding energies of Pd and Ni for PdNi/CNF. Both signals of Pd(3d) and Ni(2p) shift to higher energy fields compared to that of pure Pd and Ni metal. (c)-(d) XPS spectra of Pd and Ni in Pd_2Ni and $PdNi_2$.

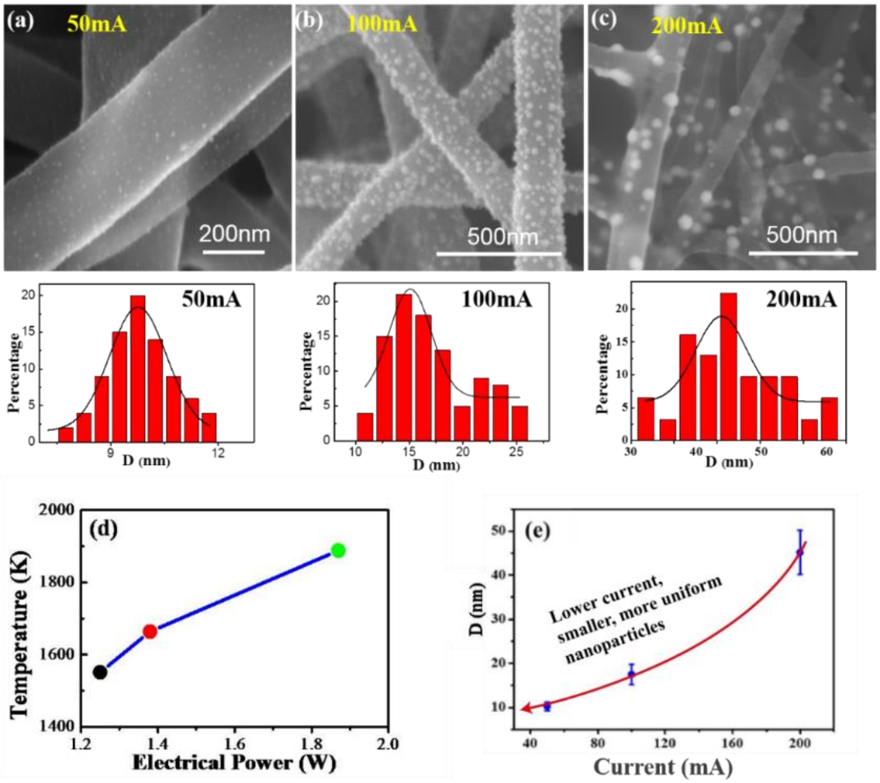

Figure 9.8. Effect of temperature in RTS process on the size distribution of PdNi bimetallic nanoparticles on the CNFs. (a)-(c) SEM images of $PdCl_2$-$NiCl_2$/CNF by 1-second RTS at 50 mA, 100 mA, 200mA, respectively. (d) The temperature of the CNF network under Joule heating using different electrical driving power. (e) Summary of average particle size as a function of Joule heating driven current (temperature). The average particles size increases from 10 ± 1.5 nm to 16.2 ± 2.5 nm to 48.3 ± 5.0 nm with increasing current, confirming the importance of the short pulse for rapid nanoparticle synthesis at a high temperature.

Chapter 10: Thermal shock synthesis of high-entropy alloy nanoparticles[*]

Abstract

The controllable incorporation of multiple immiscible elements into a single nanoparticle merits untold scientific and technological potential, yet remains a challenge using conventional synthetic techniques. We present a general route for alloying up to eight dissimilar elements into single-phase solid solution nanoparticles, referred to as high entropy alloy nanoparticles (HEA-NPs), by shocking precursor metal salt mixtures loaded onto carbon supports (~2000 K, 55 ms duration, the rate of ~10^5 K/s). We synthesized a wide range of multicomponent nanoparticles with the desired chemistry (composition), size, and phase (solid solution, phase-separated) by controlling carbo-thermal shock (CTS) parameters (temperature, shock duration, heating/cooling rate). To prove utility, we synthesized quinary HEA-NPs as ammonia oxidation catalysts with ~100% conversion and >99% NO_x selectivity over prolonged operation conditions.

10.1 Introduction

Multimetallic nanoparticles (MMNPs) are of interest in a wide range of applications including catalysis [183,186,197–201], energy storage [202], bio/plasmonic imaging [202,203], among others. Alloying multiple metallic elements into individual nanoscale products offer the promise of material properties that could exceed single element (or

---

[*] The results in this chapter have been accepted for publication: Yao, Y.; et al; Hu, L. Carbo-thermal shock synthesis of high entropy alloy nanoparticles. *Science.* Accepted, 2018.

unary) nanoparticles [197,200,201]. The current and primary approaches towards the preparation of MMNPs arise from wet chemistry synthesis, where a variety of particle sizes, shapes, and phases can be attained [155,186,198,199]. However, most reports via wet chemical methods report alloy compositions not exceeding three elements, which limits the compositional space of multicomponent nanomaterials. Additionally, more site-specific synthesis techniques including printing- and lithography-based methods [183,204,205], have shifted the compositional space towards quaternary and even quinary nanostructures, however, the subsequent reduction procedures tend to limit the structural complexity to phase-separated MMNPs, especially for immiscible elemental combinations [183,205,206]. In terms of bulk material synthesis, melt processing is a scalable method that has led to the creation of high entropy alloys (HEAs) consisting of five or more elements in a solid solution (uniform mixing), which has shown great potential as structural materials [207–211]. To date, only a limited family of HEAs have been achieved, due to the difficulty of mixing elements with vastly different chemical and physical properties as well as cooling rate constraints. Moreover, downsizing HEAs to the nanoscale is a daunting task, especially by conventional alloying methods. Therefore, the development of a synthesis method where elemental composition, particle size, and phase can be precisely controlled could bring about a new repertoire of alloys and nanostructures with advanced functionalities.

We developed a facile, two-step carbo-thermal shock (CTS) method which employs flash heating and cooling (temperature of ~2000 K, shock duration of ~55 ms, and ramp rates on the order of 10^5 K/s) of metal precursors on oxygenated carbon to produce high entropy alloy nanoparticles (HEA-NPs) with up to eight dissimilar metallic elements. MMNPs synthesized by CTS have a narrow size distribution and are uniformly dispersed across the carbon support, despite being exposed to high temperatures that conventionally cause particle coarsening. The high temperature, in conjunction with the catalytic activities of the liquid metals, drives rapid particle “fission” and “fusion” events that result in uniform mixtures of multiple elements. Subsequently, the rapid cooling rate facilitates control over kinetic and thermodynamic mixing regimes and enables the formation of crystalline solid solution nanoparticles. By adjusting the input electrical pulse parameters, we can also produce phase-separated nanoparticles by decreasing the cooling rate. This CTS technique opens up a vast space for synthesizing alloys and nanocrystals, which has potential impacts for a wide range of technological applications.

10.2 Results

The CTS method we used to synthesize uniformly dispersed, solid solution nanoparticles (up to 8 elements) requires two steps. First, we mixed metal salt precursors MCl_xH_y (M = Pt, Pd, Ni, Fe, Co, Au, Cu, Sn, among others) into a solution and loaded onto a conductive carbon support, such as carbon nanofibers (CNF). Note that CNFs carbonized at 1073K (CNF-1073K denoted as CNF hereafter) are the carbon support employed in this work unless stated otherwise. After drying, we exposed the precursor-loaded sample to a rapid thermal shock (55 ms) in an Ar-filled glovebox, which leads to a high concentration of nanoparticles (e.g. PtNi) that form across the carbon surface (Fig. 10.1A and in SI). The electrical pulse we applied controls the thermal exposure conditions (Fig. 10.1B), with a common temperature of ~2000 K and heating/cooling rates up to ~10^5 K/s as we measured with a pyrometer (SI). We found no apparent elemental segregation or phase separation for the PtNi nanoparticles (Fig. 10.1C) using scanning transmission electron microscopy (STEM) elemental maps. The high angle annular dark-field (HAADF) images and atomic maps also demonstrated both uniform atomic scale mixing and the formation of an FCC crystalline structure.

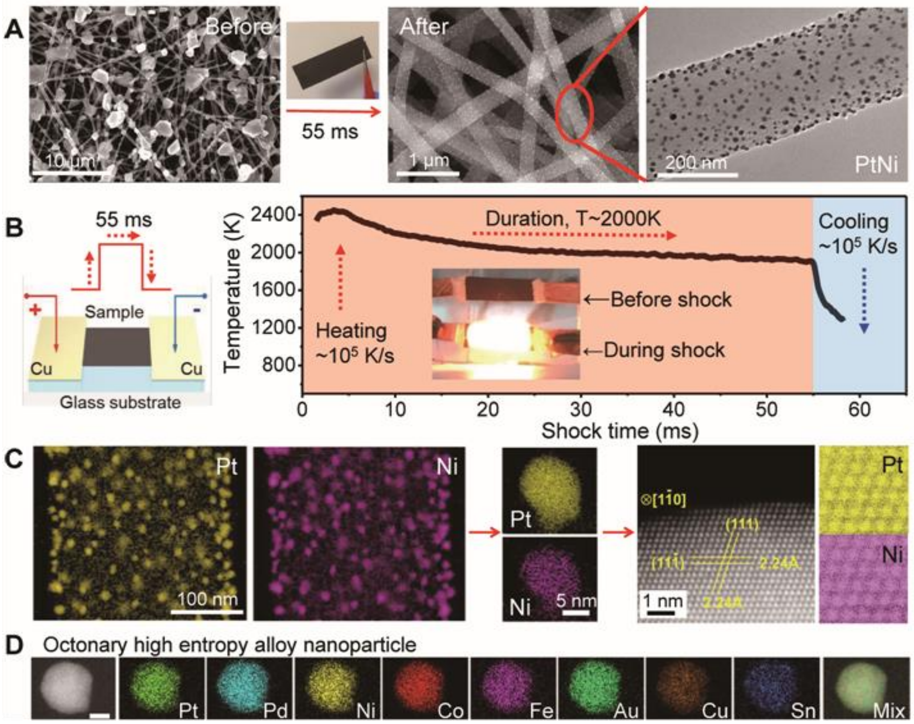

Fig. 10.1. CTS synthesis of HEA-NPs on carbon supports. (A) Microscopy images of microsized precursor salt particles on the carbon nanofiber (CNF) support prior to thermal shock as well as the synthesized, well-dispersed (PtNi) nanoparticles following CTS. (B) Sample preparation and the temporal evolution of temperature during the 55 ms thermal shock. (C) Low magnification and single particle elemental maps, a HAADF image and corresponding atomic maps for a binary PtNi alloy. (D) Elemental maps of an HEA-NP composed of eight dissimilar elements (Pt, Pd, Ni, Co, Fe, Au, Cu, Sn). Scale bar: 10 nm.

Our general method extends to more complex HEA-NPs. For example, we readily fabricated HEA-NPs composed of eight dissimilar elements (Pt, Pd, Ni, Co, Fe, Au, Cu, Sn). These elements have a range of atomic radii (1.24 Å to 1.44 Å), reduction potentials (-0.25 V to 1.5 V), preferred crystal structures (FCC, BCC, HCP, tetragonal) and melting temperatures (500 K to 2000 K) that typically prevents solid solution formation (Fig. 10.1D).

MMNPs have been previously synthesized in reported works using conventional reduction procedures [183,198]. However, these synthetic methods tend to create phase-separated heterostructures among immiscible elements, which greatly reduces the configurational entropy of mixing (SI). The CTS process leads to solid solution MMNPs (i.e. HEA-NPs), where arbitrary metallic elements are completely mixed to maximize the mixing entropy (ΔS_{mix}) (Fig. 2A). We demonstrated the versatility by synthesizing a series of multi-element nanoparticles, and characterized them by the STEM, TEM, SEM, and energy-dispersive x-ray spectroscopy (EDS). We synthesized unary (Pt, Au, Fe), binary (PtNi, AuCu, FeNi), and ternary (PtPdNi, AuCuSn, FeCoNi) nanoparticles exhibit compositional uniformity (Fig. 2B). The nanoparticles also possess size uniformity, with diameters of ≥5 nm (SI), regardless of the elemental compositions. By adding additional metal salts to the precursor solutions, we synthesized quinary (PtCoNiFeCu and PtPdCoNiFe), senary (PtCoNiFeCuAu), septenary (PtPdCoNiFeCuAu) and octonary (PtPdCoNiFeCuAuSn) HEA-NPs, which are solid solutions and evenly dispersed across the carbon support (Fig. 2C-2D, figs. S10-S16). Moreover, the HEA-NPs are in nanoscale dimensions with FCC crystal structures (Fig. 2D, and in SI).

The HEA-NPs exhibited solid solution mixing via the same 55 ms thermal shock protocol (in SI). We confirmed the structural uniformity (no phase separation) and negligible chlorine content with STEM, XRD, and XPS (in SI). A statistical study conducted over different sample regions confirms the compositional uniformity among the synthesized nanoparticles (in SI). For example, the compositional variation for each element in our quinary HEA-NPs (PtPdCoNiFe) is ~10%, which is smaller than the >50% variation reported for lithography-based techniques (*1*). Additionally, the macroscopic compositions we determined by inductively coupled plasma mass spectroscopy (ICP-MS) agree well with the STEM-derived statistics. The HEA-NP composition has a small deviation from the ideal composition based on the initial precursor salt ratios, which depends primarily on the metal vapor pressures at high temperature (in SI). To demonstrate compositional control, we employed the (precursor) compensation approach, which is a common strategy in high temperature synthesis when volatile elements are involved (in SI).

The HEA-NPs deviate from the phase-separated thermodynamic equilibrium structures reported in literature[183,198,205] due to the rapid quench-induced nucleation/growth process of the CTS method, which 'freezes' the liquid alloy state to create solid solution nanoparticles. The synthesized HEA-NPs are stable at room temperature and remained unchanged in terms of size, structure, and composition after 11 months of storage under standard conditions.

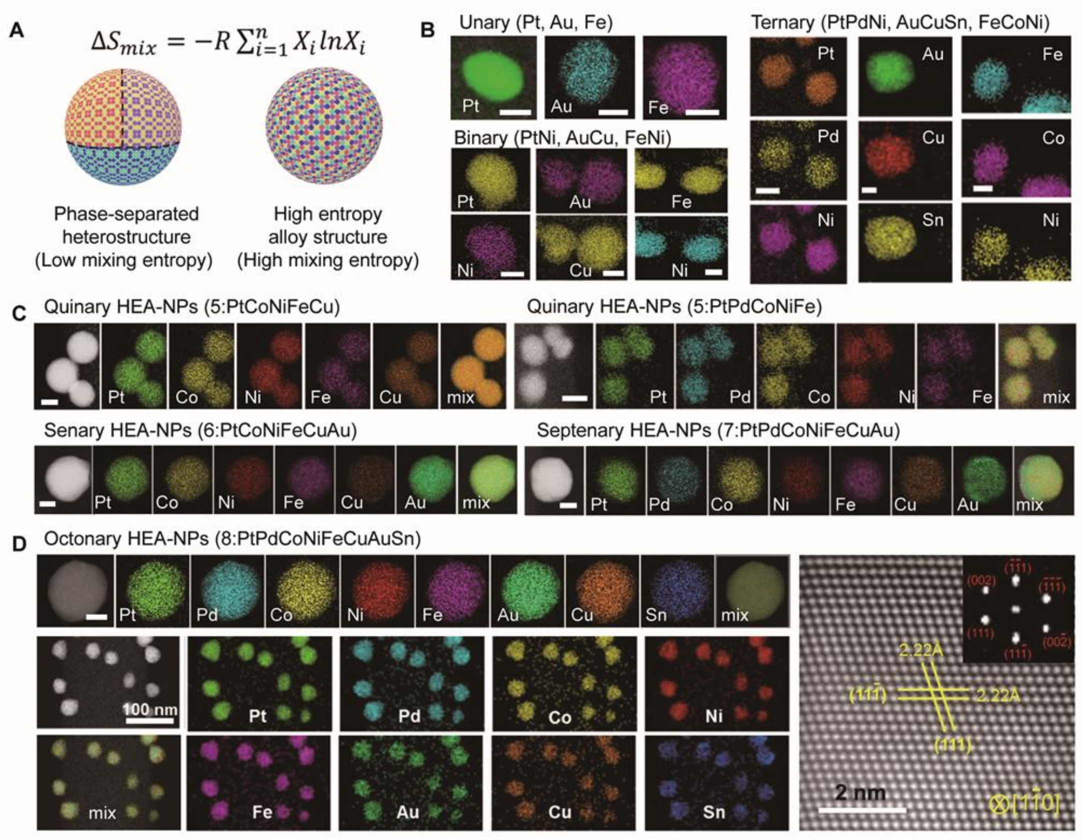

Fig. 10.2. Elemental characterization of HEA-NPs. (A) Schematic comparison of phase-separated heterostructures synthesized by a conventional slow reduction procedure (slow kinetics) vs. solid solution HEA-NPs synthesized by the CTS method (fast kinetics). (B) STEM elemental maps of unary (Pt, Au, Fe), binary (PtNi, AuCu, FeNi), and ternary (PtPdNi, AuCuSn, FeCoNi) nanoalloys. Scale bar: 5 nm. (C) HAADF images and STEM elemental maps of HEA-NPs: quinary (PtFeCoNiCu, PtPdCoNiFe), senary (PtCoNiFeCuAu), and septenary (PtPdCoNiFeCuAu). Scale bar: 10 nm. (D) Individual and low magnification elemental maps (left) and a high-resolution HAADF-STEM image with FFT analysis (right) of octonary (PtPdCoNiFeCuAuSn) HEA-NPs, showing solid solutions with an FCC structure. The low magnification elemental maps verify the structural and compositional uniformity of the HEA-NPs. Scale bar: 10 nm.

In addition to the rich chemistries, the morphologies of the synthesized nanoparticles indicate a unique formation mechanism for CTS that differs from other alloying approaches. Because ~2000 K far exceeds the thermal decomposition temperature of metal precursors (Table in SI), the salts easily decompose:

$$MCl_xH_y \rightarrow M(liq) + gases\uparrow \qquad (1)$$

However, ~2000 K is below the boiling points of the metallic elements. In this case, the metallic elements are likely in the liquid phase and should be on a similar length scale as the initial (microsized) salt precursors. Because metals are non-wetting with carbon, the liquid metals should coarsen to minimize their surface energy at high temperature [212]. Our observation departs from this behavior, requiring a mechanism to explain how single element, micron-sized liquid metal droplets form uniformly dispersed nanoparticles.

We performed two control experiments to explore HEA-NP formation. We found distinct particle morphology differences using the same CTS protocol (Fig. 10.3A and in SI), but with supports differing in carbonization temperature. Specifically, electrospun polyacrylonitrile fibers carbonized in argon at a range of temperatures (873 K, 1073 K, 1273 K) generated CNF supports with various defect concentrations. Lower carbonization temperatures resulted in smaller, more uniform particle dispersions. Each pyrolysis temperature was insufficient to drive away all surface-bound oxygen (O*) and thus, resulted in an increasing amount of O* residuals remaining on CNFs carbonized at lower temperatures. Therefore, we surmised that the surface defect concentration of the carbon support is an important parameter for particle dispersion.

Our second control experiment used identical CNF supports (CNF-1073K) and synthesis conditions (55 ms, ~2000 K), but with a variety of single-metal salt precursors (Fig. 3B and in SI). Nanoparticle size distribution changes in this case with Cu having a much larger particle size (~56.8 nm) than Au (~13.5 nm) and Pt (~6.3 nm). This trend resembles the catalytic activities of the corresponding elements with Pt and Cu being the most and least active, respectively. Because Au and Cu possess similar physical properties (Table S4), the discrepancy requires a different particle dispersion mechanism than a simple, physical melting-and-nucleation process.

Because defects and metal catalysts play a key role during the CTS process, we considered a catalytically-driven particle dispersion mechanism for the defective carbon supports. To verify this, we employed in situ mass spectrometry to analyze the gases created during CTS for defective CNF supports with and without precursor salts. Compared to bare CNF, the precursor-loaded CNF exhibited a larger and much sharper release of CO gas during the CTS process (SI). Thus, the release of CO gas upon thermal shock arises from a catalytically-driven carbon metabolism reaction:

$$C + O^{*} \rightarrow CO \uparrow \qquad (2)$$

where O* denotes surface-bound residual oxygen. The carbon metabolism reaction involves C (fuel), O* (oxidizer), and metal (catalyst), which correlates the surface defect concentration (e.g. carbonization temperature) and the metal's catalytic activity to the final nanoparticle size and level of dispersity. We hypothesize that during the 55 ms high temperature exposure, the liquid metal droplets actively travel around and split ("fission") to harvest the dispersed O* on the carbon surface based on the catalytically-driven reaction, C+O*=CO (gas) (ΔH= -110.5 kJ/mol). Previously published works [213–

[216] and an in situ TEM study [217] showed that metallic particles can move and split under a catalytic driving force, which is similar to the carbon metabolism reaction.

Mechanistically (Fig. 10.3C), a larger O* concentration and the use of catalytically active metals can drive vigorous metabolism with more frequent catalyst motion and fission events. This opposes equilibrium thermodynamic directives as the metal surface area increases. Conversely, depleted O* concentrations should lead to decreased mobility and the localization of liquid droplets that coarsen slowly to reduce their total surface energy. Note that the liquid alloys have a wide solubility range at ~2000 K. Therefore, the liquid metal movement driven by O* harvesting allows different droplet compositions to continually meet and fuse into single-phase alloys during the CTS process. Numerous particle fusion and fission events, which we estimated to be $>10^6$ times based on timescale analysis (SI) [218–220], yield a dynamic steady state during the 55 ms high temperature shock with uniform nanoscale dispersions and homogeneous high entropy mixing.

To verify the effects of supports with more surface-bound defects, we synthesized quinary HEA-NPs (PtFeCoNiCu) on CNFs with and without CO_2-activation, resulting in 5.30 nm ± 1.31 nm particles on CO_2-activated CNFs and 11.3 nm ± 2.2 nm particles on CNFs (SI). We achieved further improvements in ultrafine particle sizes and narrow distributions when more catalytically active metal combinations (PtPdIrRhRu HEA-NPs, 3.28 nm ± 0.81 nm) are employed on identical CO_2-activated CNF supports (Fig. 3D and in SI). Therefore, the catalytic metabolism-induced particle fission/fusion mechanism for metal alloying at the nanoscale is distinct compared to previously reported alloying methods [183,186,198,209].

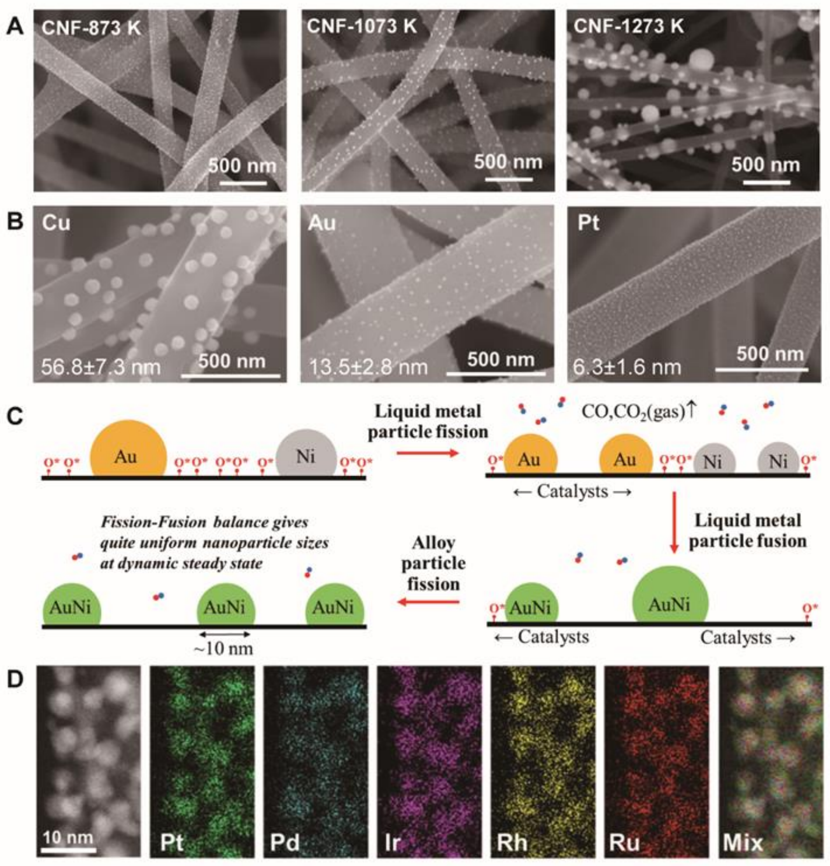

Fig. 10.3. Particle dispersion mechanism for the CTS process. (A) SEM images of synthesized AuNi nanoparticles on CNFs carbonized at different temperatures: 873 K, 1073 K and 1273 K. (B) SEM images of (Cu, Au, Pt) particle distributions synthesized on identical CNF supports via the same CTS process. The higher catalytic activities of the metal species (Au, Pt) lead to smaller nanoparticles and more uniform distributions. (C) An illustration of the catalysis-driven particle fission/fusion mechanism to synthesize uniformly dispersed HEA-NPs. (D) HAADF image and elemental maps of ultrafine and well-dispersed quinary HEA-NPs (PtPdIrRhRu) on CO_2-activated CNFs. A narrow size distribution is achieved by increasing the support's surface defect concentration through CO_2 activation as well as employing metal species with high catalytic activities.

By tuning the shock duration and heating/cooling rates, we can adjust the MMNP size, distribution, and structure. We loaded multiple CNF samples using an identical PtNi precursor solution and exposed the support to a temperature of ~2000 K for 5 ms, 55 ms, 1 s, and 10 s durations. The faster exposure times yield smaller particle sizes (3.51 nm ± 0.62 nm for 5 ms and 5.01 nm ± 1.69 nm for 55 ms) compared to prolonged shock durations (8.57 nm ± 1.98 nm for 1s and 13.30 nm ± 6.98 nm for 10 s) (Fig. 10.4A-B). We observed similar behavior with AuNi (SI). As the thermal shock duration increases to 10 s, the size of the HEA-NPs increases and the synthesized particles become less uniform since the high temperature exposure depletes the number of O* present on the CNF support, which inhibits particle dispersity (SI).

We investigated the effect of cooling rate by tuning the electrical input parameters (Fig. 10.1B) with Au/Ni and Cu/Co, which are immiscible binary elemental compositions (Fig. 10.4C-D and SI). Due to differences in lattice parameters and surface energies, these metallic combinations tend to phase separate according to equilibrium phase diagrams [198,221,222]. However, through rapid quenching, the high entropy mixing state of the liquid metals is retained and yields single-phase solid solution nanoparticles (i.e. HEA-NPs) by avoiding the time-temperature-transformation (TTT) nose (Fig. 10.4E). The AuNi binary alloy formed a solid solution when quenched at both ~10^5 K/s and ~10^3 K/s (Fig. 10.4C). However, nanoscale phase separation occurred when cooled slowly (~10 K/s), with a clear phase boundary between Au and Ni shown in the annular bright field (ABF) image (Fig. 10.4D) and HAADF image (SI). For the CuCo binary system, the 10^5 K/s produced a solid solution, but phase separation began at a cooling rate of ~10^3 K/s (SI). Very slow cooling and heating rates (~10 K/s) alters the dispersion and size distribution of the synthesized nanoparticles, leading to aggregates and a non-uniform dispersion across the CNFs (SI).

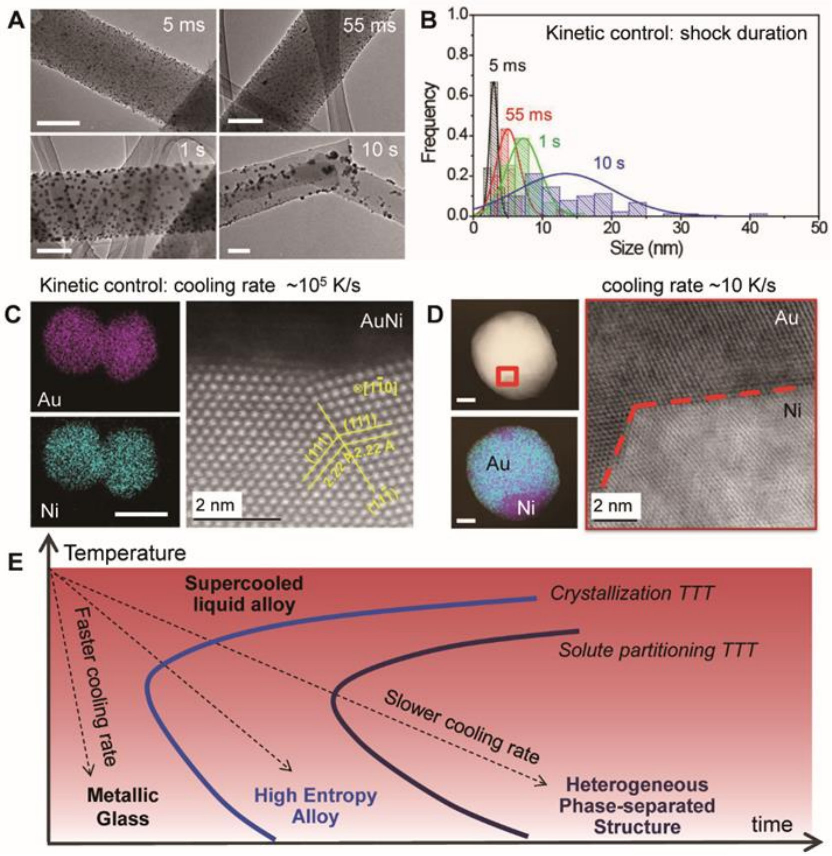

Fig. 10.4. Kinetic control over nanoparticle formation. (A) TEM images displaying the particle size and dispersity at various thermal shock durations (5 ms, 55 ms, 1 s, 10 s). Scale bars: 100 nm. (B) Particle size distribution of PtNi nanoparticles on CNFs. (C-D) Cooling rate-dependent AuNi nanostructures determined by elemental maps, HAADF, and ABF images. Ultrafast cooling rates (~10^5 K/s) enable the formation of solid solution nanoparticles, while slower rates (~10 K/s) tend to induce phase separation. Scale bar: 10 nm. (E) Time-temperature-transformation (TTT) diagram showing the kinetic formation of a metallic glass, HEA and phase-separated structure, respectively, as a function of cooling rate.

Our experimental results reveal valuable information about the nucleation and diffusion kinetics of the CTS method. The transformation of a liquid alloy into a single-phase solid solution with a specific elemental composition requires local structural rearrangements but no long-range solute partitioning. The cooling rate (~10^5 K/s) we achieved by CTS is still slow enough to form crystalline structures. If higher cooling rates are attained with the CTS method, it may be possible to use this route to synthesize metallic glasses. The ~10^5 K/s cooling rate is fast enough to prevent solute partitioning across a distance of approximately 10 nm, enabling the formation of high entropy alloy structures. On the other hand, slower cooling rates (e.g. ~10 K/s) enable solute partitioning to occur through (slow) kinetics, which caused the MMNPs to phase separate into a Janus particle. Note that both single-phase and phase-separated nanoparticles are useful for applications such as catalysis and plasmonic imaging [155,197,198,203]. The CTS method has the ability to control phase formation through ramp rates and may be useful for targeted nanoparticle synthesis.

The CTS method enables diverse compositions of uniformly mixed HEA-NPs that have the potential for a wide range of applications. As a proof-of-concept, we demonstrated quinary HEA-NPs as advanced catalysts for ammonia oxidation, which is the key processing step in the industrial synthesis of nitric acid (Fig. 10.5A) [223]. Despite extensive efforts on the exploration of new catalysts, PtPdRh-based multimetallic catalysts are still widely employed in industry to this day [224]. Beyond the high content of precious metals, these catalysts also require very high temperatures (>800°C) to achieve high yields of NO_x ($NO + NO_2$) versus N_2/N_2O, and tend to degrade under continuous operation [225]. Using the CTS method, quinary PtPdRhRuCe HEA-NPs (in SI) were prepared and employed as ammonia oxidation catalysts. We introduced Ru and Ce to improve the overall catalytic activity (oxygen mobility and storage capabilities) and reduce the Pt content [226,227].

We achieved ~100% conversion of ammonia (NH_3) and >99% selectivity toward NO_x ($NO + NO_2$) at a relatively low operation temperature of 700°C with the synthesized PtPdRhRuCe HEA-NP catalyst (Fig. 10.5B). For comparison, we prepared similar catalysts (in terms of composition) by the wet impregnation method (denoted as PtPdRhRuCe MMNP), which produced an 18.7% yield of NO_x at the same operation temperature, while most of the output was N_2 (Fig. 10.5C). An elemental map comparison between the two catalysts suggests that the enhanced catalytic selectivity of the HEA-NPs is likely due to the highly homogeneous nature of the solid solution nanoparticles compared to the phase-separated heterostructures derived from the wet impregnation method (Fig. 10.5D and in SI). Note that synthesizing solid solution PtPdRh multimetallic systems by conventional synthetic methods is challenging due to immiscibility [197,225]. We also performed degradation testing to study catalytic performance under prolonged operation conditions and we observe no degradation in terms of catalytic activity or selectivity over ~30 h of continuous operation at 700°C (Fig. 10.5E and in SI). We attributed this durability to the high entropy nature of the catalysts prepared by the CTS method, which helps stabilize the MMNPs into solid solutions (i.e. HEA-NPs) and prevents phase separation or elemental segregation owing to the intrinsically slow diffusion associated with HEAs [209,211]. Moreover, the precious metal content of the HEA-NPs can be reduced further without compromising catalytic performance or stability, by replacing ~37.5% of Pt with Co and eliminating Ru (e.g., PtPdRhCoCe HEA-NPs, and in SI). Thus, HEA-NPs fabricated by CTS may be a general route towards highly active, durable, and cost-effective catalysts.

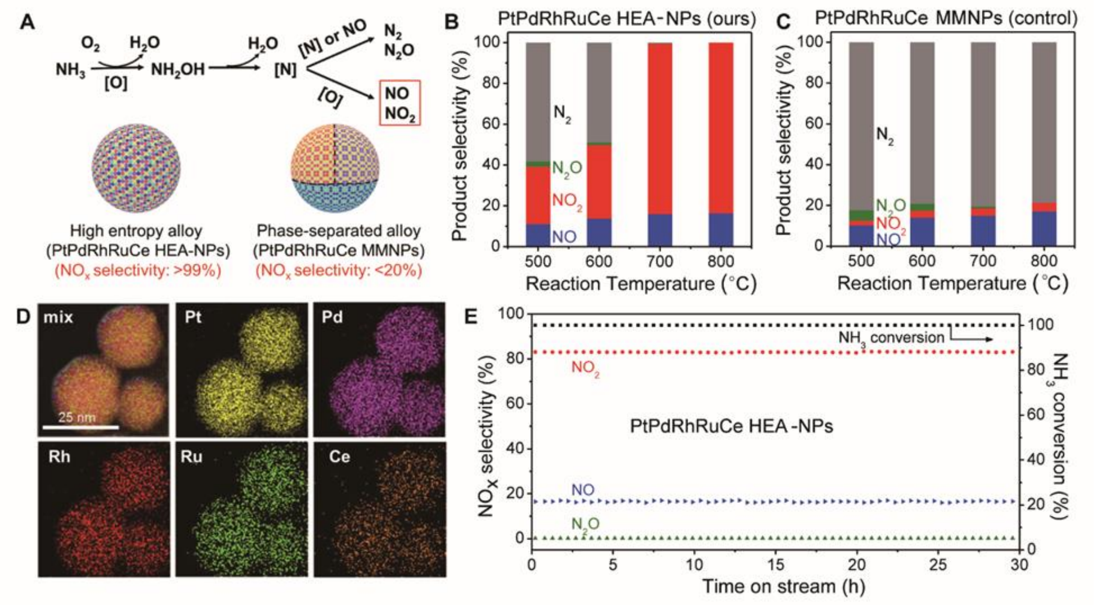

Fig. 10.5. Catalytic performance of quinary HEA-NPs (PtPdRhRuCe) for ammonia oxidation. (A) Reaction scheme for the ammonia oxidation process as well as the structural and performance differences between the PtPdRhRuCe HEA-NPs synthesized by CTS and the control sample (PtPdRhRuCe MMNPs) by wet impregnation. (B-C) Temperature-dependent product distribution and conversion of NH_3 for PtPdRhRuCe HEA-NPs and PtPdRhRuCe MMNPs, respectively. (D) STEM elemental maps for PtPdRhRuCe HEA-NPs. (E) The time-dependent catalytic performance of PtPdRhRuCe HEA-NPs at 700°C.

10.3 Discussion and conclusion

The CTS method provides an excellent platform for nanometallurgical studies. Traditionally immiscible elements are alloyed into single-phase nanoparticles on defective carbon supports with the following features: (1) high entropy mixing, where multimetallic mixing leads to the creation of solid solution nanoparticles with maximized configurational mixing entropy; (2) non-equilibrium processing, where the shock process takes milliseconds to create HEA-NPs by rapid quenching and thus, prevents phase separation among immiscible elements by avoiding the nose of the TTT curve (Fig. 10.4E); (3) uniform dispersion, where the catalytically-driven carbon metabolism at high temperature enables uniform, well-dispersed, and controllably-sized nanoparticles (as opposed to particle coarsen).

This synthetic technique also provides (1) generality, (2) tunability, and (3) potential scalability. The maximum temperature of the CTS method (2000-3000 K) is higher than the decomposition temperature of any metal salt, which promotes uniform mixing of nearly any metallic combination (i.e. generality). Precise control over the shock parameters (temperature, duration, ramp rates) effectively tunes the particle size, dispersity, as well as final structure. The synthesis of a diverse array of nanoparticles with easily tunable processing parameters is ideal for large-scale nanomanufacturing, where a rapid (synthesis in milliseconds) and energy-efficient (immediate heating through an electrical pulse) synthetic procedure could enable the high-rate and high-volume production of quality nanoparticles. Moreover, a scalability evaluation exhibited a 100-fold increase in HEA-NP production without sacrificing nanoparticle quality or dispersion by employing a 3D carbon support (figs. S73-S75). These CTS capabilities facilitate a new research area for materials discovery and optimization, where the elemental composition and mixing entropy of nanoparticles can be carefully designed and controlled, which has potential to affect a broad range of research fields and technological applications.

10.4 Experimental

Carbon nanofibers (CNF) and metal precursor loading: The PAN nanofibers were first stabilized at 533K for 5 hours in air and then carbonized at various temperatures (873 K, 1073 K, 1273 K) for 2 hours in argon. CNF-1073K acted as the ideal carbon support in this study due to its defect density for nanoparticle dispersion and ease of applying an electrical pulse within the limits of the external power source. For aqueous precursor solutions, the CNF films were dipped into the mixed metal salt solutions (0.01 mol/L for each element), placed under vacuum for 30 minutes, and then suspended in a 60°C oven to dry. For ethanol-based precursor solutions, the mixed solutions (0.05/n mol/L for each element, where n is the total number of elements) were directly dropped onto the suspended CNF film with a loading of ~120 $\mu L/cm^2$ and left to dry at room temperature. In general, the ethanol-based solutions result in more uniform loading (and particle dispersion) owing to improved wettability to carbon.

Rapid, high temperature CTS method. The CTS process was achieved by electrically-triggered Joule heating of precursor-loaded CNF films in an argon-filled glovebox. A thermal shock was applied to the CNF film using the sweep function from Keithley where the magnitude (temperature), duration (thermal shock time) and speed (ramp rate) of the electrical pulse are adjustable. A 55 ms electrical pulse was chosen as the ideal thermal shock duration and used to synthesize multimetallic nanoparticles in this work (unless noted otherwise).

*Catalytic ammonia oxidation tests.*_Catalytic oxidation of NH_3 was conducted in a fixed-bed flow reactor at atmospheric pressure. Typically, 10 mg of catalyst mixed with Al_2O_3 particles (40-60 mesh) was loaded into a quartz tube reactor (7 mm = inner diameter). The catalyst was heated to 500°C at a rate of 5°C/min under He (50 mL/min). At 500°C, the gas flow was switched to a forming gas containing 1% NH_3 and 2% O_2, balanced by He. The space velocity was adjusted to 120 L /(g_{cat}·h) by tuning the flow rate. The reaction was then carried out at various temperatures, which was increased stepwise from 500°C to 800°C. Note that a steady state was reached before the product analysis. To determine the conversion of reactants and the yield of products, a FTIR spectrometer (Nicolet 6700, Thermo Scientific) equipped with a long path (5 m) gas cell and a MCT detector (with a resolution of 8 cm^{-1}) was used to analyze NH_3 (964 cm^{-1}), NO (1905 cm^{-1}), N_2O (2237 cm^{-1}), and NO_2 (1630 cm^{-1}). N_2 was detected via a gas chromatograph (GC) equipped with a BID detector (GC-2010 plus, Shimadzu) and a HP-POLT Molesieve column. The NH_3 conversion and product selectivities were calculated using the following equations:

$$\mathrm{NH_3\ conversion} = \frac{[\mathrm{NH_3}]_{\mathrm{inlet}}-[\mathrm{NH_3}]_{\mathrm{outlet}}}{[\mathrm{NH_3}]_{\mathrm{inlet}}}\times 100\%$$

$$\mathrm{Product\ selectivity}\ (\%) = \frac{\delta\times\ [\mathrm{Product}]_{\mathrm{outlet}}}{[\mathrm{NO}]_{\mathrm{outlet}}+[\mathrm{NO_2}]_{\mathrm{outlet}}+2[\mathrm{N_2}]_{\mathrm{outlet}}+2[\mathrm{N_2O}]_{\mathrm{outlet}}}\times 100\%$$

where $[NH_3]_{inlet}$ refers to the concentration of NH_3 fed into the reactor, and $[NH_3]_{outlet}$, $[NO]_{outlet}$, $[NO_2]_{outlet}$, $[N_2]_{outlet}$, and $[N_2O]_{outlet}$ refer to the corresponding species concentrations measured from the outflow of the reactor. In terms of product selectivity, $\delta = 1$ for NO and NO_2, while $\delta = 2$ for N_2 and N_2O.

10.5 Supporting materials

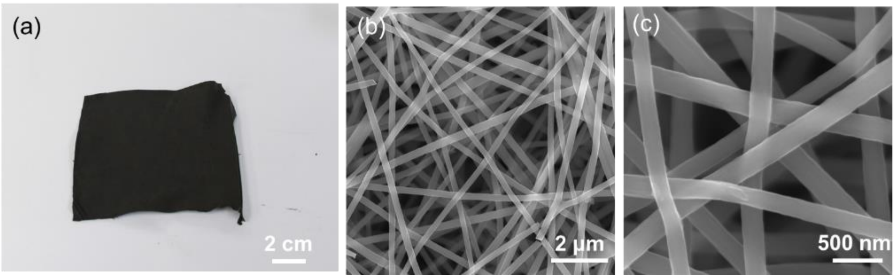

Fig. 10.6. CNFs used as the carbon support. (a) Digital image and (b-c) SEM images of PAN-derived carbon nanofibers, showing uniform nanofiber sizes and an open network structure.

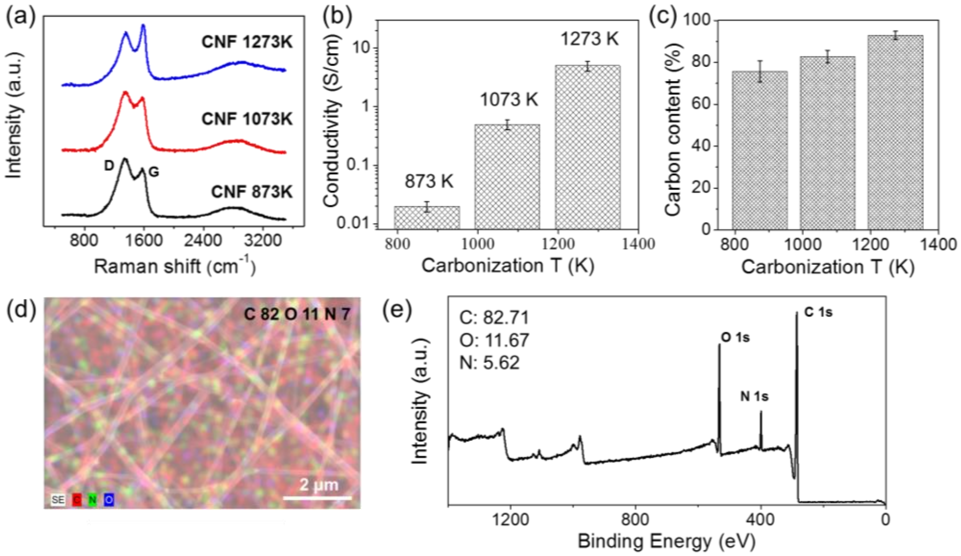

Fig. 10.7. Properties of CNF with different carbonization temperatures. (a) Raman spectra and (b) conductivity of CNF films carbonized at different temperatures: 873 K, 1073 K, and 1273 K. (c) Carbon content in CNFs carbonized at different temperatures, identified by point maps via SEM. (d) Elemental map of the carbon, nitrogen, and oxygen and (e) XPS profile of CNF carbonized at 1073 K.

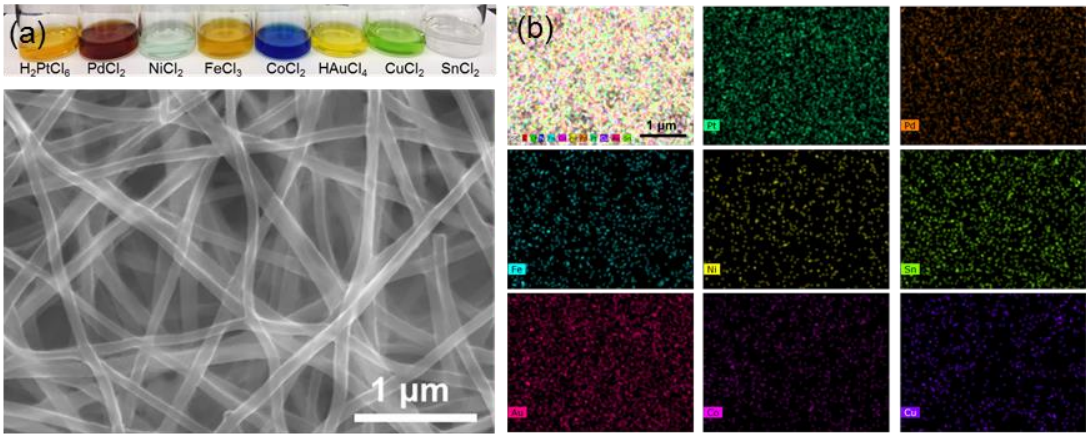

Fig. 10.8. Ethanol-based 8 elemental precursor solutions used to synthesize octonary HEA-NPs on CNFs. The SEM image and EDX mapping confirms the uniform precursor loading on CNFs, which is crucial to achieving the desired nanoparticle compositions via CTS.

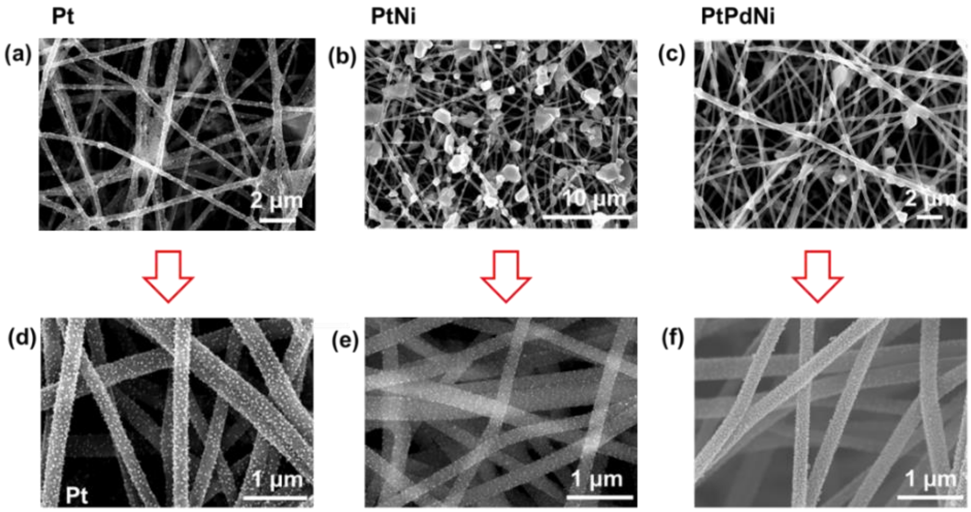

Fig. 10.9. SEM images of the decorated CNF microstructure before and after CTS: (a) Pt, (b) PtNi, and (c) PtPdNi precursors on CNFs before CTS as well as the synthesized (d) Pt, (e) PtNi, and (f) PtPdNi nanoparticles after CTS.

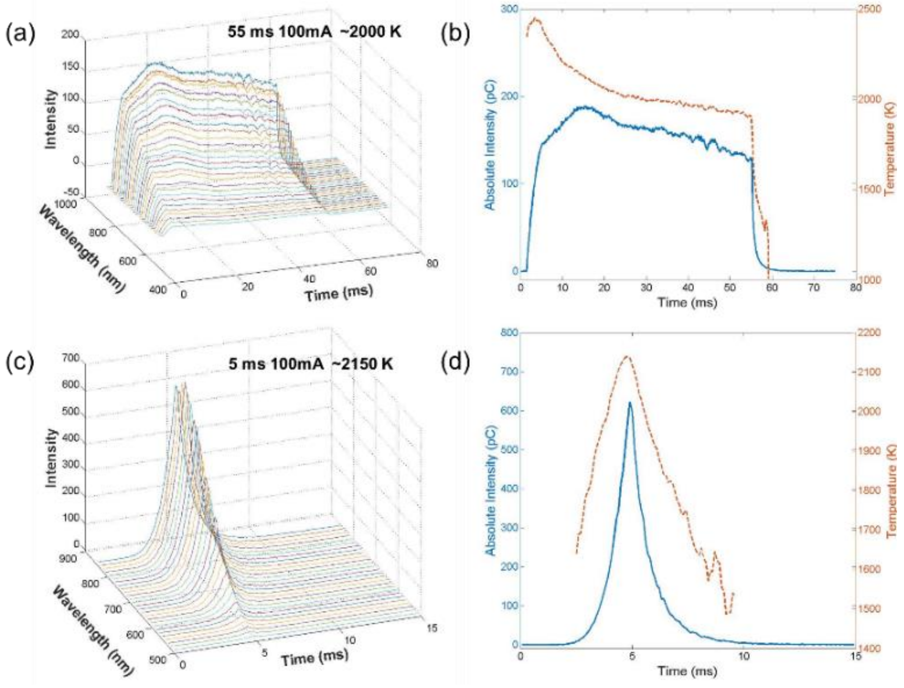

Fig. 10.10. Temporal lighting spectra and temperature fitting for the CTS method with various shock durations: (a-b) 55 ms pulse and (c-d) 5 ms pulse. These spectra were fitted to the blackbody radiation equation to acquire an approximate temperature.

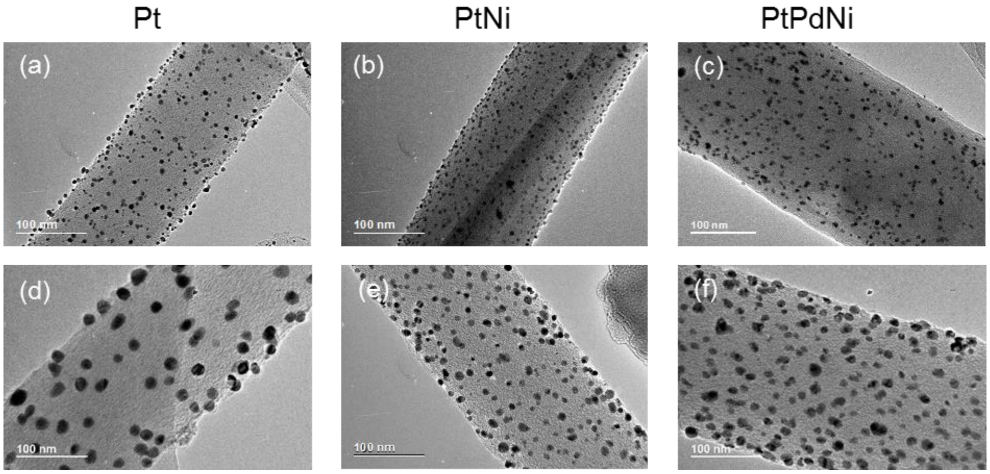

Fig. 10.11. TEM images of 1-3 element nanoparticles on CNFs with different loading concentrations. Pt, PtNi, and PtPdNi with a precursor concentration of (a-c) 0.01 mol/L and (d-f) 0.05 mol/L per composition, respectively.

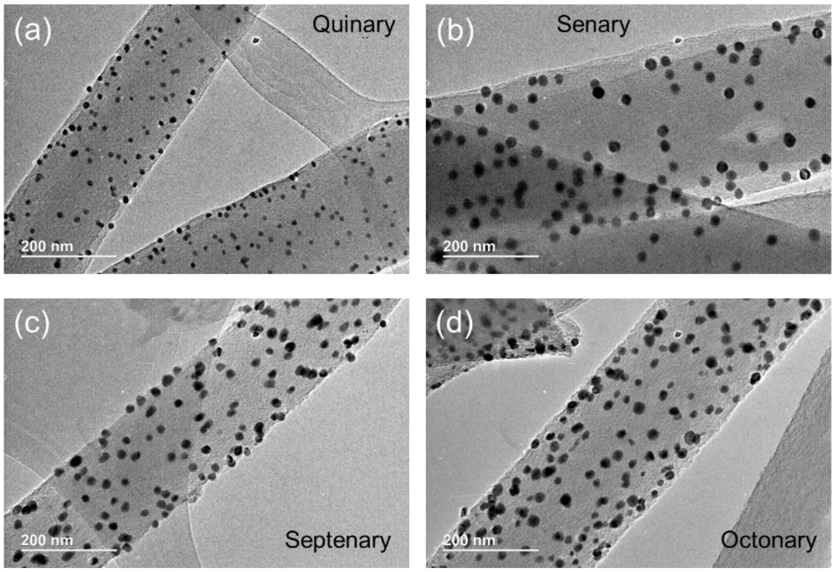

Fig. 10.12. TEM images of high entropy nanoalloys (quinary, senary, septenary and octonary nanoparticles) composed of 5-8 elements, respectively. (0.01 mol/L each composition)

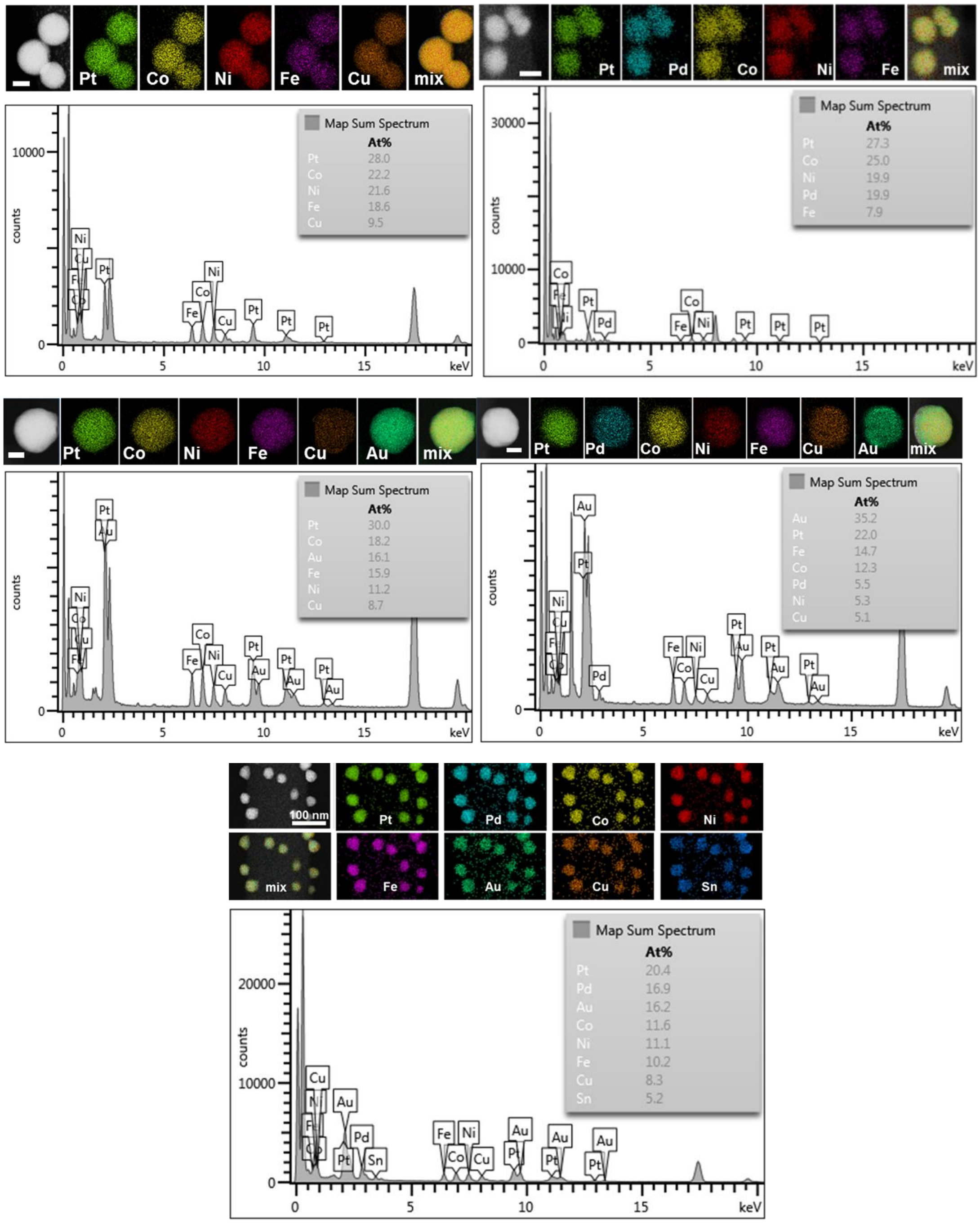

Fig. 10.13. STEM elemental maps and corresponding spectrum for HEA-NPs.

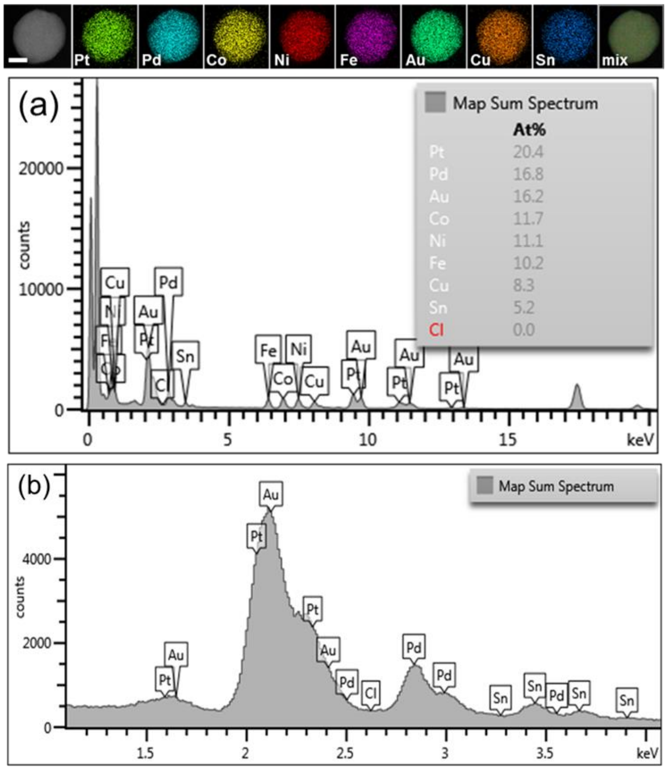

Fig. 10.14. STEM elemental spectrum of an 8 element HEA-NP including Cl (from the initial precursor salt). (a) Full spectrum with elemental ratios of all 8 metals and Cl. (b) Enlarged region of the same spectrum in (a) however, the amount of Cl is below the detection limit.

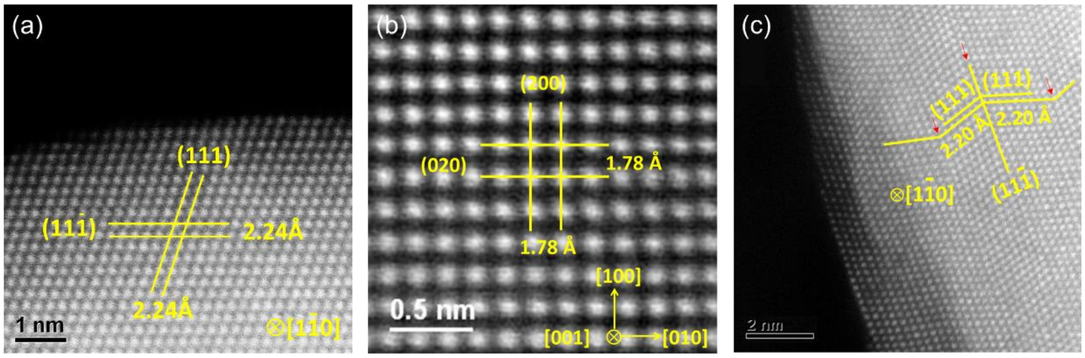

Fig. 10.15. Atomic HAADF images of HEA-NPs for (a) PtNi, (b) FeCoNi, and (c) octonary PtPdCoNiFeAuCuSn nanoparticles. They are alloyed into FCC structures achieved by the CTS method.

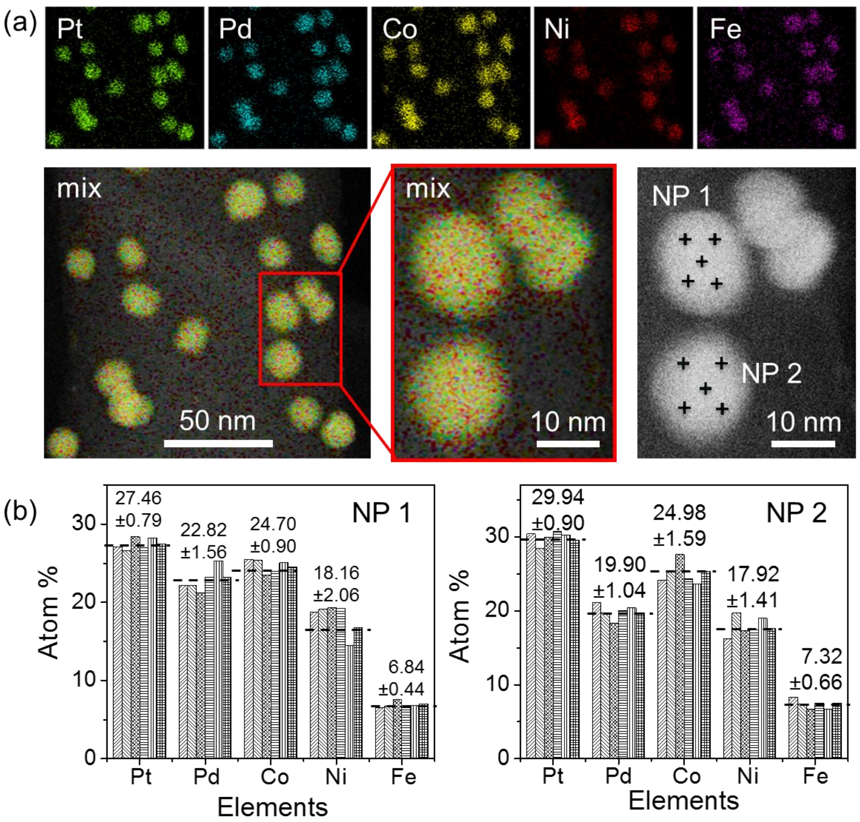

Fig. 10.16. (a) Elemental maps for quinary HEA-NPs (PtPdCoNiFe) and the position of the point maps on individual nanoparticles. (b) Point-by-point elemental maps of PtPdCoNiFe, showing uniform distributions of each element in both nanoparticles.

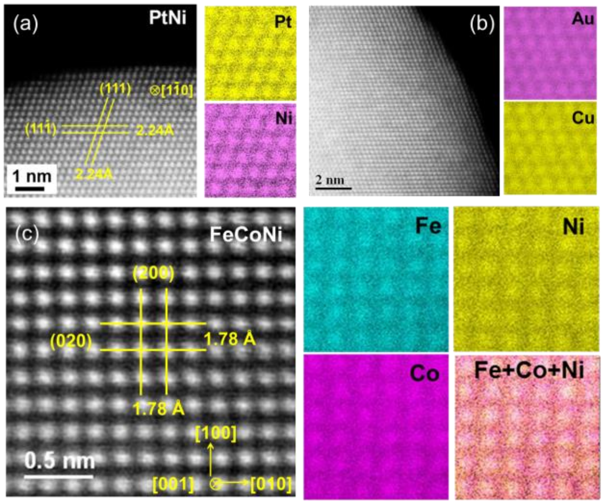

Fig. 10.17. Atomic-scale HAADF-STEM images and STEM elemental maps for binary and ternary HEA-NPs (PtNi, AuCu, FeCoNi). These elemental maps show uniform elemental distribution within the mapped region at an atomic scale.

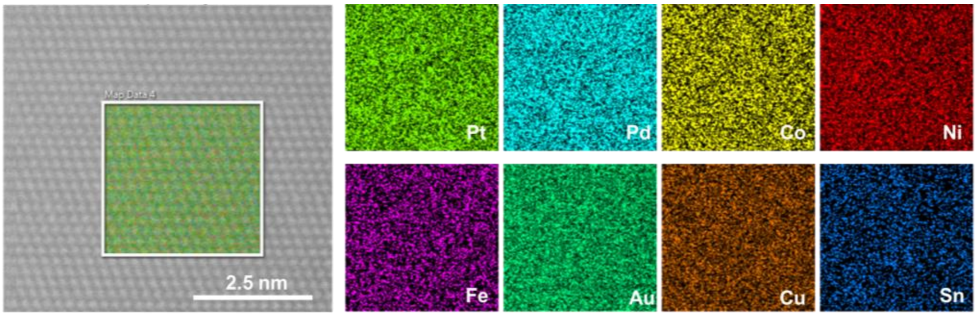

Fig. 10.18. Atomic-level STEM elemental maps of an octonary HEA-NP (PtPdCoNiFeAuCuSn), which demonstrates uniform distributions of each element within the mapped region.

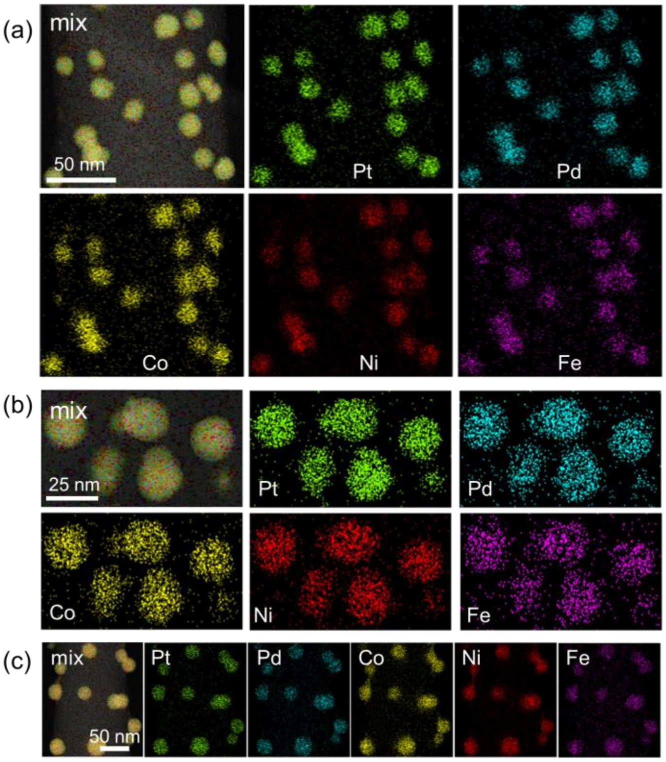

Fig. 10.19. (a)-(c) STEM elemental maps of quinary HEA-NPs (PtPdCoNiFe) at low magnifications, which demonstrates the compositional uniformity of alloy nanoparticles synthesized via the CTS method.

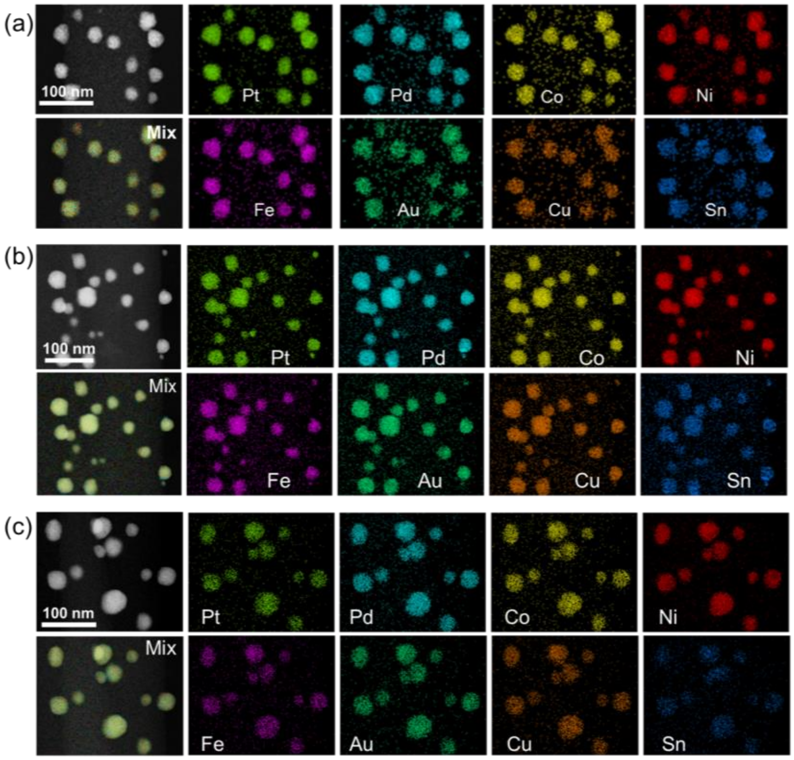

Fig. 10.20. (a)-(c) STEM elemental maps of octonary HEA-NPs (PtPdCoNiFeAuCuSn) at low magnifications at different sample regions. Solid solution nanoparticles are readily achieved via the CTS method.

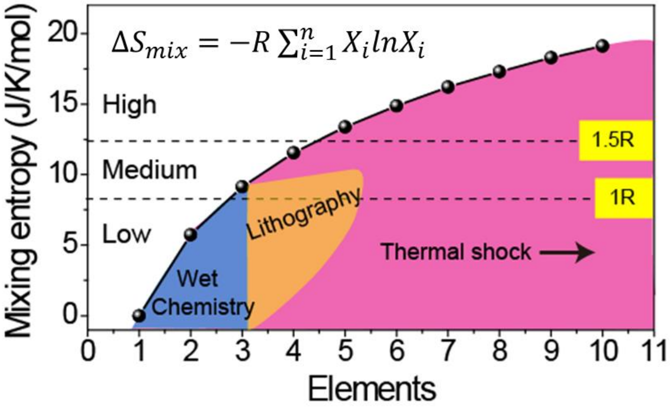

Fig. 10.21. Calculation of configurational entropy of mixing and simple classification of low, medium, and high entropy regions*(16)*. MMNPs synthesized by different methods fall into different entropy regions (based on the classical definition of high entropy alloys).

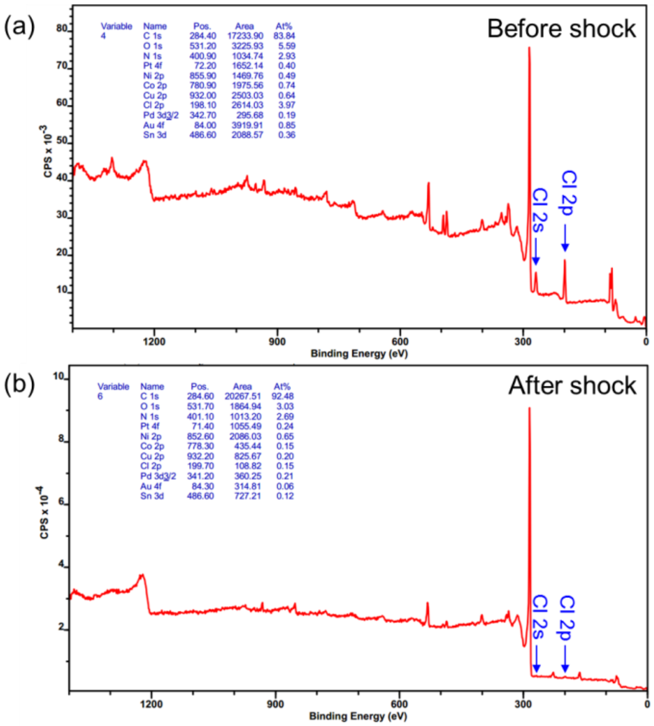

Variable	Name	Pos.	Area	At%
4	C 1s	284.40	17233.90	83.84
	O 1s	531.20	3225.93	5.59
	N 1s	400.90	1034.74	2.93
	Pt 4f	72.20	1652.14	0.40
	Ni 2p	855.90	1469.76	0.49
	Co 2p	780.90	1975.56	0.74
	Cu 2p	932.00	2503.03	0.64
	Cl 2p	198.10	2614.03	3.97
	Pd 3d3/2	342.70	295.68	0.19
	Au 4f	84.00	3919.91	0.85
	Sn 3d	486.60	2088.57	0.36

Variable	Name	Pos.	Area	At%
6	C 1s	284.60	20267.51	92.48
	O 1s	531.70	1864.94	3.03
	N 1s	401.10	1013.20	2.69
	Pt 4f	71.40	1055.49	0.24
	Ni 2p	852.60	2086.03	0.65
	Co 2p	778.30	435.44	0.15
	Cu 2p	932.20	825.67	0.20
	Cl 2p	199.70	108.82	0.15
	Pd 3d3/2	341.20	360.25	0.21
	Au 4f	84.30	314.81	0.06
	Sn 3d	486.60	727.21	0.12

Fig. 10.22. XPS spectra of 8-element (PtPdCoNiFeAuCuSn) precursor-loaded CNFs (a) before and (b) after the CTS process. The Cl peak becomes negligible after thermal shock as indicated by the arrows. From the fitted ratio, the Cl content dropped from ~4% to 0.15% due to the CTS process.

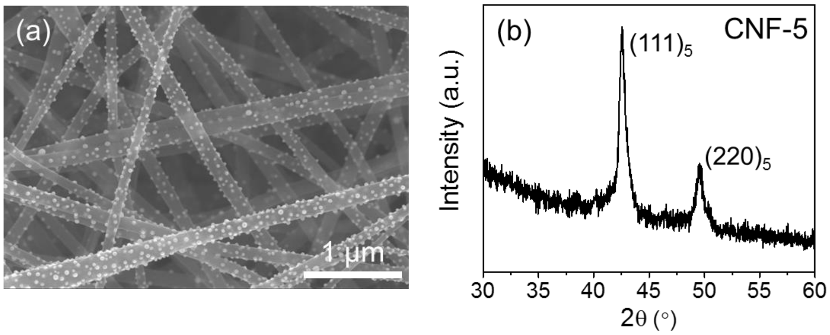

Fig. 10.23. (a) SEM and (b) XRD pattern of quinary HEA-NPs (PtPdCoNiFe) on CNFs.

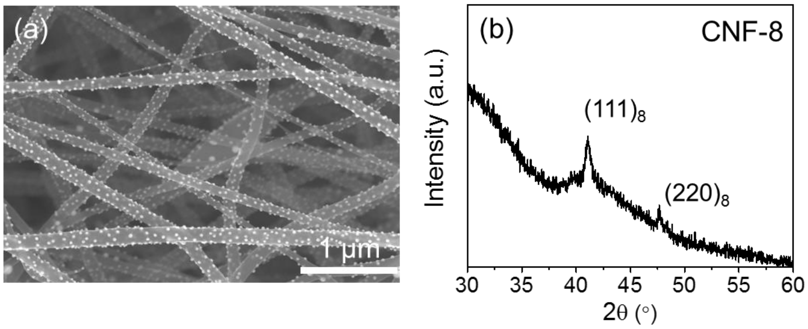

Fig. 10.24. (a) SEM image and (b) XRD pattern of octonary HEA-NPs (PtPdCoNiFeAuCuSn) on CNFs. Similar to quinary HEA-NPs, the microscopy and x-ray results prove uniformity in terms of particle dispersion and structure.

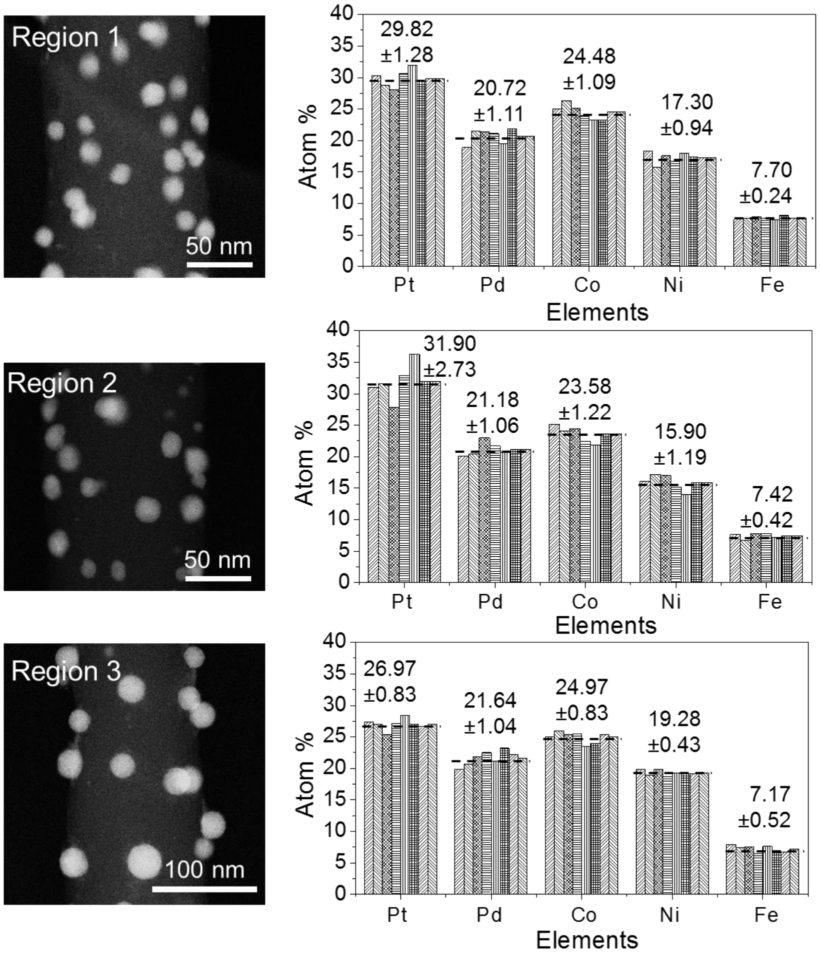

Fig. 10.25. Atomic percentage distributions for quinary HEA-NPs (PtPdCoNiFe) at different sample regions. The variations for each element is roughly below 10%.

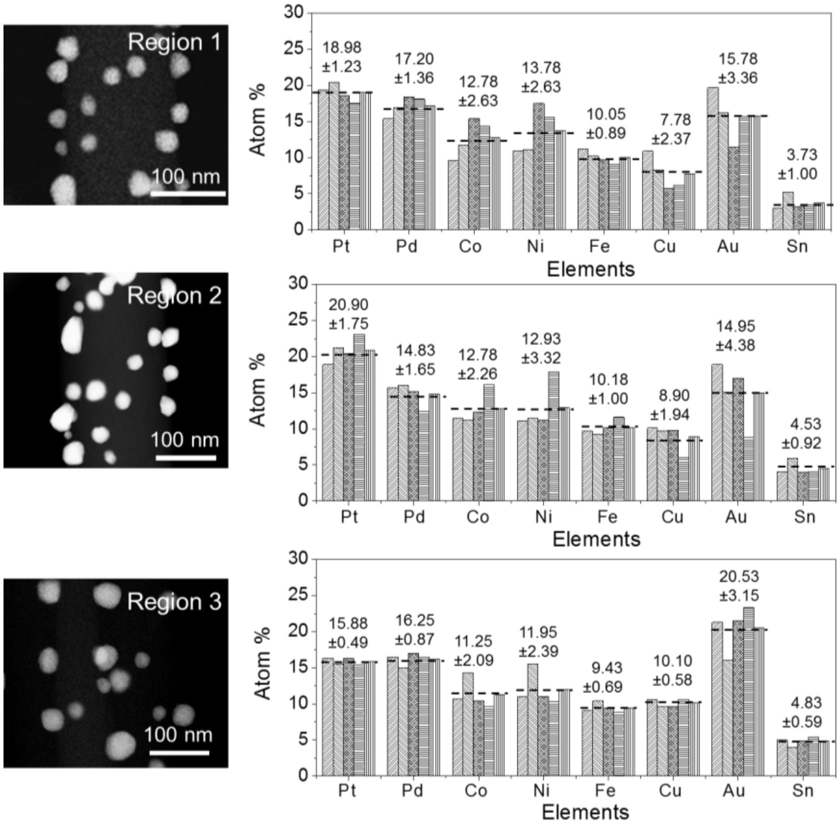

Fig. 10.26. Atomic percentage distributions for quinary HEA-NPs (PtPdCoNiFe) at different sample regions, which confirms the compositional uniformity among nanoparticles synthesized by CTS.

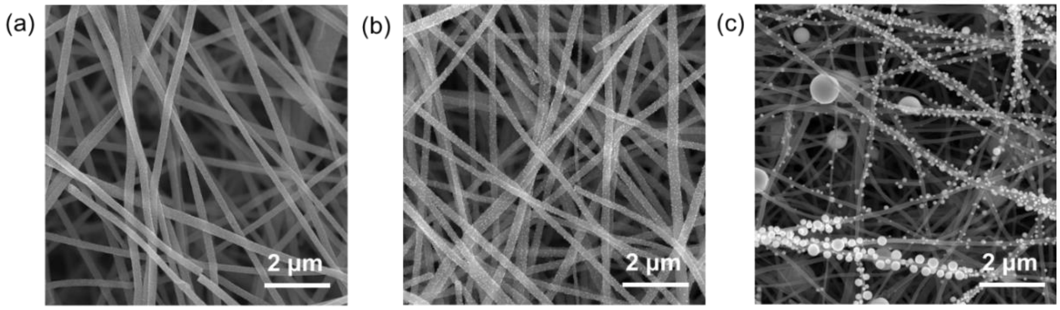

Fig. 10.27. Synthesized nanoparticles on CNFs with different defect concentrations (control experiments). (a-c) SEM images of AuNi nanoparticles on CNF films carbonized at 873 K, 1073 K, and 1273 K, respectively.

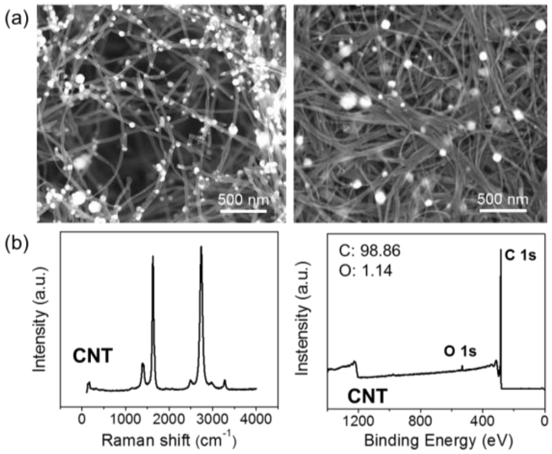

Fig. 10.28. Role of defects in nanoparticle dispersion on CNTs as a control experiment. (a) AuNi NPs on crystalline CNTs, showing only aggregates due to the lack of defects. (b) Defect characterization for CNTs by Raman and XPS spectra. Note that crystalline CNTs barely disperse metals via the CTS method.

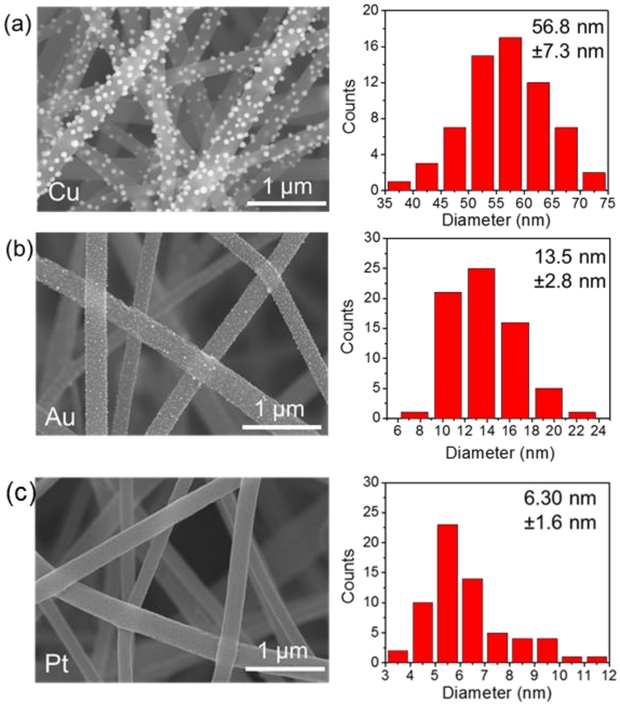

Fig. 10.29. SEM images of the metallic nanoparticle dispersions on CNFs using the same CTS synthesis conditions: (a) Cu, (b) Au, and (c) Pt. Although Au and Cu have similar physical properties, the particle size distributions achieved through the same CTS process are vastly different, which indicates a particle dispersion mechanism related to the individual metal species (i.e. catalytic activity).

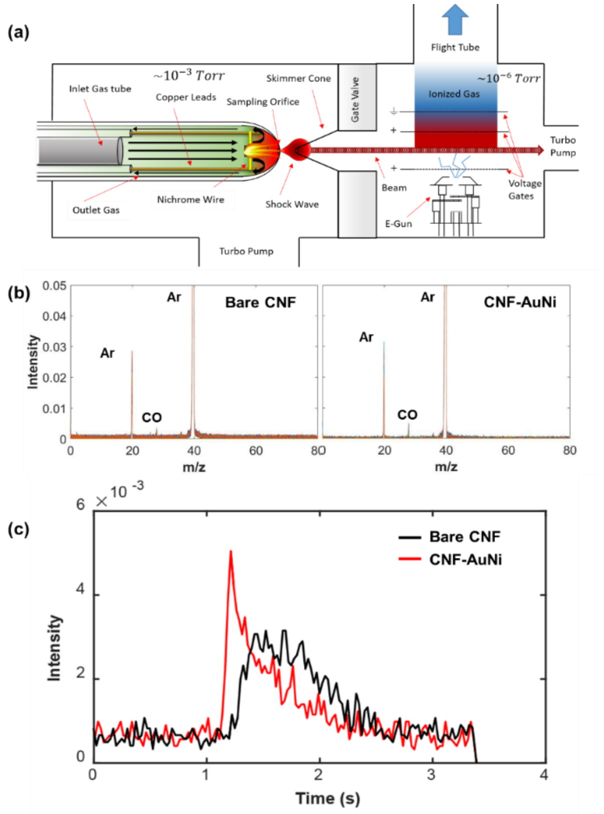

Fig. 10.30. (a) Experimental setup and Molecular Beam Mass Spectrometer. (b) The full mass spectrum obtained during a 55 ms CTS for bare CNF and CNF-AuNi. (c) Temporal CO emission profiles for bare CNF and CNF-AuNi. The CNF-AuNi sample shows a sharp peak in terms of CO release compared to bare CNF, which demonstrates a catalytic carbon metabolism (C+O*=CO↑) reaction occurs during the CTS process.

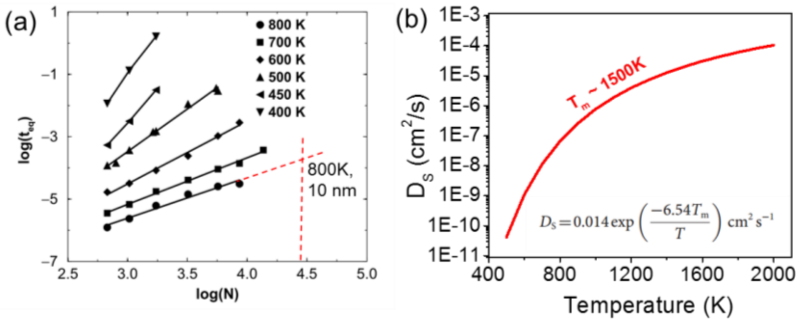

Fig. 10.31. (a) Log-log plot showing relaxation time (t_{eq}) as a function of the crystallite size (N is the number of atoms) at different temperatures. (b) Estimation of temperature-dependent surface diffusivity for metals with a melting temperature of ~1500 K. The inset equation is used for estimation, where Ds is the diffusivity, Tm is the melting point, and T is temperature.

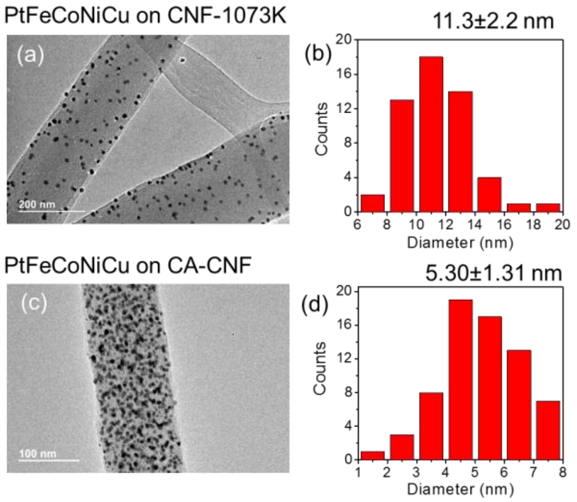

Fig. 10.32. (a)-(b) TEM and size distribution of PtFeCoNiCu on CNFs. (c)-(d) TEM and size distribution of PtFeCoNiCu on CO_2-activated CNFs (CA-CNFs).

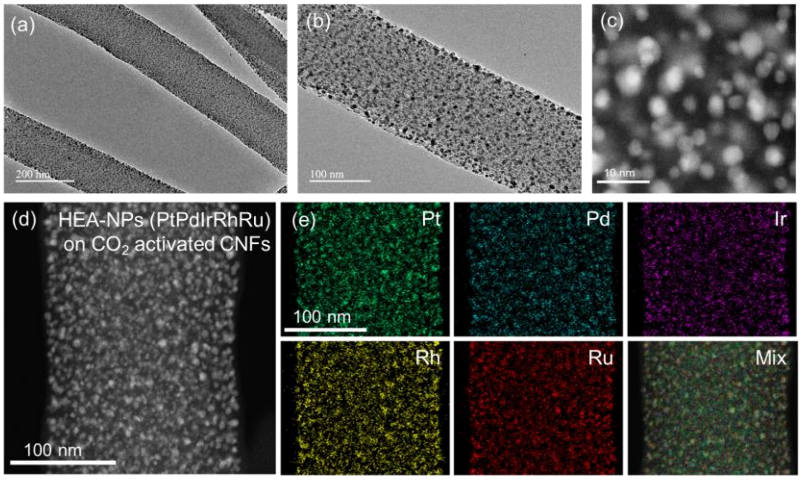

Fig. 10.33. (a)-(c) TEM and HAADF images of quinary HEA-NPs (PtPdIrRhRu) on CA-CNFs. (d)-(e) STEM elemental maps of the same quinary nanoparticle composition on CA-CNFs, showing a uniform distribution and formation of HEA-NPs.

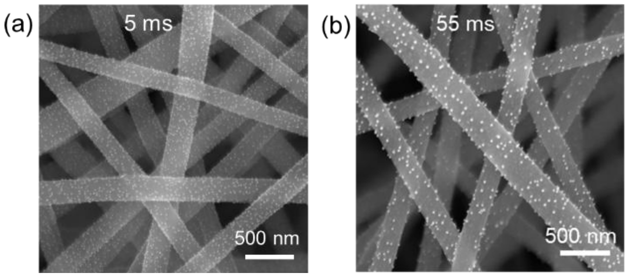

Fig. 10.34. Shock time-dependent size distributions of synthesized nanoparticles by CTS. AuNi nanoparticles formed by a (a) 5 ms and (b) 55 ms CTS process, respectively.

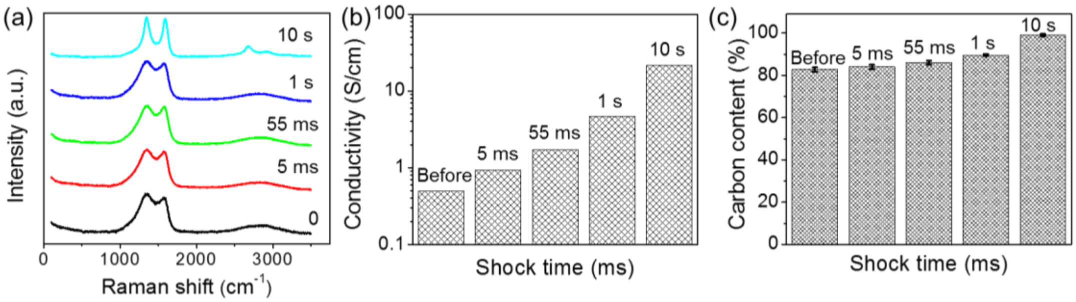

Fig. 10.35. Defect concentrations of CNFs after various shock durations. (a-c) Raman spectra, conductivity measurements and changes in carbon content for CNF-PtNi films after 5 ms, 55 ms, 1 s, and 10 s CTS processes.

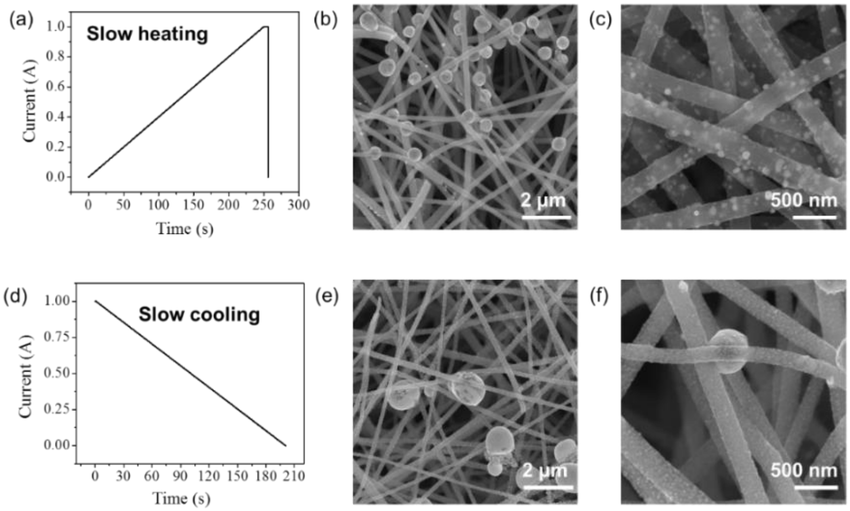

Fig. 10.36. Synthesized nanoparticles by slow heating and cooling rates (control experiments). (a-c) Slow heating profile (10 K/s) and SEM images of the CNF-AuNi system via a slow heating rate. (d-f) Slow cooling profile (10 K/s) and SEM images of the CNF-AuNi using a slow cooling rate.

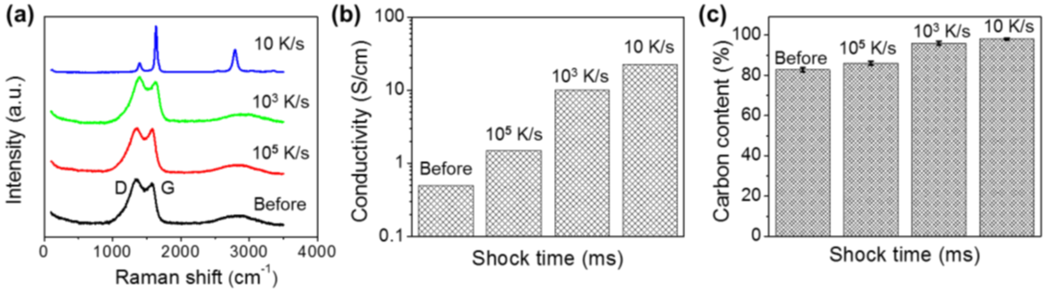

Fig. 10.37. The properties of CNF films exposed to different cooling rates. (a) Raman spectra, (b) conductivity measurements, and (c) the change in carbon content for CNF-AuNi at 10^5 K/s, 10^3 K/s, and 10 K/s cooling rates.

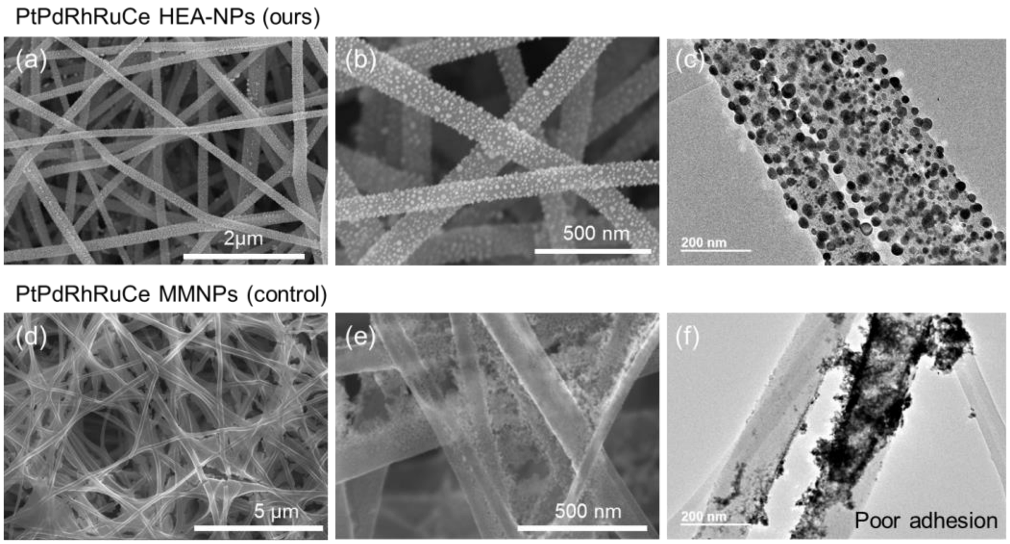

Fig. 10.38. (a)-(b) SEM and (c) TEM images of HEA-NPs synthesized by our CTS method; (d)-(e) SEM and (f) TEM images of MMNPs by the wet impregnation method. Our HEA-NPs show excellent particle formation, dispersion, and adhesion on the CNF support. However, the control sample merely reduced the precursor in situ without exhibiting particle dispersive capabilities.

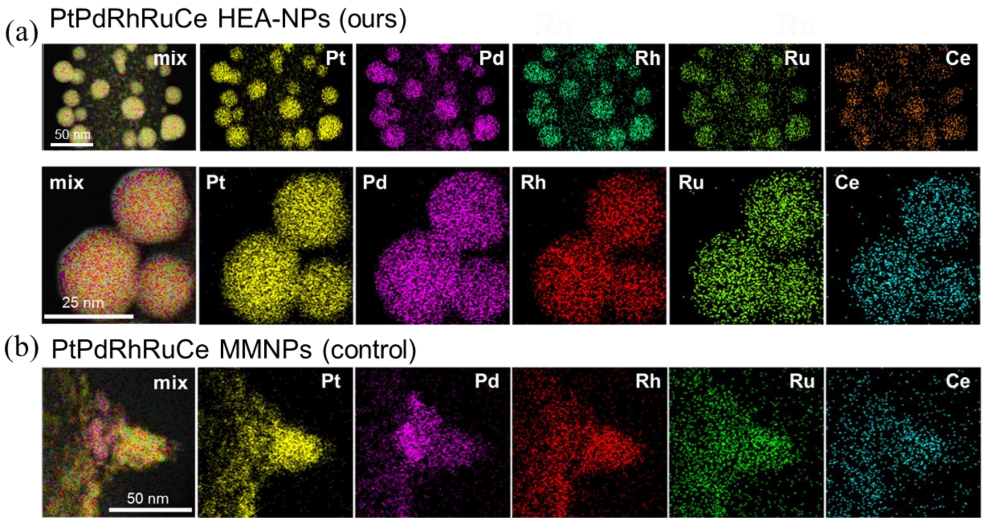

Fig. 10.39. STEM elemental maps for (a) PtPdRhRuCe HEA-NPs and (b) PtPdRhRuCe MMNPs (control). Our HEA-NPs exhibit uniform elemental distribution within the solid-solution nanoparticles. However, the control sample exhibits phase/elemental separation/segregation especially between Pt and Pd due to the slow, low-temperature reduction procedure.

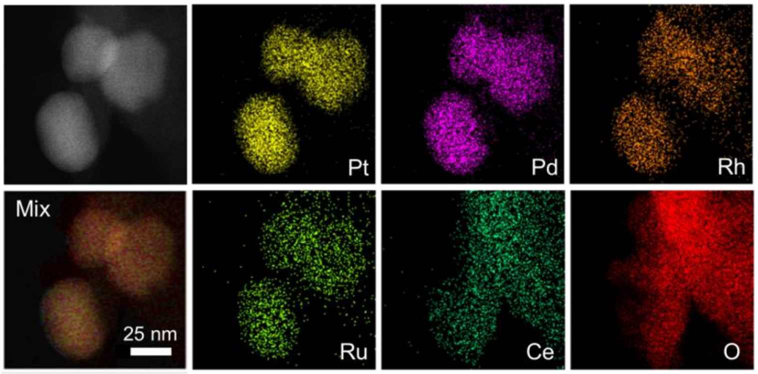

Fig. 10.40. STEM elemental maps of quinary PtPdRhRuCe HEA-NPs after catalytic reaction. The nanoparticles retain their original high entropy solid solution structure, which demonstrates the structural stability of HEA-NPs at high temperature to resist thermo-driven phase separation.

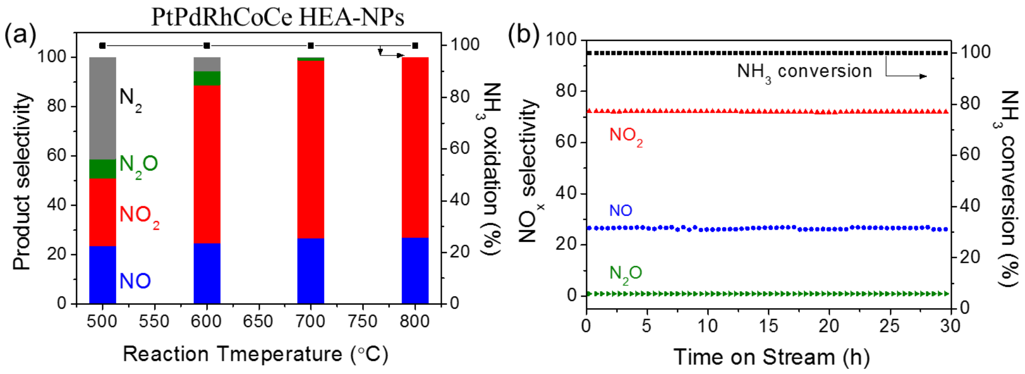

Fig. 10.41. Catalytic application of inexpensive quinary HEA-NPs (PtPdRhCoCe) for ammonia oxidation: (a) Temperature-dependent product distribution (left) and conversion (right) of NH_3 oxidation for the HEA-NP sample; (b) time-dependent catalytic performance of PtPdRhCoCe HEA-NPs at 700°C.

Table 10.1. Physi-chemical properties of the elemental precursor salts used and corresponding metals.

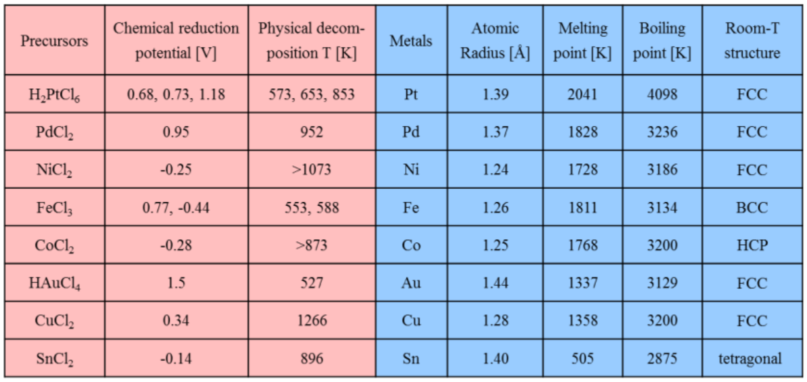

Precursors	Chemical reduction potential [V]	Physical decom-position T [K]	Metals	Atomic Radius [Å]	Melting point [K]	Boiling point [K]	Room-T structure
H_2PtCl_6	0.68, 0.73, 1.18	573, 653, 853	Pt	1.39	2041	4098	FCC
$PdCl_2$	0.95	952	Pd	1.37	1828	3236	FCC
$NiCl_2$	-0.25	>1073	Ni	1.24	1728	3186	FCC
$FeCl_3$	0.77, -0.44	553, 588	Fe	1.26	1811	3134	BCC
$CoCl_2$	-0.28	>873	Co	1.25	1768	3200	HCP
$HAuCl_4$	1.5	527	Au	1.44	1337	3129	FCC
$CuCl_2$	0.34	1266	Cu	1.28	1358	3200	FCC
$SnCl_2$	-0.14	896	Sn	1.40	505	2875	tetragonal

Reduction potential relative to standard hydrogen electrode;
FCC: face-centered-cubic; BCC: body-centered-cubic; HCP: hexagonal-close-packing.

Table 10.2. Literature comparison of catalytic ammonia oxidation performance.

Catalysts[a]	NO_x yield (%)	T^b (°C)	Reference
Pt gauze	98	800	[1]
(90-95%) Pt + (5-10%) Rh	94-96	800-950	[2]
90% Pt-5% Pd-5% Rh	96	800-1000	[3]
88% Pt-7% Pd-5% Rh	94	800-1000	[4]
92.4% Pt-4% Pd-3.5% Rh-0.1% Ce	98	900	[5]
81% Pt-15% Pd-3.5% Rh-0.5% Ru	94	900	[6]
21.7% Pt-4.68% Pd-1.3% Rh-0.34% Ru-0.23% Ce	99	700	Current work
17.2% Pt-4.1% Pd-1.1% Rh-4.1% Co-0.7% Ce	>90	600-700	Current work

[a] the composition of different metals were expressed as weight percentages

[1] J. Pérez-Ramírez, E. V. Kondratenko, G. Novell-Leruth, J. M. Ricart, Mechanism of ammonia oxidation over PGM (Pt, Pd, Rh) wires by temporal analysis of products and density functional theory. J. Catal. 261, 217–223 (2009).

[2] J. Pérez-Ramírez, B. Vigeland, Perovskite membranes in ammonia oxidation: Towards process intensification in nitric acid manufacture. Angew. Chemie - Int. Ed. 44, 1112–1115 (2005).

[3] P. A. J. Bagot et al., Oxidation and Surface Segregation Behavior of a Pt-Pd-Rh Alloy Catalyst. J. Phys. Chem. C. 118, 26130–26138 (2014).

[4] L. Xin, H. Yongqiang, J. Husheng, Pt-Rh-Pd Alloy Group Gauze Catalysts Used for Ammonia Oxidation. Rare Met. Mater. Eng. 46, 339–343 (2017).

[5] X. Hu, Y. Ning, L. Chen, Q. Shi, C. Jia, Physical Properties and Application Performance of Platinum-Palladium-Rhodium Alloys Modified with Cerium. Platin. Met. Rev. 56, 40–46 (2012).

[6] E. F. Sutormina et al., Effect of the Reaction Medium on the Physicochemical Properties of the Oxide Monolith Catalyst IK-42-1 for Ammonia Oxidation. Kinet. Catal. 50, 892–898 (2009).

Chapter 11: Thermal shock nanoparticles for applications

11.1 Uniformly dispersed nanoparticles for lithium ion battery[*]

To exploit the high energy density of the lithium (Li) metal battery, it is imperative to address the dendrite growth and interface instability of the anode. 3D hosts for Li metal are expected to suppress the growth of Li dendrites. Heterogeneous seeds are effective in guiding Li deposition and realizing spatial control over Li nucleation. Herein, it shows that ultrafine silver (Ag) nanoparticles, which are synthesized via a novel rapid Joule heating method, can serve as nanoseeds to direct the deposition of Li within the 3D host materials, resolving the problems of the Li metal anode. By optimizing the Joule heating method, ultrafine Ag nanoparticles (≈40 nm) are homogeneously anchored on carbon nanofibers. The Ag nanoseeds effectively reduce the nucleation overpotential of Li and guide the Li deposition in the 3D carbon matrix uniformly, free from the dendrites. A stable and reversible Li metal anode is achieved in virtue of the Ag nanoseeds in the 3D substrate, showing a low overpotential (≈0.025 V) for a long cycle life. The ultrafine nanoseeds achieved by rapid Joule heating render uniform deposition of Li metal anode in 3D hosts, promising a safe and long-life Li metal battery for high-energy applications.

---

[*] The results in this chapter have been published: Yang, C.; Yao, Y.; He, S.; Xie, H.; Hitz, E.; Hu, L. Ultrafine Silver Nanoparticles for Seeded Lithium Deposition toward Stable Lithium Metal Anode. Adv. Mater. 2017, 29, 1702714. Yang, C. and Yao, Y. contributed equally.

11.2 Uniformly dispersed nanoparticles for lithium-oxygen battery[*]

The lithium–air (Li–O_2) battery has been deemed one of the most promising next-generation energy-storage devices due to its ultrahigh energy density. However, in conventional porous carbon–air cathodes, the oxygen gas and electrolyte often compete for transport pathways, which limit battery performance. Here, a novel textile-based air cathode is developed with a triple-phase structure to improve overall battery performance. The hierarchical structure of the conductive textile network leads to decoupled pathways for oxygen gas and electrolyte: oxygen flows through the woven mesh while the electrolyte diffuses along the textile fibers. Due to noncompetitive transport, the textile-based Li–O_2 cathode exhibits a high discharge capacity of 8.6 mAh cm^{-2}, a low overpotential of 1.15 V, and stable operation exceeding 50 cycles. The textile-based structure can be applied to a range of applications (fuel cells, water splitting, and redox flow batteries) that involve multiple phase reactions. The reported decoupled transport pathway design also spurs potential toward flexible/wearable Li–O_2 batteries.

---

[*] The results in this chapter have been published: Xu, S.; Yao, Y.; Guo, Y.; Zeng, X.; Lacey, S. D.; Song, H.; Chen, C.; Li, Y.; Dai, J.; Wang, Y.; *et al.* Textile Inspired Lithium-Oxygen Battery Cathode with Decoupled Oxygen and Electrolyte Pathways. *Adv. Mater.* **2018**, *30*, 1704907.

11.3 Rapid thermal annealing for battery interfaces[*]

High-temperature batteries require the battery components to be thermally stable and function properly at high temperatures. Conventional batteries have high-temperature safety issues such as thermal runaway, which are mainly attributed to the properties of liquid organic electrolytes such as low boiling points and high flammability. In this work, we demonstrate a truly all-solid-state high-temperature battery using a thermally stable garnet solid-state electrolyte, a lithium metal anode, and a V_2O_5 cathode, which can operate well at 100 °C. To address the high interfacial resistance between the solid electrolyte and cathode, a rapid thermal annealing method was developed to melt the cathode and form a continuous contact. The resulting interfacial resistance of the solid electrolyte and V2O5 cathode was significantly decreased from 2.5 × 104 to 71 $\Omega\cdot cm^2$ at room temperature and from 170 to 31 $\Omega\cdot cm^2$ at 100 °C. Additionally, the diffusion resistance in the V2O5 cathode significantly decreased as well. The demonstrated high-temperature solid-state full cell has an interfacial resistance of 45 $\Omega\cdot cm^2$ and 97% Coulombic efficiency cycling at 100 °C. This work provides a strategy to develop high-temperature all-solid-state batteries using garnet solid electrolytes and successfully addresses the high contact resistance between the V_2O_5 cathode and garnet solid electrolyte without compromising battery safety or performance.

---

[*] The results in this chapter have been published: Liu, B.; Fu, K.; Gong, Y.; Yang, C.; Yao, Y.; Wang, Y.; Wang, C.; Kuang, Y.; Pastel, G.; Xie, H.; et al. Rapid Thermal Annealing of Cathode-Garnet Interface toward High-Temperature Solid State Batteries. *Nano Lett.* **2017**, 17, 4917–4923.

Chapter 12: Scalable nanomanufacturing

We have carried out additional experiments in order to justify the scalability of the reported CTS method for the synthesis of nanoparticles, especially HEA-NPs. The improvements in terms of substrates (e.g. 3D wood-based carbon) and scalable, rapid radiative heating methods are not exclusive. A further potential of the CTS method can be envisioned as long as the merits of the process remain intact.

12.1. Features of the CTS method and its potential scalability:

Our rapid, high-temperature carbo-thermal shock method offers promise in terms of scalable NP synthesis. A typical synthesis procedure consists of two steps (Fig. 12.1):

(i) Solution-based salt precursors are conformally coated on the carbon surface. Specifically, we have identified certain solvents (e.g. ethanol) for dispersing salts that lead to enhanced wettability on carbon and overall, a more uniform dispersion of precursors. Experiments also show that the same precursor salts used months later yielded similar nanoparticle sizes, compositions, and structures. Thus the precursor solutions can be recycled (important for industrial manufacturing) and exhibit reproducibility in terms of the synthesized nanoparticles.

(ii) The precursor-loaded carbon film is then Joule heated to ~2000 K rapidly followed by fast quenching. Uniformly distributed NPs are formed *in situ* on the carbon surface. The entire process takes ~ 55 milliseconds with a high quenching rate of ~10^5 K/s.

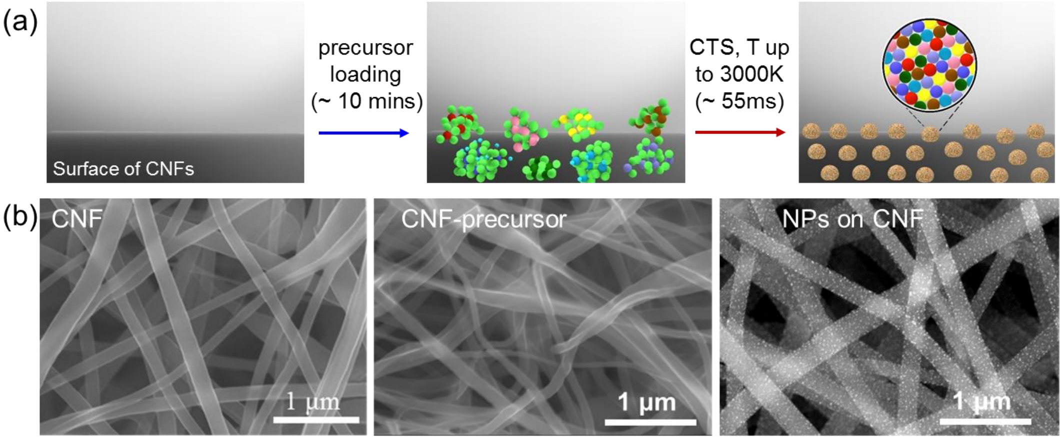

Fig. 12.1. (a) A typical CTS process has two steps: (1) precursor loading (in minutes) followed by (2) high temperature shock (55 ms) generates copious amounts of HEA-NPs on carbon substrates. (b) SEM images of CNFs, precursor loaded CNFs, and CNFs with uniformly distributed nanoparticles.

From a manufacturing point of view, the CTS method has the following advantages:

- Step 1 (precursor loading) is completely scalable; Step 2 is fast (only 55 ms) and thus, comparable with roll-to-roll processes.
- The process can be done with 3D substrates with a much higher loading of precursors; in this case, a high yield of NPs can be produced.
- The maximum temperature (up to 3000K) is much higher than the decomposition temperature of nearly any metal salt, which can lead to "mixing" of many types of metals.
- The tunable cooling rates (up to 10^5 K/s) are capable of producing both phase-separated structures (slow cooling) and high entropy solid solution structures (rapid quenching).
- The ratio of different metals can be easily controlled by tuning the amount of each precursor on the carbon substrate.

- The fabrication process shows universality, i.e. the same setup can be used to synthesize NPs with different compositions by altering the precursors deposited on the carbon substrate.
- The *in situ* formed NPs on carbon supports have direct applications. As a proof of concept, we have demonstrated these NPs as excellent catalysts for hydrogen evolution, oxygen evolution, hydroperoxide oxidation, ammonia oxidation etc as shown in the previous chapters.

The scalability of our method for synthesizing MMNPs or HEA-NPs is outstanding. We hope to compare with lithography-based methods (the only reported method to synthesize MMNPs (up to 5 elements) to date) directly to our unique CTS method. In the previous report, nanoparticles composed of up to 5 elements (AuAgCuCoNi) were synthesized by using scanning-probe block copolymer lithography. Multi-tip patterning can speed up the production of nanoparticles however, this method is very limited in terms of its capabilities:

(i) Requires advanced equipment: advanced probe lithography;

(ii) Synthesis time: takes several days due to particle patterning followed by thermal annealing (>48 h) and reduction (>12 h);

(iii) Particle density/distribution: $\sim 1/\mu m^2$ on a 2D flat surface;

(iv) Compositions and structures: up to 5 element compositions are possible however, only equilibrium structures can be achieved due to the slow annealing process;

The comparison between methods is summarized in Table 12.1. Therefore, our CTS method shows orders of magnitude improvements in terms of NP production efficiency, scalability and structural possibilities (both solid solution & phase-separated structures can be achieved).

Table 12.1. Scalability comparison between probe copolymer lithography and CTS.

Comparison of Synthesis and Scalability

	Lithography-based (Science 2016)	**Carbo-thermal shock (CTS, this work)**
Equipment	Advanced probe lithography	Electrical power supply
Synthesis	Step I. Patterning: minutes to hours Step II. 1st step reduction: 120°C, 48 h Step III. 2nd step reduction: 500°C, 12 h	Step I: Precursor loading (in minutes) Step II: One-step thermal shock: 1500 K~2000 K, 55 milliseconds
Density	• ~1/μm^2 pattern density • Pattern on extremely flat 2D plate only	• >> 10^4/μm^2 in 1μm^2 • Any (1D, 2D, 3D) carbon surfaces
Nanoparticles	• Up to 5 elements • Only equilibrium structures	• Demonstrated to 8 elements • Both equilibrium and metastable structures
Final product	• ~1/μm^2 particles on Si wafer • No applications were demonstrated	• Nanoparticles anchored on carbon • Directly used for applications

12.2. Extension of our CTS method to 3D bulk substrates

When a 3D carbon support is used, a much higher mass loading of precursors can be achieved, which leads to a 100-fold increase in HEA-NP production. For this purpose, we chose carbonized wood (Fig. 12.2) due to the following advantages:

(1) Wood-based carbon has a unique microstructure with open channels through the thickness direction (above 500 μm), which enables rapid and uniform precursor loading throughout the wood sample.

(2) The open channels are connected horizontally by the sidewall pits, which leads to 3D interconnected pathways for gas diffusion.

(3) Wood is low cost and the most abundant biomass.

The low tortuosity and interconnected structure ensure a uniform loading of precursors throughout the wood, which results in uniform particle deposition. Quinary HEA-NPs (PtPdRhRuCe) were synthesized within the wood and demonstrated as a high-performance catalyst for ammonia oxidation. As shown by the SEM images (Fig.

12.2), nanoparticles are uniformly distributed throughout the wood sample. This finding was determined by checking several spots on the carbonized wood samples along the thickness direction. It is apparent that uniform nanoparticle sizes and distributions are achieved throughout the 3D substrate by CTS. Thus, the wood carbon substrate substantially increased the effective particle loading and production.

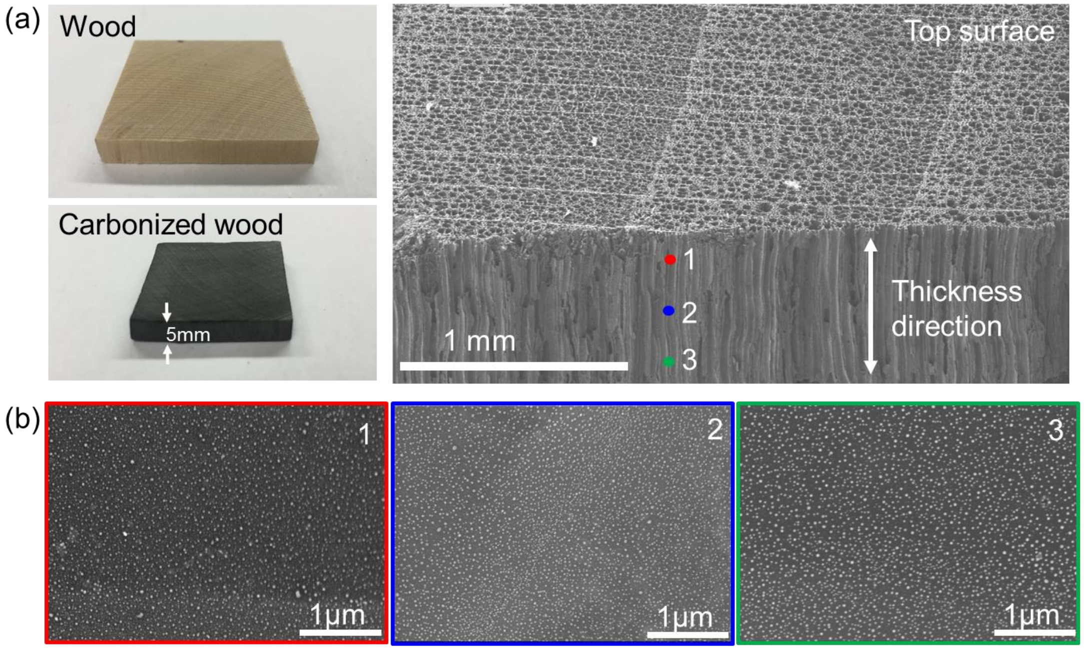

Fig. 12.2. Carbonized wood as a 3D substrate to increase the NP production of our CTS method. (a) Digital images of both wood and carbonized wood, and an SEM image of carbonized wood. The SEM images exhibit the unique microstructure of the wood sample: open microsized pores on the top surface and vertically-aligned microsized channels in the thickness direction. (b) SEM images of uniformly distributed nanoparticles in three different locations as noted in (a).

When the thickness of the wood carbon increases from 500 μm to 5000 μm (5 mm), the precursor loading increases from 60 μmol/cm^2 to 600 μmol/cm^2, respectively (Fig. 12.3). Consequently, the amount of synthesized nanoparticles on the wood carbon is ~10 mg/cm^2 and ~100 mg/cm^2, which corresponds to a 10-fold and 100-fold increase compared to the CNF films (6 μmol/cm^2 and ~1 mg/cm^2). We also acquired STEM elemental maps to confirm the high entropy mixing of these HEA-NPs synthesized within the wood substrate. Note that all 5 elements are uniformly distributed throughout the synthesized nanoparticles (Fig. 12.3b). This is similar to the HEA-NPs synthesized on CNFs *via* the CTS method that shows high entropy mixing (Fig. 12.3c). Thus, regardless of the conductive substrate, high entropy mixing structures can be readily achieved. In short, we have effectively increased the production of nanoparticles by 100-fold by replacing the 2D CNF film with a 3D carbonized wood substrate without sacrificing nanoparticle quality.

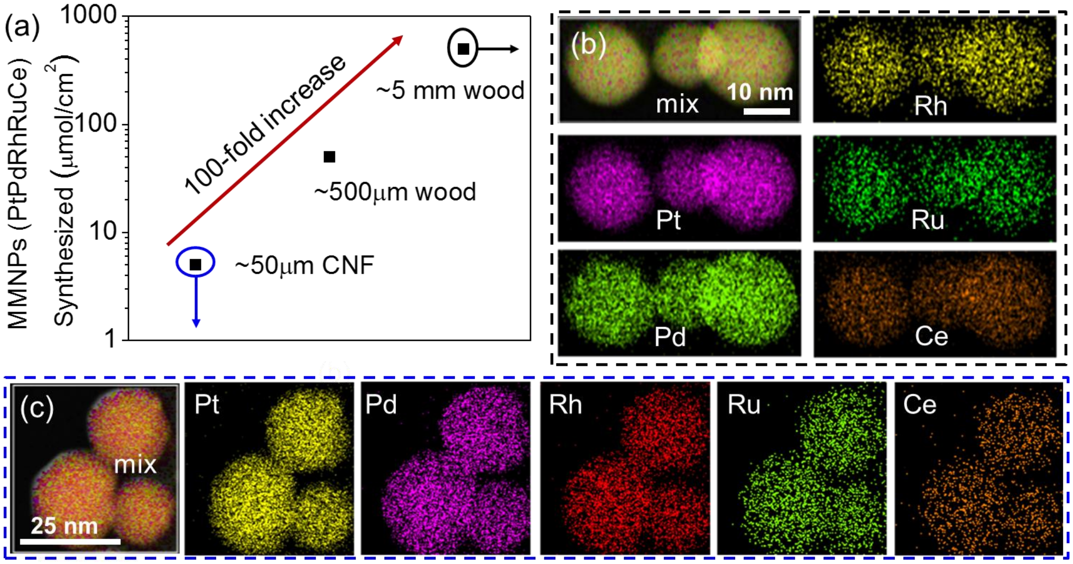

Fig. 12.3. Increased MMNPs loading on carbonized wood samples. (a) The areal loading increased from 6 μmol/cm^2 for the CNF film to 60-600 μmol/cm^2 for the carbonized wood substrate. This corresponds to a ~10X (~10 mg/cm^2) and ~100X (~100 mg/cm^2) increase in NP production compared to the CNF films. STEM elemental maps for quinary HEA-NPs (PtPdRhRuCe) prepared on (b) carbonized wood and (c) carbon nanofibers, respectively. Each HEA-NP is a uniformly mixed high entropy structure, indicating the nanoparticle quality is not compromised in during scale up.

12.3. Extension of the CTS method to rapid radiation heating

The essence of the CTS method for NPs synthesis is three-fold: (1) high temperature, (2) short duration and (3) fast quenching. While electrical Joule heating is an ideal strategy for precise control over temperature, duration and cooling rate, other rapid heating strategies (radiative heating, aerosol-spray, microwave heating, *etc.*) are also possible as long as the merits of the CTS method are maintained. Specifically, all methods should minimize the high temperature duration.

The CTS method itself can be extended to rapid radiative heating for scalable/continuous manufacturing by eliminating electrode and contact fabrication, which is normally required for the Joule heating process. We envision roll-to-roll manufacturing of nanoparticles on a carbon support can be achieved through radiation-based heating (Fig. 12.4a). The precursor loading can be easily achieved through a "coating-drying" method. As the moving film passes through the heating zone, it experiences the thermal shock in a similar manner to the Joule heating process. Rapid heating (or thermal shock duration) can be controlled by the sample transfer process through the hot zone. Specifically, the duration is a function of heating zone length and sample transfer speed ($\mathrm{t = L/v}$), which are parameters that can be easily controlled on an assembly line.

As a proof of concept, Pt nanoparticles can be synthesized through rapid radiative heating of a CNF film using a radiative heating source (Fig. 12.4b-f). The CNF film loaded with salt precursors was placed on top of a carbon felt which is heated to high temperature *via* Joule heating for 1 second and then quenched. Instead of directly heating the sample *via* Joule heating, the CNF film experienced rapid radiative heating using a heating source positioned below the substrate. Densely populated nanoparticles were synthesized *in situ* on both sides of the film (thickness of ~30 μm), which indicates the effectiveness of radiation-based heating as well as the good thermal conduction of the CNF networks (Fig. 12.4e-f).

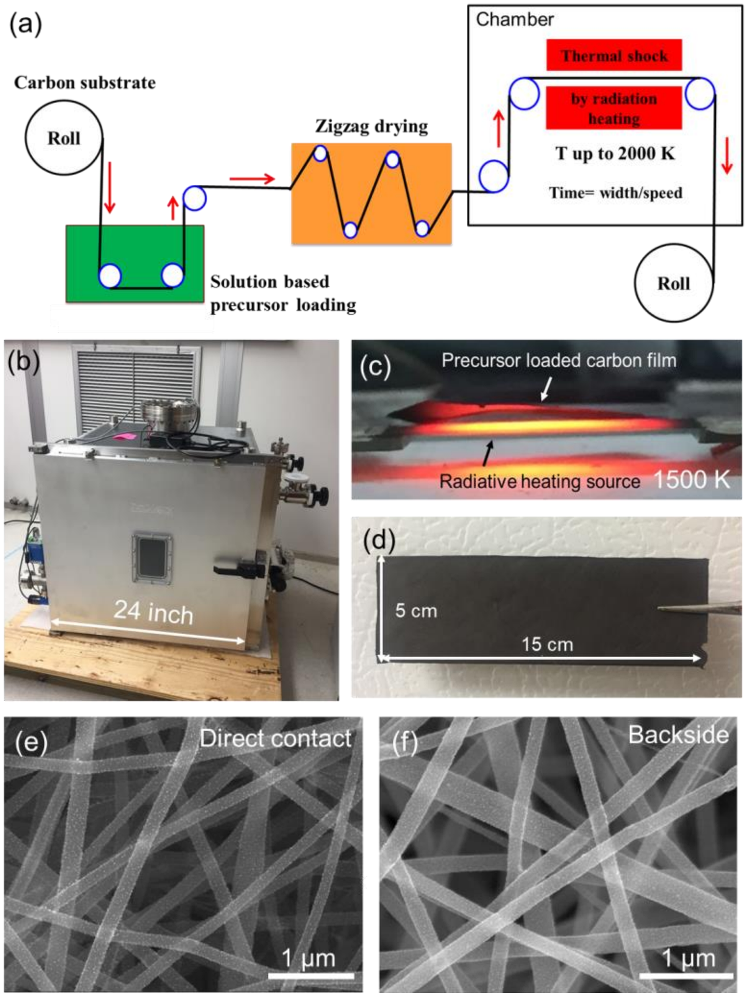

Fig. 12.4. (a) Continuous roll-to-roll manufacturing schematic of a carbon-metallic NP composite by rapid radiative heating. (b) A custom-built chamber to simulate a small-scale, roll-to-roll process located within Dr. Hu's lab at the University of Maryland, College Park. (c) To mimic the roll-to-roll process by radiation-based heating, the precursor-loaded carbon substrate was placed above the radiative heating source for ~1s at ~1500K. (d) The NP-loaded carbon film synthesized by radiation-based heating (i.e. scalable CTS). SEM image of Pt NPs synthesized by radiative heating on a ~30 μm thick CNF film: (e) direct contact and (f) backside.

Chapter 13: Discussion and conclusion

13.1 Summary

In this thesis, we have focused on the study of high temperature engineering on nanomaterials toward scalable nanomanufacturing. It is found that the electrical triggered Joule heating acts as a new route for high temperature processing of nanomaterials owing to the following features: (1) highly and precisely controllable temperature through programmable electrical input; (2) directly and localized heating of the materials leading to exceptionally high temperature (up to 3000 K) and extreme heating/cooling rate (~10^5 K/s), which enables the study of nanomaterials under these extreme conditions (ultrahigh temperature and ultrafast heating/cooling); (3) Joule heating is directly applied onto the object itself and ~90% of input energy is effectively converted into Joule heat for heating, making the process highly effective and economic for scalable nanomanufacturing. According to these features of Joule heating, we have achieved the following for the first time:

We developed highly stable and controllable high temperature heating sources for microscale/nanoscale heating, and studied the related high temperature lighting and heating phenomena. The heating sources are based on carbon-based (nano)materials that can be in 1D fiber, 2D sheets/films, or 3D printed structures. Stable high temperature (3000 K) and ultrafast heating rate (10^5 K/s) were achieved in these heating sources which is critical for later in materials processing. Compared with other heating sources, such as furnace, laser, and infrared radiation, the heaters based on Joule heating of carbon-based (nano)materials have the following distinct advantages: (1) higher temperature up to 3000 K and fast heating/cooling rates; (2) arbitrary shape design with small sizes and onto different substrates to enable heating anywhere. The stable and controllable heaters for the first time provide a facile strategy for controllable and localized heating and are essential for high temperature engineering of nanomaterials which requires extreme heating capability.

The extremely high temperature engineering is applied to carbon-based nanomaterials for ultrahigh temperature annealing (>2500 K in ~20 minutes). In the carbon nanofibers, the high temperature efficiently graphitizes the carbon materials with improved crystallinity and fewer defects. Importantly, the rapid heating (~100 K/min) is capable of fast annealing and lead to carbon welding in CNFs at junctions, namely, these CNFs are fused together for adjacent CNFs. The welded-CNFs shows greatly improved conductivity and mechanical properties as a result of forming 3D interconnected CNFs structure, addressing the poor interface problems in many carbon-based nanomaterials. In the carbon nanotubes, we continue to apply ultrahigh temperature annealing to weld crystalline CNTs together by incorporating a thin layer of the polymer as the welder to form 3D interconnected structures, defined as an “epitaxial welding” process. The pristine individual CNTs were connected by the thin polymer shell on CNTs; after high temperature annealing, these polymer shells were in situ converted into the graphitic shell using the embedded CNTs as growth templates. The final 3D CNTs shows enhanced conductivity and mechanical properties by addressing the poor interface problems. The high temperature annealing not only helps remove the defects in carbon-based nanomaterials, but also bring these nanomaterials together into an interconnected structure, which is critical to transfer their excellent properties at the nanoscale to macroscopic scale and used in devices and products.

The extremely high temperature engineering is also applied to metal salt loaded carbon substrates for ultrafast thermal shock (~2000 K in 55 ms). The rapid thermal shock method (RTS) can *in-situ* synthesize ultrasmall, well-dispersed nanoparticles on carbon matrix from metal precursor salts. Metal salts decompose rapidly at such high temperatures and nucleate into well-dispersed metallic nanoparticles during the rapid cooling step (cooling rate of ~10^5 K/s). These ultrafine, well-dispersed nanoparticles on conductive substrates can be utilized directly for catalytic reactions. In addition, by simply varying the salt precursor into different salt mixtures, we synthesized bimetallic, multimetallic and high entropy alloy nanoparticles containing up to 8 different and immiscible elements. The high temperature is well above the decomposition temperatures of salt precursors and even above their melting point, therefore, leading to the atomic mixing at high temperature (liquid alloy state). Rapid quenching (rate of ~10^5 K/s) freezes the completely mixed state to form solid solution nanoparticles with a narrow size distribution. This is for the first time synthesizing of HEA-NPs enabled by the unique high temperature shock method which combines the merits of high temperature and rapid quenching. The HEA-NPs exhibit highly improved catalytic performances for ammonia oxidation compared with phase-separated counterparts.

The high temperature engineering methods proposed in this thesis are highly facile, efficient, and reliable towards scalable nanomanufacturing. We also developed methods to further speed up or extend these processes. For example, thermal shock of 3D carbonized wood structure enables synthesis of nanoparticles in a 3D bulk structure with 100x increase in particle production efficiency. Also, by employing non-contact radiative heating, large-scale substrates can be easily incorporated (either conductive or non-conductive substrate), and a continuous roll-to-roll production process is possible for the rapid synthesis of various nanoparticles and nanostructures, pushing the synthesis capability further.

13.2 Future directions

The above results have successfully demonstrated that new structures and improved properties can be achieved for those nanomaterials with proper selection of high temperature engineering protocols, either ultrahigh temperature annealing for the interface engineering of carbon-based nanomaterials, or ultrafast thermal shock for the synthesis of well-dispersed nanoparticles. The current thesis serves as the preliminary explorations of using (extreme) high temperature engineering protocols on nanomaterials and the current results are enormous and profound. It is my strong believe that high temperature engineering of nanomaterials is just the beginning and more are waiting to be explored.

In the following research, the following topics are of interests: (1) expand high temperature engineering methods to more nanomaterials, such as semiconductors, composites, and so on; (2) understanding of the mechanisms involved in the high temperature engineering processes; and (3) process optimization and establishing toward scalable manufacturing.

Bibliography

(1) Donega, M. *Nanoparticles*; de Mello Donegá, C., Ed.; Springer Berlin Heidelberg: Berlin, Heidelberg, 2014.

(2) Yoffe, A. D. Low-Dimensional Systems: Quantum Size Effects and Electronic Properties of Semiconductor Microcrystallites (Zero-Dimensional Systems) and Some Quasi-Two-Dimensional Systems. *Adv. Phys.* **1993**, *42*, 173–262.

(3) Unruh, K. M.; Huber, T. E.; Huber, C. A. Melting and Freezing Behavior of Indium Metal in Porous Glasses. *Phys. Rev. B* **1993**, *48*, 9021–9027.

(4) Edwards, P. P.; Johnston, R. L.; Rao, C. N. R. On the Size-Induced Metal-Insulator Transition in Clusters and Small Particles. *Met. Clust. Chem.* **1999**, 1454–1481.

(5) Roduner, E. Size Matters: Why Nanomaterials Are Different. *Chem. Soc. Rev.* **2006**, *35*, 583.

(6) Jackson, M. J. *Micro-and Nanomanufacturing*; Springer, 2007.

(7) *Triennial Review of the National Nanotechnology Initiative*; National Academies Press: Washington, D.C., 2016.

(8) Geim, A. K.; Novoselov, K. S. The Rise of Graphene. *Nat. Mater.* **2007**, *6*, 183–191.

(9) Paris, O. *Structure and Multiscale Mechanics of Carbon*; 2014.

(10) Law, M.; Kind, H.; Messer, B.; Kim, F.; Yang, P. Transparent, Conductive Carbon Nanotube Films. *Science (80-.).* **2004**, *305*, 1273–1276.

(11) Zhang, D.; Ryu, K.; Liu, X.; Polikarpov, E.; Ly, J.; Tompson, M. E.; Zhou, C. Transparent, Conductive, and Flexible Carbon Nanotube Films and Their Application in Organic Light-Emitting Diodes. *Nano Lett.* **2006**, *6*, 1880–1886.

(12) Marinho, B.; Ghislandi, M.; Tkalya, E.; Koning, C. E.; de With, G. Electrical Conductivity of Compacts of Graphene, Multi-Wall Carbon Nanotubes, Carbon Black, and Graphite Powder. *Powder Technol.* **2012**, *221*, 351–358.

(13) Park, J.; Joo, J.; Soon, G. K.; Jang, Y.; Hyeon, T. Synthesis of Monodisperse Spherical Nanocrystals. *Angew. Chemie - Int. Ed.* **2007**, *46*, 4630–4660.

(14) Buffat, P.; Borel, J. P. Size Effect on the Melting Temperature of Gold Particles. *Phys. Rev. A* **1976**, *13*, 2287–2298.

(15) Kwon, S. G.; Hyeon, T. Colloidal Chemical Synthesis and Formation Kinetics of Uniformly Sized Nanocrystals of Metals, Oxides, and Chalcogenides. *Acc. Chem. Res.* **1696**, *41*.

(16) Carbone, L.; Cozzoli, P. D. Colloidal Heterostructured Nanocrystals: Synthesis and Growth Mechanisms. *Nano Today* **2010**, *5*, 449–493.

(17) Donegá, C. de M. Synthesis and Properties of Colloidal Heteronanocrystals. *Chem. Soc. Rev.* **2011**, *40*, 1512–1546.

(18) Kim, Y. S. Y. D.; Kim, H.; Cho, Y.; Ryoo, J. H.; Park, C.-H.; Kim, P.; Kim, Y. S. Y. D.; Lee, S. W. S.; Li, Y.; Park, S.-N.; *et al.* Bright Visible Light Emission from Graphene. *Nat. Nanotechnol.* **2015**, *10*, 1–7.

(19) Yu, D.; Dai, L. Voltage-Induced Incandescent Light Emission from Large-Area Graphene Films. *Appl. Phys. Lett.* **2010**, *96*, 2010–2012.

(20) Savvatimskiy, A. I. Measurements of the Melting Point of Graphite and the Properties of Liquid Carbon (a Review for 1963-2003). *Carbon N. Y.* **2005**, *43*, 1115–1142.

(21) Wei, J.; Zhu, H.; Wu, D.; Wei, B. Carbon Nanotube Filaments in Household Light Bulbs. *Appl. Phys. Lett.* **2004**, *84*, 4869–4871.

(22) Mann, D.; Kato, Y. K.; Kinkhabwala, A.; Pop, E.; Cao, J.; Wang, X.; Zhang, L.; Wang, Q.; Guo, J.; Dai, H. Electrically Driven Thermal Light Emission from Individual Single-Walled Carbon Nanotubes. *Nat. Nanotechnol.* **2007**, *2*, 33–38.

(23) Ferrari, A. C.; Basko, D. M. Raman Spectroscopy as a Versatile Tool for Studying the Properties of Graphene. *Nat. Nanotechnol.* **2013**, *8*, 235–246.

(24) Chen, Y.; Fu, K.; Zhu, S.; Luo, W.; Wang, Y.; Li, Y.; Hitz, E.; Yao, Y.; Dai, J.; Wan, J.; *et al.* Reduced Graphene Oxide Films with Ultrahigh Conductivity as Li-Ion Battery Current Collectors. *Nano Lett.* **2016**, *16*, 3616–3623.

(25) Yao, Y.; Fu, K. K.; Yan, C.; Dai, J.; Chen, Y.; Wang, Y.; Zhang, B.; Hitz, E.; Hu, L. Three-Dimensional Printable High-Temperature and High-Rate Heaters. *ACS Nano* **2016**, *10*, 5272–5279.

(26) Aruna, S. T.; Mukasyan, A. S. Combustion Synthesis and Nanomaterials. *Curr. Opin. Solid State Mater. Sci.* **2008**, *12*, 44–50.

(27) DeLisio, J. B.; Yi, F.; LaVan, D. A.; Zachariah, M. R. High Heating Rate Reaction Dynamics of Al/CuO Nanolaminates by Nanocalorimetry-Coupled Time-of-Flight Mass Spectrometry. *J. Phys. Chem. C* **2017**, *121*, 2771–2777.

(28) Xu, Y.; Liu, Q.; Zhu, Y.; Liu, Y.; Langrock, A.; Zachariah, M. R.; Wang, C. Uniform Nano-Sn/C Composite Anodes for Lithium Ion Batteries. *Nano Lett.* **2013**, *13*, 470–474.

(29) Roth, P. Particle Synthesis in Flames. *Proc. Combust. Inst.* **2007**, *31 II*, 1773–1788.

(30) Tavadze, G. F.; Shteinberg, A. S. *Production of Advanced Materials by Methods of Self-Propagating High-Temperature Synthesis*; 2013.

(31) Li, C.; Zhang, X.; Wang, K.; Sun, X.; Liu, G.; Li, J.; Tian, H.; Li, J.; Ma, Y. Scalable Self-Propagating High-Temperature Synthesis of Graphene for Supercapacitors with Superior Power Density and Cyclic Stability. *Adv. Mater.* **2016**, 1604690.

(32) Kumar, A.; Mukasyan, A. S.; Wolf, E. E. Combustion Synthesis of Ni, Fe and Cu Multi-Component Catalysts for Hydrogen Production from Ethanol Reforming. *Appl. Catal. A Gen.* **2011**, *401*, 20–28.

(33) González-Cortés, S. L.; Imbert, F. E. Fundamentals, Properties and Applications of Solid Catalysts Prepared by Solution Combustion Synthesis (SCS). *Appl. Catal. A Gen.* **2013**, *452*, 117–131.

(34) Egan, G. C.; Lagrange, T.; Zachariah, M. R. Time-Resolved Nanosecond Imaging of Nanoscale Condensed Phase Reaction. *J. Phys. Chem. C* **2015**, *119*, 2792–2797.

(35) Dinka, P.; Mukasyan, A. S. In Situ Preparation of Oxide-Based Supported Catalysts by Solution Combustion Synthesis. *J. Phys. Chem. B* **2005**, *109*, 21627–21633.

(36) Bao, W.; Pickel, A. D.; Zhang, Q.; Chen, Y.; Yao, Y.; Wan, J.; Fu, K.; Wang, Y.; Dai, J.; Zhu, H.; *et al.* Flexible, High Temperature, Planar Lighting with Large Scale Printable Nanocarbon Paper. *Adv. Mater.* **2016**, *28*, 4684–4691.

(37) Neuer, G. Spectral and Total Emissivity Measurements of Highly Emitting

Materials. *Int. J. Thermophys.* **1995**, *16*, 257–265.
(38) Xin, G.; Yao, T.; Sun, H.; Scott, S. M.; Shao, D.; Wang, G.; Lian, J. Highly Thermally Conductive and Mechanically Strong Graphene Fibers. *Science (80- .).* **2015**, *349*, 1083–1087.
(39) Zhu, Y.; James, D. K.; Tour, J. M. New Routes to Graphene, Graphene Oxide and Their Related Applications. *Advanced Materials*, 2012, *24*, 4924–4955.
(40) Pei, S.; Cheng, H. M. The Reduction of Graphene Oxide. *Carbon N. Y.* **2012**, *50*, 3210–3228.
(41) Bell, L. E. Cooling, Heating, Generating Power, and Recovering Waste Heat with Thermoelectric Systems. *Science* **2008**, *321*, 1457–1461.
(42) Joo, S. H.; Park, J. Y.; Tsung, C. K.; Yamada, Y.; Yang, P.; Somorjai, G. A. Thermally Stable Pt/mesoporous Silica Core-Shell Nanocatalysts for High-Temperature Reactions. *Nat Mater* **2009**, *8*, 126–131.
(43) Jenkins, B.; Mullinger, P. *Industrial and Process Furnaces: Principles, Design and Operation*; Butterworth-Heinemann, 2011.
(44) Qiu, T. Q.; Tien, C. L. Short-Pulse Laser Heating on Metals. *Int. J. Heat Mass Transf.* **1992**, *35*, 719–726.
(45) Qin, Z.; Bischof, J. C. Thermophysical and Biological Responses of Gold Nanoparticle Laser Heating. *Chem. Soc. Rev.* **2012**, *41*, 1191–1217.
(46) Kodama, R.; Norreys, P. a; Mima, K.; Dangor, a E.; Evans, R. G.; Fujita, H.; Kitagawa, Y.; Krushelnick, K.; Miyakoshi, T.; Miyanaga, N.; *et al.* Fast Heating of Ultrahigh-Density Plasma as a Step towards Laser Fusion Ignition. *Nature* **2001**, *412*, 798–802.
(47) Ming, L. Laser Heating in the Diamond Anvil Press up to 2000°C Sustained and 3000°C Pulsed at Pressures up to 260 Kilobars. *Rev. Sci. Instrum.* **1974**, *45*, 1115.
(48) Son, J. M.; Lee, J. H.; Kim, J.; Cho, Y. H. Temperature Distribution Measurement of Au Micro-Heater in Microfluidic Channel Using IR Microscope. *Int. J. Precis. Eng. Manuf.* **2015**, *16*, 367–372.
(49) Kang, J.; Kim, H.; Kim, K. S.; Lee, S. K.; Bae, S.; Ahn, J. H.; Kim, Y. J.; Choi, J. B.; Hong, B. H. High-Performance Graphene-Based Transparent Flexible Heaters. *Nano Lett.* **2011**, *11*, 5154–5158.
(50) Hwang, W. J.; Shin, K. S.; Roh, J. H.; Lee, D. S.; Choa, S. H. Development of Micro-Heaters with Optimized Temperature Compensation Design for Gas Sensors. *Sensors* **2011**, *11*, 2580–2591.
(51) Semancik, S.; Cavicchi, R. E.; Wheeler, M. C.; Tiffany, J. E.; Poirier, G. E.; Walton, R. M.; Suehle, J. S.; Panchapakesan, B.; DeVoe, D. L. Microhotplate Platforms for Chemical Sensor Research. *Sensors Actuators, B Chem.* **2001**, *77*, 579–591.
(52) Marcano, D. C.; Kosynkin, D. V.; Berlin, J. M.; Sinitskii, A.; Sun, Z.; Slesarev, A.; Alemany, L. B.; Lu, W.; Tour, J. M. Improved Synthesis of Graphene Oxide. *ACS Nano* **2010**, *4*, 4806–4814.
(53) Bao, W.; Pickel, A. D.; Zhang, Q.; Chen, Y.; Yao, Y.; Wan, J.; Fu, K.; Wang, Y.; Dai, J.; Zhu, H.; *et al.* Flexible, High Temperature, Planar Lighting with Large Scale Printable Nanocarbon Paper. *Adv. Mater.* **2016**, 4684–4691.
(54) Torrisi, F.; Hasan, T.; Wu, W. P.; Sun, Z. P.; Lombardo, A.; Kulmala, T. S.;

Hsieh, G. W.; Jung, S. J.; Bonaccorso, F.; Paul, P. J.; *et al.* Inkjet-Printed Graphene Electronics. *ACS Nano* **2012**, *6*, 2992–3006.

(55) Dua, V.; Surwade, S. P.; Ammu, S.; Agnihotra, S. R.; Jain, S.; Roberts, K. E.; Park, S.; Ruoff, R. S.; Manohar, S. K. All-Organic Vapor Sensor Using Inkjet-Printed Reduced Graphene Oxide. *Angew. Chemie - Int. Ed.* **2010**, *49*, 2154–2157.

(56) Fu, K.; Wang, Y.; Yan, C.; Yao, Y.; Chen, Y.; Dai, J.; Lacey, S.; Wang, Y.; Wan, J.; Li, T.; *et al.* Graphene Oxide-Based Electrode Inks for 3D-Printed Lithium-Ion Batteries. *Adv. Mater.* **2016**, *28*, 2587–2594.

(57) Zhang, Q.; Zhang, F.; Medarametla, S. P.; Li, H.; Zhou, C.; Lin, D. 3D Printing of Graphene Aerogels. *Small* **2016**, *12*, 1702–1708.

(58) García-T͡On, E.; Barg, S.; Franco, J.; Bell, R.; Eslava, S.; D'Elia, E.; Maher, R. C.; Guitian, F.; Saiz, E. Printing in Three Dimensions with Graphene. *Adv. Mater.* **2015**, *27*, 1688–1693.

(59) Naficy, S.; Jalili, R.; Aboutalebi, S. H.; Gorkin III, R. A.; Konstantinov, K.; Innis, P. C.; Spinks, G. M.; Poulin, P.; Wallace, G. G. Graphene Oxide Dispersions: Tuning Rheology to Enable Fabrication. *Mater. Horizons* **2014**, *1*, 326.

(60) Sun, K.; Wei, T. S.; Ahn, B. Y.; Seo, J. Y.; Dillon, S. J.; Lewis, J. A. 3D Printing of Interdigitated Li-Ion Microbattery Architectures. *Adv. Mater.* **2013**, *25*, 4539–4543.

(61) Kim, J. H.; Chang, W. S.; Kim, D.; Yang, J. R.; Han, J. T.; Lee, G. W.; Kim, J. T.; Seol, S. K. 3D Printing of Reduced Graphene Oxide Nanowires. *Adv. Mater.* **2015**, *27*, 157–161.

(62) Ferrari, A.; Basko, D. Raman Spectroscopy as a Versatile Tool for Studying the Properties of Graphene. *Nat. Nanotechnol.* **2013**, *8*, 235–246.

(63) Dresselhaus, M. S.; Jorio, A.; Hofmann, M.; Dresselhaus, G.; Saito, R. Perspectives on Carbon Nanotubes and Graphene Raman Spectroscopy. *Nano Lett.* **2010**, *10*, 751–758.

(64) Xin, G.; Yao, T.; Sun, H.; Scott, S. M.; Shao, D.; Wang, G.; Lian, J. Highly Thermally Conductive and Mechanically Strong Graphene Fibers. *Science (80-.).* **2015**, *349*, 1083–1087.

(65) Behabtu, N.; Young, C. C.; Tsentalovich, D. E.; Kleinerman, O.; Wang, X.; Ma, A. W. K.; Bengio, E. A.; ter Waarbeek, R. F.; de Jong, J. J.; Hoogerwerf, R. E.; *et al.* Strong, Light, Multifunctional Fibers of Carbon Nanotubes with Ultrahigh Conductivity. *Science (80-.).* **2013**, *339*, 182–186.

(66) Li, D.; Müller, M. B.; Gilje, S.; Kaner, R. B.; Wallace, G. G. Processable Aqueous Dispersions of Graphene Nanosheets. *Nat. Nanotechnol.* **2008**, *3*, 101–105.

(67) Pei, S.; Cheng, H.-M. The Reduction of Graphene Oxide. *Carbon N. Y.* **2012**, *50*, 3210–3228.

(68) Liu, Y.; Xu, Z.; Zhan, J.; Li, P.; Gao, C. Superb Electrically Conductive Graphene Fibers via Doping Strategy. *Adv. Mater.* **2016**, *28*, 7941–7947.

(69) Inagaki, M.; Yang, Y.; Kang, F. Carbon Nanofibers Prepared via Electrospinning. *Adv. Mater.* **2012**, *24*, 2547–2566.

(70) Bauhofer, W.; Kovacs, J. Z. A Review and Analysis of Electrical Percolation

in Carbon Nanotube Polymer Composites. *Compos. Sci. Technol.* **2009**, *69*, 1486–1498.

(71) Lin, Z.; Gui, X.; Gan, Q.; Chen, W.; Cheng, X.; Liu, M.; Zhu, Y.; Yang, Y.; Cao, A.; Tang, Z. In-Situ Welding Carbon Nanotubes into a Porous Solid with Super-High Compressive Strength and Fatigue Resistance. *Sci. Rep.* **2015**, *5*, 11336.

(72) Shan, C. S.; Zhao, W. J.; Lu, X. L.; O'Brien, D. J.; Li, Y. P.; Cao, Z. Y.; Elias, A. L.; Cruz-Silva, R.; Terrones, M.; Wei, B. Q.; *et al.* Three-Dimensional Nitrogen-Doped Multiwall Carbon Nanotube Sponges with Tunable Properties. *Nano Lett.* **2013**, *13*, 5514–5520.

(73) Fu, Y.; Carlberg, B.; Lindahl, N.; Lindvall, N.; Bielecki, J.; Matic, A.; Song, Y.; Hu, Z.; Lai, Z.; Ye, L.; *et al.* Templated Growth of Covalently Bonded Three-Dimensional Carbon Nanotube Networks Originated from Graphene. *Adv. Mater.* **2012**, *24*, 1576–1581.

(74) Ding, M.; Sorescu, D. C.; Kotchey, G. P.; Star, A. Welding of Gold Nanoparticles on Graphitic Templates for Chemical Sensing. *J. Am. Chem. Soc.* **2012**, *134*, 3472–3479.

(75) Hashim, D. P.; Narayanan, N. T.; Romo-Herrera, J. M.; Cullen, D. A.; Hahm, M. G.; Lezzi, P.; Suttle, J. R.; Kelkhoff, D.; Muñoz-Sandoval, E.; Ganguli, S.; *et al.* Covalently Bonded Three-Dimensional Carbon Nanotube Solids via Boron Induced Nanojunctions. *Sci. Rep.* **2012**, *2*, 363.

(76) Kim, K. H.; Oh, Y.; Islam, M. F. Graphene Coating Makes Carbon Nanotube Aerogels Superelastic and Resistant to Fatigue. *Nat. Nanotechnol.* **2012**, *7*, 562–566.

(77) Du, J.; Cheng, H.-M. The Fabrication, Properties, and Uses of Graphene/Polymer Composites. *Macromol. Chem. Phys.* **2012**, *213*, 1060–1077.

(78) Zhao, C.; Wang, C.; Gorkin, R.; Beirne, S.; Shu, K.; Wallace, G. G. Three Dimensional (3D) Printed Electrodes for Interdigitated Supercapacitors. *Electrochem. Commun* **2014**, *41*, 20–23.

(79) Poelma, R. H.; Morana, B.; Vollebregt, S.; Schlangen, E.; Van Zeijl, H. W.; Fan, X.; Zhang, G. Q. Tailoring the Mechanical Properties of High-Aspect-Ratio Carbon Nanotube Arrays Using Amorphous Silicon Carbide Coatings. *Adv. Funct. Mater.* **2014**, *24*, 5737–5744.

(80) Shan, C. S.; Zhao, W. J.; Lu, X. L.; O'Brien, D. J.; Li, Y. P.; Cao, Z. Y.; Elias, A. L.; Cruz-Silva, R.; Terrones, M.; Wei, B. Q.; *et al.* Three-Dimensional Nitrogen-Doped Multiwall Carbon Nanotube Sponges with Tunable Properties. *Nano Lett.* **2013**, *13*, 5514–5520.

(81) Kim, K. H.; Oh, Y.; Islam, M. F. Graphene Coating Makes Carbon Nanotube Aerogels Superelastic and Resistant to Fatigue. *Nat. Nanotechnol.* **2012**, *7*, 562–566.

(82) Bradford, P. D.; Wang, X.; Zhao, H.; Zhu, Y. T. Tuning the Compressive Mechanical Properties of Carbon Nanotube Foam. *Carbon N. Y.* **2011**, *49*, 2834–2841.

(83) Zhao, W.; Li, Y.; Wang, S.; He, X.; Shang, Y.; Peng, Q.; Wang, C.; Du, S.; Gui, X.; Yang, Y.; *et al.* Elastic Improvement of Carbon Nanotube Sponges by

Depositing Amorphous Carbon Coating. *Carbon N. Y.* **2014**, *76*, 19–26.

(84) Brieland-Shoultz, A.; Tawfick, S.; Park, S. J.; Bedewy, M.; Maschmann, M. R.; Baur, J. W.; Hart, a. J. Scaling the Stiffness, Strength, and Toughness of Ceramic-Coated Nanotube Foams into the Structural Regime. *Adv. Funct. Mater.* **2014**, *24*, 5728–5735.

(85) Romo-Herrera, J. M.; Terrones, M.; Terrones, H.; Dag, S.; Meunier, V. Covalent 2D and 3D Networks from 1D Nanostructures: Designing New Materials. *Nano Lett.* **2007**, *7*, 570–576.

(86) Park, S.-J. *Carbon Fibers*; Springer, 2015.

(87) Zhang, L.; Aboagye, A.; Kelkar, A.; Lai, C.; Fong, H. A Review: Carbon Nanofibers from Electrospun Polyacrylonitrile and Their Applications. *J. Mater. Sci.* **2014**, *49*, 463–480.

(88) Cho, C.-W.; Cho, D.-H.; Ko, Y.-G.; Kwon, O.-H.; Kang, I.-K. Stabilization, Carbonization, and Characterization of PAN Precursor Webs Processed by Electrospinning Technique. *Carbon Lett.* **2007**, *8*, 313–320.

(89) Plimpton, S. Fast Parallel Algorithms for Short-Range Molecular Dynamics. *J. Comput. Phys.* **1995**, *117*, 1–19.

(90) Saha, B.; Schatz, G. C. Carbonization in Polyacrylonitrile (PAN) Based Carbon Fibers Studied by ReaxFF Molecular Dynamics Simulations. *J. Phys. Chem. B* **2012**, *116*, 4684–4692.

(91) Strachan, A.; van Duin, A. C. T.; Chakraborty, D.; Dasgupta, S.; Goddard III, W. A. Shock Waves in High-Energy Materials: The Initial Chemical Events in Nitramine RDX. *Phys. Rev. Lett.* **2003**, *91*, 98301.

(92) Wang, Y.; Serrano, S.; Santiago-Aviles, J. J. Conductivity Measurement of Electrospun PAN-Based Carbon Nanofiber. *J. Mater. Sci. Lett.* **2002**, *21*, 1055–1057.

(93) Peng, H. Aligned Carbon Nanotube/polymer Composite Films with Robust Flexibility, High Transparency, and Excellent Conductivity. *J. Am. Chem. Soc.* **2008**, *130*, 42–43.

(94) Panapoy, M.; Dankeaw, A.; Ksapabutr, B.; Technology, I.; Campus, S. P. Electrical Conductivity of PAN-Based Carbon Nanofibers Prepared by Electrospinning Method. *Mater. Sci.* **2008**, *13*, 11–17.

(95) Kim, C.; Yang, K. S.; Kojima, M.; Yoshida, K.; Kim, Y. J.; Kim, Y. A.; Endo, M. Fabrication of Electrospinning-Derived Carbon Nanofiber Webs for the Anode Material of Lithium-Ion Secondary Batteries. *Adv. Funct. Mater.* **2006**, *16*, 2393–2397.

(96) Koerner, H.; Liu, W.; Alexander, M.; Mirau, P.; Dowty, H.; Vaia, R. A. Deformation-Morphology Correlations in Electrically Conductive Carbon Nanotube - Thermoplastic Polyurethane Nanocomposites. *Polymer (Guildf).* **2005**, *46*, 4405–4420.

(97) Skákalová, V.; Dettlaff-Weglikowska, U.; Roth, S. Electrical and Mechanical Properties of Nanocomposites of Single Wall Carbon Nanotubes with PMMA. *Synth. Met.* **2005**, *152*, 349–352.

(98) Sandler, J. K. W.; Kirk, J. E.; Kinloch, I. A.; Shaffer, M. S. P.; Windle, A. H. Ultra-Low Electrical Percolation Threshold in Carbon-Nanotube-Epoxy Composites. *Polymer (Guildf).* **2003**, *44*, 5893–5899.

(99) Behabtu, N.; Young, C. C.; Tsentalovich, D. E.; Kleinerman, O.; Wang, X.; Ma, A. W. K.; Bengio, E. A.; Ter Waarbeek, R. F.; De Jong, J. J.; Hoogerwerf, R. E.; *et al.* Strong, Light, Multifunctional Fibers of Carbon Nanotubes with Ultrahigh Conductivity. *Science (80-.).* **2013**, *339*, 182–186.

(100) Xu, Z.; Sun, H.; Zhao, X.; Gao, C. Ultrastrong Fibers Assembled from Giant Graphene Oxide Sheets. *Adv. Mater.* **2013**, *25*, 188–193.

(101) Li, Z.; Xu, Z.; Liu, Y.; Wang, R.; Gao, C. Multifunctional Non-Woven Fabrics of Interfused Graphene Fibres. *Nat. Commun.* **2016**, *7*, 13684.

(102) Li, H.; Tao, Y.; Zheng, X.; Luo, J.; Kang, F.; Cheng, H.-M.; Yang, Q.-H. Ultra-Thick Graphene Bulk Supercapacitor Electrodes for Compact Energy Storage. *Energy Environ. Sci.* **2016**.

(103) Zhang, Q.; Huang, J. Q.; Qian, W. Z.; Zhang, Y. Y.; Wei, F. The Road for Nanomaterials Industry: A Review of Carbon Nanotube Production, Post-Treatment, and Bulk Applications for Composites and Energy Storage. *Small* **2013**, *9*, 1237–1265.

(104) Zhou, H.; Zhu, J.; Liu, Z.; Yan, Z.; Fan, X.; Lin, J.; Wang, G.; Yan, Q.; Yu, T.; Ajayan, P. M.; *et al.* High Thermal Conductivity of Suspended Few-Layer Hexagonal Boron Nitride Sheets. *Nano Res.* **2014**, *7*, 1232–1240.

(105) Gong, K.; Du, F.; Xia, Z.; Durstock, M.; Dai, L. Nitrogen-Doped Carbon Nanotube Arrays with High Electrocatalytic Activity for Oxygen Reduction. *Science (80-.).* **2009**, *323*, 760–764.

(106) Kim, Y. D.; Kim, H.; Cho, Y.; Ryoo, J. H.; Park, C.-H.; Kim, P.; Kim, Y. S.; Lee, S.; Li, Y.; Park, S.-N.; *et al.* Bright Visible Light Emission from Graphene. *Nat. Nanotechnol.* **2015**, *10*, 1–7.

(107) Zhao, Y.; Hong, M.; Bonnet Mercier, N.; Yu, G.; Choi, H. C.; Byon, H. R. A 3.5 V Lithium–Iodine Hybrid Redox Battery with Vertically Aligned Carbon Nanotube Current Collector. *Nano Lett.* **2014**, *14*, 1085–1092.

(108) Wang, K.; Luo, S.; Wu, Y.; He, X.; Zhao, F.; Wang, J.; Jiang, K.; Fan, S. Super-Aligned Carbon Nanotube Films as Current Collectors for Lightweight and Flexible Lithium Ion Batteries. *Adv. Funct. Mater.* **2013**, *23*, 846–853.

(109) Lytle, J. C.; Wallace, J. M.; Sassin, M. B.; Barrow, A. J.; Long, J. W.; Dysart, J. L.; Renninger, C. H.; Saunders, M. P.; Brandell, N. L.; Rolison, D. R. The Right Kind of Interior for Multifunctional Electrode Architectures: Carbon Nanofoam Papers with Aperiodic Submicrometre Pore Networks Interconnected in 3D. *Energy Environ. Sci.* **2011**, *4*, 1913.

(110) Palacín, M. R. Recent Advances in Rechargeable Battery Materials: A Chemist’s Perspective. *Chem. Soc. Rev.* **2009**, *38*, 2565–2575.

(111) Magasinski, A.; Dixon, P.; Hertzberg, B.; Kvit, A.; Ayala, J.; Yushin, G. High-Performance Lithium-Ion Anodes Using a Hierarchical Bottom-up Approach. *Nat. Mater.* **2010**, *9*, 353–358.

(112) Armand, M.; Tarascon, J.-M. Building Better Batteries. *Nature* **2008**, *451*, 652–657.

(113) Suo, L.; Borodin, O.; Gao, T.; Olguin, M.; Ho, J.; Fan, X.; Luo, C.; Wang, C.; Xu, K. “Water-in-Salt” electrolyte Enables High-Voltage Aqueous Lithium-Ion Chemistries. *Science (80-.).* **2015**, *350*, 938–943.

(114) Braithwaite, J. W.; Gonzales, A.; Nagasubramanian, G.; Lucero, S. J.; Peebles,

D. E.; Ohlhausen, J. A.; Cieslak, W. R. Corrosion of Lithium-Ion Battery Current Collectors. *J. Electrochem. Soc.* **1999**, *146*, 448–456.

(115) Myung, S.-T.; Hitoshi, Y.; Sun, Y.-K. Electrochemical Behavior and Passivation of Current Collectors in Lithium-Ion Batteries. *J. Mater. Chem.* **2011**, *21*, 9891.

(116) Nautiyal, P.; Embrey, L.; Boesl, B.; Agarwal, A. Multi-Scale Mechanics and Electrical Transport in a Free-Standing 3D Architecture of Graphene and Carbon Nanotubes Fabricated by Pressure Assisted Welding. *Carbon N. Y.* **2017**, *122*, 298–306.

(117) Yao, Y.; Fu, K. K.; Zhu, S.; Dai, J.; Wang, Y.; Pastel, G.; Chen, Y.; Li, T.; Wang, C.; Li, T.; *et al.* Carbon Welding by Ultrafast Joule Heating. *Nano Lett.* **2016**, *16*, 7282–7289.

(118) Endo, M.; Muramatsu, H.; Hayashi, T.; Kim, Y. A.; Van Lier, G.; Charlier, J. C.; Terrones, H.; Terrones, M.; Dresselhaus, M. S. Atomic Nanotube Welders: Boron Interstitials Triggering Connections in Double-Walled Carbon Nanotubes. *Nano Letters,* 2005, *5*, 1099–1105.

(119) Niu, J.; Li, M.; Choi, W.; Dai, L.; Xia, Z. Growth of Junctions in 3D Carbon Nanotube-Graphene Nanostructures: A Quantum Mechanical Molecular Dynamic Study. *Carbon N. Y.* **2014**, *67*, 627–634.

(120) Romo-Herrera, J. M.; Terrones, M.; Terrones, H.; Dag, S.; Meunier, V. Covalent 2D and 3D Networks from 1D Nanostructures: Designing New Materials. *Nano Lett.* **2007**, *7*, 570–576.

(121) Krasheninnikov, A. V; Banhart, F. Engineering of Nanostructured Carbon Materials with Electron or Ion Beams. *Nat. Mater.* **2007**, *6*, 723–733.

(122) Wang, M. S.; Wang, J. Y.; Chen, Q.; Peng, L.-M. Fabrication and Electrical and Mechanical Properties of Carbon Nanotube Interconnections. *Adv. Funct. Mater.* **2005**, *15*, 1825–1831.

(123) Kis, A.; Csányi, G.; Salvetat, J. P.; Lee, T. N.; Couteau, E.; Kulik, A. J.; Benoit, W.; Brugger, J.; Forró, L. Reinforcement of Single-Walled Carbon Nanotube Bundles by Intertube Bridging. *Nat. Mater.* **2004**, *3*, 153–157.

(124) Krasheninnikov, A. V.; Nordlund, K.; Keinonen, J.; Banhart, F. Ion-Irradiation-Induced Welding of Carbon Nanotubes. *Phys. Rev. B - Condens. Matter Mater. Phys.* **2002**, *66*, 1–6.

(125) Terrones, M.; Banhart, F.; Grobert, N.; Charlier, J. C.; Terrones, H.; Ajayan, P. M. Molecular Junctions by Joining Single-Walled Carbon Nanotubes. *Phys. Rev. Lett.* **2002**, *89*, 5–8.

(126) Ozden, S.; Brunetto, G.; Karthiselva, N. S.; Galvão, D. S.; Roy, A.; Bakshi, S. R.; Tiwary, C. S.; Ajayan, P. M. Controlled 3D Carbon Nanotube Structures by Plasma Welding. *Adv. Mater. Interfaces* **2016**, *3*, 1–8.

(127) Li, R.; Gong, W.; He, Q.; Li, Q.; Lu, W.; Zhu, W. Joining Cross-Stacked Carbon Nanotube Architecture with Covalent Bonding. *Appl. Phys. Lett.* **2017**, *110*, 1–5.

(128) Pashkin, E. Y.; Pankov, A. M.; Kulnitskiy, B. A.; Perezhogin, I. A.; Karaeva, A. R.; Mordkovich, V. Z.; Popov, M. Y.; Sorokin, P. B.; Blank, V. D. The Unexpected Stability of Multiwall Nanotubes under High Pressure and Shear Deformation. *Appl. Phys. Lett.* **2016**, *109*, 81904.

(129) Di, J.; Wang, X.; Xing, Y.; Zhang, Y.; Zhang, X.; Lu, W.; Li, Q.; Zhu, Y. T. Dry-Processable Carbon Nanotubes for Functional Devices and Composites. *Small* **2014**, *10*, 4606–4625.

(130) Jiang, K.; Wang, J.; Li, Q.; Liu, L.; Liu, C.; Fan, S. Superaligned Carbon Nanotube Arrays, Films, and Yarns: A Road to Applications. *Adv. Mater.* **2011**, *23*, 1154–1161.

(131) Fu, K.; Yildiz, O.; Bhanushali, H.; Wang, Y.; Stano, K.; Xue, L.; Zhang, X.; Bradford, P. D. Aligned Carbon Nanotube-Silicon Sheets: A Novel Nano-Architecture for Flexible Lithium Ion Battery Electrodes. *Adv. Mater.* **2013**, *25*, 5109–5114.

(132) Xu, M.; Du, F.; Ganguli, S.; Roy, A.; Dai, L. Carbon Nanotube Dry Adhesives with Temperature-Enhanced Adhesion over a Large Temperature Range. *Nat. Commun.* **2016**, *7*, 13450.

(133) Faraji, S.; Yildiz, O.; Rost, C.; Stano, K.; Farahbakhsh, N.; Zhu, Y.; Bradford, P. D. Radial Growth of Multi-Walled Carbon Nanotubes in Aligned Sheets through Cyclic Carbon Deposition and Graphitization. *Carbon N. Y.* **2017**, *111*, 411–418.

(134) Lin, X.; Zhao, W.; Zhou, W.; Liu, P.; Luo, S.; Wei, H.; Yang, G.; Yang, J.; Cui, J.; Yu, R.; *et al.* Epitaxial Growth of Aligned and Continuous Carbon Nanofibers from Carbon Nanotubes. *ACS Nano* **2017**, *11*, 1257–1263.

(135) Chae, H. G.; Newcomb, B. A.; Gulgunje, P. V.; Liu, Y.; Gupta, K. K.; Kamath, M. G.; Lyons, K. M.; Ghoshal, S.; Pramanik, C.; Giannuzzi, L.; *et al.* High Strength and High Modulus Carbon Fibers. *Carbon N. Y.* **2015**, *93*, 81–87.

(136) Gupta, N.; Artyukhov, V. I.; Penev, E. S.; Yakobson, B. I. Carbonization with Misfusion: Fundamental Limits of Carbon-Fiber Strength Revisited. *Adv. Mater.* **2016**, 1–6.

(137) Suo, L.; Han, F.; Fan, X.; Liu, H.; Xu, K.; Wang, C. “Water-in-Salt” Electrolytes Enable Green and Safe Li-Ion Batteries for Large Scale Electric Energy Storage Applications. *J. Mater. Chem. A* **2016**, *4*, 6639–6644.

(138) Wang, D.; Zhu, L.; Chen, J. F.; Dai, L. Liquid Marbles Based on Magnetic Upconversion Nanoparticles as Magnetically and Optically Responsive Miniature Reactors for Photocatalysis and Photodynamic Therapy. *Angew. Chemie - Int. Ed.* **2016**, *55*, 10795–10799.

(139) Luo, Z.; Tan, C.; Zhang, X.; Chen, J.; Cao, X.; Li, B.; Zong, Y.; Huang, L.; Huang, X.; Wang, L.; *et al.* Preparation of Cobalt Sulfide Nanoparticle-Decorated Nitrogen and Sulfur Co-Doped Reduced Graphene Oxide Aerogel Used as a Highly Efficient Electrocatalyst for Oxygen Reduction Reaction. *Small* **2016**, 1–7.

(140) Li, W.; Sheehan, S. W.; He, D.; He, Y.; Yao, X.; Grimm, R. L.; Brudvig, G. W.; Wang, D. Hematite-Based Solar Water Splitting in Acidic Solutions: Functionalization by Mono- and Multilayers of Iridium Oxygen-Evolution Catalysts. *Angew. Chemie - Int. Ed.* **2015**, *54*, 11428–11432.

(141) Zhang, L.; Roling, L. T.; Wang, X.; Vara, M.; Chi, M.; Liu, J.; Choi, S.-I.; Park, J.; Herron, J. A.; Xie, Z.; *et al.* Platinum-Based Nanocages with Subnanometer-Thick Walls and Well-Defined, Controllable Facets. *Science (80-.).* **2015**, *349*, 412–416.

(142) Prieto, G.; Zečević, J.; Friedrich, H.; de Jong, K. P.; de Jongh, P. E. Towards Stable Catalysts by Controlling Collective Properties of Supported Metal Nanoparticles. *Nat. Mater.* **2013**, *12*, 34–39.
(143) Fu, K.; Yao, Y.; Dai, J.; Hu, L. Progress in 3D Printing of Carbon Materials for Energy-Related Applications. *Adv. Mater.* **2017**, *29*.
(144) Eggenhuisen, T. M.; de Jongh, P. E. *Nanoparticles*; de Mello Donegá, C., Ed.; Springer-Verlag Berlin Heidelberg, 2014.
(145) Corma, A.; Garcia, H. Supported Gold Nanoparticles as Catalysts for Organic Reactions. *Chem. Soc. Rev.* **2008**, *37*, 2096–2126.
(146) Mayavan, S.; Jang, H.-S.; Lee, M.-J.; Choi, S. H.; Choi, S.-M. Enhancing the Catalytic Activity of Pt Nanoparticles Using Poly Sodium Styrene Sulfonate Stabilized Graphene Supports for Methanol Oxidation. *J. Mater. Chem. A* **2013**, *1*, 3489.
(147) He, D.; Cheng, K.; Peng, T.; Pan, M.; Mu, S. Graphene/carbon Nanospheres Sandwich Supported PEM Fuel Cell Metal Nanocatalysts with Remarkably High Activity and Stability. *J. Mater. Chem. A* **2013**, *1*, 2126.
(148) Liu, G.; Eichelsdoerfer, D. J.; Rasin, B.; Zhou, Y.; Brown, K. A.; Liao, X.; Mirkin, C. A. Delineating the Pathways for the Site-Directed Synthesis of Individual Nanoparticles on Surfaces. *Proc. Natl. Acad. Sci.* **2013**, *110*, 887–891.
(149) Alvarado, S. R.; Guo, Y.; Ruberu, T. P. A.; Bakac, A.; Vela, J. Photochemical versus Thermal Synthesis of Cobalt Oxyhydroxide Nanocrystals. *J. Phys. Chem. C* **2012**, *116*, 10382–10389.
(150) Zhang, P.; Shao, C.; Zhang, Z.; Zhang, M.; Mu, J.; Guo, Z.; Liu, Y. In Situ Assembly of Well-Dispersed Ag Nanoparticles (AgNPs) on Electrospun Carbon Nanofibers (CNFs) for Catalytic Reduction of 4-Nitrophenol. *Nanoscale* **2011**, *3*, 3357–3363.
(151) Chen, X.; Wu, G.; Chen, J.; Chen, X.; Xie, Z.; Wang, X. Synthesis Of “clean” and Well-Dispersive Pd Nanoparticles with Excellent Electrocatalytic Property on Graphene Oxide. *J. Am. Chem. Soc.* **2011**, *133*, 3693–3695.
(152) McGilvray, K. L.; Decan, M. R.; Wang, D.; Scaiano, J. C. Facile Photochemical Synthesis of Unprotected Aqueous Gold Nanoparticles. *J. Am. Chem. Soc.* **2006**, *128*, 15980–15981.
(153) Fu, G.; Tao, L.; Zhang, M.; Chen, Y.; Tang, Y.; Lin, J.; Lu, T. One-Pot, Water-Based and High-Yield Synthesis of Tetrahedral Palladium Nanocrystal Decorated Graphene. *Nanoscale* **2013**, *5*, 8007–8014.
(154) Pang, X.; He, Y.; Jung, J.; Lin, Z. 1D Nanocrystals with Precisely Controlled Dimensions, Compositions, and Architectures. *Science (80-.).* **2016**, *353*, 1268–1272.
(155) Gilroy, K. D.; Ruditskiy, A.; Peng, H.-C.; Qin, D.; Xia, Y. Bimetallic Nanocrystals: Syntheses, Properties, and Applications. *Chem. Rev.* **2016**, *116*, 10414–10472.
(156) Fan, Z.; Zhang, H. Crystal Phase-Controlled Synthesis, Properties and Applications of Noble Metal Nanomaterials. *Chem. Soc. Rev.* **2016**, *45*, 63–82.
(157) Chen, A.; Ostrom, C. Palladium-Based Nanomaterials: Synthesis and Electrochemical Applications. *Chem. Rev.* **2015**, *115*, 11999–12044.

(158) Chen, H.; Wang, D.; Yu, Y.; Newton, K. A.; Muller, D. A.; Abruña, H.; Disalvo, F. J. A Surfactant-Free Strategy for Synthesizing and Processing Intermetallic Platinum-Based Nanoparticle Catalysts. *J. Am. Chem. Soc.* **2012**, *134*, 18453–18459.

(159) Ganguli, A. K.; Ganguly, A.; Vaidya, S. Microemulsion-Based Synthesis of Nanocrystalline Materials. *Chem. Soc. Rev.* **2010**, *39*, 474–485.

(160) Amendola, V.; Meneghetti, M. Laser Ablation Synthesis in Solution and Size Manipulation of Noble Metal Nanoparticles. *Phys. Chem. Chem. Phys.* **2009**, *11*, 3805–3821.

(161) Jin, Z.; Nackashi, D.; Lu, W.; Kittrell, C.; Tour, J. M. Decoration, Migration, and Aggregation of Palladium Nanoparticles on Graphene Sheets. *Chem. Mater.* **2010**, *22*, 5695–5699.

(162) Gao, Y.; Bando, Y. Carbon Nanothermometer Containing Gallium. *Nature* **2002**, *415*, 599–599.

(163) Gao, Y. H.; Sun, M.; Su, J.; Zhi, C. Y.; Golberg, D.; Bando, Y.; Duan, X. F. Electron-Beam Induced Electric-Hydraulic Expansion in a Silica-Shelled Gallium Microball-Nanotube Structure. *Appl. Phys. Lett.* **2011**, *99*, 1–4.

(164) Chen, Y.; Huang, Y.; Liu, N.; Su, J.; Li, L.; Gao, Y. Fabrication of Nanoscale Ga Balls via a Coulomb Explosion of Microscale Silica-Covered Ga Balls by TEM Electron-Beam Irradiation. *Sci. Rep.* **2015**, *5*, 1–7.

(165) Park, I.; Li, Z. Y.; Pisano, A. P.; Williams, R. S. Selective Surface Functionalization of Silicon Nanowires via Nanoscale Joule Heating. *Nano Lett.* **2007**, *7*, 3106–3111.

(166) Chapter 8 Wetting Properties of Metal/carbon Systems. *Wettability at High Temperatures*, 1999, *Volume 3*, 317–338.

(167) Stern, L.-A.; Feng, L.; Song, F.; Hu, X. Ni 2 P as a Janus Catalyst for Water Splitting: The Oxygen Evolution Activity of Ni 2 P Nanoparticles. *Energy Environ. Sci.* **2015**, *8*, 2347–2351.

(168) Wang, T.; Wang, H.; Chi, X.; Li, R.; Wang, J. Synthesis and Microwave Absorption Properties of Fe-C Nanofibers by Electrospinning with Disperse Fe Nanoparticles Parceled by Carbon. *Carbon N. Y.* **2014**, *74*, 312–318.

(169) Li, W. C.; Comotti, M.; Schüth, F. Highly Reproducible Syntheses of Active Au/TiO2 Catalysts for CO Oxidation by Deposition-Precipitation or Impregnation. *J. Catal.* **2006**, *237*, 190–196.

(170) Xue, Y.; Chen, H.; Yu, D.; Wang, S.; Yardeni, M.; Dai, Q.; Guo, M.; Liu, Y.; Lu, F.; Qu, J.; *et al.* Oxidizing Metal Ions with Graphene Oxide: The in Situ Formation of Magnetic Nanoparticles on Self-Reduced Graphene Sheets for Multifunctional Applications. *Chem. Commun.* **2011**, *47*, 11689.

(171) Deng, J.; Kang, L.; Bai, G.; Li, Y.; Li, P.; Liu, X.; Yang, Y.; Gao, F.; Liang, W. Solution Combustion Synthesis of Cobalt Oxides (Co3O4 and Co3O4/CoO) Nanoparticles as Supercapacitor Electrode Materials. *Electrochim. Acta* **2014**, *132*, 127–135.

(172) Manikandan, A.; Vijaya, J. J.; Mary, J. A.; Kennedy, L. J.; Dinesh, A. Structural, Optical and Magnetic Properties of Fe3O4 Nanoparticles Prepared by a Facile Microwave Combustion Method. *J. Ind. Eng. Chem.* **2014**, *20*, 2077–2085.

(173) Guo, J.; Liu, Q.; Wang, C.; Zachariah, M. R. Interdispersed Amorphous MnOx--Carbon Nanocomposites with Superior Electrochemical Performance as Lithium-Storage Material. *Adv. Funct. Mater.* **2012**, *22*, 803–811.

(174) Chen, Y.; Egan, G. C.; Wan, J.; Zhu, S.; Jacob, R. J.; Zhou, W.; Dai, J.; Wang, Y.; Danner, V. A.; Yao, Y.; *et al.* Ultra-Fast Self-Assembly and Stabilization of Reactive Nanoparticles in Reduced Graphene Oxide Films. *Nat. Commun.* **2016**, *7*, 12332.

(175) Chen, Y.; Li, Y.; Wang, Y.; Fu, K.; Danner, V. A.; Dai, J.; Lacey, S. D.; Yao, Y.; Hu, L. Rapid, in Situ Synthesis of High Capacity Battery Anodes through High Temperature Radiation-Based Thermal Shock. *Nano Lett.* **2016**, *16*, 5553–5558.

(176) Sun, X.; Li, Y. Colloidal Carbon Spheres and Their Core/Shell Structures with Noble-Metal Nanoparticles. *Angew. Chemie - Int. Ed.* **2004**, *43*, 597–601.

(177) Pennycook, S. J. Structure Determination through Z-Contrast Microscopy. *Adv. imaging electron Phys.* **2002**, *123*, 173–206.

(178) Liu, M.; Wang, L.; (Max) Lu, G.; Yao, X.; Guo, L. Twins in Cd1−xZnxS Solid Solution: Highly Efficient Photocatalyst for Hydrogen Generation from Water. *Energy Environ. Sci.* **2011**, *4*, 1372.

(179) Nie, A.; Gan, L.-Y.; Cheng, Y.; Li, Q.; Yuan, Y.; Mashayek, F.; Wang, H.; Klie, R.; Schwingenschlogl, U.; Shahbazian-Yassar, R. Twin Boundary-Assisted Lithium Ion Transport. *Nano Lett.* **2015**, *15*, 610–615.

(180) Chung, H. T.; Won, J. H.; Zelenay, P. Active and Stable Carbon Nanotube/nanoparticle Composite Electrocatalyst for Oxygen Reduction. *Nat. Commun.* **2013**, *4*, 1922.

(181) Shen, Y.; Sun, D.; Yu, L.; Zhang, W.; Shang, Y.; Tang, H.; Wu, J.; Cao, A.; Huang, Y. A High-Capacity Lithium-Air Battery with Pd Modified Carbon Nanotube Sponge Cathode Working in Regular Air. *Carbon N. Y.* **2013**, *62*, 288–295.

(182) Galwey, A. K.; Brown, M. E. *Thermal Decomposition of Ionic Solids: Chemical Properties and Reactivities of Ionic Crystalline Phases*; Elsevier, 1999; Vol. 86.

(183) Chen, P.-C.; Liu, X.; Hedrick, J. L.; Xie, Z.; Wang, S.; Lin, Q.-Y.; Hersam, M. C.; Dravid, V. P.; Mirkin, C. A. Polyememental Nanoparticle Libraries. *Science (80-.).* **2016**, *352*, 1565–1569.

(184) Li, M.; Li, M.; Zhao, Z.; Cheng, T.; Fortunelli, A.; Chen, C.; Yu, R.; Gu, L.; Merinov, B.; Lin, Z.; *et al.* Ultrafine Jagged Platinum Nanowires Enable Ultrahigh Mass Activity for the Oxygen Reduction Reaction. **2016**, *9050*.

(185) Eren, B.; Zherebetskyy, D.; Patera, L. L.; Wu, C. H.; Bluhm, H.; Africh, C.; Wang, L.-W.; Somorjai, G. A.; Salmeron, M. Activation of Cu(111) Surface by Decomposition into Nanoclusters Driven by CO Adsorption. *Science (80-.).* **2016**, *351*, 475–478.

(186) Buck, M. R.; Bondi, J. F.; Schaak, R. E. A Total-Synthesis Framework for the Construction of High-Order Colloidal Hybrid Nanoparticles. *Nat. Chem.* **2011**, *4*, 37–44.

(187) Chen, C.; Kang, Y.; Huo, Z.; Zhu, Z.; Huang, W.; Xin, H. L.; Snyder, J. D.; Li, D.; Herron, J. A.; Mavrikakis, M.; *et al.* Highly Crystalline Multimetallic

Nanoframes with Three-Dimensional Electrocatalytic Surfaces. *Science (80-.).* **2014**, *343*, 1339–1343.

(188) Xiong, Y.; Xia, Y. Shape-Controlled Synthesis of Metal Nanostructures: The Case of Palladium. *Adv. Mater.* **2007**, *19*, 3385–3391.

(189) Wang, X.; Choi, S. Il; Roling, L. T.; Luo, M.; Ma, C.; Zhang, L.; Chi, M.; Liu, J.; Xie, Z.; Herron, J. A.; *et al.* Palladium-Platinum Core-Shell Icosahedra with Substantially Enhanced Activity and Durability towards Oxygen Reduction. *Nat. Commun.* **2015**, *6*, 1–8.

(190) Zhang, H.; Jin, M.; Xiong, Y.; Lim, B.; Xia, Y. Shape-Controlled Synthesis of Pd Nanocrystals and Their Catalytic Applications. *Acc. Chem. Res.* **2013**, *46*, 1783–1794.

(191) Astruc, D.; Boisselier, E.; Ornelas, C. Dendrimers Designed for Functions: From Physical, Photophysical, and Supramolecular Properties to Applications in Sensing, Catalysis, Molecular Electronics, Photonics, and Nanomedicine. *Chem. Rev.* **2010**, *110*, 1857–1959.

(192) Bao, S.; Yang, X.; Luo, M.; Zhou, S.; Wang, X.; Xie, Z.; Xia, Y. Shape-Controlled Synthesis of CO-Free Pd Nanocrystals with the Use of Formic Acid as a Reducing Agent. *Chem. Commun.* **2016**, *52*, 12594–12597.

(193) Yao, Y.; Chen, F.; Nie, A.; Lacey, S. D.; Jacob, R. J.; Xu, S.; Huang, Z.; Fu, K.; Dai, J.; Salamanca-Riba, L.; *et al.* In Situ High Temperature Synthesis of Single-Component Metallic Nanoparticles. *ACS Cent. Sci.* **2017**, *3*, 294–301.

(194) Bao, W.; Pickel, A. D.; Zhang, Q.; Chen, Y.; Yao, Y.; Wan, J.; Fu, K.; Wang, Y.; Dai, J.; Zhu, H.; *et al.* Flexible, High Temperature, Planar Lighting with Large Scale Printable Nanocarbon Paper. *Adv. Mater.* **2016**, *28*, 4684–4691.

(195) Liu, Z.; Wang, Y.; Wang, Z.; Yao, Y.; Dai, J.; Das, S.; Hu, L. Solvo-Thermal Microwave-Powered Two-Dimensional Material Exfoliation. *Chem. Commun.* **2016**, *52*, 5757–5760.

(196) Wu, H. Bin; Xia, B. Y.; Yu, L.; Yu, X.-Y.; Lou, X. W. D. Porous Molybdenum Carbide Nano-Octahedrons Synthesized via Confined Carburization in Metal-Organic Frameworks for Efficient Hydrogen Production. *Nat. Commun.* **2015**, *6*, 6512.

(197) Bu, L.; Zhang, N.; Guo, S.; Zhang, X.; Li, J.; Yao, J.; Wu, T.; Lu, G.; Ma, J. Y.; Su, D.; *et al.* Biaxially Strained PtPb/Pt Core/shell Nanoplate Boosts Oxygen Reduction Catalysis. *Science (80-.).* **2016**, *354*, 1410–1414.

(198) Kwon, S. G.; Krylova, G.; Phillips, P. J.; Klie, R. F.; Chattopadhyay, S.; Shibata, T.; Bunel, E. E.; Liu, Y.; Prakapenka, V. B.; Lee, B.; *et al.* Heterogeneous Nucleation and Shape Transformation of Multicomponent Metallic Nanostructures. *Nat. Mater.* **2015**, *14*, 215–223.

(199) Takahashi, M.; Koizumi, H.; Chun, W.-J.; Kori, M.; Imaoka, T.; Yamamoto, K. Finely Controlled Multimetallic Nanocluster Catalysts for Solvent-Free Aerobic Oxidation of Hydrocarbons. *Sci. Adv.* **2017**, *3*, e1700101.

(200) Huang, X.; Zhao, Z.; Cao, L.; Chen, Y.; Zhu, E.; Lin, Z.; Li, M.; Yan, A.; Zettl, A.; Wang, Y. M.; *et al.* High-Performance Transition Metal – Doped Pt3Ni Octahedra for Oxygen Reduction Reaction. *Science (80-.).* **2015**, *348*, 1230–1234.

(201) Chen, G.; Zhao, Y.; Fu, G.; Duchesne, P. N.; Gu, L.; Zheng, Y.; Weng, X.;

Chen, M.; Zhang, P.; Pao, C.-W.; *et al.* Interfacial Effects in Iron-Nickel Hydroxide-Platinum Nanoparticles Enhance Catalytic Oxidation. *Science (80-.).* **2014**, *344*, 495–499.

(202) Frey, N. A.; Peng, S.; Cheng, K.; Sun, S. Magnetic Nanoparticles: Synthesis, Functionalization, and Applications in Bioimaging and Magnetic Energy Storage. *Chem. Soc. Rev.* **2009**, *38*, 2532.

(203) Cortie, M. B.; McDonagh, A. M. Synthesis and Optical Properties of Hybrid and Alloy Plasmonic Nanoparticles. *Chem. Rev.* **2011**, *111*, 3713–3735.

(204) Reddington, E.; Sapienza, A.; Gurau, B.; Viswanathan, R.; Sarangapani, S.; Smotkin, E. S.; Mallouk, T. E. Combinatorial Electrochemistry: A Highly Parallel, Optical Screening Method for Discovery of Better Electrocatalysts. *Science (80-.).* **1998**, *280*, 1735–1737.

(205) Chen, P. C.; Liu, G.; Zhou, Y.; Brown, K. A.; Chernyak, N.; Hedrick, J. L.; He, S.; Xie, Z.; Lin, Q. Y.; Dravid, V. P.; *et al.* Tip-Directed Synthesis of Multimetallic Nanoparticles. *J. Am. Chem. Soc.* **2015**, *137*, 9167–9173.

(206) Chen, P. C.; Du, J. S.; Meckes, B.; Huang, L.; Xie, Z.; Hedrick, J. L.; Dravid, V. P.; Mirkin, C. A. Structural Evolution of Three-Component Nanoparticles in Polymer Nanoreactors. *J. Am. Chem. Soc.* **2017**, *139*, 9876–9884.

(207) Ranganathan, S. Alloyed Pleasures: Multiatomic Cocktails. *Curr. Sci.* **2003**, *85*, 1404–1406.

(208) Yeh, J.-W.; Chen, S.-K.; Lin, S.-J.; Gan, J.-Y.; Chin, T.-S.; Shun, T.-T.; Tsau, C.-H.; Chang, S.-Y. Nanostructured High-Entropy Alloys with Multiple Principal Elements: Novel Alloy Design Concepts and Outcomes. *Adv. Eng. Mater.* **2004**, *6*, 299–303.

(209) Murty, B. S.; Yeh, J.-W.; Ranganathan, S. *High-Entropy Alloys*; Butterworth-Heinemann, 2014.

(210) Li, Z.; Pradeep, K. G.; Deng, Y.; Raabe, D.; Tasan, C. C. Metastable High-Entropy Dual-Phase Alloys Overcome the Strength–ductility Trade-Off. *Nature* **2016**, *534*, 227.

(211) Ye, Y. F.; Wang, Q.; Lu, J.; Liu, C. T.; Yang, Y. High-Entropy Alloy: Challenges and Prospects. *Mater. Today* **2016**, *19*, 349–362.

(212) Eustathopoulos, N.; Nicholas, M. G.; Drevet, B. B. *Wettability at High Temperatures*; 1999; Vol. 3.

(213) Lukas, M.; Meded, V.; Vijayaraghavan, A.; Song, L.; Ajayan, P. M.; Fink, K.; Wenzel, W.; Krupke, R. Catalytic Subsurface Etching of Nanoscale Channels in Graphite. *Nat. Commun.* **2013**, *4*.

(214) Tao, F.; Grass, M. E.; Zhang, Y.; Butcher, D. R.; Renzas, J. R.; Liu, Z.; Chung, J. Y.; Mun, B. S.; Salmeron, M.; Somorjai, G. A. Reaction-Driven Restructuring of Rh-Pd and Pt-Pd Core-Shell Nanoparticles. *Science (80-.).* **2008**, *322*, 932–934.

(215) Newton, M. A.; Belver-Coldeira, C.; Martínez-Arias, A.; Fernández-García, M. Dynamic in Situ Observation of Rapid Size and Shape Change of Supported Pd Nanoparticles during CO/NO Cycling. *Nat. Mater.* **2007**, *6*, 528–532.

(216) Tao, F.; Dag, S.; Wang, L. W.; Liu, Z.; Butcher, D. R.; Bluhm, H.; Salmeron, M.; Somorjai, G. A. Break-up of Stepped Platinum Catalyst Surfaces by High

Co Coverage. *Science (80-.).* **2010**, *327*, 850–853.
(217) Lu, P.-H.; Ai, F.; Xie, D.-G.; Liu, B.-Y.; Zhang, Z.-R.; Jin, M.-S.; Zhang, X. F.; Ma, E.; Li, J.; Shan, Z.-W. Highly Deformable and Mobile Palladium Nanocrystals as Efficient Carbon Scavengers. *arXiv* **2017**, *1802*, 207.
(218) Combe, N.; Jensen, P.; Pimpinelli, A. Changing Shapes in the Nanoworld. *Phys. Rev. Lett.* **2000**, *85*, 110–113.
(219) Wang, C. C.; Li, Q. J.; Chen, L.; Cheng, Y. H.; Sun, J.; Shan, Z. W.; Li, J.; Ma, E. Ultrafast Shape Change and Joining of Small-Volume Materials Using Nanoscale Electrical Discharge. *Nano Res.* **2015**, *8*, 2143–2151.
(220) Xie, D. G.; Wang, Z. J.; Sun, J.; Li, J.; Ma, E.; Shan, Z. W. In Situ Study of the Initiation of Hydrogen Bubbles at the Aluminium Metal/oxide Interface. *Nat. Mater.* **2015**, *14*, 899–903.
(221) Porter, D. A.; Easterling, K. E.; Sherif, M. Y. *Phase Transformations in Metals and Alloys*; Third Edit.; CRC Press, 2009.
(222) Wang, D.; Li, Y. One-Pot Protocol for Au-Based Hybrid Magnetic Nanostructures via a\rNoble-Metal-Induced Reduction Process. *J. Am. Chem. Soc.* **2010**, *132*, 6280–6281.
(223) Considine, D. M. *Chemical and Process Technology Encyclopedia*; CRC press, 1974.
(224) Xin, L.; Yongqiang, H.; Husheng, J. Pt-Rh-Pd Alloy Group Gauze Catalysts Used for Ammonia Oxidation. *Rare Met. Mater. Eng.* **2017**, *46*, 339–343.
(225) Bagot, P. A. J.; Kruska, K.; Haley, D.; Carrier, X.; Marceau, E.; Moody, M. P.; Smith, G. D. W. Oxidation and Surface Segregation Behavior of a Pt-Pd-Rh Alloy Catalyst. *J. Phys. Chem. C* **2014**, *118*, 26130–26138.
(226) Chernyshov, B. V. I.; Kisil, I. M. Platinum Metals Catalvtic Systems in Nitric Acid Production. *Platin. Met. Rev.* **1993**, *37*, 136–143.
(227) Hu, X.; Ning, Y.; Chen, L.; Shi, Q.; Jia, C. Physical Properties and Application Performance of Platinum-Palladium-Rhodium Alloys Modified with Cerium. *Platin. Met. Rev.* **2012**, *56*, 40–46.